The University of Nottingham

UNITED KINGDOM · CHINA · MALAYSIA

Department of Electrical and Electronic Engineering

Faculty of Engineering

Robust feedback control of flow separation using plasma actuators

Laura Pasquale

Thesis submitted to The University of Nottingham
for the degree of Doctor of Philosophy, May 2017

Abstract

This thesis addresses the problem of controlling the unsteady flow separation over an aerofoil using plasma actuators, with the aim of improving the performance of fluid systems through the use of robust feedback controllers. Despite the complexity of the dynamics of interest, it is shown how the problem of controlling flow separation can be successfully formulated and solved as a simple output regulation problem.

First, a novel control-oriented reduced-order model for nonlinear systems evolving on attractors is obtained. Its application to the incompressible Navier-Stokes equations is proposed, in order to obtain a linear reduced-order model (whose state variables have a clear and consistent physical meaning) of the complex flow/actuator dynamics.

On the basis of the proposed model, a new robust multivariable feedback control algorithm for flow separation suppression is designed, using real-time velocity measurements, which are available in realistic applications. The presented control scheme is tested in both Single-Input-Single-Output (SISO) and Multi-Input-Multi-Output (MIMO) configurations, thus allowing for optimising the closed-loop system, with the aim of selecting suitable numbers and positions of the actuator/sensor pairs along the aerofoil, as well as desired references for the real-time measurements, according to the specific application (*e.g.*, flow separation suppression, mixing enhancement *etc.*).

Accurate numerical simulations of incompressible flows around both 2D aerofoils and 3D wings are performed in order to optimise the closed-loop system and illustrate the effectiveness of the proposed approach in the presence of complex dynamics that are neglected at the design stage. Robust performances, with respect to both parameter variations (*e.g.* geometry of the domain and Reynolds

number) and model uncertainties, are demonstrated. The designed controller is able to effectively suppress the flow separation along the aerofoil, as well as the shedding vortices, thus yielding both a reduction of the drag and an increase of the lift. This allows for stall avoidance and increased efficiency.

List of Publications

[1] Pasquale, L., Broglia, R., Choi, K.-S., Durante, D., and Zanchetta, P. (2017). Robust control of flow separation over a pitching aerofoil using plasma actuators. *IFAC-PapersOnLine*, 50(1): 11120-11125, `https://doi.org/10.1016/j.ifacol.2017.08.1000`.

[2] Broglia, R., Durante, D., and Pasquale, L. (2017). Robust feedback control of two and three dimensional flow separation around a NACA0012 profile using plasma actuators. The *ERCOFTAC Workshop Direct and Large Eddy Simulation*, Pisa, Italy.

[3] Pasquale, L., Durante, D., Diez M., and Broglia, R. (2017). Optimized DBD plasma actuator system for the suppression of flow separation over NACA0012 profile. The 7th *Conference on Computational Methods in Marine Engineering*, Nantes, France.

[4] Pasquale, L., Zanchetta, P., Houston, P., and Morvan, H. (2015). Model-Reduction for closed-loop control of unsteady aerodynamic flows using plasma actuators. *SIAM International Conference on Computational Science and Engineering*, Salt Lake City, USA.

Contents

List of Symbols

$\langle C_D/C_L \rangle$ Time-averaged drag-to-lift ratio

$(\cdot)^\dagger$ Moore-Penrose pseudoinverse of $(\cdot)$

$(\cdot)^\mathrm{H}$ Conjugate transpose of $(\cdot)$

$(\cdot)^\mathrm{T}$ Transpose of $(\cdot)$

$\bar{\mathrm{x}}$ DMD reduced-order state vector

$\bar{\mathrm{y}}$ DMD approximated output vector

$\bar{F}$ Reduced-order $m \times m$ DMD state matrix

$\bar{G}$ Reduced-order $m \times n_a$ DMD input matrix

$\bar{H}$ Reduced-order $n_s \times m$ DMD output matrix

$\bar{x}_a$ Actuator's location on the aerofoil, with respect to the chord length

$\bar{x}_s$ Sensor's location on the aerofoil, with respect to the chord length

β Angle of attack

$\boldsymbol{\alpha}$ Multi-index

$\boldsymbol{\nu}_j$ Ritz vectors

$\boldsymbol{\tau}$ Wall-tangential unit vector

$\boldsymbol{\zeta}$ Vector-valued observable

$\boldsymbol{f}$ Non-dimensional body force

$\boldsymbol{f}^{(j)}$ Force distribution of the j-th actuator

$\boldsymbol{g}$ Inflow boundary condition

$\boldsymbol{n}$ Wall-normal unit vector

$\boldsymbol{u}$ Non-dimensional velocity vector

$\boldsymbol{u}_h$ Finite element velocity vector approximation

$\boldsymbol{U}_\infty$ Non-dimensionalised inflow velocity vector

$\boldsymbol{x}$ Non-dimensional coordinate vector

$\boldsymbol{x}_a$ Actuator's location

$\boldsymbol{x}_s$ Sensor's location

Δt Discrete time step

Δ_s Distance between sensor/actuator pairs, with respect to the chord length

η Unknown matched disturbance

Γ_N Aerofoil boundary

Γ_R Rectancular channel boundary

Γ_0 Wall boundary

Γ_{in} Inflow boundary

Γ_{out} Outflow boundary

$\hat{\eta}$ Estimate of the unknown disturbance

$\hat{\text{v}}^*$ Estimated input reference

Λ Eigenvalue matrix

λ_k^{POD} k-th eigenvalue of R

λ_j Ritz values

Λ_s Stable part of eigenvalue matrix

Λ_u Unstable part of igenvalue matrix

$\mathbb{C}^n$ n-dimensional complex coordinate space

$\mathbb{P}_s$ Projection operator onto stable subspace

$\mathbb{R}^n$ n-dimensional real coordinate space

$\mathcal{C}$ Closed-loop configurations

$\mathcal{F}(\cdot)$ Nonlinear function of the state variables

$\mathcal{K}_m$ Left m-th dimensional Krylov subspace

$\mathcal{L}_m$ Right m-th dimensional Krylov subspace

$\mathcal{U}$ Infinite-dimensional Koopman operator

$\mathcal{V}(\cdot)$ Lyapunov function

μ Contro gain for nonlinear term

ν Kinematic viscosity

Ω Open bounded domain

ω_j Frequency of j-th Koopman mode

ω_j Frequency of j-th Koopman mode

Ω_ε Reference set

$\partial\Omega$ Boundary of the domain

Φ Trial basis

$\Phi(\boldsymbol{\theta}_i)$ Aggregate function

ϕ_j Koopman eigenfunctions

Φ_r Balanced POD trial basis

Ψ Test basis

Ψ_r Balanced POD test basis

$\boldsymbol{q}$ State variable for incompressible flows

ρ Fluid density

ρ_j Growth rate of j-th Koopman mode

Σ Hankel matrix

σ_i Hankel singular values

$\mathrm{d} \cdot / \mathrm{d} t$ Time-derivative operator

v   Control input

v*   Input reference vector

x   Full-order state vector

y   Control output

y*   Output reference vector

z   Full-order adjoint state vector

Θ_r POD basis

Θ_r POD orthonormal basis

$\tilde{\boldsymbol{\nu}}_j$ Koopman modes

$\tilde{\chi}$ Closed-loop state vector

$\tilde{\eta}$ Input tracking error

$\tilde{\lambda}_j$ Koopman eigenvalues

$\tilde{\mathrm{y}}$ Output tracking error

$\tilde{\xi}$ State tracking error

ε_M Upper bound of output reference set

ε_m Lower bound of output reference set

ϑ_k POD modes

ξ Reduced-order state vector

ξ^* State reference vector

A Reduced-order $r \times r$ state matrix

A_c Closed-loop reduced order matrix

$a_j(t)$ POD coefficients

B Reduced-order $r \times n_a$ input matrix

C Reduced-order $n_s \times r$ output matrix

c Chord length

C_D Drag coefficient along streamwise x-axis

C_L Lift coefficient along normal y-axis

d Dimension of the geometry

E Full-order $n \times n$ mass matrix

F Full-order $n \times n$ state matrix

F_x Total force along streamwise axis per span length

f_x Streamwise component of the total plasma body force in N/m^3

F_y Total force along normal axis per span length

f_y Normal component of the total plasma body force in N/m^3

G Full-order $n \times n_a$ input matrix

H Full-order $n_s \times n$ output matrix

h_c Channel height

I_r $r \times r$ identity matrix

k Integral control gain

L Left eigenvector matrix

L^2 Lebesgue space of square-integrable functions

m Dimension of DMD model

$MODPSO$ Multi-objective deterministic particle swarm optimisation

N Number of cell-centre grid nodes

n Dimension of full-order model

n_a Number of actuators

n_p Number of actuator/sensor pairs

n_s Number of sensors

p Non-dimensional pressure

$P(0)$ Steady-state gain

$P(s)$ Open-loop transfer function

P_r Projection operator

$Q(s)$ Closed-loop transfer function

R Correlation matrix

R Right eigenvector matrix

r Dimension of reduced-order model

Re Reynolds number

S Companion matrix

s Laplace domain variable

T Non-dimensional final time

t Non-dimensional time

t_0 Feedback controller activation time

t_f Feedback controller de-activation time

U Left singular vectors

U_m Non-dimensionalised inflow velocity

U_∞ Free-stream velocity

V Right singular vectors

V_i^m Full-order data vector space of rank m with initial vector $\mathrm{x}^{(i)}$

W_c Controllability Gramian

W_o Observability Gramian

W_r POD eigenvector matrix

Z Adjoint impulse responses matrix

$\boldsymbol{v}_i^k$ Velocity of the i-th particle at the k-th iteration

$\mathcal{V}_{ijk}$ Control volume

$\boldsymbol{\mathcal{R}}_{ijk}$ Sum of the body forces and the flux balance

u_τ Wall-tangential velocity

$\boldsymbol{\theta}_i^k$ Position of the i-th particle at the k-th iteration

$\mathbf{g}_i$ Social attractor

$\mathbf{p}_i$ Cognitive attractor

DMD   Dynamic Mode Decomposition

POD   Proper Orthogonal Decomposition

ROM   Reduced-Order Model

UAV   Unmanned Aerial Vehicles

X   Snapshot matrix

List of Figures

List of Tables

Chapter 1

Introduction

Flow control is a fast growing multidisciplinary science aimed at modifying the boundary layer in order to alter natural flow states into desired target states, which are chosen depending on control objectives. Crucial examples are: manipulation of flow separation and flow reattachment (aimed, for example, at drag reduction or stall prevention), noise suppression, mixing enhancement and increase of combustion efficiency. Within this context, feedback controllers are pivotal, as they can achieve a full and efficient regulation of the flow field in real-time (see Kim and Bewley, 2007). In particular, the incorporation of control theory into many open problems in fluid mechanics presents a host of new opportunities, with a wide range of applications in disparate fields, *e.g.* wind (Whittlesey et al., 2010) and gas turbines (Huang et al., 2006), aircraft (Cho and Shyy, 2011), trains (Baker et al., 2004; Baker, 2010), as well as road (Grandemange et al., 2014) and marine vehicles (Dean and Bhushan, 2010). Among the several benefits yielded by boundary layer control, increased lift and reduced drag due to separation suppression would result in improved efficiency and reduced pollution in most energy and transportation applications: *e.g.* wind turbines, Unmanned Aerial Vehicles (UAVs), ground and marine vehicles *etc.* The transport sector is responsible itself for approximately 20% of global energy consumption (see, for example, Brunton and Noack, 2015). Thus, even a small improvement in the performance of transport systems would have a dramatic effect (see Gad-el Hak, 1989; Gad-el Hak and Tsai, 2006; Kim, 2011). The CO_2 emissions due to the automotive transport only are expected to increase by 57% by 2030 (Brunton and Noack, 2015). A large portion of this emission is due to aerodynamic drag (Gilliéron and Kourta, 2010; Grandemange et al., 2014).

1

The area of feedback flow control incorporates essential and non-trivial elements of fluid dynamics, numerical methods and control theory. This is why there has been an increased participation of researchers in apparently disparate fields. Considerable efforts have been directed towards developing and evaluating control strategies for wall-bounded turbulent flows over the past three decades (el Hak, 2000). However, communication barriers due to the disparate skill sets have historically led to slow progress (Cattafesta and Sheplak, 2011); consequently, there are several unsolved key issues which need to be addressed (Bewley, 2001; Collis and Joslin, 2004). In the remainder of the chapter, the main challenges in the flow control framework are discussed, namely: both the potential and drawbacks of feedback over the other flow control methods; the choice of the actuator and its modelling; the issues in efficiently modelling the complex flow/actuator dynamics, in view of the control design; the choice of the output measurements, in view of realistic applications.

1.1 Flow control methods

Flow control strategies can be either passive or active; active methods are categorised based on the actuation system response to changes in the flow, *i.e.*, open-loop (feedforward) or closed-loop (feedback) control. Optimised aerodynamic shapes, compliant surfaces, riblets, steady blowing/suction, as well as the evolutionary design of the skin of fish are all examples of passive flow control. Animal motion has inspired the development of passive turbulence control methods, which lead to significant advances in engineering flows (see, for example, Brunton and Noack, 2015). For instance, the tubercles of the humpback whale flipper may function to generate vortices by excitation of flow to maintain lift and prevent stall at high angles of attack. The shape of sharks, dolphins, and whales yields a low drag per volume (see, for example, Ahlborn, 2006). The boundary layer transition is delayed by the compliant skin of dolphins and the same form of transition delay is under investigation for submarine applications. Though early studies showed dramatic drag reduction benefits, later studies have only been able to confirm 7 per cent drag reduction (see Choi et al., 1989). Sharks reduce drag either by means of denticles (by which riblets are inspired) on their skin or by ejecting lubricants during high-speed chases of their prey (Dean and Bhushan, 2010; Hoyt, 1975). Bechert et al. (1997a) showed it is possible to obtain an 11% drag re-

duction in laboratory experiments by using riblets. The latter were tested on an Airbus passenger aeroplane, yielding a $2 - 3\%$ reduction in fuel consumption (see Bechert et al., 1997a). Lubricants were shown to yield up to 80% drag reduction in pipelines by adding polymer molecules to pipe flows (see, for example Frings, 1988). While this works well for the latter scenario, in which the polymer remains mixed and active throughout the length of the pipe, its application to external flows is not straightforward. For long-range applications, the polymer solution must be continuously injected in order to yield drag reduction on external flows. This would require large quantities of the solution to be used and, thus, make the strategy inefficient in terms of overall energy use (Dean and Bhushan, 2010).

The optimised shape of an aerofoil (see, for example Maki et al., 2012) is another example of passive control, which is inherently open-loop, as it cannot respond to changes in the flow state. The idea, which was proposed in Stratford (1959), is to enforce the skin friction to be just above zero along the surface. Based on this concept, an inverse design of the aerofoil shape was proposed by Liebeck (1978) in order to enhance the lift-to-drag ratio. The main drawback of these passive methods is that separation might occur whenever the angle of incidence is increased by few degrees.

The main advantage of passive actuation (e.g., Bechert et al. (1997b); Choi et al. (2011); Fukagata et al. (2000); Xu et al. (2003)), is simplicity. Passive control techniques are indeed lighter, less expensive and easier to maintain compared to active ones thereby making them the only ones that have been used in real-world applications so far, *e.g.* transport systems, wind turbines *etc.* On the other hand, there is only a very limited range of operating conditions over which passive control strategies may be effective. Furthermore, there may even be conditions for which passive control degrades system performance, since the control itself could initiate new instabilities: a significant example is the case of riblets in Bechert and Bartenwerfer (1989) used for drag reduction in turbulent boundary layers. In the best case, riblets yield approximately $5 - 11\%$ drag reduction (Bechert and Bartenwerfer, 1989; Bechert et al., 1997a) depending on their detailed geometric configuration, whilst active flow control strategies could achieve a much greater reduction in similar situations (see, for example, Collis and Joslin, 2004). For instance, Pfeiffer and King (2012) obtained a drag reduction of around 25% using active flow control strategies. The reason for this difference is due to the fact that passive control techniques produce a steady, feedforward action, which does not

take into account eventual changes in time of the physical system being controlled. Therefore, passive methods can successfully target only known, constant disturbances. Active control techniques are thus needed in order to face more realistic operating conditions.

Recent works on active flow separation control proposed open-loop approaches (see, for example, Karabelas et al., 2012; Riherd and Roy, 2013; Sato et al., 2015b; Skarolek and Karabelas, 2016). Active open-loop strategies assume exact knowledge of the system and do not respond to changes in the flow state or unknown disturbances, as the actuator parameters are set off-line at the design stage. Although a good understanding of open-loop dynamics is required in order to design closed-loop controllers, the lack of feedback implies that the high potential of active control systems is not exploited. Early studies (see, for example, Gaitonde et al., 2005; Greenblatt and Wygnanski, 2000; Moreau, 2007; Seifert et al., 1996) focused on open-loop strategies for separation control on aerofoils in order to improve the understanding of flow physics as well as the development and testing of actuators. In the recent work of Skarolek and Karabelas (2016), open-loop strategies for total drag reduction and lift increase are proposed to control the flow past an aircraft wing using blowing surfaces, placed close to the trailing edge. However, the main drawback of open-loop control is its great sensitivity to disturbances which heavily affects system performance, in particular, in conditions that exceed the design envelope. Therefore, if disturbances that are not accounted for in the model are present, the controller will in general fail.

The application of linear feedback controllers to fluid systems has been proposed by several authors in different fields. The control algorithm is usually designed based upon simple linear approximations of the actual complex nonlinear dynamics. For instance, both a pole placement and a Smith predictor approach are proposed in Litrico and Georges (1999) for the automatic control of a dam-river system. A comparison, in terms of robustness, with the classical Proportional Integral Derivative (PID) method was performed on the one-dimensional open-channel flow dynamics. Simple Proportional (P) and Proportional Integral (PI) closed-loop controllers have been used in Seatzu (2000) to regulate the stored volumes in open-channel flow systems. In Gupta et al. (2011), a discrete internal model-based controller is used to compensate the pressure pulsations in a common rail fuel injection system of internal combustion engines, using piezoelectric actuators. The control design is based on a one-dimensional distributed model of

the fuel dynamics.

Compared to open-loop control approaches, closed-loop flow control can enhance aerodynamic performance with less control effort (Taira and Colonius, 2009) and reduce the influence of disturbances (Kutay et al., 2007; Santillo et al., 2007), since it uses information from the system in order to detect unknown disturbances which are not taken into account *a priori*, thereby making it more robust to deviations from the assumed model. However, one of the drawbacks of feedback flow control is the need of real-time measurements from the system. Thus, suitable sensors, as well as an *ad hoc* hardware interface for the acquisition of the real-time signals, are required. Furthermore, the coupled actuator and flow dynamics are not trivial to control: neither the analytical model, which results in a system of nonlinear Partial Differential Equations (PDEs), nor the high-dimensional discretised dynamics, are suitable for control design purposes. The dependence of the dynamical properties on the unknown flow and geometry parameters is highly nonlinear; since both sensors and actuators are located on the wall (*e.g.* along the aerofoil), most of the flow states are unobservable and uncontrollable (see Kim and Bewley, 2007).

Recent works on feedback flow separation control using plasma actuators include Benard et al. (2009), where a slope-seeking algorithm is proposed to obtain maximum time-averaged lift, which is measured by a three-component balance. Cho and Shyy (2011) proposed a retrospective cost adaptive algorithm to minimise the variation of the aerodynamic lift. However, the latter, which is the chosen output in both Benard et al. (2009) and Cho and Shyy (2011), cannot be measured in practical flow control applications.

The key objective of this thesis is to design a feedback algorithm for flow separation control using real-time velocity measurements, which are available in realistic applications.

1.2 Plasma actuators

The feedback control input is usually an electric signal, which has to be converted to a physical quantity by means of an actuator, *i.e.*, transducers that convert an electrical signal to a desired physical quantity. Active flow control requires the input of energy into the system, in order to interact with the flow by providing an electronically controllable disturbance. The main advantage of such systems is

their ability for real-time feedback control at high frequency.

Among all the active methods, a new and original technology using non-thermal surface plasmas has witnessed a significant growth in interest in recent years (see, for example, Cho and Shyy, 2011; Choi et al., 2011; Corke et al., 2007; Feng et al., 2015; Hanson et al., 2010; Moreau, 2007; Wang et al., 2013), as they: have no moving parts; exhibit an extremely fast time-response; are characterised, depending on the power converter design, by low mass and low input power (Cattafesta and Sheplak, 2011). Moreover, they can be easily incorporated into flow solvers so that their placement and operation can be optimised. Although initially considered useful only at low speeds, plasma actuators are effective in a number of applications Corke et al. (2007); Thomas et al. (2008) at high subsonic, transonic, and supersonic Mach numbers (see Samimy et al., 2007, for jet noise reduction applications), owing largely to more optimised actuator designs that were developed through better understanding and modelling of actuator physics (Unfer and Boeuf, 2009). These surface dielectric barrier discharge (DBD) actuators are used to accelerate the near-wall flow, thus modifying the velocity profile within the boundary layer. The ionised fluid results in a localised body force vector field, which acts on the overlying neutrally charged fluid. The plasma actuator AC voltage can be used as a control input so that the generated force directly affects the flow over the aerofoil(see Figure 1.1).

This specific DBD configuration used for plasma actuators consists of two elec-
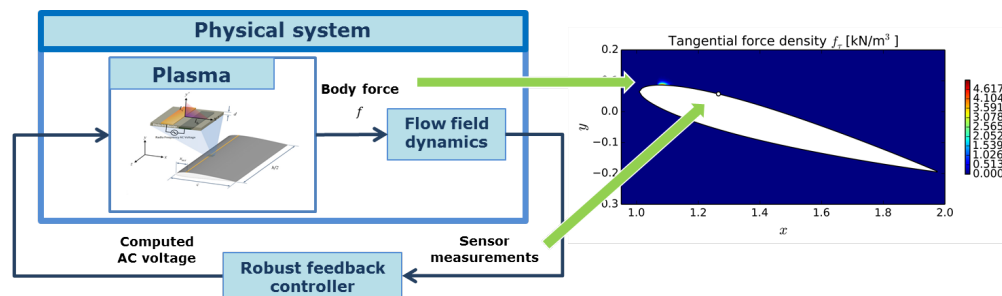
Figure 1.1: Schematic of the closed-loop system (plasma actuator from Corke et al., 2007).

trodes, one uncoated and exposed to air and the other encapsulated by a dielectric material; hence, this configuration is referred to as a single dielectric barrier discharge (SDBD). Electrodes are supplied with an AC voltage that, over a certain threshold, causes air over the covered electrode to weakly ionise. In the classic description, ionised air is a plasma, which is why these devices are referred to

as plasma actuators. In particular, air is ionised by increasing the amplitude of the electric field above the breakdown electric field E_b, which is the value needed to sustain electron-ion pairs in the gas in the absence of space-charge fields (see Kunhardt, 1980). The minimum breakdown electric field is a function of the driving frequency. Once created, the electric field needed to sustain the plasma is lower than E_b. The minimum difference between breakdown and sustaining electric fields is a function of the operating conditions (see Corke et al., 2010). In the presence of the electric field produced by the asymmetric electrode geometry, ionised air results in a localised body force vector field, which is directed downstream in most aerodynamic control applications. The mechanism of flow control exploited by these devices results in a body force vector field that couples with the momentum equations, describing the external flow dynamics. The time scale disparity between the flow and the discharge frequencies allows for assuming that the force acts on the neutral fluid in a quasi-steady manner. The body force felt by the neutral flow is equivalent to the electro-magnetic force acting on the net charge density.

Since the control input is the AC voltage, it is necessary to define the relation between the latter and the resulting body force, in order to design a model-based controller. Several models for the DBD actuator force have been proposed (see, for example, Corke et al., 2007, for a detailed review). Kotsonis et al. (2011) interpolated the body force expression from experimental measurements. Unfer and Boeuf (2009) analytically modelled and numerically simulated SDBD plasma dynamics coupled with compressible flow dynamics, but such an accurate model is not tractable for real-time control applications due to both the presence of several unknown and unobservable parameters (such as ion temperature) and the high computational cost. In contrast, Jayaraman and Shyy (2008); Shyy et al. (2002) proposed a simplified bilinear model, which is widely used in the flow control literature (see, for example, Cho and Shyy, 2011), because of its simplicity. The model assumes that the electric field lines are parallel in most of the region, except the small space near the cathode. The variation in space of the electric field, which is directly proportional to the electro-magnetic force, is linearised, without computing the detailed electric field. The resulting body force is approximated as an electro-magnetic force; other terms, such as the ones due to thermal energy, are neglected. Since the former is proportional to the bilinear electric field, the body force is characterised by a linear space dependence. The prescribed body

forces are localised in a triangular plasma region (see figure 1.2) bounded by two
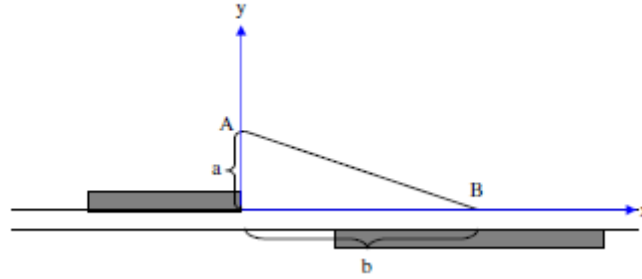
Figure 1.2: The line AB constitutes the plasma fluid boundary using linear approximation. The electric field strength outside this line is not strong enough to ionise air. Jayaraman and Shyy (2008).

electrodes and the dielectric surface. This approximation is not consistent with experiments (see, for example, Enloe et al., 2004; Orlov et al., 2006), which show an exponential spatial decay. As a result, the model over-predicts the actuator effect and it introduces further inaccuracies, which might affect model-based controllers.

In this thesis, a modified version of the recent model proposed by Yang and Chung (2015) is presented: it is characterised by an exponential dependence on the spatial coordinates and is demonstrated to yield good agreement with experimental data.

1.3 Model reduction methods

It is very difficult to obtain an accurate control-oriented model of the coupled neutrally-charged fluid and plasma dynamics and, at the same time, to design an effective control scheme that relies on such a sufficiently accurate model. In this regard, a key consideration often under-appreciated in the field of fluid mechanics is the following: "*a system model that is good enough to use for control design is not necessarily good enough for accurate numerical simulation*" (Kim and Bewley, 2007). Indeed, one has to consider that feedback controllers compute control signals on-line, based on sensor measurements and control law, which is designed upon the assumed model. This is a very challenging task from a computational point of view, as the spatial discretisation of the Navier-Stokes equations yields a very high-dimensional system ($\sim 10^4 - 10^6$ state variables, depending on the grid

resolution). Furthermore, turbulence is a multi-scale phenomenon with significant dynamics evolving relatively far from the wall, where sensors and actuators are located (*e.g.* along the aerofoil). Thus, a control-oriented model mainly needs to capture the system dynamic response, that is the relation between inputs and outputs and their influence on the "quantity of interest" (which depends on the desired target state), while taking into account both computational cost and model accuracy.

In view of the above, the introduction of reduced-order models (ROMs) is of particular interest in flow control problems (Ravindran, 2002). A ROM can be computed, using either simulation or experimental data, through either system identification methods (see, for example, Astolfi, 2010b,a; Cho and Shyy, 2011; Hanson et al., 2014; Huang and Kim, 2008; Ionescu and Astolfi, 2011) or projections of the system equations onto lower-dimensional subspaces (see, for example, Bai, 2002; Benner, 2009; Bergmann et al., 2009; Bergmann and Cordier, 2008; Bistrian and Navon, 2014; Bui-Thahn, 2008; Willcox et al., 2007; Caiazzo et al., 2014; Cammilleri et al., 2013; Fujimoto and Hikaru, 2006; Ilak et al., 2010; Ilak and Rowley, 2008, 2006; Joshi et al., 2007), with the aim of capturing the system dynamic response by retaining only few fundamental dynamic modes. Since a dedicated flow model is based on the explicit description of the relevant dynamics, the former can convey a clear understanding of the underlying physics of the problem, which is very important for control system design, including the choice of measurements, actuation and objectives (see, for example, Cho and Shyy, 2011; Collis and Joslin, 2004). On the other hand, a high fidelity model - such as Direct Numerical Simulation (DNS) - that provides the entire state of the flow field on the whole spatial domain is very expensive and unrealistic for practical real-time control applications (Moin and Temam, 2001).

In general, there is a wide range of approaches, based on either physics, mathematics or data fitting, that could be used to construct a reduced-order model. In practice, a reduced-order model may be a hybrid of one or more of these approaches. Model reduction in physics-based, ROMs is accomplished by neglecting some physical processes whilst accounting for the ones that are relevant for the system under consideration. Reynolds-Averaged Navier-Stokes (RANS) equations and Large Eddy Simulations (LES) are examples of physics-based reduced-order models. However, this reduction is not sufficient to make the resulting model available for real-time applications (Collis et al., 2000).

Data fitting methods, such as system identification (see, for example, Huang and Kim, 2008) or neural networks (see, for example, Lee et al., 1997), provide an input-output model, constructed by employing data from either high-fidelity numerical simulations or laboratory measurements. They are particularly suitable for applications with few control variables and problems where physical models are unknown or unavailable. Since the reconstruction of the flow field dynamics is not performed, the general input-output model involves a reduced set of information than model-based approaches to achieve the control objectives. Although input-output models lack a detailed description of the evolution of flow structures, the relation between actuation and measurable responses is directly accessible. Moreover, if the key dynamics of a flow system are properly captured, this "less-modelling" approach can reduce sensitivity of the control system to model uncertainties. Input-output models adopted in most flow control studies are based on linear time-invariant models and are represented by rational transfer functions or time-series models, whose coefficients can be estimated by various system identification techniques. Consequently, the state variables in an identified system do not usually have obvious physical meaning. Therefore, the control objectives may be more challenging to define. Some examples based on this approach include rejection of pressure fluctuations over an aerofoil (Tian et al., 2006), mitigation of unsteady flow speed in a channel (Santillo et al., 2007), and reduction of flow separation (Huang and Kim, 2008).

Mathematical model reduction techniques perform a projection of model equations onto a reduced basis of a low-dimensional subspace. In particular, reduced-order nonlinear models are obtained by representing the flow field as a linear combination of an appropriate set of basis functions, *i.e.*, by performing a projection of the governing equations onto a truncated set of those basis functions. The latter usually represents the spatial structure of flows, so that projection results in a system of coupled non-linear ordinary differential equations (ODEs) that has to be solved for the temporal amplitude functions corresponding to each basis function. The main difference between the usual Galerkin discretisation and the one for model reduction is the choice of the basis functions. In traditional discretisation methods (such as finite element methods), the latter are typically chosen *a priori* such that the resulting numerical method will be a compromise between accuracy, numerical efficiency and geometric flexibility. Conversely, basis functions for reduced-order models are chosen in order to capture the relevant physics of the considered system

using the fewest number of basis functions possible, thus leading to the greatest reduction in the size of the discrete problem.

Nevertheless, there are still many open questions that need to be considered: how to select a basis that captures only the relevant physics? How to retain the fundamental dynamical properties of the original system? How could the bases be adapted for closed-loop applications, for which the dynamics is substantially altered from that of uncontrolled flows?

1.3.1 Energy-based models

A classic and widely used mathematical technique for model reduction is the Karhunen-Loeve expansion also known as Proper Orthogonal Decomposition (POD), pioneered by Lumley (1967). The idea is, given a set of data (for instance, numerically or empirically obtained velocity and pressure) that lies in a vector space $\mathcal{V}$, find a subspace $\mathcal{V}_r$ of fixed dimension r such that the error in the projection onto the subspace is minimised. The space $\mathcal{V} \subset \mathbb{R}^n$ has finite dimension $n \gg r$, if the equations have already been discretised in space. The main result of POD is that the optimal subspace $\mathcal{V}_r$ is spanned by a set of orthonormal basis functions, the so-called POD modes, that contain a decreasing amount of total flow kinetic energy. The methodology proceeds by projecting the full non-linear system onto that set of basis functions. POD modes are, by design, optimal in an energy norm (L^2); that is, POD modes are the best choice in representing the energetics of a given data set. The first few POD basis functions, which are the most energetic eigenmodes, often capture a significant percentage of the relevant flow dynamics, thus suggesting that a truncated POD basis may be a promising approach to constructing reduced-order models.

However, despite substantial efforts in developing efficient reduced-order models, there are still many unsettled issues, such as how to incorporate control with POD modes (Collis and Joslin, 2004). Indeed, one potential limitation of POD (and other related methods for reduced-order models) is that the basis functions are intrinsic to a particular flow so that, as a flow is modified by the action of control, the POD basis (and the reduced-order model based on that POD) must also change. Consequently, a reduced-order model constructed from a subset of POD basis functions for one particular flow, often taken to be the uncontrolled flow, would certainly not be optimal and may not even successfully represent the dynamics of the controlled flow under some circumstances (see, for example, Prahbu

et al., 2000).

Ravindran (2002) proposed a reduced-order non-linear adaptive control of flow separation in a forward-facing step channel flow in which the reduced-order model and the optimal control input are updated, every fixed time interval, using the method of snapshots (see, for example, Ravindran, 2000) to compute POD modes. The idea behind the adaptive procedure is to compute snapshots of the flow field for some discrete times and, then, use those snapshots to construct the POD subspace in order to improve the reduced-order model and reflect the changes in the dynamics, which is altered by the controller. Although this adaptive procedure requires some additional cost compared to classic POD, it was found to be effective and feasible for real-time applications.

The key question is whether the essential flow physics is modelled by the retained modes (Kim and Bewley, 2007). In particular, the POD-based reduced-order models, in which low-energy modes are truncated, do not account for observability and controllability of the modes being truncated. Consequently, some retained modes may nearly be uncontrollable or unobservable, whereas some truncated modes actually play a more pivotal role in the input-output transfer function of the open-loop system. This is demonstrated by Rowley (2005): POD-based reduced-order model showed dynamics that were significantly different than those of the original system.

1.3.2   Control-oriented models

System identification methods yields input-output control-oriented models. For instance, in Cho and Shyy (2011), the Eigensystem Realisation Algorithm (ERA) - a system identification method introduced by Juang and Pappa (1985) - was applied to the impulse responses of the aerodynamic lift, in order to obtain a linear model, upon which the controller was designed. Ma et al. (2011) showed that ERA yields the same ROMs as the balanced truncation (Moore, 1981), in the case of stable, linear systems but the physical meaning of the state-variables is lost. On the other hand, the projection of large-scale problems onto lower-dimensional subspaces, which are based on the explicit description of the flow dynamics, can convey a clearer understanding of the underlying physics of the problem, compared to system identification approaches. In particular, the former approach can provide insight into the key spatial modes of fluid/structure systems, contrarily to black-box identification techniques (see Annoni and Seiler, 2015). This is very

important for control system design, since it leads to physically reasonable choices of measurements, actuation and objectives (see Collis and Joslin, 2004).

The most popular model reduction technique in the control community is the above-mentioned balanced truncation, a classic method developed by Moore (1981) for stable, linear systems, which was extended by Zhou et al. (1999) to unstable, linear systems. An approximated balanced truncation method, called balanced Proper Orthogonal Decomposition (POD), was extended by Rowley et al. (2010) to linear fluid systems and is based on a variant of the method proposed by Lall et al. (2002), which forms approximate empirical Gramians. Moreover, the balanced POD was extended by Ahuja and Rowley (2010) to unstable linear systems, when the dimension of the unstable subsystem is relatively small. The balanced POD projects the system onto the subspace spanned by the most observable and controllable modes and was shown to outperform the standard POD for closed-loop flow control applications (see Barbagallo et al., 2009; Ilak and Rowley, 2008). Scherpen (1993) described how to obtain a balanced realisation for certain classes of asymptotically stable nonlinear systems, using the observability and controllability functions. Later, Lall et al. (1999, 2002) extended the approximate balanced truncation to exponentially stable nonlinear systems by defining approximate observability and controllability Gramians, which result in the usual Gramians when the method is applied to stable, linear systems. This snapshot-based balancing approach requires only standard matrix computations and does not need data from adjoint simulations. The resulting reduced-order model is nonlinear and has inputs and outputs, which are suitable for control design purposes. The method has been successfully tested on a simple, low-order, nonlinear mechanical system. On the other hand, this approach involves considerably more computation than the balanced POD, and is not feasible for large systems (see Ilak and Rowley, 2008). Furthermore, this approximate balanced truncation cannot be applied to unstable, nonlinear systems, since the Gramians are not bounded and cannot be defined. Furthermore, the stable and unstable dynamics cannot be easily decoupled as in the linear case, for which a projection onto the stable subspace can be computed. Thus, in the case of unstable, nonlinear systems, the equivalence of this method (when applied to the stable dynamics of unstable, linear systems) to the usual balanced truncation is lost and the meaning of the approximate Gramians is not clear.

A nonlinear balanced realisation for possibly unstable nonlinear systems is investi-

gated in Scherpen and van der Schaft (1994), Fujimoto and Hikaru (2006), where normalised right and left coprime factorisations are introduced. Since the balanced truncation method is applicable only to asymptotically stable systems, the former was applied to a normalised coprime factorisation of the original model. Then, the reduced order model was derived from the one of the coprime factorisations. However, this method is not feasible for high-dimensional fluid systems, since it requires the solution of the Hamilton-Jacobi equations. A simpler, but presumably less effective approach is to project the full nonlinear equations onto the balanced POD modes computed for the linearised system; such a procedure involves no additional computational expense over the methods presented above and can be applied to unstable systems. This method was successfully applied by Ilak et al. (2010) for the model reduction of the nonlinear, complex Ginzburg-Landau equation, which can be used as a model for instabilities of spatially developing flows. Its linearised version has been used by Bagheri (2013) to model both globally unstable flows (so-called oscillators) and convectively unstable flows (so-called noise amplifiers) for feedback control purposes.

Several authors have focused on the feedback control of balanced POD models, based on the Navier-Stokes equations, linearised about a single steady trajectory, (see, for example, Ahuja and Rowley, 2010; Ahuja et al., 2007; Ahuja and Rowley, 2008; Barbagallo et al., 2009; Joshi et al., 2007; Lee et al., 2001). These linearisation-based approaches allows for the application of well-established linear model reduction methods. However, an accurate approximation of the nonlinear behaviour can only be obtained in a small neighbourhood of the considered trajectory, whose choice heavily affects the control performance. Moreover, the resulting model is unstable, in contrast with the typical stability properties of fluid systems. The key idea is, then, to take advantage of the effectiveness of this linear model reduction method, while avoiding the restrictions related to linearisation approaches.

A variant of the Arnoldi algorithm called Dynamic Mode Decomposition (DMD) was proposed by Schmid (2010) to approximate part of the spectrum of the Koopman operator (see Bagheri, 2013; Koopman, 1931). The latter is an infinite-dimensional linear operator describing the evolution of observables in the phase space, which has been used to analyse uncontrolled, nonlinear dynamical systems (see Mezić, 2013, 2005; Mezić and Banaszuk, 2004) evolving on an attractor. Rowley et al. (2009) showed that the DMD modes approximate some of the Koopman

modes, which can be interpreted as the eigenmodes of a finite-dimensional linear map that approximates the true, nonlinear one. This method does not rely on linearisation of the dynamics: indeed, it captures the full information of the nonlinear system. On the other hand, the order of the DMD linear model is high and depends on the number of linearly independent snapshots needed to describe the dynamics of interest. Furthermore, there are no well-defined selection criteria for selecting the DMD modes to be retained in the ROM (see Barbagallo et al., 2009), thereby making the use of DMD as a model reduction method less straightforward.

1.4 Aims and Objectives

The focus of this thesis is the robust control of unsteady flow separation using plasma actuators. As in many flow control applications, the objective is to suppress the separation bubble, which is responsible for both a loss of the lift and an increase of the drag and might lead to stall conditions.

In particular, the aim of this work is to show how, despite the high complexity of the system, a very simple robust output regulator is sufficient to effectively suppress the flow separation along an aerofoil, using the actuators' voltage as the control inputs and real-time velocity measurements, which are available in realistic applications (see, for example, Buder et al., 2008; Hanson et al., 2010; Ozaki et al., 2000; Segawa et al., 2010; Spazzini et al., 2001, 1999), as the control outputs. First, a novel control-oriented reduced-order model for nonlinear systems evolving on attractors is obtained. Its application to the incompressible Navier-Stokes equations is proposed, in order to obtain a linear reduced-order model (whose state variables have a clear and consistent physical meaning) of the complex flow/actuator dynamics. The method combines DMD, as an alternative to linearisation, and balanced POD, as a way to select the most observable and controllable DMD modes. The high-order DMD model is projected using the balanced POD modes, thus yielding a balanced, stable, linear ROM.

Furthermore, on the basis of the so-obtained model, the recent theoretical results in Marino and Tomei (2015) are extended to a wider class of control systems and propose their application to the specific flow separation control problem, which is of practical interest. A major advantage of the proposed approach is that the chosen outputs can be easily measured in realistic applications; moreover, the re-

sulting control scheme is simple and computationally cheap.

In particular, the problem of controlling flow separation along the aerofoil is formulated and solved as a simple output regulation problem, so that a simple control strategy may be used. A robust multivariable feedback control is designed for both Single-Input-Single-Output (SISO) and Multi-Input-Multi-Output (MIMO) configurations. This allows for optimising the closed-loop system, with the aim of selecting suitable numbers and positions of the actuator/sensor pairs along the aerofoil, as well as desired references for the real-time measurements, according to the specific application (*e.g.*, lift increase, drag reduction, stall avoidance *etc.*, for UAVs and wind turbines applications).

Accurate numerical simulations of incompressible flows past a NACA 0012 at different Reynolds numbers $Re \in [10^3, 2 \times 10^4]$ and time-varying angles of attack $\beta \in [5°, 25°]$ are performed in order to illustrate the effectiveness of proposed approach and validate the modelling assumptions, in the presence of uncertain parameters and complex nonlinear dynamics, which are neglected in the control design. The upper bound $Re = 2 \times 10^4$ of the considered range corresponds to the Reynolds number considered in the experimental works of Choi et al. (2011) and Feng et al. (2015). Robust performances, with respect to both parameter variations (*e.g.* geometry of the domain and Reynolds number) and model uncertainties, are demonstrated.

1.5 Structure of the thesis

Chapter 2 outlines a novel control-oriented model reduction method for nonlinear systems evolving on attractors. The proposed approach combines DMD, as an alternative to linearisation, and balanced POD, as a way to select the most observable and controllable DMD modes. The high-order DMD model is projected using the balanced POD modes, thus yielding a balanced, stable, linear ROM.

The application of the model reduction method to fluid systems is proposed to obtain a low-order, stable, linear model of the nonlinear flow/actuator dynamics, which are modelled in Chapter 3. An analytical model, based on the incompressible Navier-Stokes equations, which are coupled with the plasma dynamics through the body force that is generated by the actuator, is proposed. Its numerical discretisation is performed using two different numerical schemes: a finite element

method, which is used to both simulate low Reynolds number flows and obtain a simple low-order model of the flow dynamics, and an overlapping grid approach implemented in a second order, finite volume, multi-block, unsteady Reynolds-Averaged Navier-Stokes (RANS) equations based solver, which is used for more realistic simulations at higher Reynolds numbers.

Chapter 4 shows how the problem of controlling flow separation can be formulated as a simple output regulation problem, so that a simple control strategy may be used. A robust output regulator is designed, on the basis of the low-order, linear, dynamical model approximating the incompressible Navier-Stokes equations, presented in Chapter 2. The proposed control algorithm guarantees exponential output regulation when the steady-state gain of the approximated linear model is non-zero and of known sign. Fast flow reattachment is achieved, along with both stabilization and increase/reduction of the lift/drag, respectively. Accurate 2D finite element simulations of the full-order nonlinear equations illustrate the effectiveness of the proposed approach: good dynamic performances are obtained, as both the Reynolds number and the angle of attack are varied.

Chapter 5, extends the results obtained in Chapter 4 to MIMO configurations, with the aim of optimising the closed-loop system. The resulting robust multi-variable feedback control algorithm is designed and tested in different scenarios, in order to identify an optimal configuration. The proposed novel control algorithm only requires a non-zero steady-state gain of known sign for each actuator/sensor pair. Several 2D numerical simulations of incompressible flows around a pitching NACA 0012 at Reynolds $Re = 20,000$ are performed using the in-house developed finite volume solver, described in Chapter 3. Boundary layer separation suppression is achieved in both stationary and transitional regimes. Furthermore, accurate 3D simulations are performed to show the ability of the designed control algorithm to both regulate the transition to turbulence and suppress the flow separation, in the presence of realistic three-dimensional turbulent dynamics.

Appendix A shows the final assembly of the electronic interface for both data acquisition (real-time measurements from hot wire and piezoelectric cantilever sensors) and control of the high voltage power converter, which generates the plasma over the aerofoil. A functionality test is performed to evaluate the perfor-

mance of the circuit: an accurate data acquisition is achieved, along with a fast regulation of the converter's output voltage magnitude.

In Chapter 6 conclusions, potential applications and possible further developments are discussed.

Chapter 2

Control-oriented Model Reduction

The objective of this chapter is to obtain a rigorous, physics-based, control-oriented model of the flow/actuator dynamics, in view of the practical application to the flow separation control design. A novel model reduction method, whose state variables have a clear and consistent physical meaning, is proposed. The method combines DMD, as an alternative to linearisation, and balanced POD, as a way to select the most observable and controllable DMD modes. The high-order DMD model is projected using the balanced POD modes, thus yielding a balanced, stable, linear ROM.

2.1 Problem Statement and Objectives

Given any nonlinear high-order system of the form ($x = x(t) : \mathbb{R} \to \mathbb{R}^n$,
$\dot{x} = dx/dt$, $E \in \mathbb{R}^{n \times n}$, $\mathcal{F}(\cdot) : \mathbb{R}^n \to \mathbb{R}^n$, $G \in \mathbb{R}^{n \times p}$, $v = v(t) : \mathbb{R} \to \mathbb{R}^p$,
$y = y(t) : \mathbb{R} \to \mathbb{R}^q$)

$$\begin{cases} E\dot{x} & = \mathcal{F}(x) + Gv, \quad x(0) = x_0, \\ y & = Hx, \end{cases} \tag{2.1}$$

we obtain in this chapter a linear, stable reduced-order representation of 2.1, given by

$$\begin{cases} \dot{\xi} & = A\xi + Bv, \quad \xi(0) = \xi_0, \\ y & = C\xi, \end{cases} \tag{2.2}$$

under the assumption that the open-loop asymptotic trajectories of the full-order nonlinear dynamics (2.1) in the phase space evolve towards finite dimensional attractors. The objective is to transform system (2.1), which represents the spatially

19

discretised flow dynamics, into a simple, low-order linear system (2.2), which is suitable for control design purposes.

2.2 Reduced-order Modelling

The objective of a reduced-order model is to capture the essential physics of the flow to be controlled, while reducing the computational cost associated with computing the solution of the dynamic system. Of course, the key challenge is to determine a proper balance between complexity and accuracy, as well as between observability and controllability.

Most large-scale model reduction techniques perform a projection of model equations onto a reduced basis of a low-dimensional subspace. This projection approach can be described in general terms as follows. Consider the dynamical system

$$\begin{cases} F(\dot{x}(t), x(t), \vartheta, v(t)) = 0, & x(0) = x_0 \\ y = h(x(t), \vartheta, v(t)), \end{cases} \tag{2.3}$$

where $\vartheta \in \mathbb{R}^{N_\vartheta}$ is the parameter vector containing N_ϑ parameters of interest (*e.g.* the angle of incidence of the aerofoil or the Reynolds number) and F is the residual operator resulting from the spatial discretisation of the PDEs. The objective is to seek an approximate solution

$$x = \Phi x_r, \tag{2.4}$$

where $\Phi = [\varphi_1, ..., \varphi_r] \in \mathbb{R}^{n \times r}$ is the trial basis. We also introduce the test basis $\Psi \in \mathbb{R}^{n \times r}$, such that $\Psi^H \Phi = I_r$, where $(\cdot)^H$ denotes the conjugate transpose of $(\cdot)$ and I_r is the $r \times r$ identity matrix. The reduced-order model reads

$$\begin{cases} \Psi^H F(\Phi \dot{x}_r(t), \Phi x_r(t), \vartheta, v(t)) = 0, & x_r(0) = \Psi^H x_{r_0} \\ y = h(\Phi x_r(t), \vartheta, v(t)). \end{cases} \tag{2.5}$$

If the test space is the same as the trial space, *i.e.*, $\Psi = \Phi$, the reduced-order model (2.5) is obtained by representing the flow field as a linear combination of the basis functions and by performing a Galerkin projection of the governing equations. If the test space is different from the trial space, the reduced system (2.5) is obtained via a Petrov-Galerkin projection. Note that the scalar product can be weighted by the matrix E in order to obtain reduced-order models in the usual state-space form

$$\begin{cases} \dot{\xi} &= \Psi^H \mathcal{F}(\Phi \xi) + \Psi^H G v \\ y &= H \Phi \xi, \end{cases} \tag{2.6}$$

by projection of the dynamic system (2.1). The bi-orthogonality condition then reads

$$\Psi^{\mathrm{H}} E \Phi = I_r. \tag{2.7}$$

The basis functions represent the spatial structure of flows, thus that projection results in a system of coupled nonlinear Ordinary Differential Equations (ODEs) that has to be solved for the temporal amplitude functions corresponding to each basis function. The main difference between the usual Galerkin discretisation and the one for model reduction is the choice of the basis functions. In traditional discretisation methods, the latter are typically chosen *a priori* such that the resulting numerical method will be a compromise between accuracy, numerical efficiency and geometric flexibility. Conversely, basis functions for reduced-order models are chosen in order to capture the relevant physics of the considered system using the fewest number of basis functions, thus leading to the greatest reduction in the size of the discrete problem. Nevertheless, there are still many open questions that need to be considered: how to select a basis that captures only the essential dynamics? How to obtain a linear model without loosing the stability properties of the original system? How to account for the closed-loop dynamics, which are substantially different from that of uncontrolled turbulent flows?

2.2.1 Proper Orthogonal Decomposition

A classic and widely used mathematical technique for model reduction of nonlinear systems is the POD, also known as principal component analysis or Karhunen-Loeve expansion, pioneered by Lumley (1967). The idea is as follows: given a set of data (for instance, numerically or empirically obtained velocity and pressure) that lies in a vector space $\mathcal{V}$, find a subspace $\mathcal{V}_r$ of fixed dimension r such that the error in the projection onto the subspace is minimised. The space $\mathcal{V} \subset \mathbb{R}^n$ has finite dimension $n \gg r$ after the equations have been discretised in space. The optimal POD subspace $\mathcal{V}_r$ is spanned by a set of orthonormal basis functions, containing a decreasing amount of energy. That is, POD modes describe a flow field in terms of coherent structures ranked by their inherent energy content.

The POD model reduction method projects the full nonlinear system onto that set of basis functions. Thus, POD modes are, by design, optimal in an energy norm (L^2). The first few POD basis functions, which are the most energetic eigenmodes,

often capture a significant percentage of the relevant flow dynamics, and their corresponding temporal coefficients are characterised by several frequencies.

Suppose a set of data $\mathrm{x}(t) \in \mathbb{R}^n$, with $0 \leq t \leq T$, is given. The aim is to seek a projection $P_r : \mathbb{R}^n \to \mathbb{R}^r$ of fixed rank $r \ll n$ that minimises the energy norm of the projection error (see Lumley, 1967)

$$\int_0^T \|\mathrm{x}(t) - P_r\mathrm{x}(t)\|^2 \mathrm{d}t. \tag{2.8}$$

By introducing the $n \times n$ correlation matrix

$$R^{\mathrm{POD}} = \int_0^T \mathrm{x}(t)\mathrm{x}(t)^{\mathrm{T}}\mathrm{d}t, \tag{2.9}$$

where $(\cdot)^{\mathrm{T}}$ denotes the transpose of $(\cdot)$, this is equivalent to finding the eigenvalues and eigenvectors of R^{POD}, given by

$$R^{\mathrm{POD}}\vartheta_k = \lambda_k^{\mathrm{POD}}\vartheta_k, \quad \lambda_1^{\mathrm{POD}} \geq ... \geq \lambda_n^{\mathrm{POD}} \geq 0. \tag{2.10}$$

Since R^{POD} is symmetric, positive-semidefinite, all the eigenvalues λ_k^{POD} are real and non-negative and the eigenvectors ϑ_k may be chosen to be orthonormal, so that $\Theta_r^{\mathrm{T}}\Theta_r = I_r$, where $\Theta_r = [\vartheta_1, ..., \vartheta_r] \in \mathbb{R}^{n \times r}$. The main result of the POD is that the optimal subspace of dimension r is spanned by $\vartheta_1, ..., \vartheta_r$ (POD modes), and the optimal projection P_r is then given by

$$P_r = \sum_{k=1}^{r} \vartheta_k\vartheta_k^{\mathrm{T}} = \Theta_r\Theta_r^{\mathrm{T}}.$$

The vectors ϑ_k are called POD modes.

One can then form reduced order models using a Galerkin projection onto this r-dimensional subspace. Suppose the dynamics of a system are described by (2.1). Substituting

$$\mathrm{x}(t) = \Theta_r\mathrm{x}_r(t) = \sum_{j=1}^{r} a_j(t)\vartheta_j \tag{2.11}$$

into the equations, and multiplying by ϑ_k^{T}, one obtains the projected dynamics of the reduced-order state vector $\mathrm{x}_r(t) \in \mathcal{V}_r = \mathrm{span}\{\vartheta_1, ..., \vartheta_r\}$

$$\begin{cases} E_r\dot{\mathrm{x}}_r &= \Theta_r^{\mathrm{T}}\mathcal{F}(\Theta_r\mathrm{x}_r) + G_r\mathrm{v}, \\ \mathrm{y} &= H_r\mathrm{x}_r, \end{cases} \tag{2.12}$$

where

$$E_r = \Theta_r^{\mathrm{T}}E\Theta_r, \tag{2.13}$$

$$G_r = \Theta_r^{\mathrm{T}}G, \tag{2.14}$$

$$H_r = C\Theta_r. \tag{2.15}$$

The POD modes maximise the average energy in the projection of the data onto the lower-dimensional subspace $\mathcal{V}_r$ spanned by the modes. Since P_r is an orthogonal projection, minimising the error (2.8) is indeed equivalent to solving

$$\max_{\{\vartheta_k\}} \left\langle \|P_r\mathrm{x}\|^2 \right\rangle, \tag{2.16}$$

where $\langle \cdot \rangle$ is the average over the data ensemble. The energy in the projection is given by

$$\int_0^T \|P_r\mathrm{x}(t)\|^2 \mathrm{d}t = \sum_{k=1}^r \lambda_k^{\mathrm{POD}}. \tag{2.17}$$

Note that in the case of homogeneous boundary conditions, the snapshots, as well as their linear combinations, will naturally satisfy the same boundary conditions. If there are non-homogeneous Dirichlet boundary conditions, the linear combinations of snapshots will not in general satisfy them, and neither will the reduced-order model solution. To remedy this problem we can either subtract the non-homogeneous boundary values, a mean flow, or a steady-state solution, from the snapshots before constructing the POD basis. Alternatively, an additional constraint equation could be added to the reduced-order model that enforces the boundary condition.

2.2.2 Method of snapshots

To compute the POD modes, one must solve an $n \times n$ eigenvalue problem (2.10), where n is the dimension of the semi-discrete flow dynamics, which often exceeds 10^6. Thus, a direct solution is often non feasible, but the dimension of the eigenvalue problem can be reduced to $m \ll n$ by using snapshots $\mathrm{x}(t_j)$ of the state vector at discrete time $t_1, ..., t_m$ (see Rowley, 2005; Ravindran, 2000). The integral in (2.9) becomes

$$R^{\mathrm{POD}} = \sum_{j=1}^m \mathrm{x}(t_j)\mathrm{x}(t_j)^{\mathrm{T}}\delta_j, \tag{2.18}$$

where δ_j are quadrature coefficients that can be chosen to be equal to $1/m$. Defining

$$X = [\mathrm{x}(t_1)\sqrt{\delta_1}, ..., \mathrm{x}(t_m)\sqrt{\delta_m}], \tag{2.19}$$

the sum (2.18) can be written

$$R^{\mathrm{POD}} = XX^{\mathrm{T}}. \tag{2.20}$$

One can now solve the $m \times m$ eigenvalue problem

$$X^{\mathrm{T}}Xw_k = \lambda_k^{\mathrm{POD}}w_k, \quad \lambda_1^{\mathrm{POD}} \geq ... \geq \lambda_m^{\mathrm{POD}} \geq 0, \tag{2.21}$$

where the eigenvalues λ_k^{POD} are the same as in (2.10) and the eigenvectors $w_k \in \mathbb{R}^m$ may be chosen to be orthonormal. The POD modes are then given by

$$\vartheta_k = Xw_k/\sqrt{\lambda_k^{\mathrm{POD}}}, \quad k = 1, ..., r, \tag{2.22}$$

where $r \leq m$ has to be chosen such that the projection error (2.8) is small enough. In matrix form this becomes

$$\Theta_r = XW_r\Lambda_{\mathrm{POD}}^{-1/2}, \tag{2.23}$$

where $W_r = [w_1, ..., w_r]$. Note that, if the snapshots represent only the velocity field, the information content reduces to the kinetic energy and the POD modes are (discretely) divergence-free. Thus, if the snapshots satisfy zero Dirichlet boundary condition (this can be done by subtracting to the snapshots a mean or steady-state flow, which satisfies the boundary conditions, as in Burkardt et al., 2006; Chen et al., 2012; Ravindran, 2006), the projected low-order system is of the form (2.6). However, Noack et al. (2005) showed that, for convectively unstable shear flows, neglecting the pressure terms may lead to large amplitude errors in the Galerkin model. For this reason, velocity-pressure POD models have been recently considered. In particular, two different methods have been proposed: the decoupled approach (see, for example Caiazzo et al., 2014), in which velocity and pressure snapshots are considered separately and the pressure field is reconstructed *a posteriori* using the reduced-order velocity solution; and the coupled approach (see, for example Bergmann and Cordier, 2008), which uses both velocity and pressure snapshots to compute the POD modes and leads to one global basis (whose velocity part is not divergence-free) with the same number of modes for velocity and pressure.

Though POD modes are very effective (indeed optimal) at approximating a given dataset, that does not imply that they are effective at describing the dynamics that generate a particular dataset, since low-energy features may be critically important to the system dynamic response. Despite substantial efforts in developing efficient reduced-order models, there are still many unsettled issues, such as how to incorporate control with POD modes (see Collis and Joslin, 2004). Indeed, one potential limitation of POD (and other related methods for reduced-order models)

is that basis functions are intrinsic to a particular flow so that as a flow is modified by the action of control, the POD basis (and the reduced-order model based on that POD) must also change. Consequently, a reduced-order model constructed from a subset of POD basis functions for one particular flow, often taken to be the uncontrolled flow, would certainly not be optimal and may not even successfully represent the dynamics of the controlled flow under some circumstances (see, for example Prahbu et al., 2000). An adaptive POD basis could prevent reductions in model effectiveness.

Ravindran (2002) proposed a reduced-order nonlinear adaptive control of flow separation in a forward-facing step channel flow. The idea is to construct the POD subspace using the snapshots of the flow field for a given control input and, then, update the control input based upon the the previous reduced-order model. The new control input is then used to update the POD subspace in order to improve the reduced-order model and reflect the changes in the dynamics, which is altered by the feedback. Although this adaptive procedure was found to be effective for full-state information control problems, it is not feasibile in practical applications, since it requires the online solution of the full-order system. A similar, but cheaper, approach is used in Ravindran (2006), where the snapshots are computed offline for a linear time-varying control input. Alternatively, the trust-region method introduced by Fahl (2000) can be used to automatically decided whether or not a POD model has to be adapted to a new flow configuration (see, for example Bergmann and Cordier, 2008). However, all these methods are computationally expensive.

Furthermore, POD-based reduced-order models, in which low-energy modes are truncated, do not account for observability and controllability of the modes being truncated. Consequently, some retained modes may be uncontrollable or unobservable, whereas some truncated modes may actually play a pivotal role in the input-output transfer function of the open-loop system. This is demonstrated by Rowley (2005): POD-based reduced-order model showed dynamics that were significantly different than those of the original system. Therefore, POD models are not suitable for feedback control design.

If POD modes are constructed using snapshots of the impulse responses of the dynamic system, an expansion in POD modes produces optimal controllability of the reduced-order system. On the other hand, the application of POD modes to partial-state information control problems (where observability is equally impor-

tant) may often lead to unsatisfactory results (Barbagallo et al., 2009). Contrarily, adjoint POD modes produce optimal observability of the reduced-order model, but usually at the expense of controllability, which makes them less suitable for control problems. It has long been recognised that in order to reduce control problems to a desired size, both controllability, *i.e.*, the ability of the applied forcing to reach flow states, and observability, *i.e.*, the ability of flow states to register at the sensor locations, are equally important. An expansion basis that balances these two concepts are equally important in order to express the flow of information from the actuator, *via* the dynamic system, to the sensor. Thus, a "balanced" basis would yield a reduced-order model which is suitable for optimal control design.

2.2.3   Balanced Truncation

A related method, known as balanced truncation, was proposed by Moore (1981), as a model reduction technique for stable, linear systems which does not suffer the same limitations as the POD method. Most notably, balanced truncation has *a priori* error bounds that are close to the lowest error possible of any reduced-order model (see Rowley, 2005). Furthermore, compared to most other methods, including POD, balanced truncation has the key advantage of guaranteeing stability of the reduced-order model (if the original high-order system is stable). The main idea of balanced truncation is to achieve system reduction by retaining only certain states in the representation, that is equivalent to defining a certain subspace within the state-space. In particular, controllable and observable subspaces, which are spanned, respectively, by eigenvectors of controllability and observability Gramians, are considered in order to obtain a balanced representation of the system. This is done by choosing a state transformation such that controllability and observability Gramians are diagonal and equal. This method has been extended to exponentially stable, nonlinear systems by Scherpen (1993), Scherpen (1996), Scherpen and van der Schaft (1994), based on energy functions, and more recently by Lall et al. (2002), Lall et al. (1999), based on empirical Gramians used to compute an approximate balanced truncation. In both cases, when the method is applied to stable, linear systems, it results in the usual balanced truncation method. The approach requires only matrix computations, both in the linear and nonlinear cases, and has been very successfully used in control design. However, the technique does not extend easily to high-order systems (*e.g.*,

10^4 unknowns or more), such as the ones describing spatially discretised flow dynamics.

Balanced truncation typically produces better control-oriented reduced-order models than POD, but is not computationally tractable for systems of a very large dimension and thus not practical for most fluid systems. As a result, several methods have combined ideas from POD and balanced truncation, including the original work of Moore (1981).

Lall et al. (2002) noted the connection between system Gramians and POD and used a Kahunen-Loeve decomposition to compute empirical Gramians that were used to obtain an approximate balanced truncation of stable, nonlinear systems. Similarly, Willcox and Peraire (2002) used a POD method of snapshots to obtain low-rank approximations of Gramians in order to perform a balanced reduction of a high-order linear system. There are though several drawbacks; in particular, this *balanced* POD method, that is an approximate balanced truncation, becomes intractable when the number of outputs is large, as a separate adjoint simulation is required for each output. Furthermore, the rank of controllability and observability Gramians is reduced before balancing is performed, thus one risks prematurely truncating states that may be important from a control view point, which may lead to less accurate models.

The balanced POD method presented by Rowley (2005) for stable, linear systems, which relies on the work of Lall et al. (2002) as well, attempted to overcome the above issues by computing the balancing transformation directly from snapshots, without individual reduction of empirical Gramians. This method appears to be promising, especially for high-order linear systems, as it avoids directly computing Gramians, which is computationally expensive. On the other hand, the presented method is limited to stable, linear systems.

In contrast, Zhou et al. (1999), and then Ahuja and Rowley (2008), Ahuja and Rowley (2010), presented a modified balanced truncation procedure to obtain reduced order models valid for a unstable, linear systems.

Consider a stable, linear system (F, G, H) with p inputs and q outputs, namely:

$$\begin{cases} \dot{\mathrm{x}} &= F\mathrm{x} + G\mathrm{v} \\ \mathrm{y} &= H\mathrm{x}. \end{cases} \tag{2.24}$$

The controllability and observability Gramians are the solutions of the Lyapunov equations

$$FW_c + W_cF^{\mathrm{T}} + GG^{\mathrm{T}} = 0, \quad F^{\mathrm{T}}W_o + W_oF + H^{\mathrm{T}}H = 0, \tag{2.25}$$

which exists if and only if the linear system is stable. In particular, they are symmetric, positive-semidefinite matrices defined by

$$W_c = \int_0^{+\infty} e^{Ft}GG^{\mathrm{T}}e^{F^{\mathrm{T}}t}\mathrm{d}t, \quad W_o = \int_0^{+\infty} e^{F^{\mathrm{T}}t}H^{\mathrm{T}}He^{Ft}\mathrm{d}t. \qquad (2.26)$$

The controllability Gramian W_c measures to what degree each state is excited by an input. For two states $\bar{\mathrm{x}}$, $\tilde{\mathrm{x}}$, with $\|\bar{\mathrm{x}}\| = \|\tilde{\mathrm{x}}\|$, if $\bar{\mathrm{x}}^{\mathrm{T}}W_c\bar{\mathrm{x}} > \tilde{\mathrm{x}}^{\mathrm{T}}W_o\tilde{\mathrm{x}}$, then the state $\bar{\mathrm{x}}$ is more controllable than $\tilde{\mathrm{x}}$, that is, a smaller input is required to drive the system from the initial state x_0 to $\bar{\mathrm{x}}$. The Gramian W_c has full rank if and only if all states are reachable with some input $\mathrm{v}(t)$.

Conversely, the observability Gramian W_o measures to what degree each state excites future outputs. For an initial state x_0 and zero input, one has $\|\mathrm{y}\|^2_{L^2[0,+\infty)} = \mathrm{x}_0^{\mathrm{T}}W_o\mathrm{x}_0$, which is a measure of how much the state excites the output. The Gramian W_o is nonsingular if and only if the system is observable.

The balanced truncation method aims to find a transformation $T_n \in \mathbb{R}^{n \times n}$ such that the controllability and observability properties are balanced, that is, the transformed Gramians are equal and diagonal:

$$T_n^{-1}W_cT_n = T_nW_oT_n^{-1} = \Sigma = \mathrm{diag}(\sigma_1, ...\sigma_n), \quad \sigma_1 \geq ... \geq \sigma_n \geq 0, \qquad (2.27)$$

where $\sigma_1, ...\sigma_n$ are the Hankel singular values of the system and are invariant respect to a coordinate transformation. The matrix T_n is found by finding the eigenvectors of the product W_cW_o:

$$W_cW_oT_n = T_n\Sigma^2. \qquad (2.28)$$

In the balanced coordinates, the states that are least influenced by the input also have the least influence on the output. Balanced truncation involves first changing to these coordinates, and then truncating the least controllable/observable states, which correspond to small Hankel singular values and have little effect on the input-output behavior.

Instead of computing the Gramians by solving Lyapunov equations (2.25), which is computationally expensive, one may compute them from data from numerical simulations. This was the original approach used by Moore (1981), and was used in Lall et al. (2002), Lall et al. (1999) to extend balanced truncation to nonlinear systems.

To compute the controllability Gramian for the system (2.24) one forms the state responses $\mathrm{x}_1(t), ..., \mathrm{x}_p(t)$ to unit impulses $\mathrm{v}_1(t) = \delta(t), ..., \mathrm{v}_p(t) = \delta(t)$. Then, the

Gramian is given by

$$W_c = \int_0^{+\infty} (x_1(t)x_1(t)^\mathrm{T} + \ldots + x_p(t)x_p(t)^\mathrm{T})\mathrm{d}t. \qquad (2.29)$$

Note the similarity between the expression above and the operator in (2.9) that arises in POD of the dataset $\{x_1(t), \ldots, x_p(t)\}$. In fact, the POD modes for this dataset of impulse responses are just the largest eigenvectors of W_c, or, in other words, the most controllable modes of the realisation. Note that since the Gramian matrices depend on the coordinate system, so do the POD modes of this dataset. Let $x_i(t_j)$, for $i = 1, \ldots, p$, $j = 1, \ldots, m$, be the snapshots of the impulse responses at discrete times. As discussed above, the integral in (2.29) becomes a quadrature sum. Writing

$$X = [x_1(t_1), \ldots, x_1(t_m), \ldots, x_p(t_1), \ldots, x_p(t_m)], \qquad (2.30)$$

then the quadrature approximation to (2.29) is

$$W_c = XX^\mathrm{T}. \qquad (2.31)$$

To compute the observability Gramian for a system with q outputs, one computes the impulse responses $z_1(t), \ldots, z_q(t)$ of the adjoint system

$$\begin{cases} E^\mathrm{T}\dot{z} &= F^\mathrm{T}z + G^\mathrm{T}v \\ w &= H^\mathrm{T}z, \end{cases} \qquad (2.32)$$

which is equivalent to integrating the uncontrolled system $E\dot{z} = Fz$ with initial condition $z_k(0) = H^\mathrm{T}\vartheta_k$. Then, the Gramian is given by

$$W_o = \int_0^{+\infty} (z_1(t)z_1(t)^\mathrm{T} + \ldots + z_q(t)z_q(t)^\mathrm{T})\mathrm{d}t. \qquad (2.33)$$

The adjoint data matrix Z is formed as in (2.30), and the quadrature approximation to (2.33) is given by

$$W_o = ZZ^\mathrm{T}. \qquad (2.34)$$

Note that this method requires q integrations of the adjoint system, where q is the number of outputs. Thus, this method is not feasible when the number of outputs is large, for instance if the output is the full state.

2.2.4   Balanced Proper Orthogonal Decomposition

The balanced POD is an extension of the balanced truncation for large (*e.g.*, fluid) systems. The method was proposed by Rowley (2005) for stable, linear

systems to compute the balancing transformation directly from snapshots, without having to compute and individually reduce the Gramians. The balancing modes are computed by performing the singular value decomposition (SVD) of the matrix $Z^T X$:

$$Z^T X = U \Sigma V^T = \begin{pmatrix} U_1 & U_2 \end{pmatrix} \begin{pmatrix} \Sigma_1 & 0 \\ 0 & 0 \end{pmatrix} \begin{pmatrix} V_1^T \\ V_2^T \end{pmatrix}, \qquad (2.35)$$

where $\Sigma_1 \in \mathbb{R}^{r_1 \times r_1}$ is invertible, r_1 is the rank of $Z^T X$, and $U_1^T U_1 = V_1^T V_1 = I_{r_1}$. Define the matrices $\Phi_r \in \mathbb{R}^{n \times r}$, $\Psi_r \in \mathbb{R}^{n \times r}$ as

$$\Phi_r = X V_1 \Sigma_1^{-1/2}, \quad \Psi_r^T = \Sigma_1^{-1/2} U_1^T Z^T, \qquad (2.36)$$

where $r \leq r_1$ can be chosen in order to neglect the smallest Hankel singular values. The columns of $\Phi_r = [\varphi_1, ..., \varphi_r]$ forms the first r columns of the balancing transformation, e.g., the balancing modes. The rows of $\Psi_r^T = [\psi_1, ..., \psi_r]^T$ forms the first r rows of the balancing transformation, e.g., the adjoint modes. The major advantage of the above method for computing the balancing transformation is that the Gramians themselves never need to be computed.

The main drawback of this powerful technique is that it cannot be directly applied to the semi-discrete Navier-Stokes equations (2.1), as they are nonlinear.

2.2.5 Spectral decomposition of nonlinear systems

Rowley et al. (2010), Rowley et al. (2009), presented a technique for describing the global behaviour of complex nonlinear flows by performing a modal decomposition based on spectral analysis of the Koopman operator, an infinite-dimensional, linear operator associated with the full (finite-dimensional) nonlinear system. This operator describes the evolution of observables on the phase space. The Koopman modes, are associated with a particular observable, and may be determined directly from data (either numerical or experimental) using a variant of a standard Arnoldi method. They have an associated temporal frequency and growth rate and may be viewed as a nonlinear generalisation of global eigenmodes of a linearised system. This method does not rely on linearisation of the dynamics: indeed, it captures the full information of the nonlinear system and can be used as an alternative to linearisation-based approaches. Rowley et al. (2009) showed that the global eigenmodes of the Navier-Stokes equations linearised about an unstable steady-state solution capture the dynamics only in a neighbourhood of the unstable equilibrium point, while the Koopman modes correctly capture the behaviour

on the attractor. They also compared the Koopman modes with the POD modes of the same dataset: while a single Koopman mode contains, by construction, only a single frequency component, the POD modes capture the most energetic structures, resulting in modes that contain several frequencies. The Koopman operator has been used to analyse nonlinear dynamical systems (see, for example Mezić, 2013, 2005; Mezić and Banaszuk, 2004) and Mezić (2005)) and in these works it was shown that for nonlinear systems evolving on an attractor, modes corresponding to eigenvalues of the Koopman operator may be computed using harmonic averages or discrete Fourier transforms.

The Krylov method used for computations is identical to the DMD algorithm presented in Schmid (2010), Schmid (2010). Thus, DMD can be thought of as an algorithm for finding Koopman modes, as well as global stability modes of linear dynamical systems, with the aim of projecting large-scale problems onto lower-dimensional subspaces.

Koopman modes

Let $x^{(k)} = x(t_k) = x(k\Delta t)$ be the iterates of the state, sampled at regular time intervals $k\Delta t$, where Δt is a fixed time step. Consider a dynamical system evolving on a manifold M such that, for $x^{(k)} \in M$,

$$x^{(k+1)} = \mathcal{F}(x^{(k)}), \tag{2.37}$$

where $\mathcal{F}$ is a map from M to itself and k is an integer index. Note that one could equivalently study continuous-time systems of the form $\dot{x}(t) = \mathcal{F}(x(t))$, but here a discrete-time setting is adopted, as we are ultimately interested in analysing discrete time data (snapshots). The Koopman operator is a linear operator $\mathcal{U}$ that acts on scalar-valued functions on M in the following manner. For any scalar-valued function $\zeta : M \to \mathbb{R}$, $\mathcal{U} : L^2 \to L^2$ maps ζ into a new function $\mathcal{U}\zeta$ given by

$$\mathcal{U}\zeta(x) = \zeta \circ \mathcal{F}(x). \tag{2.38}$$

Although the dynamical system is nonlinear and evolves on a finite-dimensional manifold M, the Koopman operator $\mathcal{U}$ is linear, but infinite dimensional. The idea is to analyse the flow dynamics governed by (2.37) only from available data (collected either numerically or experimentally) using the eigenfunctions and eigenvalues of $\mathcal{U}$.

Let $\phi_j : M \to \mathbb{R}$ denote the eigenfunctions and $\tilde{\lambda}_j \in \mathbb{C}$ denote the eigenvalues of the Koopman operator:

$$\mathcal{U}\phi_j(\mathrm{x}) = \tilde{\lambda}_j\phi_j(\mathrm{x}), \quad j = 1, 2, ..., \tag{2.39}$$

and consider a vector-valued observable $\boldsymbol{\zeta} : M \to \mathbb{R}^q$, representing any quantity of interest. If each of the q components of $\boldsymbol{\zeta}$ lies within the span of the eigenfunctions ϕ_j of $\mathcal{U}$, then, as in Rowley (2005), one may expand the $\boldsymbol{\zeta}$ as a linear combination of the Koopman eigenfunctions ϕ_j:

$$\boldsymbol{\zeta}(\mathrm{x}) = \sum_{j=1}^{\infty} \phi_j(\mathrm{x})\tilde{\boldsymbol{\nu}}_j, \tag{2.40}$$

where $\tilde{\boldsymbol{\nu}}_j$ are the (vector) coefficients in the expansion, called Koopman modes. If the components of $\boldsymbol{\zeta}$ do not lie within the span of the the eigenfunctions of U, then one may split $\mathcal{U}$ into regular and singular components, with discrete and continuous spectrum respectively, and project the components of $\boldsymbol{\zeta}$ onto the span of the eigenfunctions, as done in Mezić (2005).

Note that the iterates of x_0 are then given by

$$\boldsymbol{\zeta}(\mathrm{x}) = \sum_{j=1}^{\infty} \mathcal{U}^k \phi_j(\mathrm{x}_0)\tilde{\boldsymbol{\nu}}_j = \sum_{j=1}^{\infty} \tilde{\lambda}_j^k \phi_j(\mathrm{x}_0)\tilde{\boldsymbol{\nu}}_j, \tag{2.41}$$

where $\phi_j(x(0))$ is the Koopman eigenfunction and $\tilde{\boldsymbol{\nu}}_j$ is the Koopman mode, representing a complex-valued flow structure. The Koopman eigenvalues $\tilde{\lambda}_j$ therefore characterise the temporal behaviour of the corresponding Koopman mode $\tilde{\boldsymbol{\nu}}_j$: the phase of $\tilde{\lambda}_j$ determines its frequency and the magnitude determines the growth rate. Note that, for a system evolving on an attractor, the Koopman eigenvalues always lie on the unit circle (see Mezić, 2005).

Rowley et al. (2009) showed that the commonly used Arnoldi algorithm, when applied to a nonlinear system, actually produces approximations to eigenvalues of the Koopman operator, and their corresponding modes as defined above. For linear systems, the presented version of the Arnoldi algorithm does not require explicit knowledge of the underlying operator describing the dynamics of the system. This variant of the algorithm was introduced by Saad and Schultz (1980), and it is the same as that referred to as DMD by Schmid (2010).

Dynamic mode decomposition

In the first step, it is assumed that a linear mapping F connects the flow field $x^{(k)} = x(t_k)$ to the subsequent flow field $x^{(k+1)} = x(t_{k+1})$, that is

$$x^{(k+1)} = F x^{(k)}, \tag{2.42}$$

and that this mapping is approximately the same over the full sampling interval. If the flow fields stem from a nonlinear process, this assumption amounts to a linear tangent approximation. For slowly varying systems, a multiple-scale argument can provide a foundation for the above assumption. In the special case of a purely linear process, no approximation is invoked by assuming a constant mapping. Krylov methods are standard methods for computing estimates of the eigenvalues of F, in which one starts with an initial vector $x^{(0)}$ (often chosen to be a random vector), and computes iterates of $x^{(0)}$. After $m-1$ iterations, one has a collection of m vectors that span a Krylov subspace, given by

$$\mathcal{K}_m(F, x^{(0)}) = \text{span} \left\{ x^{(0)}, F x^{(0)}, ..., F^{m-1} x^{(0)} \right\}. \tag{2.43}$$

We wish to find approximate eigenvectors of F as linear combinations of the columns of

$$V_0^m = \left[x^{(0)}, F x^{(0)}, ..., F^{m-1} x^{(0)} \right] = \left[x^{(0)}, x^{(1)}, ..., x^{(m-1)} \right]. \tag{2.44}$$

As the number of snapshots increases and the data sequence given by V_0^m captures the dominant features of the underlying physical process, it is reasonable to assume that, beyond a critical number of snapshots, the vectors given by (2.42) become linearly dependent. In other words, adding further flow fields $x^{(k)}$ to the data sequence will not improve the vector space V_0^m. When this limit is reached, the vector $x^{(m)}$ can be expressed as a linear combination of the previous, linearly independent, vectors

$$x^{(m)} = c_0 x^{(0)} + c_1 x^{(1)} + ... + c_{m-1} x^{(m-1)} + \mathbf{r}, \tag{2.45}$$

or in matrix form

$$x^{(m)} = V_0^m \mathbf{c} + \mathbf{r}, \tag{2.46}$$

where $\mathbf{c}^T = \{c_0, ..., c_{m-1}\}$ and $\mathbf{r}$ as the residual vector. Then,

$$F V_0^m = V_1^m = V_0^{m-1} S + \mathbf{r} e_m^{\mathrm{T}}, \tag{2.47}$$

where $e_m^{\mathrm{T}} = [0, ..., 0, 1] \in \mathbb{R}^m$ is a unit vector,

$$V_1^m = \left[\mathrm{x}^{(1)}, \mathrm{x}^{(2)}, ..., \mathrm{x}^{(m)} \right], \tag{2.48}$$

and

$$S = \begin{pmatrix} 0 & & & & c_1 \\ 1 & 0 & & & c_2 \\ & \ddots & \ddots & & \vdots \\ & & 1 & 0 & c_{m-2} \\ & & & 1 & c_{m-1} \end{pmatrix} \tag{2.49}$$

is of companion type. The residual

$$\mathbf{r} = \mathrm{x}^{(m)} - V_0^{m-1}\mathbf{c} \tag{2.50}$$

is minimised when c is chosen such that $\mathbf{r}$ is orthogonal to $\mathrm{span}\{\mathrm{x}^{(0)}, \mathrm{x}^{(1)}, ..., \mathrm{x}^{(m-1)}\}$. The eigenvalues of S, such that

$$S\mathbf{w} = \lambda\mathbf{w}, \tag{2.51}$$

are then approximations of some of the eigenvalues of F, called Ritz values, and the corresponding approximate eigenvectors are given by

$$\boldsymbol{\nu} = V_0^{m-1}\mathbf{w}, \tag{2.52}$$

and are called Ritz vectors. The Ritz values of the decomposition yield growth rates and frequencies, and the Ritz vectors yield the corresponding directions.

The well-known Arnoldi method is closely related to the decomposition above but successively orthogonalises the vectors of V_0^m resulting in a decomposition of the form $FQ \approx QH_m$ with $V_0^{m-1} = QR$ and $H_m = RSR^{-1}$ is a Hessenberg matrix. Again, the eigenvalues of H_m approximate some of the eigenvalues of F. In practice, the reduction of F to Hessenberg form by the Arnoldi method is accomplished by a sequence of projections onto successive Krylov subspaces. This yields a more stable algorithm, but for these projections the matrix F has to be available. The algorithm proposed by Schmid (2010), instead, does not require explicit knowledge of the matrix F: it is exclusively based on the sequence of the flow field snapshots and is thus equally applicable to experimental data and large-scale numerical simulations. This approach can be summarised as follows. Consider a sequence $\{\mathrm{x}^{(0)}, ..., \mathrm{x}^{(m)}\}$, where $\mathrm{x}^{(j)} \in \mathbb{R}^n$.

1. Define V_0^{m-1} and find constants c_j such that

$$\mathbf{r} = \mathrm{x}^{(m)} - V_0^{m-1}\mathbf{c}, \quad \mathbf{c} \perp \mathrm{span}\{\mathrm{x}^{(0)}, ..., \mathrm{x}^{(m-1)}\}. \tag{2.53}$$

2. Define the companion matrix S by (2.49) and find its eigenvalues and eigenvectors

$$S = T_m^{-1} \Lambda T_m, \quad \Lambda = \mathrm{diag}(\lambda_1, ..., \lambda_m), \tag{2.54}$$

   where eigenvectors are columns of T_m^{-1}.

3. Define $\boldsymbol{\nu}_j$ to be the columns of $V = V_0^{m-1} T_m^{-1}$.

Rowley et al. (2009) showed that for a nonlinear system, the above algorithm produces approximations of the Koopman modes and associated eigenvalues. This is summarised by the following proposition.

Proposition 1. *Consider a set of data $\{x^{(0)}, ..., x^{(m)}\}$ and let λ_j, $\boldsymbol{\nu}_j$ be the empirical Ritz values and vectors of this sequence. Assume the λ_j are distinct. Then*

$$x^{(k)} = \sum_{j=1}^{m} \lambda_j^k \boldsymbol{\nu}_j, \quad k = 0, ..., m - 1, \tag{2.55}$$

$$x^{(m)} = \sum_{j=1}^{m} \lambda_j^m \boldsymbol{\nu}_j + \boldsymbol{r}, \quad \boldsymbol{r} \perp span\{x^{(0)}, ..., x^{(m-1)}\}. \tag{2.56}$$

To illustrate how this proposition provides a connection with Koopman modes, consider a vector-valued observable $\boldsymbol{\zeta} : M \to \mathbb{R}^q$ for the dynamical system (2.37) and its expansion (2.40) in the Koopman modes. Suppose a sequence of observations (*e.g.*, the snapshots $u^{(k)}$ of the velocity field) $\boldsymbol{\zeta}(\mathrm{x}^{(k)})$, for $k = 0, ..., m$ is available, and let λ_j and $\boldsymbol{\nu}_j$ be the empirical Ritz values and vectors for this sequence. Then, by Proposition 1, we have

$$\boldsymbol{\zeta}(\mathrm{x}^{(k)}) = \sum_{j=1}^{m} \lambda_j^k \boldsymbol{\nu}_j, \quad k = 0, ..., m - 1, \tag{2.57}$$

$$\boldsymbol{\zeta}(\mathrm{x}^{(m)}) = \sum_{j=1}^{m} \lambda_j^m \boldsymbol{\nu}_j + \mathbf{r}, \quad \mathbf{r} \perp \mathrm{span}\{\boldsymbol{\zeta}(\mathrm{x}^{(0)}), ..., \boldsymbol{\zeta}(\mathrm{x}^{(m-1)})\}. \tag{2.58}$$

Comparing with the expansion (2.40), the empirical Ritz values λ_j and vectors $\boldsymbol{\nu}_j$ behave in precisely the same manner as the eigenvalues $\tilde{\lambda}_j$ and modes $\tilde{\boldsymbol{\nu}}_j$ of $\mathcal{U}$, but for the finite sum in (2.57) instead of the infinite sum (2.41).

When the observable is the full state, the DMD algorithm approximates the flow

field $x^{(k)}$ as the sum of the first m approximated Koopman modes, called DMD modes $\boldsymbol{\nu}_j$, weighted by the powers λ_j^k of their corresponding eigenvalues:

$$x(t) = \sum_{j=0}^{+\infty} \phi_j(x(0))\tilde{\boldsymbol{\nu}}_j e^{(\rho_j + i\omega_j)t} \approx x^{(k)} = \sum_{j=0}^{m} \boldsymbol{\nu}_j \lambda_j^k, \qquad (2.59)$$

where ρ_j represents the growth rate and ω_j the frequency of the associated Koopman mode $\tilde{\boldsymbol{\nu}}_j$. If $\mathbf{r} = 0$, then, as far as the data is concerned, the approximate modes are indistinguishable from eigenvalues and Koopman modes of U, with the expansion consisting only of a finite number of terms. If $\mathbf{r} \neq 0$, then there is some error, but this is in a sense the best one can do, since the $m + 1$ observations cannot in general be spanned by m modes. Note that to use DMD modes in a reduced-order Galerkin model of a PDE, one must typically subtract a "base flow" from the data-set, which satisfies the appropriate boundary conditions. The mean of the data is a common choice for a base flow, especially in POD-based analyses. The application of the DMD to a mean-subtracted set of data, however, is exactly equivalent to a temporal discrete Fourier transform (DFT) and harmonic averaging. This is restrictive and generally undesirable. On the other hand, subtracting an equilibrium point generally preserves the DMD spectrum and modes (Chen et al., 2012).

The main drawback of this method is that it does not take into account the closed-loop dynamics and there are no appropriate selection criteria for selecting the modes to be retained. One could think of modifying the algorithm by changing the Krylov subspace (2.43). For instance, consider the Single-Input-Single-Output (SISO) system $\dot{x} = Fx + Gv$, with output $y = Hx$. One could choose the Krylov subspace spanned by the state responses to unit impulses

$$\mathcal{K}_m(F, G) = \text{span}\left\{ G, FG, ..., F^{m-1}G \right\}, \qquad (2.60)$$

which corresponds to considering the uncontrolled system $\dot{x} = Fx$, with initial conditions $x_i^{(0)} = h_i$, for $i = 1, ..., p$, where h_i denotes the i-th column of the $n \times p$ matrix H. However, this method does not take into account the observability properties of the system, thus it is not feasible for partial-state information control problems.

Other Krylov subspace techniques attempt to approximate the transfer function of stable, linear systems (see, for example, Astolfi, 2010b; Bai, 2002; Jaimoukha and Kasenally, 1997), in order to properly capture the input-output behaviour.

This is done by considering the right (input) and left (output) Krylov subspaces

$$\mathcal{K}_m(F, G) = \text{span} \left\{ g, FG, ..., F^{m-1}G \right\} \tag{2.61}$$

$$\mathcal{L}_m(F^\mathrm{T}, H^\mathrm{T}) = \text{span} \left\{ H^\mathrm{T}, F^\mathrm{T}H^\mathrm{T}, ..., (F^{m-1})^\mathrm{T}H^\mathrm{T} \right\}, \tag{2.62}$$

which are parts of the controllability and observability subspaces, respectively. The direct Φ and adjoint Ψ matrices, whose columns span the desired right and left Krylov subspaces, respectively, are computed using a Gram-Schmidt (*e.g.*, Arnoldi method) or a Lanczos process and are such that $\Psi^\mathrm{T}\Phi = I$. However, care should be taken as oblique projections onto a Krylov subspace may lead to unstable reduced-order models (see Benner, 2009), thus, appropriate modifications are needed in order to preserve stability (see, for example, Jaimoukha and Kasenally, 1997). Moreover, since the definition of the left Krylov subspace requires adjoint information, this method relies on the knowledge of a suitable linear operator F describing the system dynamics. Thus, it cannot be directly applied to nonlinear systems.

Other difficulties arise from the fact that Krylov subspace methods often generate partial realisations that contain non-essential modes. An appropriate selection criterion, which weights the importance of the modes (*e.g.*, according to their controllability, observability and damping frequency), can be considered in order to overcome the problem (see Bagheri, 2013; Barbagallo et al., 2009). This method can be adopted, for example, along with the DMD in order to choose the global/Koopman modes to be retained. Other Krylov-based model reduction methods can be used and extended to stable nonlinear systems; for instance, using a nonlinear enhancement of the notion of moment, the approximated reduced-order system can be obtained by moment matching as in Astolfi (2010a). Furthermore, this method can be extended to unstable nonlinear systems, if the moments are computed by mean of the Sylvester equation. However, this is computationally expensive and perhaps not feasible for very large systems.

In this thesis, a novel method to approximate the nonlinear dynamics of controlled flow systems is proposed. In particular, the DMD algorithm can be seen as a way approximate the Koopman operator, in order to obtain a high dimensional linear operator (2.42), which accurately describes the discretised, fully nonlinear, open-loop dynamics. Then, the balanced POD is applied to the resulting linear system, while taking into account the closed-loop dynamics.

2.2.6 A new approach: Balanced DMD

Since a time-stepping is required, in order to compute the n states of system (2.1), a discrete-time setting is used in this section, to derive the ROM. Following Schmid (2010), $m + 1$ snapshots of the state responses of the full-order nonlinear system (2.1) are collected, which corresponds in this work to the finite element approximation of the incompressible Navier-Stokes equations, to a finite-amplitude impulsive input $\delta(t - t_0)$, $t_0 \geq 0$, and arrange them in two matrices: $X_{\mathrm{NL}} = [\mathrm{x}^{(0)}, ..., \mathrm{x}^{(m-1)}]$ and $Z_{\mathrm{NL}} = [\mathrm{x}^{(1)}, ..., \mathrm{x}^{(m)}]$. We then perform the reduced SVD of the matrix X_{NL}:

$$X_{\mathrm{NL}} = U\Sigma V^{\mathrm{T}}, \tag{2.63}$$

where $\Sigma \in \mathbb{R}^{m \times m}$ is diagonal, $U \in \mathbb{R}^{n \times m}$, $V \in \mathbb{R}^{m \times m}$ and $U^{\mathrm{T}}U = V^{\mathrm{T}}V = I_m$. Define the $m \times m$ matrix

$$\bar{F} = U^{\mathrm{T}} Z_{\mathrm{NL}} V \Sigma^{-1}, \tag{2.64}$$

whose eigendecomposition is given by

$$\bar{F}R = R\Lambda, \tag{2.65}$$

with $R = [r_1, ..., r_m]$ and $\Lambda = \mathrm{diag}(\lambda_1, ..., \lambda_m)$. The dynamic modes $\boldsymbol{\nu}_j$ are then given by

$$\Phi_m = [\boldsymbol{\nu}_1, ..., \boldsymbol{\nu}_m] = URD, \tag{2.66}$$

where D is a diagonal matrix, used to scale the modes, computed as in Belson et al. (2014), so that the sum of the modes equals the first data vector $\mathrm{x}(t_0)$. If the snapshots are computed from a system with no inputs, it is assumed, as in Schmid (2010), that the evolution of the flow field can be expressed by a linear map $F \in \mathbb{R}^{n \times n}$:

$$\mathrm{x}^{(k+1)} = F\mathrm{x}^{(k)}. \tag{2.67}$$

A least square approximation of the matrix F is given by

$$F = Z_{\mathrm{NL}} X_{\mathrm{NL}}^{\dagger} \approx Z_{\mathrm{NL}} V \Sigma^{-1} U^{\mathrm{T}}, \tag{2.68}$$

where $(\cdot)^{\dagger}$ denotes the Moore-Penrose pseudoinverse of $(\cdot)$, *i.e.*, $X_{\mathrm{NL}}^{\dagger} = [X_{\mathrm{NL}} X_{\mathrm{NL}}^{\mathrm{T}}]^{-1} X_{\mathrm{NL}}$. In the case of a system with inputs, a linear system, approximating the nonlinear one, can be obtained as follows:

$$\begin{cases} \mathrm{x}^{(k+1)} &\approx U\bar{F}U^{\mathrm{T}}\mathrm{x}^{(k)} + U\bar{G}\mathrm{v}^{(k)}, \\ \mathrm{y}^{(k)} &\approx \bar{H}U^{\mathrm{T}}\mathrm{x}^{(k)}, \end{cases} \tag{2.69}$$

where $\bar{G} = U^{\mathrm{T}}\mathrm{x}^{(0)} \in \mathbb{R}^m$ and $\bar{H} = CU \in \mathbb{R}^{1 \times m}$. Note that the input vector $U\bar{G}$ is chosen as the projection of the excited initial condition $\mathrm{x}^{(0)}$ onto the POD basis, spanned by the columns of U. This choice is motivated by the fact that the impulse responses of system (2.69), needed to compute the balanced modes, can be expressed as $\mathrm{x}^{(k)} \approx F^k\mathrm{x}^{(0)} = U\bar{F}^kU^{\mathrm{T}}\mathrm{x}^{(0)}$.

In fluid systems, the dimension of the attractor is bounded, so that the essential dynamics is finite-dimensional (see Mezić, 2005). Therefore, there cannot be any asymptotically growing structures and thus $\rho_j \leq 0$ for all $j = 0, ..., +\infty$ (Bagheri, 2013) - *i.e.*, all the Ritz values λ_j lie within the unit cycle. The so-obtained DMD linear model (2.69), is thus stable (*i.e.*, $|\lambda_j| \leq 1$, $j = 1, ..., m$) but the dynamic properties of the attracting set are lost. Since limit cycles cannot be described using linear dynamics, a projection onto the asymptotically stable eigenspace is performed.

Let $L \in \mathbb{R}^m$ be the left eigenvector matrix of $\bar{F}$: $\bar{F}^{\mathrm{T}}L = L\Lambda^{\mathrm{H}}$, where $(\cdot)^{\mathrm{H}}$ denotes the Hermitian transpose of $(\cdot)$. The right and left eigenvectors are partitioned as $R = [R_s, R_u]$ and $L = [L_s, L_u]$, respectively, where the subscripts $_s$ and $_u$ refer to the parts of the spectrum Λ_s, which is asymptotically stable, and Λ_u, which lies on the unit circle, respectively. The projection operator

$$\mathbb{P}_s = I_m - R_u(L_u^{\mathrm{H}}R_u)^{-1}L_u^{\mathrm{H}}, \tag{2.70}$$

where I_m is the $m \times m$ identity matrix, is used to restrict the dynamics of (2.69) to the asymptotically stable subspace of $\bar{F}$. The balanced POD is computed using the full state (direct and adjoint) snapshots of the reduced m-*th* order projected system

$$\begin{cases} \bar{\mathrm{x}}_s^{(k+1)} &= \bar{F}\bar{\mathrm{x}}_s^{(k)} + \mathbb{P}_s\bar{G}\mathrm{v}^{(k)}, \\ \bar{\mathrm{y}}^{(k)} &= \bar{H}\mathbb{P}_s\bar{\mathrm{x}}_s^{(k)}, \end{cases} \tag{2.71}$$

where $\bar{\mathrm{x}}_s^{(k)} = \mathbb{P}_s\bar{\mathrm{x}}^{(k)} = \mathbb{P}_sU^{\mathrm{T}}\mathrm{x}^{(k)} \in \mathbb{R}^m$, in order to select the $r \ll m$ relevant modes to be retained in the reduced-order model. The full-order balanced-POD modes

$$\begin{aligned} \Phi &= U\Phi_r, \\ \Psi &= U\Psi_r, \end{aligned} \tag{2.72}$$

with Φ_r, Ψ_r defined in (2.36), yield the asymptotically stable, linear model of order r:

$$\begin{cases} \xi^{(k+1)} &= \bar{A}\xi^{(k)} + \bar{B}\mathrm{v}^{(k)}, \\ \bar{\mathrm{y}}^{(k)} &\approx \bar{C}\xi^{(k)}, \end{cases} \tag{2.73}$$

where $\bar{A} = \Psi_r^{\mathrm{T}} \bar{F} \Phi_r$, $\bar{B} = \Psi_r^{\mathrm{T}} \bar{G}$ and $\bar{C} = \bar{H} \Phi_r$. For the specific application to flow separation control, the sampling time $k\Delta t$, used to construct the ROM is much smaller compared to the fluid time-scales. Therefore, the action of the discrete-time input $\mathrm{v}^{(k)}$ on the flow field can be considered continuous. The discrete-time ROM (2.73) can be thus converted into a continuous-time system ($\mathrm{w} \in \mathbb{R}$)

$$
\begin{cases}
\dot{\xi} &= A\xi + B\mathrm{v}, \quad \xi(0) = \xi_0, \\
\mathrm{y} &= C\xi.
\end{cases}
\tag{2.74}
$$

This solves the model reduction problem stated in the first section of this chapter.

2.3 Summary

A novel control-oriented model reduction method for nonlinear systems evolving on attractors has been proposed. The method can be used to obtain a low-order, stable, linear model of the nonlinear flow/actuator dynamics, whose state variables have a clear and consistent physical meaning. The method combines DMD, as an alternative to linearisation, and balanced POD, as a way to select the most observable and controllable DMD modes. The high-order DMD model is projected using the balanced POD modes, thus yielding a balanced, stable, linear ROM.

Chapter 3

A Practical Application: Controlled Fluid Systems

The objective of this chapter is to obtain an accurate model of the flow/actuator dynamics, in view of the practical application to the flow separation control problem. The analytical model, which is based on the incompressible Navier-Stokes equations, consists of a nonlinear system of PDEs, which are coupled with the plasma dynamics through the body force that is generated by the actuator. The PDEs are spatially discretised using two different numerical methods: a finite element method and a finite volume method. The semi-discretisation of the equations yields a nonlinear, high-dimensional, system of ODEs of the form (2.1), which represents the full order state-space model. The snapshots of the flow field are obtained by applying suitable time-stepping techniques. The proposed model reduction method can then be applied to the former, in order to obtain a control-oriented ROM of the unsteady incompressible Navier-Stokes equations, in the presence of a body force distribution generated by the plasma actuator.

3.1 Analytical Model

Let Ω be an open bounded domain in $\mathbb{R}^d$, where d denotes the dimension of the geometry, and let $T > 0$ denote the (non-dimensional) final time. The flow of an incompressible viscous Newtonian fluid can be described by the non-dimensionalised Navier-Stokes equations, which are derived from the conservation

of mass and momentum, namely,

$$
\begin{aligned}
\partial_t \boldsymbol{u} &= -(\boldsymbol{u} \cdot \nabla)\boldsymbol{u} - \nabla p + \frac{1}{Re}\Delta \boldsymbol{u} + \boldsymbol{f} &&\text{in } (0,T] \times \Omega, \\
0 &= \nabla \cdot \boldsymbol{u} &&\text{in } (0,T] \times \Omega,
\end{aligned}
\tag{3.1}
$$

with initial condition

$$
\boldsymbol{u}(0, \boldsymbol{x}) = \boldsymbol{u}_0(\boldsymbol{x}) \quad \text{in} \quad \Omega,
\tag{3.2}
$$

and boundary conditions

$$
\begin{aligned}
\boldsymbol{u}(t, \boldsymbol{x}) &= \boldsymbol{g}(t, \boldsymbol{x}) &&\text{on } \Gamma_{\text{in}}, \\
\boldsymbol{u}(t, \boldsymbol{x}) &= 0 &&\text{on } \Gamma_0, \\
(\tfrac{1}{Re}\nabla \boldsymbol{u} - p I_d)\boldsymbol{n} &= 0 &&\text{on } \Gamma_{\text{out}}.
\end{aligned}
\tag{3.3}
$$

Here: $t \in [0, T]$ is the non-dimensional time; $\boldsymbol{x} \in \Omega$; $\boldsymbol{n}$ denotes the unit outward normal vector on $\partial\Omega = \Gamma_{\text{in}} \cup \Gamma_0 \cup \Gamma_{\text{out}}$; Γ_{in}, Γ_{out} and Γ_0 denote the inflow, outflow and wall boundaries, respectively; $\boldsymbol{g} : [0, T] \times \Omega \to \mathbb{R}^d$ is a sufficiently smooth function denoting the inflow boundary condition; $\boldsymbol{u} : [0, T] \times \Omega \to \mathbb{R}^d$ is the velocity vector; $p : [0, T] \times \Omega \to \mathbb{R}$ is the non-dimensional pressure; $I_d \in \mathbb{R}^{d \times d}$ is the identity matrix; $Re = \rho U_\infty c / \mu$ is the Reynolds number; U_∞ is the free-stream velocity (in m/s); μ is the viscosity; ρ is the fluid density (in kg/m³); $c = 0.1$m is the chord length (as in Choi et al. (2011); Feng et al. (2015), for the wind tunnel tests); $\boldsymbol{f} : [0, T] \times \Omega \to \mathbb{R}^d$ is the total body force vector field, which is assumed to be linearly dependent on the control inputs, *i.e.*, the voltage signals of the plasma actuators, as in Jayaraman and Shyy (2008); Shyy et al. (2002). An accurate body force model that couples the fluid discharge equations with the NavierStokes equations, including momentum and thermal transfer from plasma to neutral gas, could be obtained as in Unfer and Boeuf (2009) but most of its parameters are unknown and would still need to be approximated. Such a detailed model is not necessary here, as the feedback control compensates for these uncertainties and the linear approximation shows good agreement with the experiments Moreau (2007). In particular, the plasma can be expressed as

$$
\boldsymbol{f}(t, \boldsymbol{x}) = c/\rho U_\infty^2 (f_x(t, \boldsymbol{x}), f_y(t, \boldsymbol{x}), 0) = c/\rho U_\infty^2 \sum_{j=1,\dots,n_a} \boldsymbol{f}^{(j)}(t, \boldsymbol{x}),
\tag{3.4}
$$

where n_a denotes the number of actuators, f_x, f_y are the streamwise and normal component (in N/m³) and $\boldsymbol{f}^{(j)}$ is the single force distribution of the j-th actuator (in N/m³). All the above listed functions are assumed to be sufficiently smooth. The wall-tangential velocities,

$$
\mathrm{y}_i(t) = u_\tau(t, \boldsymbol{x}_{s_i}) = \boldsymbol{\tau}(\boldsymbol{x}_{s_i}) \cdot \boldsymbol{u}(t, \boldsymbol{x}_{s_i}),
\tag{3.5}
$$

evaluated at the selected sensor locations $\boldsymbol{x}_{s_i}$, for $i = 1, ..., n_s$, with n_s being the number of sensors and $\boldsymbol{\tau}$ being the wall-tangential unit vector, are chosen as the measured outputs.

3.2 Semi-discrete state-space model

A full-order, nonlinear state-space system of the form (2.1) can be obtained by spatially discretising the system of nonlinear PDEs (3.1), (3.3), (3.2), (3.5), using numerical methods, thus yielding a nonlinear system of n ODEs,

$$\begin{cases} E\dot{\mathrm{x}} = \mathcal{F}(\mathrm{x}) + G\mathrm{v} & \text{in} \quad (0, T], \\ \mathrm{y} = H\mathrm{x} & \text{in} \quad (0, T], \end{cases} \tag{3.6}$$

with initial conditions

$$\mathrm{x}(0) = \mathrm{x}_0, \tag{3.7}$$

where: $n = (d+1)N$ is the number of states; $\mathrm{x} = \mathrm{x}(t) : \mathbb{R} \to \mathbb{R}^n$ is the state vector representing the evolution in time of the nodal values of the flow fields (both pressure and velocity); $\dot{\mathrm{x}} = \mathrm{dx}/\mathrm{d}t$; $E \in \mathbb{R}^{n \times n}$ is related to the mass matrix; $\mathcal{F}(\cdot) : \mathbb{R}^n \to \mathbb{R}^n$ is a sufficiently smooth nonlinear function; $G \in \mathbb{R}^{n \times n_a}$ is the input matrix representing the nodal values of the time-independent part of the body force; $\mathrm{v} = \mathrm{v}(t) : \mathbb{R} \to \mathbb{R}^{n_a}$ is the control input vector; $\mathrm{y} = \mathrm{y}(t) : \mathbb{R} \to \mathbb{R}^{n_s}$ is the chosen control output; $H \in \mathbb{R}^{n_s \times n}$ is the output matrix representing the space-discretisation of (3.5).

Two different numerical methods have been considered, in order to show the robustness of the proposed approach: the control algorithm will be first designed upon a reduced-order model, which is built using the snapshots of the 2D finite element simulations at low Reynolds numbers $Re = 1000$, and then applied to more accurate 3D finite volume approximation of the Navier-Stokes equations at $Re = 20,000$.

In particular, a finite element method has been implemented in Python using the FEniCS library (see Logg et al., 2012) to solve the Navier-Stokes equations for two-dimensional configurations at low Reynolds numbers; for more accurate simulations at higher Reynolds numbers, equations (3.1), (3.3), (3.2), (3.5) are approximated by a finite volume technique, with pressure and velocity co–located at the cell center, which is implemented in $\chi navis$, a general-purpose, second order, multi-block, unsteady RANS equations based solver, developed at CNR-INSEAN.

3.3   Finite Element Approximation

One way of obtaining a spatial discretisation of the system of nonlinear PDEs (3.1), (3.3), (3.2), (3.5) is to use the continuous Galerkin finite element method. Then, a time-stepping is required to solve the resulting semi-discrete system (3.6). In particular, quadratic and linear Lagrange polynomials are used for the velocity and pressure fields, respectively. An implicit, first-order backward Euler scheme is used for the time-discretisation. The FEniCS Python library (see Logg et al., 2012) is used to implement the finite element method for the automatic generation of a fast, parallelised $C + +$ code with the aim of performing accurate numerical simulations. The computational grid is generated using Triangle (see Shewchuk, 2002). Note that the number n of states of system (3.6) is large ($\approx 10^4/10^6$) and depends on the grid resolution.

3.3.1   Continuous Galerkin Finite Element Method

Define the Hilbert spaces

$$L^2(\Omega) = \left\{ q : \ \Omega \to \mathbb{R} \text{ such that } \|q\|_{L^2(\Omega)} = \left(\int_\Omega |q(\boldsymbol{x})|^2 \mathrm{d}\boldsymbol{x} \right)^{\frac{1}{2}} < +\infty \right\}, \quad (3.8)$$

$$H^k(\Omega) = \left\{ q \in L^2(\Omega) : \ D^{\boldsymbol{\alpha}} q \in L^2(\Omega), \forall |\boldsymbol{\alpha}| \leq k \right\}, \quad (3.9)$$

where $\boldsymbol{\alpha} = (\alpha_1, ..., \alpha_d)$ is a d-dimensional multi-index, $\alpha_1, ..., \alpha_d, k$ are non-negative integers and

$$D^{\boldsymbol{\alpha}} q(\boldsymbol{x}) = \frac{\partial^{|\boldsymbol{\alpha}|} q(\boldsymbol{x})}{\partial x_1^{\alpha_1} ... \partial x_d^{\alpha_d}} \quad (3.10)$$

is a partial differential operator of order $|\boldsymbol{\alpha}| = \alpha_1 + ... + \alpha_d$. Let W be any Hilbert space with norm $\| \cdot \|_W$ and let

$$L^2(\mathbb{R}^+; W) = \bigg\{ q : \mathbb{R}^+ \to W \mid t \to q(t) \text{ is measurable and}$$

$$\int_0^{+\infty} \|q(t)\|_W^2 \mathrm{d}t < +\infty \bigg\}. \quad (3.11)$$

Assume $\boldsymbol{u} \in L^2(\mathbb{R}^+; H^1(\Omega))^d$, $p \in L^2(\mathbb{R}^+; L^2(\Omega))$, $\boldsymbol{f} \in L^2(\mathbb{R}^+; L^2(\Omega))^d$, $\boldsymbol{u}_0 \in L^2(\Omega)$, $\boldsymbol{g}(t, \cdot) \in L^2(\mathbb{R}^+; H^{1/2}(\Gamma_{\text{in}}))$, where $H^{1/2}(\Gamma_{\text{in}})$ denotes the $L^2(\Gamma_{\text{in}})$ functions that are traces of $H^1(\Omega)$ functions. The weak formulation of equations (3.1), (3.2), (3.5) with boundary conditions (3.3), for a d-dimensional flow, can be written as

follows: find $(\boldsymbol{u}(t,\cdot), p(t,\cdot)) \in \boldsymbol{V}_{\Gamma_{\text{in}} \cup \Gamma_0} \times Q \subset H^1(\Omega)^d \times L^2(\Omega)$ such that

$$\int_\Omega \partial_t \boldsymbol{u} \cdot \boldsymbol{v} \mathrm{d}\boldsymbol{x} = -\frac{1}{Re} \int_\Omega \nabla \boldsymbol{u} \cdot \nabla \boldsymbol{v} \mathrm{d}\boldsymbol{x} - \int_\Omega (\boldsymbol{u} \cdot \nabla \boldsymbol{u}) \cdot \boldsymbol{v} \mathrm{d}\boldsymbol{x} + \int_\Omega p \nabla \cdot \boldsymbol{v} \mathrm{d}\boldsymbol{x} \quad (3.12)$$

$$+ \int_\Omega \boldsymbol{f} \cdot \boldsymbol{v} \mathrm{d}\boldsymbol{x}, \quad (3.13)$$

$$0 = \int_\Omega q \nabla \cdot \boldsymbol{u} \mathrm{d}\boldsymbol{x}, \quad (3.14)$$

for all test functions $(\boldsymbol{v}, q) \in \boldsymbol{V}_0 \times Q \subset H^1(\Omega)^d \times L^2(\Omega)$, where $\boldsymbol{f}(t, \cdot) \in L^2(\Omega)^d$,

$$\boldsymbol{V}_{\Gamma_{\text{in}} \cup \Gamma_0} = \left\{ \boldsymbol{v} \in H^1(\Omega)^d : \quad \boldsymbol{v}|_{\Gamma_{\text{in}} \cup \Gamma_0} = \boldsymbol{u}_D \in L^2(\mathbb{R}^+; H^{1/2}(\partial\Omega)) \right\} \quad (3.15)$$

$$\boldsymbol{V}_0 = \left\{ \boldsymbol{v} \in H^1(\Omega)^d : \quad \boldsymbol{v}|_{\Gamma_{\text{in}} \cup \Gamma_0} = 0 \right\}, \quad (3.16)$$

and

$$\boldsymbol{u}_D(t, \boldsymbol{x}) = \begin{cases} \boldsymbol{g}(t, \boldsymbol{x}) & \text{on } \Gamma_{\text{in}}, \\ 0 & \text{on } \Gamma_0, \end{cases} \quad (3.17)$$

on the Dirichlet boundary. Let $\mathcal{T}_h$ be a non-degenerate mesh consisting of elements of granularity h such that

$$\bar{\Omega} = \bigcup_{\kappa \in \mathcal{T}_h} \kappa \quad (3.18)$$

and let

$$\boldsymbol{V}^h = \left\{ \boldsymbol{v}_h \in \mathcal{C}^0(\Omega)^d : \quad \boldsymbol{v}_h|_\kappa \in \mathcal{P}_2(\kappa)^d, \quad \forall \kappa \in \mathcal{T}_h \right\}, \quad (3.19)$$

$$Q^h = \left\{ q_h \in \mathcal{C}^0(\Omega)^d : \quad q_h|_\kappa \in \mathcal{P}_1(\kappa)^d, \quad \forall \kappa \in \mathcal{T}_h \right\}, \quad (3.20)$$

be finite element spaces, where $\mathcal{C}^0(\Omega)$ is the space of continuous functions on Ω and $\mathcal{P}_k$ is the polynomial space of degree at most k. Then, the weak form can be approximated as follows: find $(\boldsymbol{u}_h(t,\cdot), p_h(t,\cdot)) \in \boldsymbol{V}^h_{\Gamma_{\text{in}} \cup \Gamma_0} \times Q^h$ such that

$$\int_\Omega \dot{\boldsymbol{u}}_h \cdot \boldsymbol{v}_h \mathrm{d}\boldsymbol{x} = -\frac{1}{Re} \int_\Omega \nabla \boldsymbol{u}_h \cdot \nabla \boldsymbol{v}_h \mathrm{d}\boldsymbol{x} - \int_\Omega (\boldsymbol{u}_h \cdot \nabla \boldsymbol{u}_h) \cdot \boldsymbol{v}_h \mathrm{d}\boldsymbol{x} + \int_\Omega p_h \nabla \cdot \boldsymbol{v}_h \mathrm{d}\boldsymbol{x},$$

$$+ \int_\Omega \boldsymbol{f} \cdot \boldsymbol{v}_h \mathrm{d}\boldsymbol{x}, \quad \forall \boldsymbol{v}_h \in \boldsymbol{V}^h_0$$

$$0 = \int_\Omega q_h \nabla \cdot \boldsymbol{u}_h \mathrm{d}\boldsymbol{x}, \quad \forall q_h \in Q^h,$$

$$(3.21)$$

yielding the semi-discrete system (3.6), where

$$\boldsymbol{V}^h_{\Gamma_{\text{in}} \cup \Gamma_0} = \left\{ \boldsymbol{v}_h \in V^h : \quad \boldsymbol{v}_h|_{\Gamma_{\text{in}} \cup \Gamma_0} = \boldsymbol{u}_D \right\} \quad (3.22)$$

$$\boldsymbol{V}^h_0 = \left\{ \boldsymbol{v}_h \in V^h : \quad \boldsymbol{v}_h|_{\Gamma_{\text{in}} \cup \Gamma_0} = 0 \right\}. \quad (3.23)$$

are finite element approximations of $\boldsymbol{V}_{\Gamma_{\text{in}} \cup \Gamma_0}$ and $\boldsymbol{V}_0$, respectively. Note that by using a divergence-free basis for the test space $\boldsymbol{V}_0^h$, the singularity of E can be overcome and the state vector x will only represent the nodal values of the velocity field. For instance, this can be done by projecting the system onto the POD subspace, when its basis functions are computed using the snapshots of the velocity field only, which is (discretely) divergence-free. Thus, the weak form (3.21) becomes: find $\boldsymbol{u}_h(t, \cdot) \in \boldsymbol{V}_{\Gamma_{\text{in}} \cup \Gamma_0}^h$ such that

$$
\begin{aligned}
\int_\Omega \partial_t \boldsymbol{u}_h \cdot \boldsymbol{v}_h \mathrm{d}\boldsymbol{x} = & -\frac{1}{Re} \int_\Omega \nabla \boldsymbol{u}_h \cdot \nabla \boldsymbol{v}_h \mathrm{d}\boldsymbol{x} - \int_\Omega (\boldsymbol{u}_h \cdot \nabla \boldsymbol{u}_h) \cdot \boldsymbol{v}_h \mathrm{d}\boldsymbol{x}, \\
& + \int_\Omega \boldsymbol{f} \cdot \boldsymbol{v}_h \mathrm{d}\boldsymbol{x}, \quad \forall \boldsymbol{v}_h \in V_0^h,
\end{aligned}
\tag{3.24}
$$

yielding a semi-discrete nonlinear system in the usual state-space form

$$
\begin{cases}
\dot{\mathrm{x}} & = E^{-1} \mathcal{F}(\mathrm{x}) + E^{-1} G \mathrm{v} \\
\mathrm{y} & = H \mathrm{x},
\end{cases}
\tag{3.25}
$$

where the state vector x represents the nodal values of the velocity field only and the function $\tilde{\mathcal{F}}(\mathrm{x})$ and the non-singular mass matrix has been inverted.

3.3.2 Implicit pressure-correction scheme

An implicit pressure-correction scheme has been implemented, in order to solve the system of ODEs (3.6), resulting from the spatial discretisation. Pressure-correction schemes are time-stepping methods composed of two sub-steps for each time step: in the first sub-step, the pressure is treated explicitly or ignored; in the second sub-step, the pressure is corrected by projecting the provisional velocity, computed at the previous sub-step, onto a divergence-free subspace. The simplest pressure-correction scheme was originally proposed by Chorin (1968). When an implicit Euler method is used, the algorithm reads as follows. Set $\tilde{\boldsymbol{u}}^{(0)} = \boldsymbol{u}_0$. The first sub-step solves the momentum equation with a zero pressure gradient, namely: find $\boldsymbol{u}_h^{(k+1)} \in \boldsymbol{V}_{\Gamma_{\text{in}} \cup \Gamma_0}^h$ such that

$$
\begin{aligned}
\frac{1}{\Delta t} \int_\Omega \left(\tilde{\boldsymbol{u}}_h^{(k+1)} - \boldsymbol{u}_h^{(k)} \right) \cdot \boldsymbol{v}_h \mathrm{d}\boldsymbol{x} = & -\frac{1}{Re} \int_\Omega \nabla \tilde{\boldsymbol{u}}_h^{(k+1)} \cdot \nabla \boldsymbol{v}_h \mathrm{d}\boldsymbol{x} \\
& - \int_\Omega \left(\tilde{\boldsymbol{u}}_h^{(k+1)} \cdot \nabla \tilde{\boldsymbol{u}}_h^{(k+1)} \right) \cdot \boldsymbol{v}_h \mathrm{d}\boldsymbol{x} + \int_\Omega \boldsymbol{f}^{(k+1)} \cdot \boldsymbol{v}_h \mathrm{d}\boldsymbol{x}, \quad \forall \boldsymbol{v}_h \in \boldsymbol{V}_0^h,
\end{aligned}
\tag{3.26}
$$

where $\tilde{\boldsymbol{u}}_h^{(k+1)}$ represents the provisional velocity. In the second sub-step, both the velocity and pressure are updated by solving: find $(\boldsymbol{u}_h^{(k+1)}, p_h^{(k+1)}) \in \boldsymbol{V}_{\Gamma_{\text{in}} \cup \Gamma_0}^h \times Q^h$

such that

$$\frac{1}{\Delta t}\int_{\Omega}\left(\boldsymbol{u}_h^{(k+1)} - \tilde{\boldsymbol{u}}_h^{(k+1)}\right)\cdot\boldsymbol{v}_h\mathrm{d}\boldsymbol{x} + \int_{\Omega}\nabla p_h^{(k+1)}\cdot\boldsymbol{v}_h\mathrm{d}\boldsymbol{x} = 0, \quad \forall\boldsymbol{v}_h\in\boldsymbol{V}_0^h,$$
$$\int_{\Omega}\nabla\cdot\boldsymbol{u}_h\cdot q_h\mathrm{d}\boldsymbol{x} = 0, \quad \forall q_h\in Q^h. \tag{3.27}$$

In particular, first, the pressure is updated solving the Poisson equation

$$\int_{\Omega}\nabla p_h^{(k+1)}\cdot\nabla q_h\mathrm{d}\boldsymbol{x} = \frac{1}{\Delta t}\int_{\Omega}\nabla\cdot\tilde{\boldsymbol{u}}_h^{(k+1)}\cdot q_h\mathrm{d}\boldsymbol{x}. \tag{3.28}$$

Then, the corrected weakly divergence-free velocity is computed as

$$\int_{\Omega}\boldsymbol{u}_h^{(k+1)}\cdot\boldsymbol{v}_h\mathrm{d}\boldsymbol{x} = \int_{\Omega}\tilde{\boldsymbol{u}}_h^{(k+1)}\cdot\boldsymbol{v}_h\mathrm{d}\boldsymbol{x} - \Delta t\int_{\Omega}\nabla p_h^{(k+1)}\cdot\boldsymbol{v}_h\mathrm{d}\boldsymbol{x}. \tag{3.29}$$

More accurate and complex time-stepping methods may be used but this is outside the scope of this work.

3.4 Finite Volume Approximation

In view of the spatial discretisation of equations (3.1), (3.3), (3.2), (3.5), let (3.1) be rewritten using the integral vectorial form of the unsteady Reynolds averaged Navier-Stokes equations for the generic three-dimensional case $d = 3$, namely:

$$\boldsymbol{\Lambda}\frac{\partial}{\partial t}\int_{\mathcal{V}}\boldsymbol{q}\,\mathrm{d}V + \int_{\mathcal{S}(\mathcal{V})}\left(\boldsymbol{F}^c(\boldsymbol{q}) - \boldsymbol{F}^d(\boldsymbol{q})\right)\mathrm{d}S - \int_{\mathcal{V}}\boldsymbol{f}\,\mathrm{d}V = 0, \tag{3.30}$$

where $\boldsymbol{q} = (p, u, v, w)^{\mathrm{T}}$ represents the state variable for incompressible flows, $(\cdot)^{\mathrm{T}}$ denotes the transpose of $(\cdot)$, $\boldsymbol{\Lambda} = \mathrm{diag}\,(0, 1, 1, 1)$ and

$$\boldsymbol{F}^c = \left(\sum_{i=1}^{d}u_i n_i;\ u_1\sum_{i=1}^{d}u_i n_i + pn_1;\ u_2\sum_{i=1}^{d}u_i n_i + pn_2;\ u_3\sum_{i=1}^{d}u_i n_i + pn_3\right)^{\mathrm{T}},$$

$$\boldsymbol{F}^d = \left(0;\ \sum_{j=1}^{d}\tau_{1j}n_j;\ \sum_{j=1}^{d}\tau_{2j}n_j;\ \sum_{j=1}^{d}\tau_{3j}n_j\right)^{\mathrm{T}},$$

$$\tag{3.31}$$

are the convective (inviscid and pressure) and diffusive normal fluxes through the surface $\mathcal{S}(\mathcal{V})$ of the finite volume $\mathcal{V}$, respectively; $\mathbf{n} = (n_1, n_2, n_3)$ is the outward unit normal vector; u_i is the i–th Cartesian component of the velocity vector (in the following, the Cartesian components of the velocity are also denoted as u, v,

and w); $\tau_{ij} = \nu(u_{i,j} + u_{j,i})$ is the stress tensor; ν is the kinematic viscosity. The problem is closed by enforcing appropriate conditions at physical and computational boundaries. As in (3.3), on solid walls, the velocity is set to zero (whereas no condition on the pressure is required); at the inflow boundary, velocity is set to the undisturbed flow value, and the pressure is extrapolated from inside; on the contrary, the pressure is set to zero at the outflow, whereas velocity is extrapolated from the inner points. The initial conditions are specified for the velocity field as in (3.2). In this section, a finite volume discretisation of equations (3.30) is presented; the numerical solution of the discretised equations is obtained using $\chi navis$, a general-purpose, second order, multi-block with overlapping grids, finite volume unsteady RANS equations based solver, developed in Fortran 90 at CNR-INSEAN. The residual on each control volume is computed as an interface flux balance; the fluid domain Ω is partitioned into N_l structured adjacent or overlapped blocks Ω^l, each one subdivided into $N_i \times N_j \times N_k$ disjoint hexahedrons Ω^l_{ijk}. Conservation laws are applied to the (i, j, k)-th control volume:

$$\mathbf{\Lambda}\frac{\partial}{\partial t}\int_{\mathcal{V}_{ijk}} \boldsymbol{q}\ \mathrm{d}V + \sum_{s=1}^{6}\int_{\mathcal{S}_s}(\boldsymbol{F}^c_s(\boldsymbol{q}) - \boldsymbol{F}^d_s(\boldsymbol{q}))\ \mathrm{d}S - \int_{\mathcal{V}_{ijk}} \boldsymbol{f}\ \mathrm{d}V = 0, \qquad (3.32)$$

where $\mathcal{S}_s$ is the s-th face of the finite volume Ω_{ijk}, whose measure is $\mathcal{V}_{ijk}$. Defining $\overline{\boldsymbol{q}} = \frac{1}{\mathcal{V}_{ijk}}\int_{\mathcal{V}_{ijk}} \boldsymbol{q}\ \mathrm{d}V$ the volume average of the unknowns $\boldsymbol{q}$, the semi-discrete system of equations can be rewritten as:

$$\mathbf{\Lambda}\ \frac{\partial \overline{\boldsymbol{q}}}{\partial t}\Big|_{ijk} + \frac{1}{\mathcal{V}_{ijk}}\boldsymbol{\mathcal{R}}_{ijk} = 0, \qquad (3.33)$$

being $\boldsymbol{\mathcal{R}}_{ijk}$ the sum of the body forces and the flux balance on the current control volume $\mathcal{V}_{ijk}$. The surface integrals are evaluated by means of the (second order) trapezoidal rule. In the viscous fluxes, the computation of the velocity gradients, required for the computation of the stress tensor at the cell interface, are computed using a standard second order centered finite volume approximation (Hirsch, 2007). For the inviscid part, the fluxes are computed as the solution of a Riemann problem $\boldsymbol{F}^c_s = \boldsymbol{F}^c(\boldsymbol{q}_s) = \boldsymbol{F}^c(\boldsymbol{q}_l, \boldsymbol{q}_r)$; the right and left states can be estimated by several schemes implemented in the solver $\chi navis$, ranging from the first order Total Variation Diminishing scheme, the second order Essentially Non Oscillatory (ENO) scheme (Harten et al., 1987), the third-order upwind-based scheme (Van Leer, 1979) and the classical fourth-order centered scheme (for more details see Di Mascio et al., 2007b). Moreover, a second order accurate solution of the Riemann problem (Di Mascio et al., 2001) is used in place of the exact

one, which should be computed iteratively, given the non-linearity of the problem. It can be proved that the resulting scheme is second order accurate, and yields oscillation–free discrete solutions, also when the exact solutions are discontinuous (see Di Mascio et al., 2001, 2007b, and the references therein).

3.4.1 Temporal integration

Given the solution at a time instant $t = t^{n_t}$, the solution at the new time step $n_t + 1$ is computed by the following procedure. The time derivatives in the previous equations are approximated by means of a second order accurate three–point backward finite difference approximation formula; for example, for the governing equations (3.32), the time integration reads:

$$\mathbf{\Lambda} \frac{3\overline{\boldsymbol{q}}_{ijk}^{n_t+1} - 4\overline{\boldsymbol{q}}_{ijk}^{n_t} + \overline{\boldsymbol{q}}_{ijk}^{n_t-1}}{2\Delta t} + \frac{1}{\mathcal{V}_{ijk}} \mathcal{R}_{ijk}^{n_t+1} = 0, \tag{3.34}$$

where the superscript n_t denotes the time levels and Δt is the physical time step. The previous equation represents a system of coupled non-linear algebraic equations, which are solved iteratively by a dual (or pseudo) time integration (see Merkle and Athavale (1987) for more details). To this end, a pseudo-time derivative is introduced in the discrete system of equations

$$\widetilde{\mathbf{\Lambda}} \left. \frac{\partial \overline{\boldsymbol{q}}}{\partial \tau} \right|_{ijk} + \mathbf{\Lambda} \frac{3\overline{\boldsymbol{q}}_{ijk}^{n_t+1} - 4\overline{\boldsymbol{q}}_{ijk}^{n_t} + \overline{\boldsymbol{q}}_{ijk}^{n_t-1}}{2\Delta t} + \frac{1}{\mathcal{V}_{ijk}} \mathcal{R}_{ijk}^{n_t+1} = 0, \tag{3.35}$$

with $\Delta\tau$ being the pseudo–time step, $\widetilde{\mathbf{\Lambda}} = \mathrm{diag}\,(1/\beta_{\mathrm{pc}}, 1, 1, 1)$, and β_{pc} being the pseudo-compressibility factor (Chorin, 1968). Then, the solution is iterated to steady state with respect to the pseudo–time τ, for each physical time step. The integration with respect to the pseudo–time is carried out by means of an implicit Euler scheme, *i.e.*,

$$\widetilde{\mathbf{\Lambda}} \frac{\overline{\boldsymbol{q}}_{ijk}^{m_t+1} - \overline{\boldsymbol{q}}_{ijk}^{m_t}}{\Delta\tau} + \mathbf{\Lambda} \frac{3\overline{\boldsymbol{q}}_{ijk}^{m_t+1} - 4\overline{\boldsymbol{q}}_{ijk}^{n_t} + \overline{\boldsymbol{q}}_{ijk}^{n_t-1}}{2\Delta t} + \frac{1}{\mathcal{V}_{ijk}} \mathcal{R}_{ijk}^{m_t+1} = 0, \tag{3.36}$$

where the superscripts n_t and m_t denote the physical and dual time levels, respectively. The previous system of equations is then solved with respect to $\boldsymbol{q}_{ijk}^{m_t+1}$ as in the Beam and Warming's scheme (Beam and Warming, 1978) , *i.e.*, the equation is rewritten in "delta" form

$$\left(\widetilde{\mathbf{\Lambda}} + \frac{3\Delta\tau}{2\Delta t}\mathbf{\Lambda} \right) \delta\overline{\boldsymbol{q}}_{ijk}^{m_t} + \frac{\Delta\tau}{\mathcal{V}_{ijk}} \left. \frac{\partial \mathcal{R}}{\partial \boldsymbol{q}} \right|_{ijk}^{m_t} \delta\overline{\boldsymbol{q}}_{ijk}^{m_t}$$
$$+ \Delta\tau \left[\mathbf{\Lambda} \frac{3\overline{\boldsymbol{q}}_{ijk}^{m_t} - 4\overline{\boldsymbol{q}}_{ijk}^{n_t} + \overline{\boldsymbol{q}}_{ijk}^{n_t-1}}{2\Delta t} + \frac{1}{\mathcal{V}_{ijk}} \mathcal{R}_{ijk}^{m_t} \right] = 0, \tag{3.37}$$

where $\delta\overline{\boldsymbol{q}}_{ijk}^{m_t} = \overline{\boldsymbol{q}}_{ijk}^{m_t+1} - \overline{\boldsymbol{q}}_{ijk}^{m_t}$. The operator on the left hand side of the previous equation is solved by an approximate factorisation technique. The resulting scheme is unconditionally stable. A local dual time step and a multi-grid technique (Brandt, 1984; Favini et al., 1996) are used in order to improve the convergence rate of the sub–iteration algorithm.

3.4.2 Overlapping grid approach

For the numerical computations at higher Reynolds numbers, overlapping grid capabilities have been employed for both grid refinement/coarsening purposes and the inclusion of the plasma actuator. The basic elements of the overlapping grid approach (or "Chimera" method) implemented in the solver $\chi navis$ are reported here. For more details the reader is referred to Muscari and Di Mascio (2005); Di Mascio et al. (2006); Broglia et al. (2007b); Zaghi et al. (2015). The introduction of overlapping grid capabilities in the RANS code is made through a modification of both the boundary conditions and the internal point treatment for those zones where overlapping occurs. The approach is based on the search of the "donors" for those cells ("chimera cells") for which an overlap is found or for the cells on the non physical or computational boundaries (*i.e.*, on the boundaries of the blocks that are immersed in the computational domain). Once the donor is identified, then a convex set of eight donor cell centers is searched, and a tri-linear interpolation is used to transfer the solution from the "donor" set to the "chimera" cell. Differently from standard chimera approaches, however, the cell marked as "chimera" cells are not removed from the computation but the interpolated solution is enforced by adding a forcing term to the Navier-Stokes equations (3.36), in a "body-force" fashion:

$$
\widetilde{\boldsymbol{\Lambda}} \frac{\overline{\boldsymbol{q}}_{ijk}^{m_t+1} - \overline{\boldsymbol{q}}_{ijk}^{m_t}}{\Delta\tau} \quad + \boldsymbol{\Lambda} \frac{3\overline{\boldsymbol{q}}_{ijk}^{m_t+1} - 4\overline{\boldsymbol{q}}_{ijk}^{n_t} + \overline{\boldsymbol{q}}_{ijk}^{n_t-1}}{2\Delta t} \\
+ \left[\frac{1}{\mathcal{V}_{ijk}} \boldsymbol{\mathcal{R}}_{ijk}^{m_t+1} + \frac{k}{\delta} \left(\overline{\boldsymbol{q}}_{ijk}|^{m_t} - \overline{\boldsymbol{q}}_{\mathsf{interp}}|^{m_t} \right) \right] = 0,
\tag{3.38}
$$

In the previous equation $\overline{\boldsymbol{q}}_{ijk}$ is the vector of the dependent variables at the cell ijk marked as "chimera" cell, and $\overline{\boldsymbol{q}}_{interp}$ is the tri-linear interpolation of the solution from the donor cells. Moreover, $k = \mathcal{O}(10)$ is a parameter chosen through numerical tests, and δ is the minimum between the cell non-dimensional diameter and the non-dimensional time step. This approach is particularly useful when using multigrid and approximate factorisation, as it allows to maintain a structured data set.

3.4.3   Code parallelisation

The coarse/fine grain parallelisation of the unsteady RANS code has been achieved by distributing the structured blocks among the available distributed (nodes) or shared memory (threads) processors, and by spreading the computational work to be done (mostly in terms of do loop inside each block among available shared memory processors). Useful pre-processing tools, which allows the splitting of the structured blocks and the distribution of them among the processors, were developed for load balancing (Broglia et al., 2014), whereas fine tuning is left to the user. Communication between processors for the coarse grain parallelisation is obtained by using standard Message Passing Interface (MPI) library, whereas fine grain (shared memory) parallelisation is achieved by means of the Open Message Passing (OpenMP) library. The efficiency of the parallel code has been investigated in Broglia et al. (2007a, 2014) (to which the reader is referred for details), where satisfactory speed up performances have been shown in different test cases.

3.5 Summary

An analytical control-oriented model of the flow/actuator dynamics has been presented. It is based on the incompressible Navier-Stokes equations, which are coupled with the plasma dynamics through the body force that is generated by the actuator. Two different numerical schemes have also been discussed: a finite element method, which will be used in the next chapter to both simulate low Reynolds number flows and obtain a simple low-order model of the flow dynamics; a finite volume method, which will be used for more realistic simulations at higher Reynolds numbers.

SISO Flow Separation Control

This chapter addresses the practical problem of robustly controlling the flow separation over an aerofoil, using the plasma actuator voltage as the control input and realistically available real-time velocity measurements as the control output (see, for example, Buder et al., 2008; Segawa et al., 2010; Spazzini et al., 2001, 1999). Despite the complexity of the dynamics of interest, it is shown how the problem of controlling flow separation can be formulated as a simple output regulation problem, so that a simple control strategy may be used. A robust output feedback control is designed, on the basis of the low-order, linear, dynamical model approximating the incompressible Navier-Stokes equations, which has been presented in Chapter 2. Fast flow reattachment is achieved, along with both stabilisation and increase/reduction of the lift/drag, respectively. Two-dimensional finite element simulations of the full-order nonlinear equations illustrate the effectiveness of the proposed approach: good dynamic performances are obtained, as both the Reynolds number and the angle of attack are varied. The chosen output can be experimentally measured by appropriate sensors and the extension of the proposed approach to 3D configurations is straightforward.

4.1   Problem Statement and Objectives

The aim is to formulate and solve the flow separation problem, *i.e.*, to make

$$\partial_{\boldsymbol{n}} u_{\boldsymbol{\tau}}(t, \boldsymbol{x})|_{\Gamma_N} = \big(\boldsymbol{\tau}(\boldsymbol{x}) \cdot \nabla \boldsymbol{u}(t, \boldsymbol{x}) \cdot \boldsymbol{n}(\boldsymbol{x})\big)|_{\Gamma_N} > 0, \tag{4.1}$$

as a simple output regulation problem, *i.e.*, to make the measured output

$$\mathrm{y}(t) = u_\tau(t, \boldsymbol{x}_s) > \varepsilon > 0. \tag{4.2}$$

Here: $\boldsymbol{u}$ is the time-dependent flow velocity vector; $\boldsymbol{x}$ and $\boldsymbol{x}_s$ denote the spatial coordinates and the sensor location, respectively; Γ_N represents the aerofoil boundary; $\boldsymbol{n}$ and $\boldsymbol{\tau}$ are the normal and tangent unit vectors to Γ_N, respectively. The objective is to design a simple robust output feedback control, along with a suitable reference signal y* for y, in order to suppress the flow separation along the aerofoil, *i.e.*, to drive the regulation error ỹ = y − y* to zero. To this end, the recent results in Marino and Tomei (2015) are extended to a wider class of control-systems, which are suitable for the considered specific scenario, and propose their application to the flow separation control problem. The resulting set-point tracking control is designed upon a single ROM approximation of the nonlinear flow dynamics, for given parameters. The proposed control-oriented ROM is obtained from the snapshots of a finite element approximation of the incompressible Navier-Stokes equations, which govern the evolution of $\boldsymbol{u}$, in the presence of a body force distribution, which represents the action of the plasma actuators on the neutrally-charged flow dynamics.

4.2 Actuator Model

The time scale disparity between the flow and the discharge frequencies allows for assuming that the force acts on the neutral fluid in a quasi-steady manner. The body force felt by the neutral flow is equivalent to the electro-magnetic force acting on the net charge density. Several models for the DBD actuator force have been proposed (see, for example, (Corke et al., 2007) for a detailed review). The bilinear model proposed by Shyy et al. (2002) is widely used in the flow control literature (see, for example, Cho and Shyy, 2011), because of its simplicity. However, this model is based on the linear approximation of the variation in space of the electric field generated by the electrodes. This simplifying assumption is not consistent with experiments (see, for example, Enloe et al., 2004; Orlov et al., 2006), which show an exponential spatial decay. As a result, the model over-predicts the actuator effect.

Here, a control-oriented modified version of the recent model studied in Yang and Chung (2015) is proposed, which demonstrated good agreement with experimental data. The model is characterised by an exponential dependence on the spatial coordinates and, in particular, the force is modelled by a Rayleigh distribution (see Yang and Chung, 2015). The total body force vector field $\boldsymbol{f} : [0, T] \times \Omega \rightarrow \mathbb{R}^d$,

which appears in the Navier-Stokes equations (3.1), reads

$$
\begin{aligned}
\boldsymbol{f}(t, \boldsymbol{x}) &= f_\tau(t, x_\tau, y_n)\boldsymbol{\tau}(\boldsymbol{x}) + f_n(t, x_\tau, y_n)\boldsymbol{n}(\boldsymbol{x}) \\
&= I(t)\frac{\lambda_f x_\tau}{\sigma_f^2}e^{-x_\tau^2/2\sigma_f^2 - \lambda_f y_n}\boldsymbol{\tau}(\boldsymbol{x}),
\end{aligned}
\tag{4.3}
$$

where: $f_n(t, x_\tau, y_n) \equiv 0$, $I(t) = k_v \mathrm{V}(t)/\mathrm{V}_m$ ($k_v \in \mathbb{R}$, V_m [kV]) is the total plasma force; $\mathrm{V}(t) : \mathbb{R} \to \mathbb{R}$ is the amplitude variation of the operation voltage (in kV); $\mathrm{v}(t) = \mathrm{V}(t)/\mathrm{V}_m$ is the corresponding non-dimensionalised voltage input, scaled by V_m; f_τ, f_n (in N/m³) are the tangential and normal components, with respect to the aerofoil, of the force density, respectively; $x_\tau, y_n \geq 0$ are related to $\boldsymbol{x} = (x, y)$ by a coordinate transformation and respectively refer to the tangent and normal components, relative to the geometry, in the reference frame centred in $\boldsymbol{x}_a$ (see figure 4.1). The parameters $\lambda_f = 1.6$, $\sigma_f = 1.9$, $k_v = 5200e^{1/2}\sigma_f/\lambda_f$ are chosen
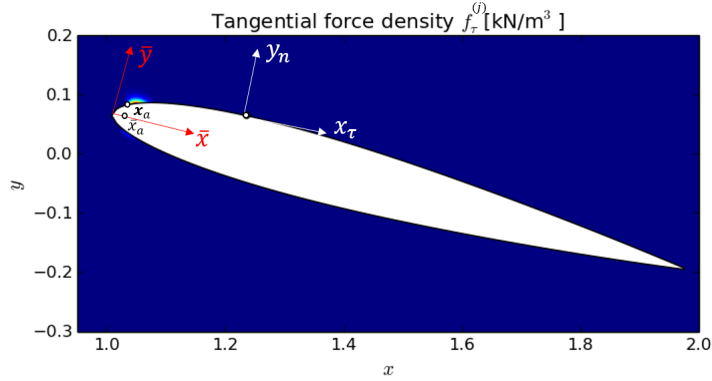
Figure 4.1: Tangential force density $f_\tau^{(j)}$ and reference frames.

as in Yang and Chung (2015), where this model has been compared with particle image velocimetry (PIV) data, whilst, for sake of simplicity, a simple linear dependence of the body force on the applied peak-to-peak voltage is assumed here (see Jayaraman and Shyy, 2008; Shyy et al., 2002). The presence of the feedback control makes a detailed characterisation of the plasma force/voltage dependence not necessary, due to its capability of automatically modifying the control action in order to compensate for model inaccuracies.

4.2.1 Preliminaries

Similarly to Marino et al. (2015), the control problem is to design a suitable feedback law $\mathrm{v}(t)$ for system (2.74), based on the real-time measurement $\mathrm{y}(t)$, in

order to robustly regulate the latter to a given reference region (*e.g.*, $y(t) \geq \varepsilon > 0$). The key objective is to design v such that the closed-loop trajectories of system (2.1) are guaranteed to evolve within some "safe" invariant set in different scenarios, depending on uncertain parameters (*e.g.*, the Reynolds number Re and angle of attack β). However, as the linear ROM (2.74) is computed at given parameters (*i.e.*, Re and β), it cannot give an accurate approximation of the full-order nonlinear dynamics (2.1) when the unknown parameters are varied. Furthermore, the dependence of dynamical properties of fluid systems on such parameters is highly nonlinear. Therefore, on the basis of the recent results in Marino and Tomei (2015), a robust output regulator guaranteeing exponential convergence of the regulation error is designed: it only requires the system to have a non-zero steady-state gain of known sign. Let

$$y^* = -d\mathrm{w} \tag{4.4}$$

be a constant reference signal for the output, where $d \in \mathbb{R}$ and w is generated by the exosystem

$$\dot{\mathrm{w}} = 0, \quad \mathrm{w}(0) = \mathrm{w}_0. \tag{4.5}$$

Let

$$P(s) = C(sI - A)^{-1}B, \tag{4.6}$$

whose poles have all negative real part, be the open-loop transfer function of system (2.74), which is both controllable and observable by construction. Therefore, the necessary and sufficient conditions for the solution of the regulator problem are satisfied (see Francis and Wonham, 1976). In particular, in the case of constant reference signals, $P(0) \neq 0$ is a necessary and sufficient condition for the existence of a unique pair of matrices (Γ, γ), which solves the regulator problem

$$
\begin{aligned}
0 &= A\Gamma + B\gamma, \\
C\Gamma + d &= 0.
\end{aligned}
\tag{4.7}
$$

The pair (Γ, γ) defines both the references $\xi^* = \Gamma\mathrm{w}$ and $\mathrm{v}^* = \gamma\mathrm{w}$ for the state and control input, respectively. Denoting $\tilde{\xi} = \xi - \xi^*$ and $\eta = -\mathrm{v}^*$, the error dynamics are given by

$$
\begin{cases}
\dot{\tilde{\xi}} &= A\tilde{\xi} + B(\mathrm{v} + \eta), \\
\dot{\eta} &= 0, \quad \eta(0) = \eta_0, \\
\tilde{y} &= C\tilde{\xi},
\end{cases}
\tag{4.8}
$$

so that the control problem can be formulated as a disturbance rejection problem, where the reference input $v^* = -\eta$ can be viewed as a scalar disturbance, which matches the control input v (see Marino and Tomei, 2015). The uncertain matrices A, B, C, as well as the order of the model, highly depend on the uncertain set of parameters which defines the physical problem, such as, in our specific application, the Reynolds number Re and angle of attack β. Given a certain range for the uncertain parameters (*e.g.*, Re and β), it is only assumed that there exist some positive constants r, $\epsilon_{a_{jk}}$, ϵ_{b_j} and ϵ_{c_j}, such that the coefficients of A, B, C, belong to their corresponding compact sets $[a_{jk}-\epsilon_{a_{jk}}, a_{jk}+\epsilon_{a_{jk}}]$, $[b_j-\epsilon_{b_j}, b_j+\epsilon_{b_j}]$, $[c_j - \epsilon_{c_j}, c_j + \epsilon_{c_j}]$, for any $j, k = 1, ..., r$, and are such that $P(0)$ does not change sign, within the whole range.

4.3 Control Algorithm: Constant Output Reference

Let $\hat{\eta} = -\hat{v}^*$ be the estimate of the unknown disturbance. A variant of the control algorithm presented in Marino and Tomei (2015) is proposed, in the case of constant disturbances:

$$\begin{cases} \dot{\hat{\eta}} & = k \, \text{sign}(P(0))\tilde{y} - \mu\hat{\eta}\tilde{y}^2, \quad \hat{\eta}(0) = \hat{\eta}_0, \\ v & = -\hat{\eta}, \end{cases} \tag{4.9}$$

where $k > 0$ and $\mu \geq 0$ are chosen control gains. Let

$$y^* \equiv \varepsilon > 0 \tag{4.10}$$

be a constant reference signal. The control algorithm (4.9) depends on: the measured output y; the constant reference y^*; the known sign of $P(0)$; the positive design parameters k, μ ε.

Remark 1. *The anti-windup term $\mu\hat{\eta}\tilde{y}^2$ plays a stabilising role similar to the one played by the well-known term $\mu\hat{\eta}$, where the quadratic function of the tracking error $\tilde{y}^2$ has been introduced in order not to affect the stability analysis, when μ is sufficiently small.*

The main result of this section, which extends the results obtained in Marino and Tomei (2015) to the proposed control algorithm (4.9), on the basis of the proposed balanced DMD model (2.74), is summarised in the following theorem: it

establishes the sufficient conditions under which the the designed SISO set-point tracking controller guarantees the solution of the flow separation problem (4.1) for the reduced-order dynamics.

Theorem 1. *Consider the closed-loop system (2.74), (4.9). Assume that $P(0) \neq 0$ with known sign. Then, for any initial condition $(\xi_0, \eta_0, \hat{\eta}_0)$, there exist a $k^* > 0$ and a sufficiently small $\mu^* \geq 0$, depending on k^*, such that the regulation error $\tilde{y}(t)$ and the control input error $v(t) - v^*$ exponentially tend to zero, as t tends to infinity, for any $0 < k \leq k^*$, $0 \leq \mu \leq \mu^*$.*

4.3.1 Stability Analysis

The stability analysis of the closed-loop system is given in the following proof.

Proof. Case $\mu = 0$. System (4.8) can be rewritten as

$$\tilde{Y}(s) = P(s)\left(v(s) + \eta\right), \quad P(s) = \frac{n_P(s)}{d_P(s)}. \tag{4.11}$$

The stability of the closed-loop system is determined by the zeros of the transfer function

$$Q(s) = 1 + kP(s)\left(\frac{\text{sign}(P(0))}{s}\right) = \frac{n_Q(s)}{d_Q(s)}. \tag{4.12}$$

By the root locus, for sufficiently small $k > 0$, r zeros of $Q(s)$ are sufficiently close to the r poles of $P(s)$ and, therefore, they have negative real part. The remaining branch of the root locus starts from 0 in the s-plane with angle π, so that also the remaining zeros of $Q(s)$ have negative real part.

Case $\mu > 0$. Let $\tilde{\eta} = v - v^* = \eta - \hat{\eta}$ and

$$\tilde{\chi} = \begin{bmatrix} \tilde{\xi} \\ \tilde{\eta} \end{bmatrix}. \tag{4.13}$$

The closed-loop error dynamics can be written as

$$\dot{\tilde{\chi}} = \begin{bmatrix} A & B \\ -k \text{ sign}(P(0))C & 0 \end{bmatrix} \tilde{\chi} + \begin{bmatrix} 0 \\ \mu \tilde{\xi}^{\text{T}} C^{\text{T}} C \tilde{\xi}(\eta - \tilde{\eta}) \end{bmatrix} = A_c \tilde{\chi} + l(\tilde{\chi}),$$

$$\tilde{y} = [C, 0]\,\tilde{\chi}.$$

The characteristic polynomial of the closed-loop matrix A_c can be computed as

$$p_{A_c}(s) = \det(sI_{r+1} - A_c) = \det\begin{bmatrix} sI_r - A & B \\ -k \text{ sign}(P(0))C & s \end{bmatrix}$$

$$= \det(sI_r - A)\left(s + kC(sI_r - A)^{-1}B\text{sign}(P(0))\right)$$

$$= sd_P(s) + kn_P(s)\text{sign}(P(0)) = n_Q(s).$$

Therefore, A_c is Hurwitz, as its eigenvalues coincide with roots of $n_Q(s)$ and have negative real part for any sufficiently small k. Thus, there exist two symmetric, positive definite matrices $\mathcal{P}$ and $\mathcal{Q}$ satisfying the Lyapunov equation: $\mathcal{P}A_c + A_c^{\mathrm{T}}\mathcal{P} = -\mathcal{Q}$. Consider the candidate Lyapunov function

$$\mathcal{V}(t) = \tilde{\chi}^{\mathrm{T}}(t)\mathcal{P}\tilde{\chi}(t), \tag{4.14}$$

satisfying

$$\alpha_1 \|\tilde{\chi}(t)\|^2 \leq \mathcal{V}(t) \leq \alpha_2 \|\tilde{\chi}(t)\|^2, \tag{4.15}$$

where α_1, $\alpha_2 > 0$ are positive constants. The time derivative of $\mathcal{V}(t)$, along the trajectories of the closed-loop system satisfies the following inequality:

$$\dot{\mathcal{V}} \leq -\tilde{\chi}^{\mathrm{T}}\mathcal{Q}\tilde{\chi} + 2\tilde{\chi}^{\mathrm{T}}\mathcal{P}l(\tilde{\chi}) \leq -\mathcal{M}_1 \|\tilde{\chi}\|^2 + 2\mathcal{M}_2\mu\|\tilde{\chi}\|^2 \left|\eta\tilde{\eta} - \tilde{\eta}^2\right|$$
$$\leq -\left(\mathcal{M}_1 - \frac{\mathcal{M}_2\mu\eta^2}{2}\right)\|\tilde{\chi}\|^2,$$

where $\mathcal{M}_1 = \|\mathcal{Q}\|$, $\mathcal{M}_2 = \|\mathcal{P}\|\|C\|^2$. Therefore, for sufficiently small μ, there exists an $\alpha_3 > 0$ such that

$$\dot{\mathcal{V}} \leq -\alpha_3 \|\tilde{\chi}\|^2 \leq -\frac{\alpha_3}{\alpha_2}\mathcal{V}, \tag{4.16}$$

thus implying the closed-loop boundedness and the exponential convergence to zero of both the regulation error $\tilde{\mathrm{y}}(t)$ and the control input error $\mathrm{v}(t) - \mathrm{v}^*$, as t tends to infinity. $\qquad\square$

4.4 Control Algorithm: Reference Region

The control algorithm (4.9) can be slightly modified in order to allow the output y to belong to a set, rather than imposing a single, constant reference. This is translated into the following, simpler, control objective:

$$\mathrm{y} \in \Omega_\varepsilon = [\varepsilon_m, \varepsilon_M], \tag{4.17}$$

where ε_m and ε_M are chosen positive constants. This control objective is less restrictive and gives greater flexibility in the choice of the output reference. In particular, the lower bound for the output reference can be chosen in order to guarantee any a priori fixed requirement, such as, in the present application, the suppression of the separation bubble over the aerofoil; the upper bound can be chosen in order to limit the power consumption. Therefore, the control problem

(similarly to Marino et al., 2015) becomes to design v such that the chosen controlled output y belongs to a "safe" compact set Ω_ε.

In particular, the reference output y^* is chosen as

$$
y^*(t) = \begin{cases} \varepsilon_m, & \text{if } y(t) < \varepsilon_m, \\ y(t), & \text{if } y(t) \in \Omega_\varepsilon, \\ \varepsilon_M, & \text{if } y(t) > \varepsilon_M. \end{cases} \tag{4.18}
$$

The references for the state and the input are defined as

$$
\xi^*(t) = \begin{cases} \xi_m, & \text{if } y(t) < \varepsilon_m, \\ \xi(t), & \text{if } y(t) \in \Omega_\varepsilon, \\ \xi_M, & \text{if } y(t) > \varepsilon_M, \end{cases} \tag{4.19}
$$

$$
v^*(t) = \begin{cases} v_m, & \text{if } y(t) < \varepsilon_m, \\ \text{argmin}_{\bar{v} \in \Omega_\eta} |\bar{v} + \hat{\eta}|, & \text{if } y(t) \in \Omega_\varepsilon, \\ v_M, & \text{if } y(t) > \varepsilon_M, \end{cases} \tag{4.20}
$$

where the constant pairs ξ_m, v_m and ξ_M, v_M can be computed by solving the regulator problem (4.7) for $y^* = \varepsilon_m$ and $y^* = \varepsilon_M$, respectively.

The overall control algorithm (4.9), (4.18) depends on: the measured output y; the bounded reference y^*; the known sign of $P(0)$; the positive design parameters k, μ ε_m, ε_M. Note that, when $\varepsilon = \varepsilon_m = \varepsilon_M$, the control algorithm (4.9), (4.18) reduces to (4.9), with a constant output reference.

4.4.1 Stability Analysis

By Theorem 1, given any constant output reference $\varepsilon \in \Omega_\varepsilon$, $\xi(t)$ and $v(t)$ exponentially converge to their corresponding constant references $\bar{\xi} \in \Omega_\xi$ and $\bar{v} \in \Omega_\eta$, respectively, where Ω_ξ, Ω_η are suitable compact sets containing all the state and input references which guarantee perfect output regulation $y(t) \equiv \varepsilon$, for compatible initial conditions. Thus, the reference $\bar{\chi} = [\bar{\xi}^{\mathrm{T}}, \bar{v}]$ for $\chi = [\xi^{\mathrm{T}}, v]$ belongs to the compact set $\Omega_\chi = \Omega_\xi \times \Omega_\eta$. We can then extend Theorem 1 to the control algorithm (4.9), with the output reference (4.18).

Corollary 1. *Consider the closed-loop system (2.74), (4.9), (4.18). Assume that $P(0) \neq 0$ with known sign. Then, for any initial condition $(\xi_0, \eta_0, \hat{\eta}_0)$, there exist sufficiently small $k^* > 0$ and $\mu^* \geq 0$, such that the regulation error $y(t) - y^*(t)$ and the control input error $v(t) - v^*(t)$ exponentially tend to zero, as t tends to infinity, for any $0 < k \leq k^*$, $0 \leq \mu \leq \mu^*$.*

Proof. Consider the candidate Lyapunov function defined in (4.14). Let $\tilde{\chi}$ be defined as in (4.13), $\tilde{\xi} = \xi - \xi^*$ and $\tilde{\eta} = v - v^*$, where ξ^* and v^* are defined in (4.19) and (4.20), respectively. When the output belongs to the compact set Ω_ε, we have: $\tilde{\xi} \equiv 0$, $\dot{\tilde{\xi}} \equiv 0$, $\dot{\tilde{\eta}} \equiv 0$. Thus, for any $t \geq 0$ such that $y(t) \in \Omega_\varepsilon$, $\dot{\mathcal{V}}(t) \equiv 0$. When the output does not belong to the reference region, as in the previous proof, there exist three positive constants α_1, α_2, $\alpha_3 > 0$ such that $\mathcal{V}(t)$ and its time derivative satisfy (4.15) and (4.16), respectively. Therefore, for any $t \geq 0$ such that $y(t) \notin \Omega_\varepsilon$, $\dot{\mathcal{V}}(t) < 0$ and the distance

$$\mathrm{d}_{\mathcal{P}}\left(\chi(t), \Omega_\chi\right) = \inf_{\bar{\chi} \in \Omega_\chi} \|\chi - \bar{\chi}\|_{\mathcal{P}} = \sqrt{\tilde{\chi}^{\mathrm{T}} \mathcal{P} \tilde{\chi}},$$

between χ and its reference set Ω_χ satisfies

$$\mathrm{d}_{\mathcal{P}}^2\left(\chi(t), \Omega_\chi\right) \leq \alpha_2 \|\tilde{\chi}\|^2 \leq e^{-\alpha t}\delta,$$

where $\alpha = \alpha_3/\alpha_2$ and $\delta = \mathcal{V}(0)\alpha_2/\alpha_1$. Since $0 \leq \mathcal{V}(t) \in \mathcal{C}^1$ is lower bounded and its derivative is semi-negative definite, it admits a finite limit (see Courant, 1937, p. 61). Closed-loop boundedness and exponential convergence of $\dot{\mathcal{V}}(t)$ (and, therefore, of $\tilde{\xi}$ and $\dot{\tilde{\eta}}$) to zero are thus guaranteed, according to Barbalats lemma (see section 4.5.2 in Slotine and Li, 1991), as $\mathcal{V}(t)$ is uniformly continuous. Consequently, $\xi(t)$ converges to a constant reference $\bar{\xi} \in \Omega_\xi$ and $v(t)$ converges to a constant value $\bar{v}$, as t tends to infinity. If $\bar{v} \notin \Omega_\eta$, then $\bar{y} = C\bar{\xi} = -P(0)\bar{v} \notin \Omega_\varepsilon$, which contradicts $\bar{\xi} \in \Omega_\xi$. Therefore, $\bar{v} \in \Omega_\eta$ and the distance $\mathrm{d}_{\mathcal{P}}\left(\chi(t), \Omega_\chi\right)$ exponentially tends to zero, as t tends to infinity. □

The following theorem establishes that, if the conditions of Corollary 1 are restricted, a robust universal controller (4.9), (4.18) can be designed without any restrictions on the control gain k.

Theorem 2. *Consider the closed-loop system (2.74), (4.9), (4.18). Assume that $Re\{P(i\omega)\} > 0$ for all $\omega \in \mathbb{R}$. Then, for any initial condition $(\xi_0, \eta_0, \hat{\eta}_0)$, there exists a sufficiently small $\mu^* \geq 0$ such that the regulation error $y(t) - y^*(t)$ and the control input error $v(t) - v^*(t)$ exponentially tend to zero as t tends to infinity, for any $k > 0$, $0 \leq \mu \leq \mu^*$.*

Proof. Corollary 1 implies the exponential convergence of $y(t)$ and $v(t)$ to their corresponding reference sets Ω_ε and Ω_η, respectively, for sufficiently small k and μ. To complete the proof it is, therefore, sufficient to show (as in Marino and Tomei, 2015) that there are no solutions on the imaginary axis of the equation

$$1 + kP(s)\frac{1}{s} = 0,$$

so that the positive root locus cannot cross the imaginary axis. The point $s = 0$ is not a zero of $Q(s)$, as $P(0) > 0$. The phase condition for a point $s = j\omega$ to belong to the positive root locus for $\omega \neq 0$ becomes

$$\arg[P(j\omega)] - \frac{\pi}{2} = \pi.$$

Since, by hypothesis, $-\pi/2 < \arg[P(j\omega)] < \pi/2$, the previous condition is never satisfied. Therefore, all branches must lie in the open left-hand complex half-plane. $\qquad\square$

4.4.2 Variant: Time-varying Gain

Let

$$\begin{cases} \dot{\hat{\eta}} &= k\,\text{sign}(P(0))\tilde{y} - \mu\hat{\eta}\tilde{y}^2, \quad \hat{\eta}(0) = \hat{\eta}_0, \\ \text{v} &= -\sigma(\text{y})\hat{\eta}, \end{cases} \tag{4.21}$$

in which: $0 < \sigma(\text{y}) \leq 1$ is any real-valued, bounded, continuous function. In particular, similarly to the projection algorithm defined in Marino et al. (2008), $\sigma(\text{y})$ is chosen as

$$\sigma(\text{y}) = \begin{cases} 1 & \text{if } \text{y} < \varepsilon_m \text{ or } \hat{\text{v}}^* < 0, \\ 1 - \sigma_\varepsilon(\text{y}) & \text{if } \text{y} \in \Omega_\varepsilon \text{ and } \hat{\text{v}}^* > 0, \\ 1 - \sigma_\varepsilon(\varepsilon_M) & \text{if } \text{y} > \varepsilon_M \text{ and } \hat{\text{v}}^* > 0, \end{cases} \tag{4.22}$$

$$\sigma_\varepsilon(\text{y}) = \frac{\text{y}^2 - \varepsilon_m^2}{\text{y}_M^2 - \varepsilon_m^2}, \tag{4.23}$$

where $\text{y}_M > \varepsilon_M \geq \varepsilon_m > 0$ are positive design parameters. Note that, when $\varepsilon = \varepsilon_m = \varepsilon_M$, the control algorithm (4.18), (4.21), (4.22), (4.23) reduces to (4.9), with a constant output reference.

Remark 2. *The introduction of the function $\sigma(y)$ is used, for this specific application, to reduce the control action, once the controlled output reaches the desired region. This time-varying gain, along with the less restrictive reference signal, allows for the use of higher gains k, thus leading to faster dynamic performances, whilst limiting the overshoot.*

Theorem 3. *Corollary 1 and Theorem 2 hold for the closed-loop system (2.74), (4.18), (4.21), (4.22), (4.23).*

Proof. When the output does not belong to the reference region, the closed-loop error dynamics becomes

$$\dot{\tilde{\chi}} = \begin{bmatrix} A & B \\ -k\sigma(\mathrm{y})\mathrm{sign}(P(0))C & 0 \end{bmatrix} \tilde{\chi} + \begin{bmatrix} 0 \\ \mu\tilde{\xi}^{\mathrm{T}}C^{\mathrm{T}}C\tilde{\xi}(\eta - \tilde{\eta}) \end{bmatrix} = A_\sigma\tilde{\chi} + l(\tilde{\chi}),$$

$$\tilde{\mathrm{y}} = [C, 0]\,\tilde{\chi},$$

so that, since $k\sigma(\varepsilon_M) \leq k\sigma(\mathrm{y}) \leq k$, A_σ is Hurwitz for sufficiently small k and Corollary 1 holds. Furthermore, there are no solutions on the imaginary axis of the equation

$$1 + K_\sigma(s)P(s)\frac{1}{s} = 0,$$

where $K_\sigma(s) > 0$ is the Laplace transform of $k\sigma(\varepsilon_M) < k\sigma(\mathrm{y}(t)) \leq k$, for any finite $K_\sigma(s)$, so that the positive root locus cannot cross the imaginary axis and Theorem 2 holds. □

4.5 Simulation Results: FEniCS, 2D case

The considered two-dimensional configuration is a NACA 0012 aerofoil geometry, denoted by Γ_N, in a rectangular channel $\Gamma_R = \Gamma_{\mathrm{in}} \cup \Gamma_R^+ \cup \Gamma_R^- \cup \Gamma_{\mathrm{out}} = \partial R$, where $R = [0, 10] \times [-2, 2]$. Here, the wall boundary is $\Gamma_0 = \Gamma_N \cup \Gamma_R^+ \cup \Gamma_R^-$, where Γ_R^+ and Γ_R^- are the upper and lower walls of the channel, respectively. The inflow boundary condition on Γ_{in} is a parabolic velocity profile

$$\boldsymbol{g}(t, \boldsymbol{x}) = \left(-\frac{4U_m}{h_c^2}\left(y^2 - \frac{h_c^2}{4}\right), 0\right), \tag{4.24}$$

where $h_c = 4$ is the channel height and $U_m = 1$ is the maximum, non-dimensionalised inflow velocity.

The presented continuous Galerkin finite element method has been implemented in Python, as described in Section 3.3, in order to spatially discretise both the velocity and pressure fields, using second-order and first-order Lagrange polynomials, respectively. The FEniCS Python library has been used to implement the finite element formulation and perform Direct Numerical simulations (DNS) of unsteady flows. FEniCS is a collection of different components, including: a problem-solving environment DOLFIN, the form compiler FFC, the finite element tabulator FIAT, the just-in-time compiler Instant, the code generation interface UFC, the form language UFL. In particular, although the code has been written

in Python, FEniCS allows for the auto-generation of a fast, parallelised C^{++} code, which can be run efficiently on high-performance computers.

The reduced-order DMD model (2.71) has been obtained from $m = 745$ snapshots of the state responses of system (3.6) to an impulsive input $\delta(t - t_0)$. For $m > 745$ the snapshots became approximately linearly dependent, as the residual defined in (2.50) was $\|\boldsymbol{r}\| < 10^{-10}$ for $m = 745$, due to the periodic nature of the attractor. The input is centred at $t_0 = 0.2$, with amplitude $\Delta v = 2/\Delta t$, which was chosen so that $\delta(t - t_0)$ has unitary integral. The snapshots are taken every $20\Delta t$, where $\Delta t = 0.002$ is the simulation time-step, until the trajectories of the system approach a periodic orbit. The considered two-dimensional configuration, which is used to build the ROM, is the flow around a NACA 0012 aerofoil, with angle of attack $\beta = 20°$ and $Re = 1000$. The sensor was placed at $2c/5$ and the actuator at $c/5$, corresponding to $x_\tau, y_n = 0$, where c is the chord length (see Figure 4.2). In this section, very low Reynolds numbers (representative, for example, of micro UAVs) and fixed actuator/sensor positions are considered in order to test the effectiveness of the proposed reduced-order modelling technique. The objective is to show that, although the control algorithm is designed upon a simple linear ROM computed using the snapshots of the full-order nonlinear system, good performances are achieved when such control algorithm is applied to the latter. In the next section, the same feedback control scheme will be applied to the full-order nonlinear system, discretised using an accurate finite volume method, at $Re = 20,000$ (20 times greater than the Reynolds number at which the ROM is computed) and the position of the actuator/sensor pair will be varied in order to optimise the closed-loop system. Finite element simulations have been per-
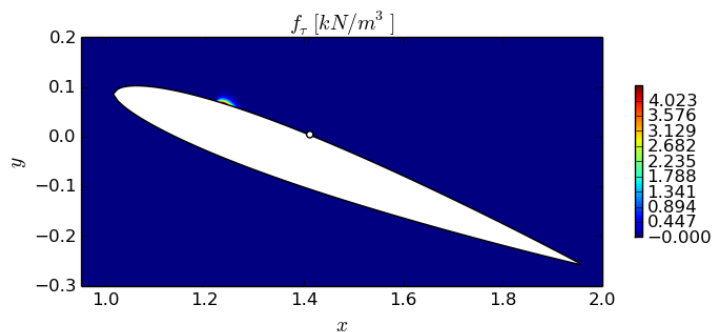
Figure 4.2: Actuator force density and sensor position (white dot).

formed, as described in Section 3.3, to compute the snapshots of the flow past the aerofoil. The dimension of the full-order system (3.6), describing the evolution in
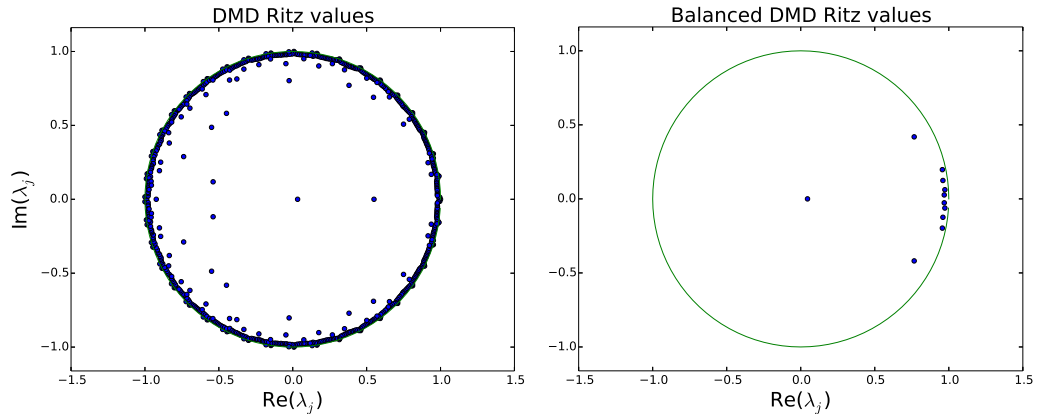
Figure 4.3: DMD (left) and balanced DMD (right) Ritz values $Re = 1000$, $\beta = 20°$.
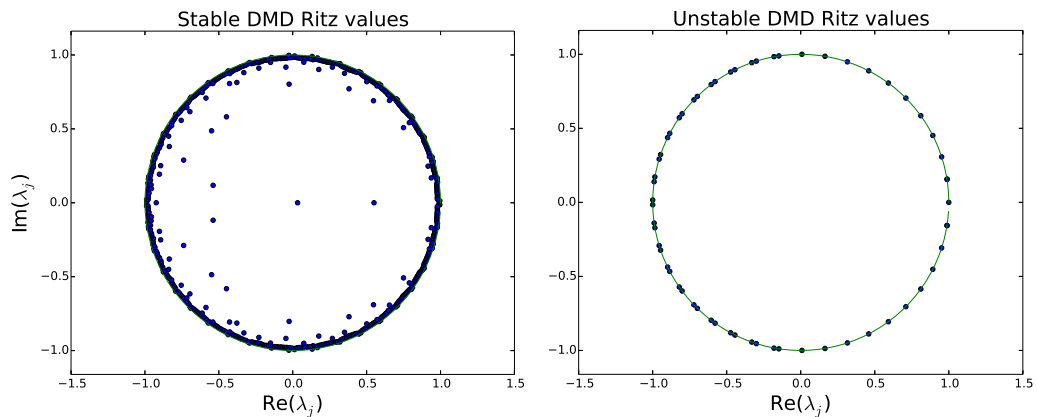
Figure 4.4: Stable (left) and unstable (right) Ritz values $Re = 1000$, $\beta = 20°$.

time of the two components of the fluid velocity, is $n \approx 2 \times 48000$, where 48000 are the elements of the unstructured grid. The balanced POD has been then computed using the direct and adjoint impulse responses of system (2.71), yielding a linear system with a positive steady-state gain: $\mathrm{sign}P(0) = 1$. The order r of the ROM is chosen so that $\sum_{i=1}^{r} \sigma_i / \sum_{i=1}^{r1} \sigma_i = 99\%$, where σ_i are the Hankel singular values defined in Section 2.2.6, thus yielding the reduced-order, stable, balanced DMD model (2.73) of order $r = 11$, which is both controllable and observable.

All the reported quantities are non-dimensional. Figure 4.3 shows the Ritz values computed by the DMD (left) and the proposed balanced DMD (right). Figure 4.4 shows the unstable (left) and stable (right) DMD Ritz values. The tails of the impulse responses of the full-order system (in blue) are compared in Figure 4.5 with both the reconstructed outputs $\mathrm{y}_{DMD}(t)$ of the DMD model (in magenta), and the reconstructed outputs $\mathrm{y}_{BDMD}(t)$ of the proposed balanced DMD model (in green). An effective reconstruction of the full-order output dynamics is obtained,
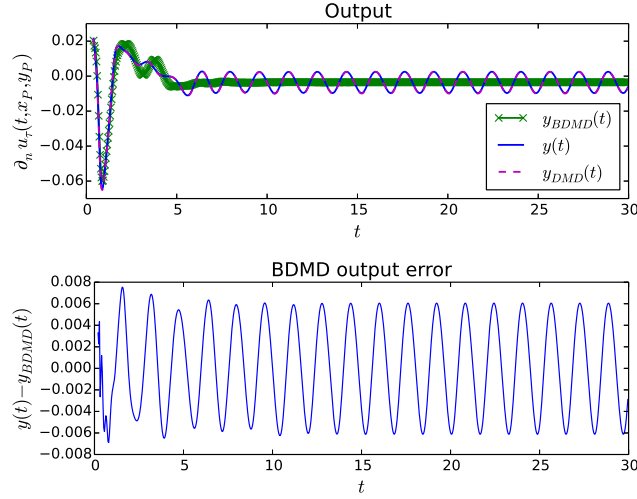
Figure 4.5: Balanced DMD (green), DMD (magenta) and full-order (blue) output responses to impulsive input (left) and balanced DMD output reconstruction error (right), for $t \geq 0.2$, $Re = 1000$, $\beta = 20°$.

by retaining only $r = 11$ modes in the ROM and with the additional advantage, with respect to system-identification methods, of retaining physical meaning in the ROM. Although the model well approximates the flow dynamics for $Re = 1000$, $\beta = 20°$ (see figure 4.5), it is not guaranteed to be a good approximation of the full-order, nonlinear dynamics when the parameters vary. The robustness of the proposed control scheme (4.18), (4.21), (4.22), (4.23), which is based on the constructed ROM, is thus tested in four different scenarios and both Reynolds number and angle of attack are varied: $Re = 1000$, $\beta = 15°$; $Re = 1000$, $\beta = 20°$; $Re = 2000$, $\beta = 20°$; $Re = 5000$, $\beta = 15°$. The control parameters are the same for the four cases and are chosen as: $k = 3$, $\mu = 10k$, $\varepsilon_m = 0.1$, $\varepsilon_M = 0.15$, $y_M = \varepsilon_m + \varepsilon_M$. The controller is turned on at $t = 4.5$. All the controller initial conditions are set to zero, whilst the initial velocity $\boldsymbol{u}$ and pressure fields p are in the limit cycle regime. Figures 4.6, 4.7 show the simulation results for $Re = 1000$, $\beta = 15°$.

Drag and lift coefficients

$$
\begin{aligned}
C_D &= 2F_x/(\rho U_m^2 c, \\
C_L &= 2F_y/(\rho U_m^2 c),
\end{aligned}
\tag{4.25}
$$

are computed along the streamwise (x) and normal (y) axis, respectively, where F_x, F_y denote the corresponding components (parallel and perpendicular to the inflow velocity, respectively) of the total forces on the aerofoil profile. The snapshots of

Figure 4.6: Simulation results for $Re = 1000$, $\beta = 15°$. The controller is activated between $t_0 = 4, 5$ and $t_f = T = 15$.

Figure 4.7: Snapshots of the velocity magnitude contours and streamlines, for $Re = 1000$, $\beta = 15°$, before the controller is turned on (left) and at $t = 15$ (right).

the velocity magnitude contours and streamlines in figure 4.7 show an evident flow reattachment: the proposed adaptive control effectively reduced the separation

Figure 4.8: Simulation results for $Re = 1000$, $\beta = 20°$. The controller is activated between $t_0 = 4,5$ and $t_f = T = 15$.
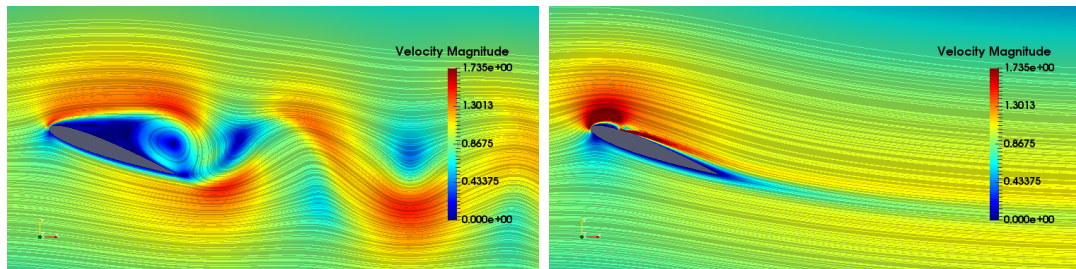
Figure 4.9: Snapshots of the velocity magnitude contours and streamlines, for $Re = 1000$, $\beta = 20°$, before the controller is turned on (left) and at $t = 15$ (right).

bubble, as well as the shedding vortices. Both a significant increase of the lift coefficient, as well as a significant reduction of the drag coefficient (figure 4.6),
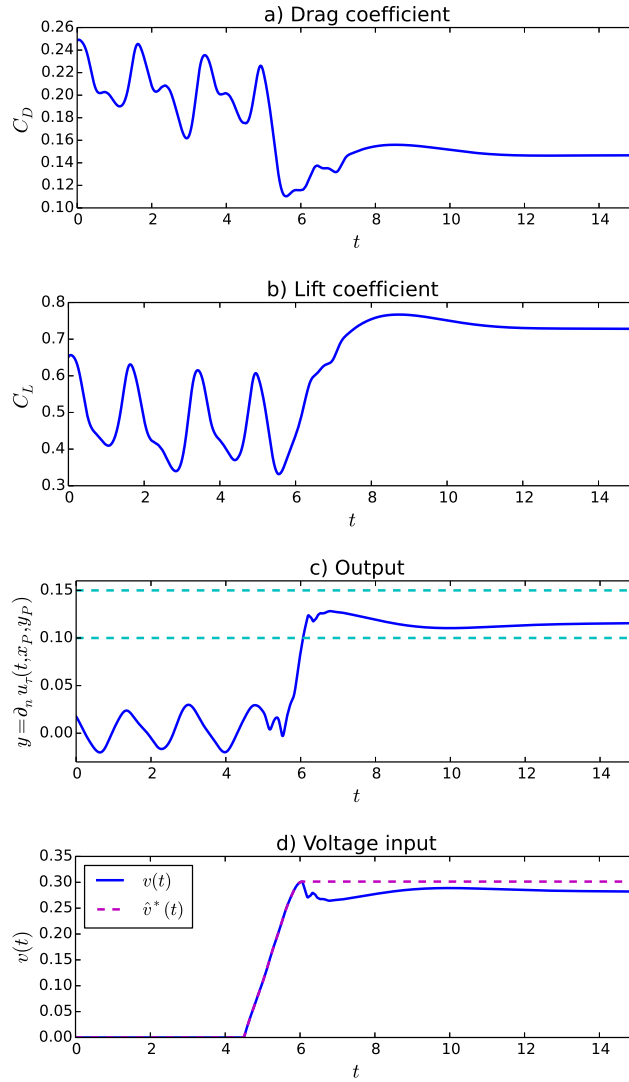
Figure 4.10: Simulation results for $Re = 2000$, $\beta = 20°$. The controller is activated between $t_0 = 4, 5$ and $t_f = T = 15$.

are achieved. A fast and smooth output regulation to $y^* \in \Omega_\varepsilon$ is shown in figure 4.6. The scaled, non-dimensionalised voltage input $v(t) = \sigma(y)\hat{v}^*(t)$ is shown in figure 4.6, along with its corresponding estimated reference input $\hat{v}^*(t)$. The same considerations hold for the simulation results at both $Re = 1000$, $\beta = 20°$ (depicted in figures 4.8, 4.9), $Re = 2000$, $\beta = 20°$ (depicted in figures 4.10, 4.11) and $Re = 5000$, $\beta = 15°$ (depicted in figures 4.12, 4.13). Note that, although a simple linear model, build upon a single scenario, is used for the control design, good dynamic performances are achieved as both the flow and geometry parameters are varied.
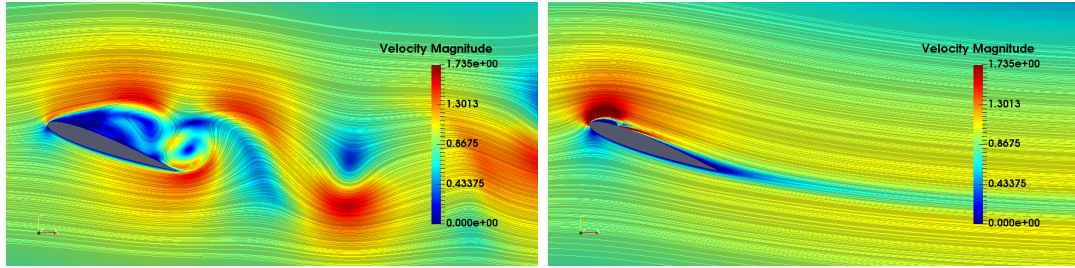
Figure 4.11: Snapshots of the velocity magnitude contours and streamlines, for $Re = 2000$, $\beta = 20°$, before the controller is turned on (left) and at $t = 15$ (right).
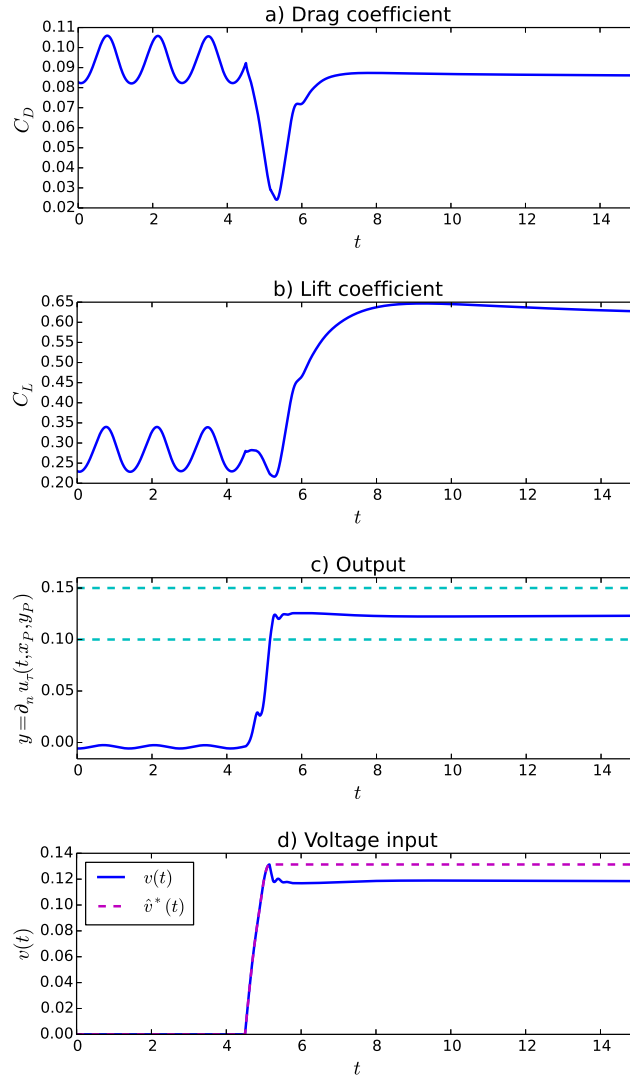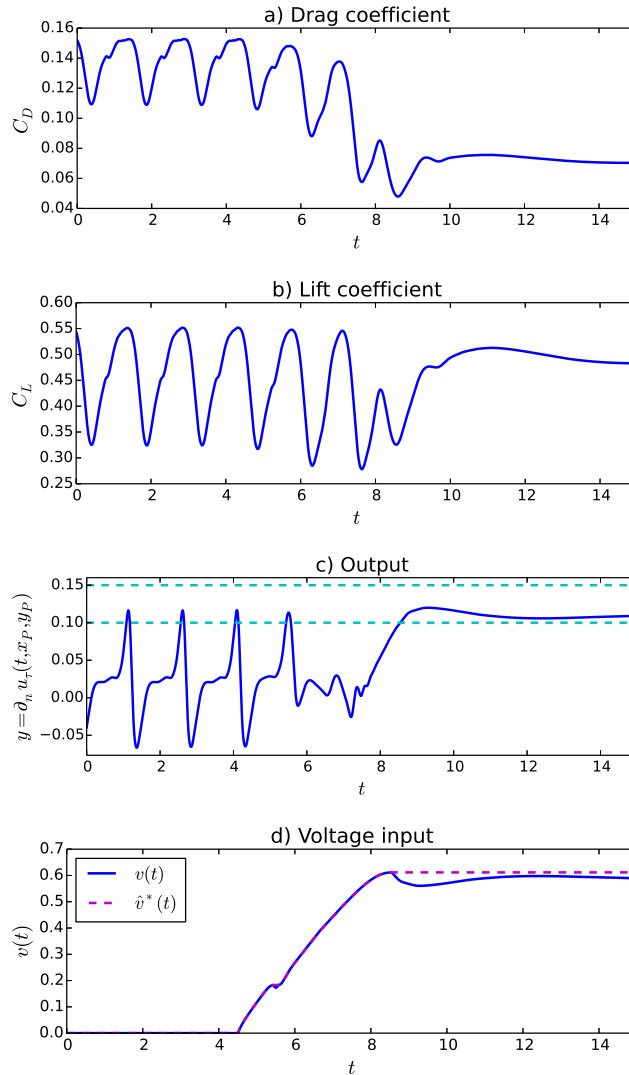

Figure 4.12: Simulation results for $Re = 5000$, $\beta = 15°$. The controller is activated between $t_0 = 4,5$ and $t_f = T = 15$.
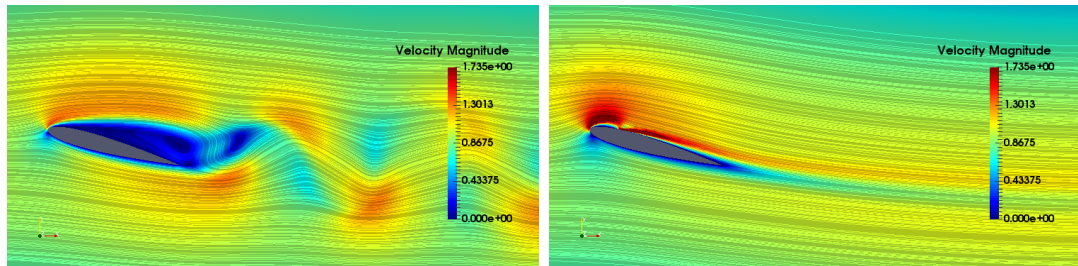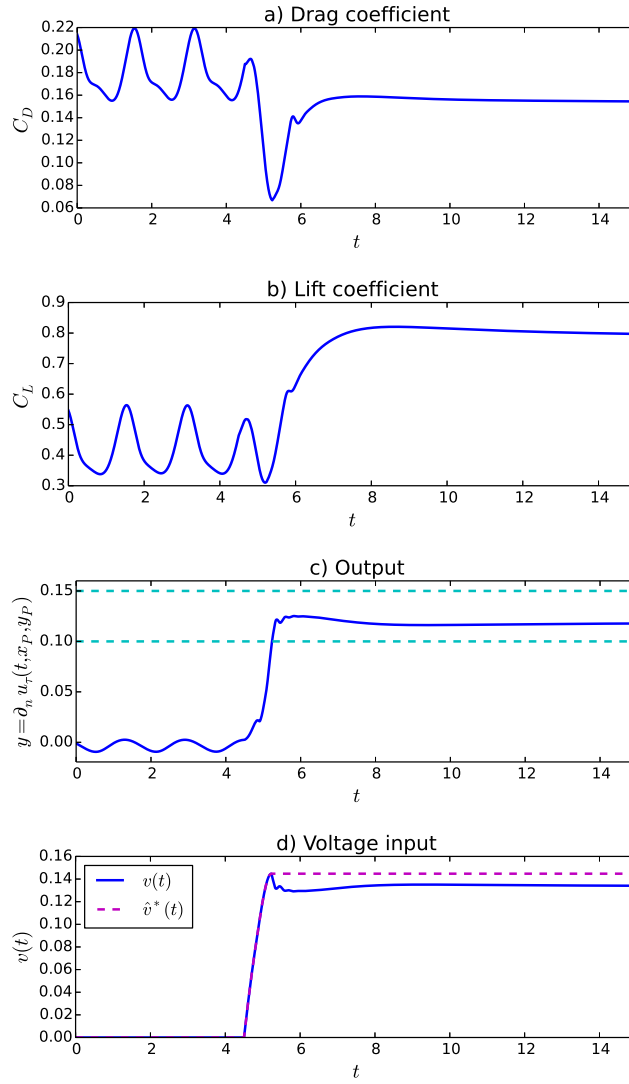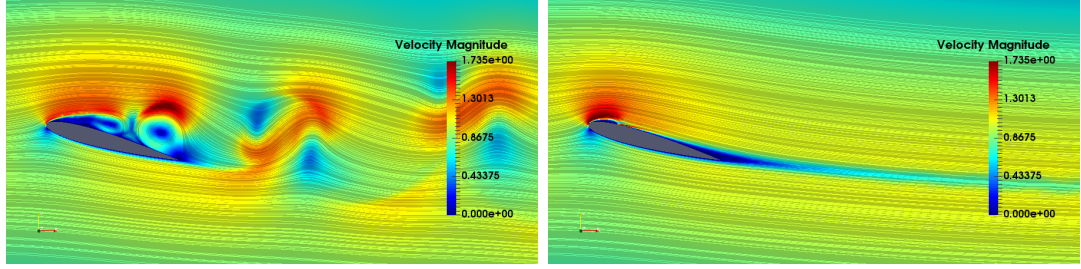
Figure 4.13: Snapshots of the velocity magnitude contours and streamlines, for $Re = 5000$, $\beta = 15°$, before the controller is turned on (left) and at $t = 15$ (right).

4.6 Optimal Sensor Placement

A multi-objective deterministic particle swarm optimisation (MODPSO) algorithm is proposed, in this section, to study the trade-off between the time-averaged input signal and the drag-to-lift ratio, varying the positions of the actuator/sensor pairs along the aerofoil, as well as the corresponding reference for the available real-time velocity measurements. Among deterministic methods, deterministic particle swarm optimization (DPSO) has several attractive characteristics such as the simplicity of the heuristics, the ease of implementation, and its often fairly remarkable effectiveness (see Serani et al., 2016). The aim is to identify an optimal set of non dominated configurations. In particular, the MODPSO algorithm is used here for the minimisation of both the time-averaged input signal and the drag-to-lift ratio, $\boldsymbol{\phi} \doteq \{\langle v \rangle, \langle C_D/C_L \rangle\}^T$, versus the optimisation variables, $\boldsymbol{\theta} \doteq \{\Delta_s, \varepsilon_m\}^T \in \mathcal{D}$. Here, $\langle \cdot \rangle$ denotes the time-average; $\Delta_s = |\bar{x}_a - \bar{x}_s|$ is the distance between the sensor and the actuator, with respect to the chord length; $\bar{x}_a$ and $\bar{x}_s$ denote the position of the actuator - i.e. the origin of the local reference frame used for the body force computations as in (4.3), which corresponds to the position of the first electrode - and sensor, with respect to the chord length, respectively (see figure 4.1). The inverse of the aerodynamic efficiency is considered here in order to perform a minimisation of the former along with the control variable, while avoiding eventual infinite terms due to zero denominators. The original PSO algorithm was introduced in Kennedy and Eberhart (1995), based on the social-behavior metaphor of a swarm of bees searching for food and belongs to the class of metaheuristic algorithms for single-objective derivative-free global optimisation. Pinto et al. (2007) proposed a

multi-objective deterministic extension of the method as

$$\begin{cases} \boldsymbol{v}_i^{k+1} = \gamma \left[\boldsymbol{v}_i^k + c_1 \left(\mathbf{p}_i - \boldsymbol{\theta}_i^k \right) + c_2 \left(\mathbf{g}_i - \boldsymbol{\theta}_i^k \right) \right] \\ \boldsymbol{\theta}_i^{k+1} = \boldsymbol{\theta}_i^k + \boldsymbol{v}_i^{k+1} \end{cases} \tag{4.26}$$

where $\boldsymbol{v}_i^k$ and $\boldsymbol{\theta}_i^k$ are the velocity and the position of the i-th particle at the k-th iteration, γ is a constriction factor, c_1 and c_2 are the cognitive and social learning rate, and $\mathbf{p}_i$ and $\mathbf{g}_i$ are the cognitive and social attractor.
The algorithm formulation and setup is defined as suggested in (Pellegrini et al., 2014): the cognitive attractor $\mathbf{p}_i$ is the personal minimiser of the aggregate function $\Phi(\boldsymbol{\theta}_i) = \sum_{m=1}^{M} w_m \phi_m(\boldsymbol{\theta}_i)$, where $w_m = 1/M$ ($\forall m$) is the weight associated to the m-th objective function with M the number of objective functions; the social attractor $\mathbf{g}_i$ is the closest point to the i-th particle of the Pareto front; the number of particles is set equal to 32, initialised over the domain $\mathcal{D}$ its boundary with a Hammersley distribution and non-null velocity (Chen et al., 2015); the coefficients correspond to $\gamma = 0.721$, $c_1 = c_2 = 1.655$ (Clerc, 2006); a semi-elastic wall-type approach (Serani et al., 2016) is used to keep the particles within $\mathcal{D}$. The number of iterations is set to 1000.

4.7 Simulation Results: χnavis, 2D case

Although the resulting robust control algorithm is designed on the basis of an unknown theoretical linear model at $Re = 1,000$, its robustness is tested in this section at $Re = 20,000$ using a different numerical technique. Only a positive steady-state gain for any actuator/sensor pair is assumed. The simulations are performed using the unsteady RANS equations based solver χnavis, with no turbulence model, described in Chapter 3. The code has been widely applied and validated for several problems, mainly in the framework of naval hydrodynamics; for an overview of the applications and validations of the mathematical model the reader is referred to Dubbioso et al. (2016); Di Mascio et al. (2007a,b); Dubbioso et al. (2017); Muscari et al. (2013); Zaghi et al. (2011), where numerical studies of maneuverability of surface vessels and submarines, naval propellers and hydrodynamics of multihull vessels have been conducted.
The considered geometry is a NACA 0012 aerofoil, denoted by Γ_N, and the domain boundaries are $\partial \Omega = \Gamma_{\text{in}} \cup \Gamma_0 \cup \Gamma_{\text{out}}$. Here, the wall boundary is $\Gamma_0 = \Gamma_N$.

The inflow boundary condition on Γ_{in} is a constant velocity profile

$$\boldsymbol{g}(t, \boldsymbol{x}) \equiv \boldsymbol{U}_\infty, \tag{4.27}$$

where $\boldsymbol{U}_\infty = (1, 0, 0)$ is the non-dimensionalised inflow velocity. The 2D computational grid has $N = 127,872$ total volumes and is divided into extremely fine actuator grids, a fine C-type inner grid and coarser outer grids. The two-dimensional grid, whose size is similar to those found in the literature (*e.g.*, $N = 115,213$ in Riherd and Roy, 2013) is extruded in the spanwise direction using 8 uniformly distributed grid volumes and the spanwise length is 0.125 (so that the dynamics are two-dimensional). It is worth to stress that the use of the overlapping grid approach allows to achieve a highly refined grid in the region of interest, while limiting the total number of control volumes. In order to avoid reflections, the outer boundaries are placed at a distance of 50 chords. The inner region around the profile (see figure 4.14) has 320×96 volumes, in the tangent and normal direction, respectively; the points are clustered towards the wall, where the mesh spacing is equal to 2.1×10^{-4}. The grid resolution at the wall is the same as the one in Jones et al. (2008); Riherd and Roy (2013). The near-wake region is discretised with 128×192 volumes distribuited in the streamwise and vertical direction, respectively. Drag and lift coefficients are defined as
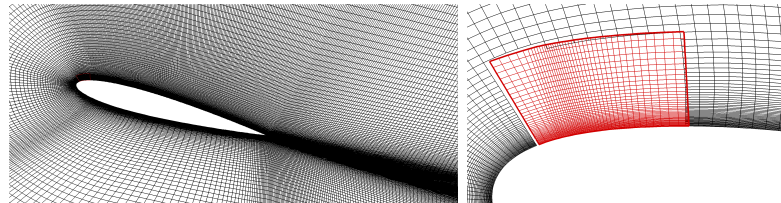
Figure 4.14: Computational grid around the NACA 0012 profile (left) and actuator's block (right).

$$\begin{aligned} C_D &= 2F_x/(\rho U_\infty^2 c, \\ C_L &= 2F_y/(\rho U_\infty^2 c), \end{aligned} \tag{4.28}$$

and are computed along the streamwise (x) and normal (y) axis, respectively, where F_x, F_y denote the corresponding components (parallel and perpendicular to the inflow velocity, respectively) of the total forces on the aerofoil profile per span length. The performance of the proposed control scheme (4.9), (4.18) is tested for the flow past a NACA 0012 profile at $Re = 20,000$, in 21 different configurations: the actuator is placed at $\bar{x}_a = 0.02$, as preliminary tests (which are not
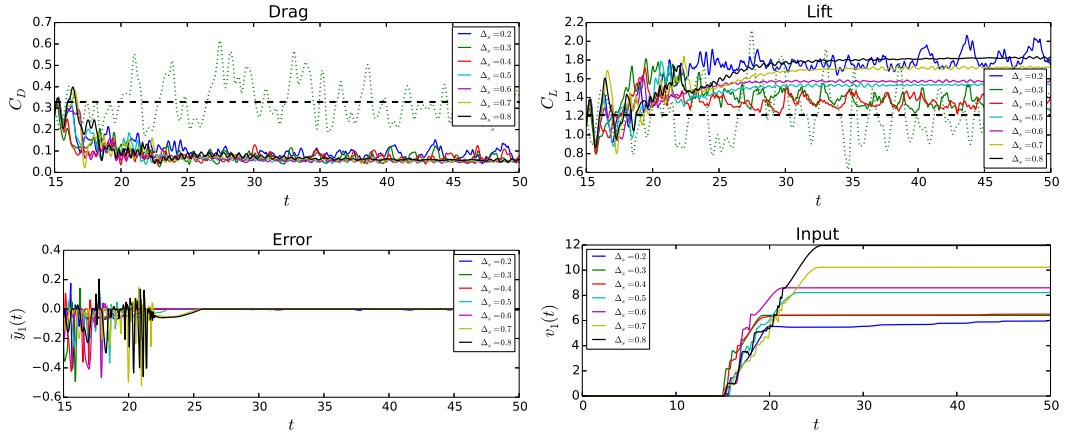
Figure 4.15: Simulation results in the scenario $\varepsilon_m = 0.05$ for $\beta = 15°$: drag and lift coefficient (top) for both uncontrolled (dashed lines) and closed-loop scenarios (solid lines); regulation error and control input for closed-loop scenarios (bottom).
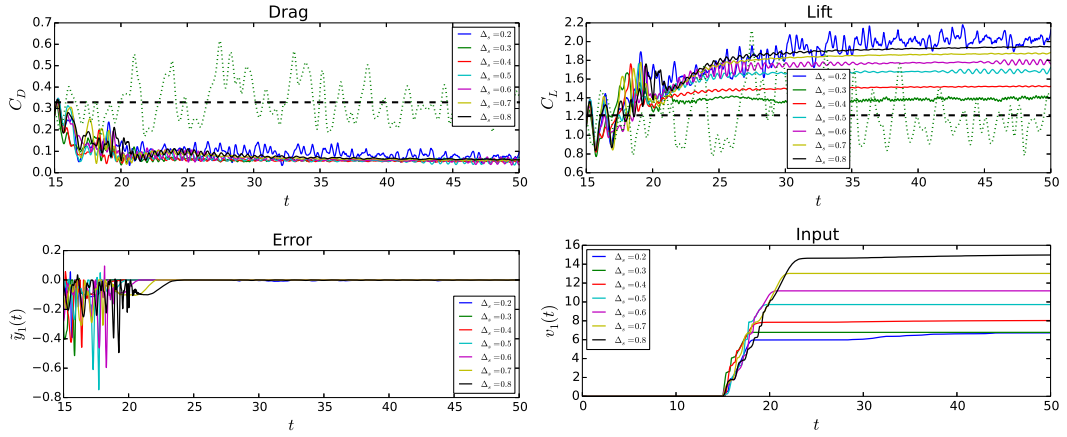
Figure 4.16: Simulation results in the scenario $\varepsilon_m = 0.1$ for $\beta = 15°$: drag and lift coefficient (top) for both uncontrolled (dashed lines) and closed-loop scenarios (solid lines); regulation error and control input for closed-loop scenarios (bottom).

reported here for the sake of brevity) showed a deterioration in the performance when it is moved further downstream, because the separation occurs very close to the leading edge; the distance Δ_s between the sensor and the actuator, with respect to the chord length, is varied between 0.2 and 0.8; three different lower bounds $\varepsilon_m = 0.05$, $\varepsilon_m = 0.1$, $\varepsilon_m = 0.2$ of the reference set Ω_ε are considered, while the upper bound is $\varepsilon_M = \varepsilon_m + 0.05$. The corresponding results are shown in figures 4.15-4.18. The controller is activated between $t_0 = 15$ and $t_f = T = 50$. The angle of attack is $\beta_0 = 15°$. The output measurements $\mathrm{y}(t) = u_{\boldsymbol{\tau}}(t, x_s, y_s)$ are taken at $y_n = 0.0005$ above the aerofoil. For the sake of simplicity, $\mu = 0$ is set in
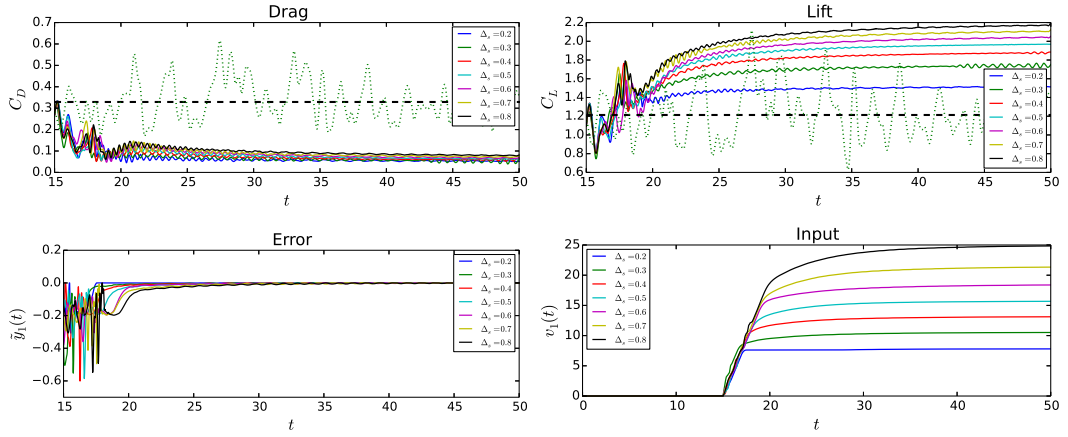
Figure 4.17: Simulation results in the scenario $\varepsilon_m = 0.2$ for $\beta = 15°$.
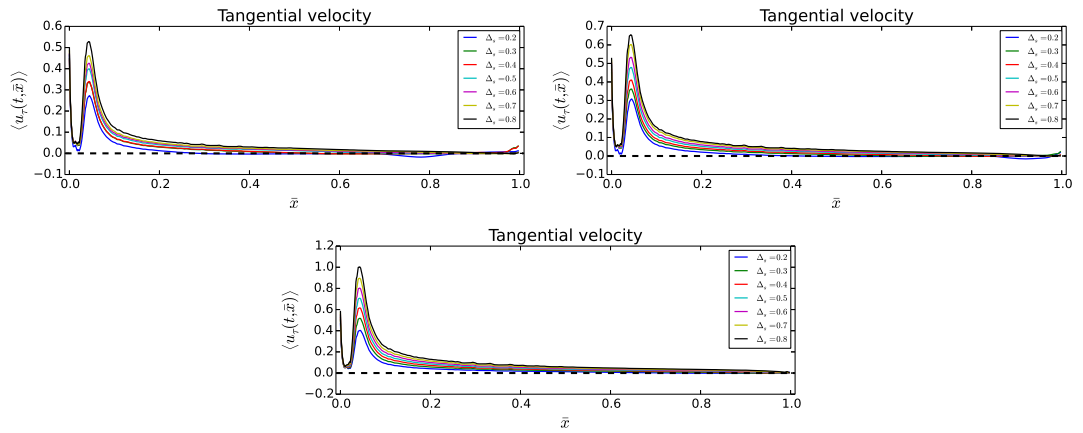
Figure 4.18: Time-averaged tangential velocity for $\beta = 15°$: $\varepsilon_m = 0.05$ (top left), $\varepsilon_m = 0.1$ (top right) and $\varepsilon_m = 0.2$ (bottom).

all the simulations, while the control chosen gain is $k = 20$.

The time histories of the closed-loop drag and lift coefficients are compared (top figures) with the corresponding time histories (dashed green) and time average (dashed black) coefficients yielded by the uncontrolled simulations. All the considered solutions yield both drag reduction and lift increase compared to the uncontrolled scenario. coefficients for the simulations with no actuation (figure 4.16, 4.15, 4.17). The Pareto front of the non dominated solutions obtained by MODPSO is shown in Fig. 4.19 (a). The associated configurations in the Δ_s-ε_m plane are shown in Figs. 4.19 (b) and (c) versus $\langle v \rangle$ and $\langle C_D/C_L \rangle$ ($C_D = 2F_x/(\rho U_\infty^2 c)$ and $C_L = 2F_y/(\rho U_\infty^2 c)$), respectively, where F_x, F_y denote the total forces per span length), respectively. Three sub-sets are identified based on the clustering in the Δ_s-ε_m plane. The clustering reflects clearly on the $\langle v \rangle$-$\langle C_D/C_L \rangle$

trade-off. For each set, one solution is selected for further analysis. Specifically, solution 1 corresponds to $\Delta_s = 0.4$ and $\varepsilon_m = 0.1$, providing a quite balanced compromise between $\langle v \rangle$ and $\langle C_D/C_L \rangle$. Solution 2 has $\Delta_s = 0.3$ and $\varepsilon_m = 0.2$ and one of the lowest values for $\langle C_D/C_L \rangle$, whereas solution 3 corresponds to $\Delta_s = 0.2$ and $\varepsilon_m = 0.1$ with quite a low value of $\langle v \rangle$.

The instantaneous vorticity contours for the selected solutions, are shown in figure 4.20; 101 non-dimensional vorticity levels over the range $[-15, 15]$, results for both with and without the actuation are reported for comparison purposes. Without the actuation, strong vortex structures are generated as a consequence of both the strong adverse pressure gradients and the boundary layer separation, which occurs on the upper side of the profile. The proposed control algorithm significantly reduces the boundary layer separation and avoids the generation of large vortical structures.
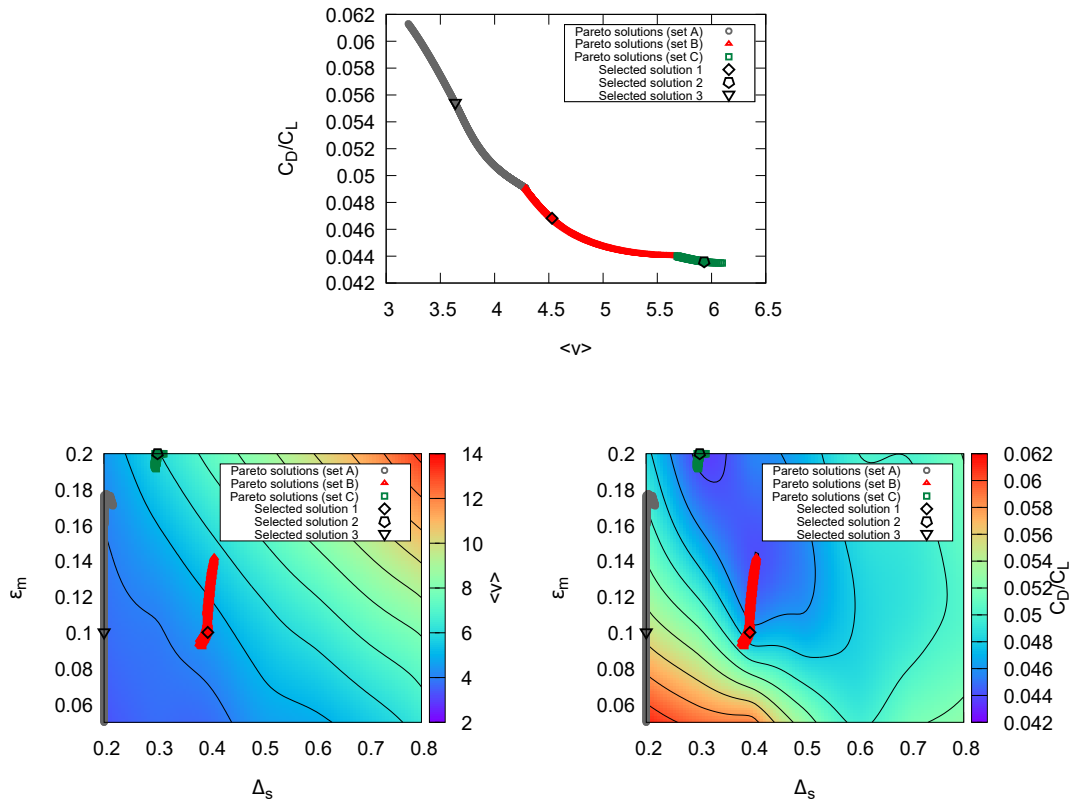
Figure 4.19: Pareto front obtained by MODPSO (top), $\langle v \rangle$ (bottom left), and $\langle C_D/C_L \rangle$ (bottom right) versus Δ_s and ε_m showing Pareto sub-sets and selected solutions
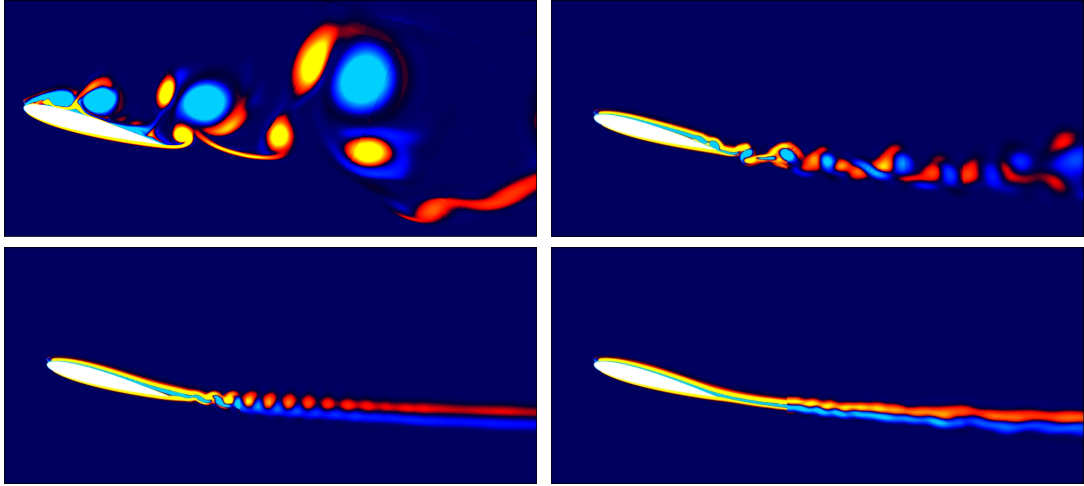
Figure 4.20: Instantaneous vorticity contours for $\beta = 15°$ and $Re = 20,000$ using 101 levels over the range $[-15, 15]$: without control (top left), solutions 3 (top right), 1 (bottom left) and 2 (bottom right).

4.8 Summary

The novel low-order, control-oriented, linear model proposed in Chapter 2 has been obtained for unsteady flows past a NACA 0012 aerofoil, at Reynolds $Re = 1,000$ and angle of attack $\beta = 20°$, in the presence of a DBD body force. On the basis of the proposed model, a robust output feedback control of flow separation using plasma actuators has been designed: it guarantees exponential output regulation when the steady-state gain of the approximated linear model is non-zero and of known sign. A simple configuration, with one sensor and one actuator is considered. Accurate 2D finite element simulations show that a fast flow reattachment is achieved, along with both stabilisation and increase/reduction of the lift/drag, respectively. Although the proposed controller is simple, as it is based on an integral action, it is able to effectively reduce the separation bubble, as well as the shedding vortices, while achieving good dynamic performances, as both the Reynolds number and the angle of attack are varied.

Furthermore, accurate finite volume simulations of flows past a NACA 0012 at Reynolds $Re = 20,000$ and angle of attack $\beta = 15°$ are performed in order to both test the control effectiveness in conditions that significantly exceed the design envelope (the Reynolds number is 20 times larger than the one used to compute the ROM) and optimise the performance of the closed-loop system. Different configurations were tested, with the aim of identifying optimal positions of the actuator/sensor pairs along the aerofoil and the corresponding references for the

available real-time velocity measurements. Finally, a multi-objective deterministic particle swarm optimisation algorithm was applied to identify the Pareto set of non dominated configurations, considering as objectives the time-averaged input signal and drag-to-lift ratio. Three sub-sets of non dominated configurations were identified based on the solution clustering and, for each set, one solution was selected for the demonstration of the methodology.

Note that the chosen output can be experimentally measured by appropriate sensors and the extension of the proposed approach to 3D configurations is straightforward (as it is demonstrated in the next chapter).

Chapter 5

MIMO Flow Separation Control

This chapter extends the results obtained so far to MIMO control systems. In particular, a robust output feedback control is designed and tested in different configurations with multiple actuators and sensors, thus allowing for optimising the closed-loop system, with the aim of selecting suitable numbers and positions of the actuator/sensor pairs along the aerofoil, as well as desired references for the real-time measurements, according to the specific application (*e.g.*, flow reattachment, noise suppression, mixing enhancement *etc.*). As in the previous chapter, the unsteady flow separation problem for MIMO systems is solved using real-time velocity measurements, which are available in realistic applications (see, for example, Hanson et al., 2010; Ozaki et al., 2000; Segawa et al., 2010; Spazzini et al., 1999).

The objective is to show how, despite the high complexity of the system, a very simple and computationally cheap robust multivariable output regulator is sufficient to effectively suppress the flow separation along an aerofoil, using DBD plasma actuators. Although the resulting robust control algorithm is designed on the basis of a simple theoretical linear model, its application to the flow separation control problem is proposed. Only a non-zero steady-state gain of known sign for each actuator/sensor pair is assumed. Different configurations are tested in order to optimise the closed-loop system, so that suitable numbers and positions of the actuator/sensor pairs along the aerofoil, as well as the desired references for the real-time measurements, can be chosen according to the requirements of the specific application.

Accurate numerical simulations of incompressible flows around a NACA 0012 at Reynolds $Re = 20,000$ are performed in order to illustrate the effectiveness of

proposed approach, in the presence of uncertain parameters and complex non-linear dynamics, which are neglected in the control design. Robust, fast flow reattachment is achieved, along with both stabilisation and increase/reduction of the lift/drag, respectively. The control system shows good dynamic performances, as the angle of attack is varied.

5.1 Problem Statement and Objectives

As in the previous chapter, the aim is to formulate and solve the flow separation problem, *i.e.*, to make

$$\partial_{\boldsymbol{n}} u_{\boldsymbol{\tau}}(t, \boldsymbol{x})|_{\Gamma_N} = \Big(\boldsymbol{n}(\boldsymbol{x}) \cdot \nabla\big(\boldsymbol{\tau}(\boldsymbol{x}) \cdot \boldsymbol{u}(t, \boldsymbol{x})\big)\Big)\Big|_{\Gamma_N} > 0, \tag{5.1}$$

as a simple output regulation problem (this time allowing for multiple actuator/sensor pairs), *i.e.*, to make the measured outputs

$$\mathrm{y}_i(t) = u_{\tau}(t, \boldsymbol{x}_{s_i}) \geq \varepsilon_i > 0, \tag{5.2}$$

for $i = 1, ..., n_s$. Here, $\boldsymbol{u}$ is the time-dependent flow velocity vector; $\boldsymbol{x}$ and $\boldsymbol{x}_{s_i}$ denote the spatial coordinates and the i-th sensor location, respectively; Γ_N represents the aerofoil boundary; $\boldsymbol{n}$ and $\boldsymbol{\tau}$ are the normal and tangent unit vectors to Γ_N, respectively; n_s is the number of sensors. Our objective is to design a simple robust output feedback control, along with suitable reference signals y_i^* for y_i, in order to suppress the flow separation along the aerofoil in different scenarios, depending on uncertain parameters, *i.e.*, Reynolds number Re and angle of attack β. To this end, it is assumed there exist suitable configurations of actuators and sensors, along with suitable references ε_i for the outputs $\mathrm{y}_i(t)$, which guarantee that, given a certain range for both Re and β, the solution of the output regulation problem (5.2) implies the solution of the flow separation problem (5.1). This is formalised by the following assumption.

Assumption 1. *For any $\delta \geq 0$ there exist some references $\varepsilon_i > 0$, a $T_{\varepsilon_i} > 0$ and a $T_{\delta} \geq max_{i=1,...,n_s} T_{\varepsilon_i}$ such that, if $\mathrm{y}_i(t) > \varepsilon_i$ for all $t > T_{\varepsilon_i}$, $i = 1, ..., n_s$, then $\partial_{\boldsymbol{n}} u_{\boldsymbol{\tau}}(t, \boldsymbol{x})|_{\Gamma_N} > -\delta$ for all $t > T_{\delta}$, $Re \in \mathcal{R}_{Re} = [Re_m, Re_M]$, $\beta \in \mathcal{R}_{\beta} = [\beta_m, \beta_M]$.*

In this chapter, the recent theoretical results in Marino and Tomei (2015) are extended to MIMO systems, using the actuators' voltage as the control input and real-time velocity measurements as the control output. This allows for the

application of the resulting control algorithm to configurations with multiple actuator/sensor pairs and, thus, for the optimisation of the performance of the system. In particular, the aim is to identify an optimal configuration

$$\left\{ n_a, \bar{x}_a^{(1)}, ..., \bar{x}_a^{(n_a)}, n_s, \bar{x}_s^{(1)}, ..., \bar{x}_s^{(n_s)}, y_1^*, ..., y_{n_s}^* \right\}, \tag{5.3}$$

for which assumption 1 holds. Here, n_a denotes the number of actuators; $\bar{x}_a^{(j)}$ and $\bar{x}_s^{(i)}$ denote the position of the j-th actuator and the i-th sensor with respect to the chord length, respectively (see figure 4.1).

5.2   Actuator Model

The total body force vector field $\boldsymbol{f} : [0, T] \times \Omega \to \mathbb{R}^d$, which appears in the Navier-Stokes equations (3.1), depends on the multiple control inputs and can be expressed as

$$\boldsymbol{f}(t, \boldsymbol{x}) = c/\rho U_\infty^2 (f_x(t, \boldsymbol{x}), f_y(t, \boldsymbol{x}), 0) = c/\rho U_\infty^2 \sum_{j=1,...,n_a} \boldsymbol{f}^{(j)}(t, \boldsymbol{x}), \tag{5.4}$$

where f_x, f_y are the streamwise and normal component (in N/m^3) and $\boldsymbol{f}^{(j)}$ is the single force distribution of the j-th actuator (in N/m^3). All the above listed functions are assumed to be sufficiently smooth. The wall-tangential velocities, evaluated at the selected sensor locations $\boldsymbol{x}_{s_i}$,

$$y_i(t) = u_\tau(t, \boldsymbol{x}_{s_i}) = \boldsymbol{\tau}(\boldsymbol{x}_{s_i}) \cdot \boldsymbol{u}(t, \boldsymbol{x}_{s_i}), \tag{5.5}$$

are chosen as the measured outputs. As in the previous chapter, the model is characterised by an exponential dependence on the spatial coordinates and, in particular, the force is modelled by a Rayleigh distribution (see Yang and Chung, 2015); thereby,

$$\begin{aligned} \boldsymbol{f}^{(j)}(t, \boldsymbol{x}) &= f_\tau^{(j)}(t, x_\tau^{(j)}, y_n^{(j)}) \boldsymbol{\tau}(\boldsymbol{x}) + f_n^{(j)}(t, x_\tau^{(j)}, y_n^{(j)}) \boldsymbol{n}(\boldsymbol{x}) \\ &= I^{(j)}(t) \frac{\lambda_f^{(j)} x_\tau^{(j)}}{\left(\sigma_f^{(j)}\right)^2} e^{-x_\tau^{(j)2} / \left(2\sigma_f^{(j)2} - \lambda_f^{(j)} y_n^{(j)}\right)} \boldsymbol{\tau}(\boldsymbol{x}), \end{aligned} \tag{5.6}$$

for $j = 1, ..., n_a$, where, $f_n^{(j)} = 0$; $I^{(j)}(t) = k_v^{(j)} V^{(j)}(t)/V_m$ ($k_v \in \mathbb{R}$, V_m [kV]) is the total plasma force; $V^{(j)}(t) : \mathbb{R} \to \mathbb{R}$ is the amplitude variation of the operation voltage (in kV); $v_j(t) = V^{(j)}(t)/V_m$ is the corresponding non-dimensionalised voltage input, scaled by V_m; $f_\tau^{(j)}, f_n^{(j)}$ (in N/m^3) are the tangential and normal components, with respect to the aerofoil, of the force density , respectively;

$x_\tau^{(j)}, y_n^{(j)} \geq 0$ are related to (x, y) by a coordinate transformation and respectively refer to the tangent and normal components, relative to the geometry, in the reference frame centred in $\boldsymbol{x}_a$ (see figure 5.1). The parameters $\lambda_f^{(j)} = 1.6$, $\sigma_f^{(j)} = 1.9$,
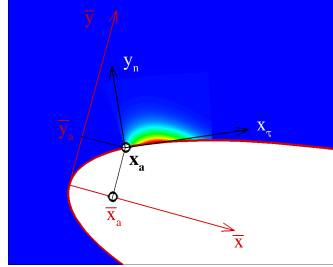
Figure 5.1: Tangential force density $f_\tau^{(j)}$ and reference frames.

$k_v^{(j)} = 5200e^{1/2}\sigma_f^{(j)}/\lambda_f^{(j)}$, for $j = 1, ..., n_a$, are again chosen as in Yang and Chung (2015).

The problem is closed by enforcing appropriate conditions at physical and computational boundaries. As in (3.3), on solid walls, the velocity is set to zero (whereas no condition on the pressure is required); at the inflow boundary, velocity is set to the undisturbed flow value, and the pressure is extrapolated from inside; on the contrary, the pressure is set to zero at the outflow, whereas velocity is extrapolated from the inner points. The initial conditions are specified for the velocity field as in (3.2).

5.3 Extension to MIMO systems

A Balanced Dynamic Mode Decomposition (BDMD) linear model approximating system (3.6), for given Reynolds number Re and angle of attack β, has been obtained in the following form:

$$\begin{cases} \dot{\xi} = A\xi + B\mathrm{v}, & \xi(0) = \xi_0, \\ \mathrm{y} = C\xi, \end{cases} \qquad (5.7)$$

where, $\xi : \mathbb{R} \to \mathbb{R}^r$ is the reduced-order state vector; $A \in \mathbb{R}^{r \times r}$ is a low-order linear operator approximating the nonlinear dynamics, whose eigenvalues belong to the open left half of the complex plane; $B \in \mathbb{R}^{r \times n_a}$ is the input matrix; $C \in \mathbb{R}^{n_s \times r}$ is

the output matrix. Let: I_r be the $r \times r$ identity matrix and

$$P(s) = \begin{bmatrix} P_{11}(s) & P_{12}(s) & \ldots & \ldots & P_{1,n_a}(s) \\ P_{21}(s) & P_{22}(s) & & & \vdots \\ \vdots & & \ddots & \ddots & \vdots \\ \vdots & & & & P_{n_s-1,n_a}(s) \\ P_{n_s,1}(s) & \ldots & \ldots & P_{n_s,n_a-1}(s) & P_{n_s,n_a}(s) \end{bmatrix}$$

$$= C(sI - A)^{-1}B,$$
(5.8)

whose poles have all negative real part, be the open-loop $n_s \times n_a$ transfer function matrix of system (5.7). Define

$$P_{ii}(s) = \frac{n_{P_{ii}}(s)}{d_{P_{ii}}(s)}$$
(5.9)

and let v^*, y^* and ξ^* be the references for the input, output and state, respectively. Denoting $\tilde{\xi} = \xi - \xi^*$ and $\eta = -v^* : \mathbb{R} \to \mathbb{R}^{n_a}$, the error dynamics are given by

$$\begin{cases} \dot{\tilde{\xi}} &= A\tilde{\xi} + B(v + \eta), \\ \dot{\eta} &= 0, \quad \eta(0) = \eta_0, \\ \tilde{y} &= C\tilde{\xi}, \end{cases}$$
(5.10)

so that the control problem can be formulated as a disturbance rejection problem, where the reference input $v^* = -\eta$ can be viewed as a disturbance vector, which matches the control input v (see Marino and Tomei, 2015). The uncertain matrices A, B, C, as well as the order of the model, highly depend on the uncertain set of parameters which defines the physical problem, such as, in our specific application, the Reynolds number Re and angle of attack β. We aim to modify the results in Marino and Tomei (2015) for our MIMO system (5.7), in the case equal number of sensors and actuators, *i.e.*, $n_p = n_a = n_s \geq 1$, where n_p denotes the number of actuator/sensor pairs. To this end, the following is assumed.

Assumption 2. *Given any* $i \in [1, ..., n_p]$, *there exist some positive constants* r, $\varepsilon_{a_{kl}}$, ε_{b_k} *and* ε_{c_k}, *such that the coefficients of* A, B, C, *belong to their corresponding compact sets* $[a_{kl} - \varepsilon_{a_{kl}}, a_{kl} + \varepsilon_{a_{kl}}]$, $[b_k - \varepsilon_{b_k}, b_k + \varepsilon_{b_k}]$, $[c_k - \varepsilon_{c_k}, c_k + \varepsilon_{c_k}]$, *for any* $k, l = 1, ..., r$, *and are such that* $P_{ii}(0)$ *does not change sign, for any* $Re \in \mathcal{R}_{Re} = [Re_m, Re_M]$, $\beta \in \mathcal{R}_\beta = [\beta_m, \beta_M]$, *where* Re_m *and* Re_M *denote the minimum and maximum Reynolds numbers, respectively, and* β_m *and* β_M *denote the minimum and maximum angles of attack, respectively.*

Assumption 3. *The n_p pairs are numbered so that $\bar{x}_a^{(i)} < \bar{x}_s^{(i)} < \bar{x}_a^{(i+1)} < \bar{x}_s^{(i+1)}$, for $i = 1, ..., n_p - 1$.*

Assumption 4. *The distance $|\bar{x}_a^{(i+1)} - \bar{x}_s^{(i)}|$ is sufficiently large and, thus, the transfer function between the output y_i and the input v_j is such that $P_{ij}(s) = 0$, for any $i < j$.*

In particular, Assumption 2 implies that the steady-state gains of the system do not change sign within a given range for the uncertain parameters; Assumption 3 implies that the actuator/sensor pair $(\bar{x}_a^{(i)}, \bar{x}_s^{(i)})$ is located further upstream than the pair $(\bar{x}_a^{(i+1)}, \bar{x}_s^{(i+1)})$; Assumption 4 implies that the dynamics of the outputs do not depend on the actuators that are located further downstream, so that, by virtue of Assumption 3, $P(s)$ is a lower triangular matrix.

Similarly to Marino et al. (2015), the control problem becomes to design suitable feedback laws $v_j(t)$ for system (5.7), based on the real-time measurements $y_i(t)$, in order to robustly regulate the latter to given reference regions, as in (5.2). The key objective is to design v such that the closed-loop trajectories of system (5.7) are guaranteed to evolve within some "safe" invariant set in different scenarios, depending on uncertain parameters (*e.g.*, the Reynolds number Re and angle of attack β). However, as the linear ROM (5.7) is computed at given parameters (*i.e.*, Re and β), it cannot give an accurate approximation of the full-order non-linear dynamics (3.6) when the unknown parameters are varied. Furthermore, the dependence of dynamical properties of fluid systems on such parameters is highly nonlinear. Therefore, on the basis of the recent results in Marino and Tomei (2015) a robust output regulator guaranteeing exponential convergence of the regulation error is designed: it only requires the system to have a non-zero steady-state gain of known sign.

5.3.1   Control Algorithm

We translate the initial control objective (5.2) into the following:

$$y_i(t) \in \Omega_{\varepsilon_i} = [\varepsilon_{m_i}, \varepsilon_{M_i}], \tag{5.11}$$

where ε_{m_i} and ε_{M_i} are chosen positive constants. In particular, the lower bound for the output reference can be chosen in order to guarantee any a priori fixed requirement, such as, in the present application, the suppression of the separation bubble over the aerofoil; the upper bound can be chosen in order to limit the

power consumption. Therefore, the control problem (similarly to Marino et al., 2015) becomes to design v such that the chosen controlled output y belongs to a "safe" compact set

$$\Omega_\varepsilon = \Omega_{\varepsilon_1} \times \Omega_{\varepsilon_2} \times ... \times \Omega_{\varepsilon_{n_p}}. \tag{5.12}$$

To this aim, the reference outputs y_i^* are chosen as

$$y_i^*(t) = \begin{cases} \varepsilon_{m_i}, & \text{if } y_i(t) < \varepsilon_{m_i}, \\ y_i(t), & \text{if } y_i(t) \in \Omega_{\varepsilon_i}, \\ \varepsilon_{M_i}, & \text{if } y_i(t) > \varepsilon_{M_i}. \end{cases} \tag{5.13}$$

The resulting control algorithm reads

$$\begin{cases} \dot{\hat{\eta}}_i &= k_i \, \text{sign}(P_{ii}(0))\tilde{y}_i - \mu_i \hat{\eta}_i \tilde{y}_i^2, \quad \hat{\eta}_i(0) = \hat{\eta}_{0_i}, \\ v_i &= -\hat{\eta}_i, \end{cases} \tag{5.14}$$

for $i = 1, ..., n_p$. The overall control algorithm (5.14), (5.13) depends on: the measured outputs y_i; the bounded references y_i^*; the known sign of the diagonal elements $P_{ii}(0)$; the positive design parameters k_i, μ_i, ε_{m_i}, ε_{M_i}. Note that, when $\varepsilon_i = \varepsilon_{m_i} = \varepsilon_{M_i}$, for $i = 1, ..., n_p$, the control algorithm (5.14), (5.13) reduces to an output regulator with a constant output reference.

Assumption 5. *The positive control gains $k_i > 0$ and $\mu_i \geq 0$ are chosen so that the dynamics of the i-th input v_i, which is related to the pair $(\bar{x}_a^{(i)}, \bar{x}_s^{(i)})$, are much faster than the ones of the $i + 1$-th input v_{i+1}, which is related to the pair $(\bar{x}_a^{(i+1)}, \bar{x}_s^{(i+1)})$, for any $i = 1, ..., n_p$.*

Assumption 5 implies a time-scale separation between the actuator/sensor pairs, so that the dynamics of v_j act as constant inputs for the dynamics of y_i, for any $i > j$. Furthermore, by virtue of Assumptions 3, 4, the dynamics of y_i do not depend on v_j, for any $i < j$.

Remark 3. *The anti-windup term $\mu_i \hat{\eta}_i \tilde{y}_i^2$ plays a stabilising role only, where the quadratic function of the tracking error $\tilde{y}_i^2$ has been introduced in order not to affect the stability analysis, when μ_i is sufficiently small. This might be useful to guarantee the boundedness of the control input when the operating conditions exceed the design envelope.*

5.3.2 Stability Analysis

The main result of this section, which extends the results obtained in the previous chapter to MIMO systems of the form (5.7), is summarised in the following

theorem: it establishes the sufficient conditions under which the the designed MIMO set-point tracking controller guarantees the solution of the flow separation problem (5.1) for the reduced-order dynamics.

Theorem 4. *Consider the closed-loop system (5.7), (5.14), (5.13). Assume that $P_{ii}(0) \neq 0$ with known sign. Then, for any initial condition $(\xi_0, \eta_0, \hat{\eta}_0)$, there exist sufficiently small $k_i^* > 0$ and $\mu_i^* \geq 0$, such that the regulation error $\tilde{y} = y(t) - y^*(t)$ and the control input error $v(t) - v^*(t)$ exponentially tend to zero, as t tends to infinity, for any $0 < k_i \leq k_i^*$, $0 \leq \mu_i \leq \mu_i^*$, $i = 1, ..., n_p$.*

Proof. a). Case $\mu = 0$, $\varepsilon_i = \varepsilon_{m_i} = \varepsilon_{M_i}$. By virtue of assumption 4, system (5.10) can be rewritten as

$$\tilde{Y}(s) = P(s)\left(V(s) + \eta\right)$$

$$= \begin{bmatrix} P_{11}(s) & 0 & \cdots & & 0 \\ P_{21}(s) & P_{22}(s) & \ddots & & 0 \\ \vdots & & \ddots & 0 & \vdots \\ P_{n_p,1}(s) & & & P_{n_p-1,n_p-1}(s) & 0 \\ P_{n_p,1}(s) & \cdots & \cdots & P_{n_p,n_p-1}(s) & P_{n_p,n_p}(s) \end{bmatrix} \begin{bmatrix} V_1(s) + \eta_1 \\ \vdots \\ V_{n_p}(s) + \eta_{n_p} \end{bmatrix}.$$

$$(5.15)$$

The dynamics of the generic i-th output read

$$\tilde{Y}_i(s) = \sum_{j=1}^{i-1} P_{ij}(s)(V_j(s) + \eta_j) + P_{ii}(s)(V_i(s) + \eta_i). \qquad (5.16)$$

Define
$$Q_{ii}(s) = 1 + k_i P_{ii}(s)\left(\frac{\text{sign}(P_{ii}(0))}{s}\right) = \frac{n_{Q_{ii}}(s)}{d_{Q_{ii}}(s)}, \qquad (5.17)$$

which represents the closed-loop transfer function of the first pair $i = 1$, *i.e.*, by assumption 3, the most upstream pair. By the root locus, for sufficiently small $k_i > 0$, r zeros of $Q_{ii}(s)$ are sufficiently close to the r poles of $P_{ii}(s)$ and, therefore, they have negative real part. The remaining branch of the root locus starts from 0 in the s-plane with angle π, so that also the remaining zeros of $Q_{ii}(s)$ have negative real part. The exponential convergence to zero of both the regulation error $\tilde{y}_1(t)$ and the control input error $v_1(t) + \eta_1$, as t tends to infinity, is thus guaranteed. Since the dynamics of the first pair are much faster than the ones of the pairs located further downstream, the exponentially decaying signal $v_1(t) + \eta_1$ does not affect the error dynamics $\tilde{y}_i(t)$, for any $i = 2, ..., n_p$. Therefore, the stability of

the closed-loop system relative to the second pair is determined by the zeros of (5.17), for $i = 2$. This implies the exponential convergence to zeros of the both the regulation $\tilde{\mathrm{y}}_2(t)$ and input error $\mathrm{v}_2(t) + \eta_2$. Thus, we can iteratively approximate (5.16) as

$$\tilde{Y}_i(s) \approx P_{ii}(s)(V_i(s) + \eta_i), \tag{5.18}$$

so that the stability of the closed-loop system is determined only by the zeros of the transfer function (5.17), which have negative real part for sufficiently small k_i, $i = 1, ..., n_p$.

b). Case $\mu > 0$, $\varepsilon_i = \varepsilon_{m_i} = \varepsilon_{M_i}$. Let $\tilde{\eta} = \mathrm{v} - \mathrm{v}^* = \eta - \hat{\eta}$ and

$$\tilde{\chi} = \begin{bmatrix} \tilde{\xi} \\ \tilde{\eta} \end{bmatrix}. \tag{5.19}$$

Define

$$K = \mathrm{diag}\left(k_1\ \mathrm{sign}(P_{11}(0)), ..., k_{n_p}\ \mathrm{sign}(P_{n_p,n_p}(0)) \right), \tag{5.20}$$

$$M = \mathrm{diag}\left(\mu_1, ..., \mu_{n_p} \right). \tag{5.21}$$

The closed-loop error dynamics can be written as

$$\dot{\tilde{\chi}} = \begin{bmatrix} A & B \\ -KC & 0 \end{bmatrix}\tilde{\chi} + \begin{bmatrix} 0 \\ M\tilde{\xi}^{\mathrm{T}}C^{\mathrm{T}}C\tilde{\xi}(\eta - \tilde{\eta}) \end{bmatrix} = A_c\tilde{\chi} + l(\tilde{\chi}),$$

$$\tilde{\mathrm{y}} = [C, 0]\,\tilde{\chi}.$$

The characteristic polynomial of the closed-loop matrix A_c can be computed as

$$\begin{aligned}
p_{A_c}(s) &= \det(sI_{r+n_p} - A_c) = \det\begin{bmatrix} sI_r - A & B \\ -KC & sI_{n_p} \end{bmatrix} \\
&= \det(sI_r - A)\det\left(sI_{n_p} + KC(sI_r - A)^{-1}B \right) \\
&= \det(sI_r - A)\det\left(sI_{n_p} + KP(s) \right) \\
&= \left(sd_{P_{11}}(s) + k_1 n_{P_{11}}(s)\mathrm{sign}\left(P_{11}(0) \right) \right) \dots \\
&\qquad \left(sd_{P_{n_p,n_p}}(s) + k_{n_p} n_{P_{n_p,n_p}}(s)\mathrm{sign}\left(P_{n_p,n_p}(0) \right) \right) \\
&= n_{Q_{11}}(s)n_{Q_{22}}(s)\dots n_{Q_{n_p,n_p}}(s) = n_Q(s),
\end{aligned}$$

where I_{n_p} is the $n_p \times n_p$ identity matrix. Therefore, A_c is Hurwitz, as its eigenvalues coincide with roots of $n_Q(s)$ and have negative real part for any sufficiently small k_i, $i = 1, ..., n_p$. Thus, there exist two symmetric, positive definite matrices $\mathcal{P}$ and $\mathcal{Q}$ satisfying the Lyapunov equation

$$\mathcal{P}A_c + A_c^{\mathrm{T}}\mathcal{P} = -\mathcal{Q}. \tag{5.22}$$

Consider the candidate Lyapunov function

$$\mathcal{V}(t) = \tilde{\chi}^{\mathrm{T}}(t)\mathcal{P}\tilde{\chi}(t), \tag{5.23}$$

satisfying

$$\alpha_1\|\tilde{\chi}(t)\|^2 \leq \mathcal{V}(t) \leq \alpha_2\|\tilde{\chi}(t)\|^2, \tag{5.24}$$

where α_1, $\alpha_2 > 0$ are positive constants. The time derivative of $\mathcal{V}(t)$, along the trajectories of the closed-loop system satisfies the following inequality:

$$\dot{\mathcal{V}} \leq -\tilde{\chi}^{\mathrm{T}}\mathcal{Q}\tilde{\chi} + 2\tilde{\chi}^{\mathrm{T}}\mathcal{P}l(\tilde{\chi}) \leq -\mathcal{M}_1\|\tilde{\chi}\|^2 + 2\mathcal{M}_2\|M\|\|\tilde{\chi}\|^2 \left|\eta\tilde{\eta} - \tilde{\eta}^2\right|$$
$$\leq -\left(\mathcal{M}_1 - \frac{\mathcal{M}_2\|M\|\eta^2}{2}\right)\|\tilde{\chi}\|^2,$$

where $\mathcal{M}_1 = \|\mathcal{Q}\|$, $\mathcal{M}_2 = \|\mathcal{P}\|\|C\|^2$. Therefore, for sufficiently small μ_i, there exists an $\alpha_3 > 0$ such that

$$\dot{\mathcal{V}} \leq -\alpha_3\|\tilde{\chi}\|^2 \leq -\frac{\alpha_3}{\alpha_2}\mathcal{V}, \tag{5.25}$$

thus implying the closed-loop boundedness and the exponential convergence to zero of both the regulation error $\tilde{y}(t)$ and the control input error $v(t) - v^*$, as t tends to infinity.

c). Case $\mu > 0$, $\varepsilon_{m_i} < \varepsilon_{M_i}$. Consider the candidate Lyapunov function defined in (5.23). Let $\tilde{\chi}$ be defined as in (5.19), $\tilde{\xi} = \xi - \xi^*$ and $\tilde{\eta} = v - v^*$. When the output vector belongs to the compact set Ω_ε, we have: $\tilde{\xi} \equiv 0$, $\dot{\tilde{\xi}} \equiv 0$, $\dot{\tilde{\eta}} \equiv 0$. Thus, for any $t \geq 0$ such that $y(t) \in \Omega_\varepsilon$, $\dot{\mathcal{V}}(t) \equiv 0$. When the output does not belong to the reference region, as in the previous proof, there exist three positive constants α_1, α_2, $\alpha_3 > 0$ such that $\mathcal{V}(t)$ and its time derivative satisfy (5.24) and (5.25), respectively. Therefore, for any $t \geq 0$ such that $y(t) \notin \Omega_\varepsilon$, $\dot{\mathcal{V}}(t) < 0$ and the distance

$$\mathrm{d}_{\mathcal{P}}\left(\chi(t), \Omega_\chi\right) = \inf_{\bar{\chi}\in\Omega_\chi}\|\chi - \bar{\chi}\|_{\mathcal{P}} = \sqrt{\tilde{\chi}^{\mathrm{T}}\mathcal{P}\tilde{\chi}},$$

between χ and its reference set Ω_χ satisfies

$$\mathrm{d}_{\mathcal{P}}^2\left(\chi(t), \Omega_\chi\right) \leq \alpha_2\|\tilde{\chi}\|^2 \leq e^{-\alpha t}\delta,$$

where $\alpha = \alpha_3/\alpha_2$ and $\delta = \mathcal{V}(0)\alpha_2/\alpha_1$. Since $0 \leq \mathcal{V}(t) \in \mathcal{C}^1$ is lower bounded and its derivative is semi-negative definite, it admits a finite limit (see Courant, 1937, p. 61). Closed-loop boundedness and exponential convergence of $\dot{\mathcal{V}}(t)$ (and, therefore, of $\tilde{\xi}$ and $\dot{\tilde{\eta}}$) to zero are thus guaranteed, according to Barbalat's lemma, as $\mathcal{V}(t)$ is uniformly continuous. Consequently, $\xi(t)$ converges to a constant reference $\bar{\xi} \in \Omega_\xi$ and $v(t)$ converges to a constant value $\bar{v}$, as t tends to infinity. If $\bar{v} \notin \Omega_\eta$, then

$\bar{\text{y}} = C\bar{\xi} = -P(0)\bar{\text{v}} \notin \Omega_\varepsilon$, which contradicts $\bar{\xi} \in \Omega_\xi$. Therefore, $\bar{\text{v}} \in \Omega_\eta$ and the distance $\text{d}_{\mathcal{P}}(\chi(t), \Omega_\chi)$ exponentially tends to zero, as t tends to infinity. $\qquad\square$

The following theorem establishes that, if the conditions of Theorem 4 are restricted, a robust universal controller (5.14), (5.13) can be designed without any restrictions on the control gain k.

Theorem 5. *Consider the closed-loop system (5.7), (5.14), (5.13). Assume that $Re\{P_{ii}(j\omega)\} > 0$ for all $\omega \in \mathbb{R}$, $i = 1, ..., n_p$. Then, for any initial condition $(\xi_0, \eta_0, \hat{\eta}_0)$, there exist sufficiently small $\mu_i^* \geq 0$ such that the regulation error $y(t) - y^*(t)$ and the control input error $v(t) - v^*(t)$ exponentially tend to zero as t tends to infinity, for any $k_i > 0$, $0 \leq \mu_i \leq \mu_i^*$, $i = 1, ..., n_p$.*

Proof. Theorem 4 implies the exponential convergence of $\text{y}(t)$ and $\text{v}(t)$ to their corresponding reference sets Ω_ε and Ω_η, respectively, for sufficiently small k_i and μ_i. To complete the proof it is, therefore, sufficient to show (as in Marino and Tomei (2015)) that there are no solutions on the imaginary axis of the equation

$$1 + k_i P_{ii}(s)\frac{1}{s} = 0,$$

so that the positive root locus cannot cross the imaginary axis. The point $s = 0$ is not a zero of $Q_{ii}(s)$, as $P_{ii}(0) > 0$. The phase condition for a point $s = j\omega$ to belong to the positive root locus for $\omega \neq 0$ becomes

$$\arg\left[P_{ii}(j\omega)\right] - \frac{\pi}{2} = \pi.$$

Since, by hypothesis, $-\pi/2 < \arg\left[P_{ii}(j\omega)\right] < \pi/2$, the previous condition is never satisfied. Therefore, all branches must lie in the open left-hand complex half-plane. $\qquad\square$

5.4 Choice of the Actuators/Sensors Configuration

Consider a generic configuration

$$\mathcal{C} = \left\{n_p, \bar{x}_a^{(1)}, ..., \bar{x}_a^{(n_p)}, \Delta_s^{(1)}, ..., \Delta_s^{(n_p)}, \Omega_{\varepsilon_1}, ..., \Omega_{\varepsilon_{n_p}}\right\}, \tag{5.26}$$

which satisfies Assumptions 2, 3, 4, and let k_i, μ_i be some positive control gains satisfying the time-scale separation Assumption 5 for any $i = 1, ..., n_p$. Here,

$$\Delta_s^{(i)} = |\bar{x}_a^{(i)} - \bar{x}_s^{(i)}|, \quad i = 1, ..., n_p, \tag{5.27}$$

denotes the distance between the actuator and the sensor of the i-th pair. Then, the proposed controller (5.14), (5.13) guarantees the exponential regulation of the output measurements y_i to the chosen reference sets Ω_{ε_i}.

The objective of this section is to provide a criterion for selecting optimal configurations, whose reference sets are such that Assumption 1 holds, for any $\varepsilon_i \in \Omega_{\varepsilon_i}$, $i = 1, ..., n_p$, in order to maximise the performance of the closed-loop system. Equivalently, suitable numbers n_p and positions $(\bar{x}_a^{(i)}, \bar{x}_s^{(i)})$ of the actuator/sensor pairs along the aerofoil have to be chosen, along with their corresponding reference sets Ω_{ε_i}, according to some performance measure. To this end, define a suitable cost functional

$$
\begin{aligned}
J_\beta(\mathcal{C}) =& \gamma_1 || \left\langle \partial_{\boldsymbol{n}} u_{\boldsymbol{\tau}}^-(t, \boldsymbol{x}) \right\rangle ||_{L^2(\Gamma_N)} + \gamma_2 \sum_{i=1}^{n_p} \frac{||\mathrm{v}_i(t)||_{L^2(t_0,t_f)}}{t_f - t_0} \\
&+ \gamma_3 \sum_{i=1}^{n_p} \frac{||\tilde{\mathrm{y}}_i(t)||_{L^2(t_0,t_f)}}{t_f - t_0} + \gamma_4 \left\langle \frac{C_D}{C_L} \right\rangle + \gamma_5 l_s,
\end{aligned}
\tag{5.28}
$$

depending on the angle of attack $\beta \in \mathcal{R}_\beta$, where: t_0 and t_f denote the initial and final time, respectively;

$$
\partial_{\boldsymbol{n}} u_{\boldsymbol{\tau}}^-(t, \boldsymbol{x}) = \begin{cases} 0, & \text{if } \partial_{\boldsymbol{n}} u_{\boldsymbol{\tau}}(t, \boldsymbol{x}) \geq 0, \\ |\partial_{\boldsymbol{n}} u_{\boldsymbol{\tau}}(t, \boldsymbol{x})|, & \text{if } \partial_{\boldsymbol{n}} u_{\boldsymbol{\tau}}(t, \boldsymbol{x}) < 0 \end{cases}
\tag{5.29}
$$

is proportional to the magnitude of the negative wall shear stress along the aerofoil;

$$
|| \left\langle \partial_{\boldsymbol{n}} u_{\boldsymbol{\tau}}^-(t, \boldsymbol{x}) \right\rangle ||_{L^2(\Gamma_N)} = \frac{1}{t_f - t_0} \left(\int_{\Gamma_N} \left| \int_{t_0}^{t_f} \partial_{\boldsymbol{n}} u_{\boldsymbol{\tau}}^-(t, \boldsymbol{x}) \mathrm{d}t \right|^2 \mathrm{d}\boldsymbol{x} \right)^{1/2}
\tag{5.30}
$$

represents a measure of the flow separation;

$$
||\mathrm{v}_i(t)||_{L^2(t_0,t_f)} = \left(\int_{t_0}^{t_f} |\mathrm{v}_i(t)|^2 \mathrm{d}t \right)^{1/2}
\tag{5.31}
$$

represents a measure of power spent by the control action; the time averaged output regulation error

$$
||\tilde{\mathrm{y}}_i(t)||_{L^2(t_0,t_f)} = \left(\int_{t_0}^{t_f} |\tilde{\mathrm{y}}_i(t)|^2 \mathrm{d}t \right)^{1/2}
\tag{5.32}
$$

is introduced to evaluate the performance of the controller; C_D/C_L is the ratio between the drag and the lift coefficients, respectively, and

$$
\left\langle \frac{C_D}{C_L} \right\rangle = \frac{1}{t_f - t_0} \left(\int_{t_0}^{t_f} \frac{C_D(t)}{C_L(t)} \mathrm{d}t \right);
\tag{5.33}
$$

the non-dimensional length

$$l_s = \int_0^1 l^-(\bar{x})\mathrm{d}\bar{x}, \tag{5.34}$$

with

$$l^-(\bar{x}) = \begin{cases} 0, & \text{if } \partial_{\boldsymbol{n}} u_{\boldsymbol{\tau}}(t, \boldsymbol{x}) \geq 0, \\ \bar{x}, & \text{if } \partial_{\boldsymbol{n}} u_{\boldsymbol{\tau}}(t, \boldsymbol{x}) < 0, \end{cases} \tag{5.35}$$

represents the part of the chord where the flow is separated; the angle of attack β can be either a constant or a time-varying angle of attack, in order to test both the steady-state and the transient performances.

The coefficients $\gamma_1, ..., \gamma_5$ are positive design parameters, which can be chosen according to the specific application. In particular, γ_1 weights the surface of the laminar separation bubble; γ_2 and γ_3 penalise the requested input power and the closed-loop output error, respectively, in order to evaluate the dynamic performance of the control system; γ_4 weights the inverse of the aerodynamic efficiency; γ_5 is used to evaluate the length of the laminar separation bubble with respect to the chord length. Furthermore, define a total cost functional

$$J(\mathcal{C}) = \sum_{\beta \in \mathcal{R}_\beta} J_\beta(\mathcal{C}), \tag{5.36}$$

in order to evaluate the robustness of the system with respect to the variation of the uncertain angle β. In particular, the aim is to find an optimal configuration

$$\mathcal{C}^* = \operatorname{argmin}\left(J(\mathcal{C})\right), \tag{5.37}$$

so that the regulation of the output $\mathrm{y}(t)$ to its reference set Ω_ε guarantees a consistent reduction of the flow separation along the aerofoil, for a chosen range $\mathcal{R}_\beta$ of angles of incidence β.

5.5   Simulation Results: χnavis, 2D case

In the previous chapter, a balanced DMD model, yielding a positive steady-state gain of the reduced-order transfer function, has been obtained for 2D flows around a NACA 0012 aerofoil, with angle of attack $\beta = 20°$ and $Re = 1000$. The sensor was placed at $2c/5$ and the actuator at $c/5$. Based on this single reduced-order approximation of the incompressible Navier-Stokes equations (3.1), (3.3), (3.2), (3.5), it is assumed, coherently with Assumption 2, a positive sign of the steady-state gains of the transfer function between any pair, *i.e.*, $P_{ii}(0) > 0$,

$i = 1, ..., n_p$, if the sensor is close enough to the actuator, *i.e.*, the distance $\Delta_s^{(i)}$ is sufficiently small. The robustness of the proposed control scheme (5.13), (5.14), is tested at $Re = 20,000$ in different 2D configurations, where the angle of attack is varied within the range $\mathcal{R}_\beta = [5, 25]$, in order to maximise the system performance and validate the modelling assumptions. The simulations are performed using the unsteady RANS equations based solver χnavis, described in Chapter 3. In particular, two different scenarios are considered:

$$
\beta_1(t) = \begin{cases}
\frac{2\beta_0 - \Delta\beta}{2} + \frac{\Delta\beta}{2}\cos\left(\frac{\pi(t-t_m)}{\Delta t}\right) & \text{if } t \geq t_m \text{ and } t \leq t_m + \Delta t, \\
\beta_0 - \Delta\beta & \text{if } t > t_m + \Delta t \text{ or } t < t_M - \Delta t, \\
\frac{2\beta_0 - \Delta\beta}{2} + \frac{\Delta\beta}{2}\cos\left(\frac{\pi(t-t_M+2\Delta t)}{\Delta t}\right) & \text{if } t \geq t_M - \Delta t \text{ and } t \leq t_M, \\
\beta_1 & \text{if } t < t_m \text{ or } t > t_M,
\end{cases}
$$

$$(5.38)$$

$$
\beta_2(t) = \begin{cases}
\frac{2\beta_0 + \Delta\beta}{2} - \frac{\Delta\beta}{2}\cos\left(\frac{\pi(t-t_m)}{\Delta t}\right) & \text{if } t \geq t_m \text{ and } t \leq t_m + \Delta t, \\
\beta_0 + \Delta\beta & \text{if } t > t_m + \Delta t \text{ or } t < t_M - \Delta t, \\
\frac{2\beta_0 + \Delta\beta}{2} - \frac{\Delta\beta}{2}\cos\left(\frac{\pi(t-t_M+2\Delta t)}{\Delta t}\right) & \text{if } t \geq t_M - \Delta t \text{ and } t \leq t_M, \\
\beta_1 & \text{if } t < t_m \text{ or } t > t_M,
\end{cases}
$$

$$(5.39)$$

where $\beta_0 = 15°$, $\Delta_\beta = 10°$, $t_m = 30$, $t_M = 50$, $T = 60$, $\Delta t = 5$ (see figure 5.2). The measure $\| \langle \partial_n u_\tau^-(t, \boldsymbol{x}) \rangle \|_{L^2(\Gamma_N)}$ of the flow separation in (5.28) is approximated as

$$
\| \langle \partial_n u_\tau^-(t, \boldsymbol{x}) \rangle \|_{L^2(\Gamma_N)} \approx \left\| \frac{\langle u_\tau^-(t, \bar{x}) \rangle}{\Delta y_n} \right\|_{L^2(0,c)}
$$

$$
= \frac{\Delta y_n^{-1}}{t_f - t_0} \left(\int_0^1 \left| \int_{t_0}^{t_f} u_\tau^-(t, \bar{x}) \mathrm{d}t \right|^2 \mathrm{d}\bar{x} \right)^{1/2},
$$

$$(5.40)$$

where

$$
u_\tau^-(t, \bar{x}) = \begin{cases}
0, & \text{if } u_\tau(t, \boldsymbol{x}_N) \geq 0, \\
|u_\tau(t, \boldsymbol{x}_N)|, & \text{if } u_\tau(t, \boldsymbol{x}_N) < 0,
\end{cases}
$$

$$(5.41)$$

and $\boldsymbol{x}_N$ denotes the first cell centre above the aerofoil, at $\Delta y_n \approx 10^{-4}$, in the direction perpendicular to the aerofoil surface. The controller is activated between $t_0 = 15$ and $t_f = T = 60$ and the coefficients in (5.28) are chosen as follows: $\gamma_1 = 1/200$, $\gamma_2 = 2/100$, $\gamma_3 = 5/100$, $\gamma_4 = 2$, $\gamma_5 = 1/2000$. The output measurements $y_i(t) = u_\tau(t, \boldsymbol{x}_{s_i})$ are taken at $y_n = 0.0005$ above the aerofoil, which is approximately half the thickness of the boundary layer. Three cases are tested, with different numbers of actuator/sensor pairs: $n_p = 1$, $n_p = 2$ and $n_p = 3$. For
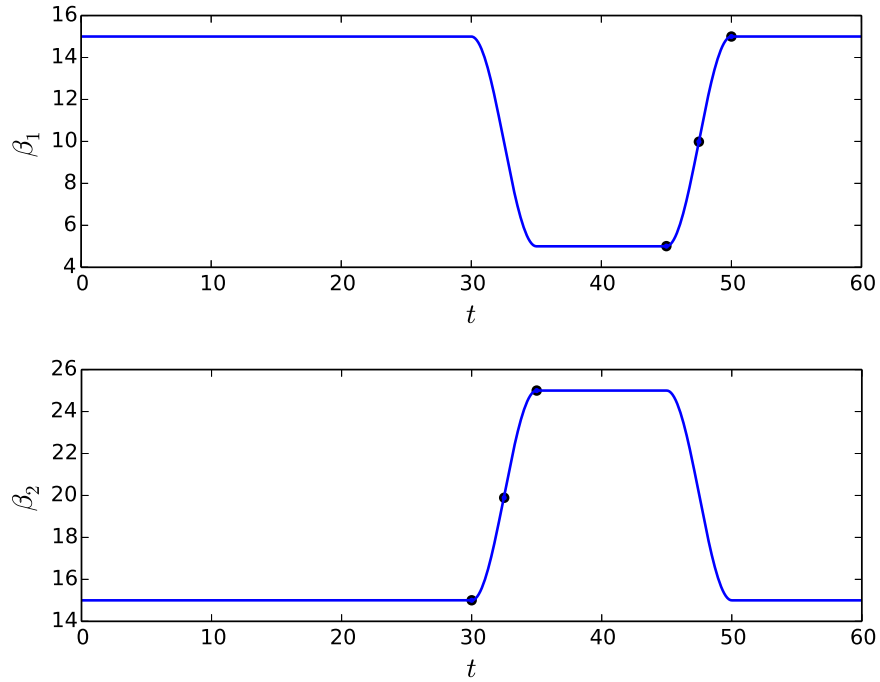
Figure 5.2: Time-varying angles $\beta_1(t)$ (top) and $\beta_2(t)$ (bottom).

the sake of simplicity, it is set $\mu_i = 0$ in all the simulations, while the control gains k_i are chosen so that Assumption 5 is satisfied. All the reported quantities are non-dimensional.

The considered geometry is a NACA 0012 aerofoil, denoted by Γ_N, and the domain boundaries are $\partial\Omega = \Gamma_{\text{in}} \cup \Gamma_0 \cup \Gamma_{\text{out}}$. Here, the wall boundary is $\Gamma_0 = \Gamma_N$. The inflow boundary condition on Γ_{in} is a time-varying velocity profile

$$\boldsymbol{g}(t, \boldsymbol{x}) = \boldsymbol{U}_\infty(t), \tag{5.42}$$

where $\boldsymbol{U}_\infty(t) = (\cos(\beta_0 - \beta(t)), \sin(\beta_0 - \beta(t)), 0)$ is the non-dimensionalised inflow velocity. The computational grid has $N = 127,872$ total volumes and is divided into extremely fine actuator grids, a fine C-type inner grid and coarser outer grids. The two-dimensional grid, whose size is similar to those found in the literature (*e.g.*, $N = 115,213$ in Riherd and Roy, 2013) is extruded in the spanwise direction using 8 uniformly distributed grid volumes and the spanwise length is 0.125 (so that the dynamics are two-dimensional). It is worth to stress that the use of the overlapping grid approach allows to achieve a highly refined grid in the region of interest, while limiting the total number of control volumes. In order to avoid reflections, the outer boundaries are placed at a distance of 50 chords. The inner region around the profile (see figure 5.3) has 320×96 volumes, in the tangent and

normal direction, respectively; the points are clustered towards the wall, where the mesh spacing is equal to 2.1×10^{-4}. The grid resolution at the wall is similar to that found in the literature (5×10^{-4} and 1.2×10^{-4} in Riherd and Roy, 2013; Sato et al., 2015b, , respectively, where LES simulations of flow past aerofoils in the presence of plasma actuation are performed). The near wake region is discretised with 128×192 volumes distribuited in the streamwise and vertical direction, respectively. The presence of the plasma actuator is taken into account
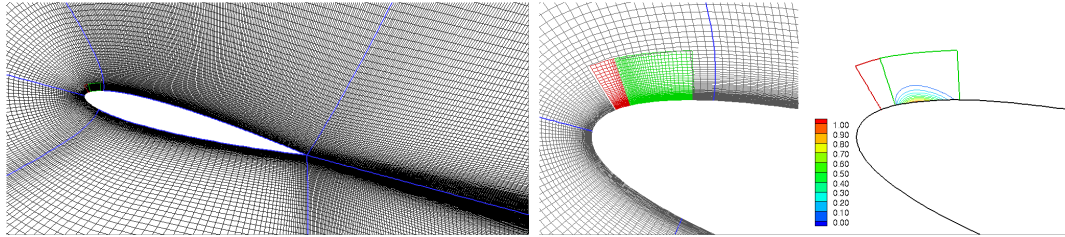

Figure 5.3: Computational grid and actuator: left, detailed view around the NACA 0012 profile; middle, detail of the actuator region; right, normalised plasma actuator force.

by a system of body forces distributed in the flow field within a block of fixed dimension and position. Both an example of the plasma actuator block and the distribution of the magnitude of its corresponding body force, normalised with respect to its maximum value, are shown in figure 5.3. The grid for the actuator region (see figure 5.3) is built as in Sato et al. (2015b). In particular, the actuator system is composed of two adjacent blocks: the one upstream (in red) is used to smoothly link the mesh to the profile mesh (in gray), whereas the downstream block (in green) is the one where the body forces are distributed accordingly to (5.6). The origin of the local reference frame $(x_\tau^{(i)}, y_n^{(i)})$ is placed at the bottom left edge of the latter block (see figure 5.3). The points are clustered towards both the origin of the local reference frame and the aerofoil surface, *i.e.* where the largest gradients of the actuator forces are expected. The plasma actuator blocks are considered as a dominant mesh, *i.e.*, its cells, regardless of their dimension, cannot be tagged as "chimera" cells.

The time-averaged drag and lift coefficients

$$
\begin{aligned}
C_D &= 2F_x/(\rho U_\infty^2 c, \\
C_L &= 2F_y/(\rho U_\infty^2 c),
\end{aligned}
\tag{5.43}
$$

for the simulations with no actuation, computed along the streamwise (x) and normal (y) axis, respectively, where F_x, F_y denote the corresponding components

(parallel and perpendicular to the inflow velocity, respectively) of the total forces on the aerofoil profile per span length, are very close to those found experimentally in Feng et al. (2015) for a NACA 0012 at $Re = 20,000$. The greater time-averaged values of the force coefficients are related to the total kinetic energy, which is not distributed along the spanwise direction and remains confined in a 2D framework. The increase of the 2D forces, compared to the 3D case, is commonly observed in many circumstances: *e.g.*, for the flow past a circular cylinder, which exhibits larger mean values of C_D and C_L (see, for example, Singh and Mittal, 2005). Compared to the configuration without actuation, in all the considered feedback configurations a significant reduction of the drag coefficient, along with a significant increase of the lift coefficient, is robustly achieved in the presence of the time-varying angle of attack, during both the transient and the steady-state regimes. In particular, high values of the lift coefficient are obtained by the proposed control algorithm because it has been designed with the aim of reducing the separation bubble. This is particularly desirable either for wind turbines, in order to increase lift at low wind speeds, or in aeronautic applications, during both take-off and sudden manoeuvres, in order to avoid stall conditions (*e.g.*, UAVs). However, lower references $\varepsilon_m, \varepsilon_M$ can be selected, depending on the specific application, in order to reduce the control effort.

Note that, for the sake of brevity, the time-averaged wall shear-stress, the vorticity contours and the instantaneous streamlines are shown and discussed at the end of section 5.5 for the optimal configuration only.

5.5.1 SISO Case: $n_p = 1$

Figures 5.4-5.8 show the simulation results for six different SISO configurations $\mathcal{C}_1 - \mathcal{C}_6$, whose details are reported in table 5.1. The chosen control gains are $k_1 = 20$. Since the uncertain angle of attack may vary significantly and, therefore, the flow detachment might occur very close to the leading edge, the actuator's position is fixed at $\bar{x}_a = 0.02$, whereas both the distance Δ_s and the reference set Ω_ε are varied. In particular, higher references ε_{m_1} are chosen for sensors that are located upstream and *vice versa* (see table 5.1), aiming to obtain a full flow reattachment along the aerofoil, in order to satisfy Assumption 1. In general, the closer the sensor is to the actuator, the better dynamic performance is obtained. However, the further upstream the sensor is located, the more the corresponding configuration loses robustness, as a very high reference ε_{m_1} would be needed in

Configuration	n_p	$\bar{x}_a$	Δ_s	Ω_ε
$\mathcal{C}_1$	1	0.02	0.3	[0.2,0.25]
$\mathcal{C}_2$	1	0.02	0.4	[0.2,0.25]
$\mathcal{C}_3$	1	0.02	0.5	[0.1,0.15]
$\mathcal{C}_4$	1	0.02	0.6	[0.1,0.15]
$\mathcal{C}_5$	1	0.02	0.7	[0.05,0.1]
$\mathcal{C}_6$	1	0.02	0.8	[0.05,0.1]

Table 5.1: SISO configurations.
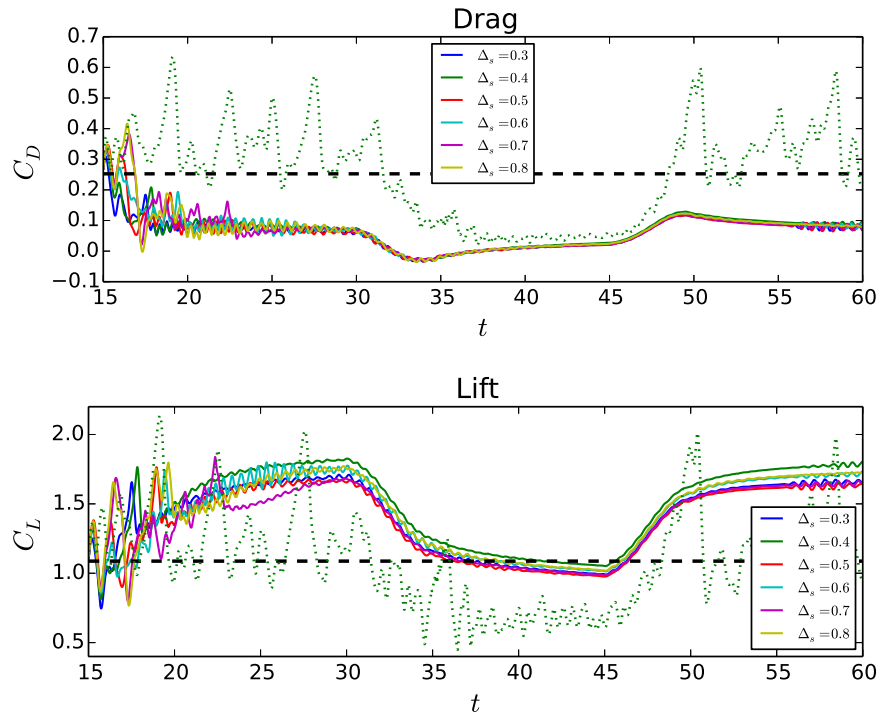

Figure 5.4: Drag and lift coefficients of the configurations $\mathcal{C}_j$, $j = 1, ..., 6$ in the scenario $\beta(t) = \beta_1(t)$ with (solid lines) and without actuation (dashed lines, green for time histories and black for time-averaged). The variation of β occurs between $t = 30$ and $t = 35$, from 15° to 5°, and between $t = 45$ and $t = 50$, from 5° to 15°.

order to guarantee full flow reattachment for high angles of attack; on the contrary, a much lower ε_{m_1} would be sufficient for lower angles.

The time histories (solid lines) of the drag and lift coefficients are compared with the corresponding time histories (dashed green) and time averaged coefficients
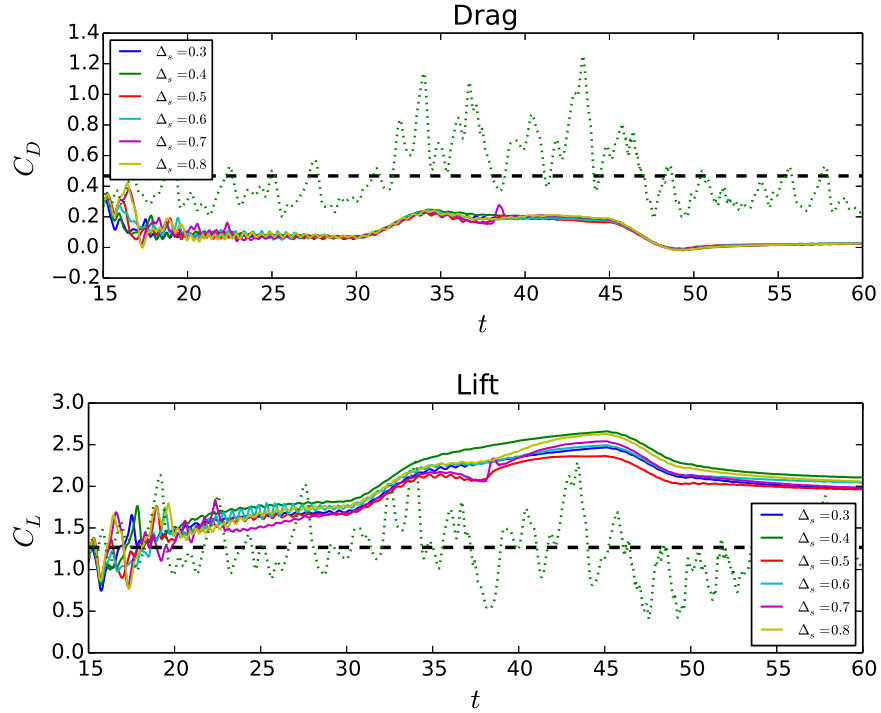
Figure 5.5: Drag and lift coefficients of the configurations $\mathcal{C}_j$, $j = 1, ..., 6$ in the scenario $\beta(t) = \beta_2(t)$ with (solid lines) and without actuation (dashed lines, green for time histories and black for time-averaged). The variation of β occurs between $t = 30$ and $t = 35$, from 15° to 25°, and between $t = 45$ and $t = 50$, from 25° to 15°.

(dashed black) for the simulations without actuators (see figures 5.4 and 5.5), in both scenarios $\beta_1(t)$ and $\beta_2(t)$. In the first scenario, the controller is first tested at 15° in a pre-stall condition, then the angle of attack is further decreased to 5° between $t = 30$ and $t = 35$, kept constant at 5° between $t = 35$ and $t = 45$ and, finally increased back to 15° between $t = 45$ and $t = 50$. In the second scenario, the controller is first tested at 15° in a pre-stall condition, then the angle of attack is increased to a post-stall angle of attack $\beta = 25°$ between $t = 30$ and $t = 35$, kept constant at $\beta = 25°$ between $t = 35$ and $t = 45$ and, finally increased back to 15° between $t = 45$ and $t = 50$. The snapshots of the flow field at the different angles of attack $\beta = 5°, 15°, 25°$, in both steady-state and transient conditions, with and without control are shown for comparison purposes in figures 5.37, 5.38, 5.36 and discussed at the end of section 5.5.
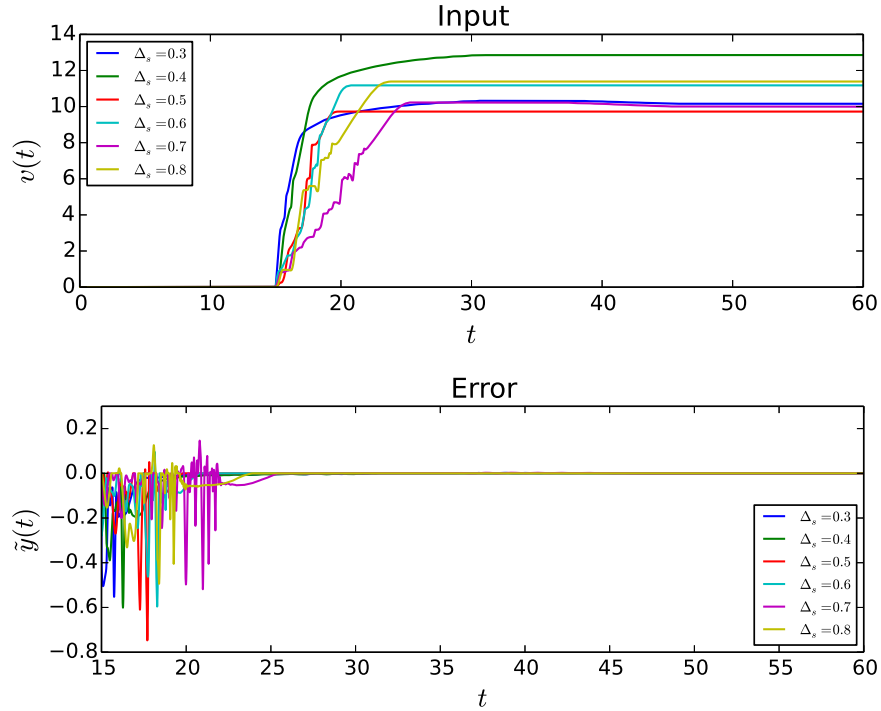
Figure 5.6: SISO simulation results for $\mathcal{C}_j$, $j = 1, ..., 6$ in the scenario $\beta(t) = \beta_1(t)$: controlled input (top) and output error (bottom). The variation of β occurs between $t = 30$ and $t = 35$, from $15°$ to $5°$, and between $t = 45$ and $t = 50$, from $5°$ to $15°$.

Note that the drag and lift coefficients

$$C_D = 2F_x/(\rho U_\infty^2 c,$$
$$C_L = 2F_y/(\rho U_\infty^2 c), \tag{5.44}$$

are computed from the total force, which includes the input of energy from the actuator. When the angle of attack is decreased, the streamwise coefficient C_D becomes negative during the closed-loop transients because of the active contribution of the actuators, which produces a force in the opposite direction of the drag force. This is due to the fluid time scales, which are much slower compared to the variation of the angle of attack: the energy spent by the system at $25°$ is much higher than the one required at $5°$ but the effect of the adapted feedback control input on the overall dynamics is not immediately visible. Thus, at the beginning of the transient, the force produced by the actuator is greater than the drag force, thereby making the corresponding coefficient negative. Also in the uncontrolled case, a huge reduction of the drag coefficient can be seen when the angle of attack decreases to $5°$, due to the shortened length of the separation bubble (see figures
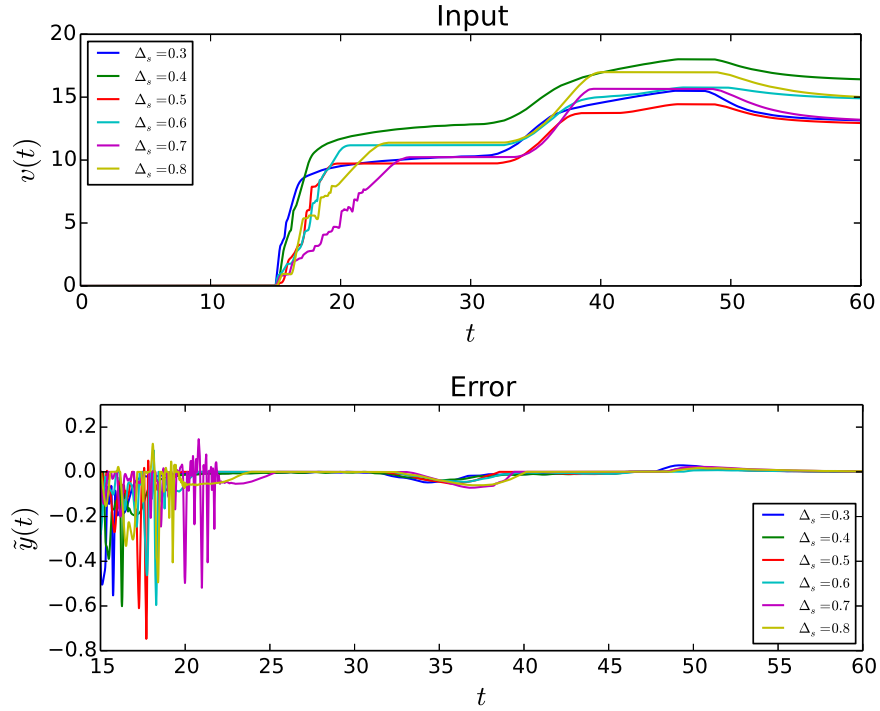
Figure 5.7: SISO simulation results for $\mathcal{C}_j$, $j = 1, ..., 6$ in the scenario $\beta(t) = \beta_2(t)$: controlled input (top) and output error (bottom). The variation of β occurs between $t = 30$ and $t = 35$,from $15°$ to $25°$, and between $t = 45$ and $t = 50$, from $25°$ to $15°$.

5.37, 5.38, 5.36).

Figures 5.6, 5.7 show a comparison between the six different SISO configurations, in the scenarios $\beta_1(t)$ and $\beta_2(t)$, respectively: as discussed above, the regulation of the error to zero, along with the regulation of the corresponding control input, becomes slower as the sensor is moved away from the actuator. In particular, in the scenario $\beta_1(t)$, with a negative angle variation of $-10°$, the output does not leave the reference region although the angle of attack varies. Thus, the control input remains constant after it reaches its reference, in all the configurations apart from $\mathcal{C}_1$, where the sensor is located in the furthest upstream position. In the scenario $\beta_2(t)$, with a positive angle variation of $10°$, the output decreases below the lower-bound ε_m of the reference region (resulting in a negative regulation error $\tilde{y}_i$), as the angle increases to $25°$, and it increases over the upper-bound ε_M (resulting in a positive regulation error $\tilde{y}_i$), as the angle decreases back to $15°$. The resulting control input is automatically adjusted online by the designed control algorithm, without requiring the knowledge of the uncertain angle of in-
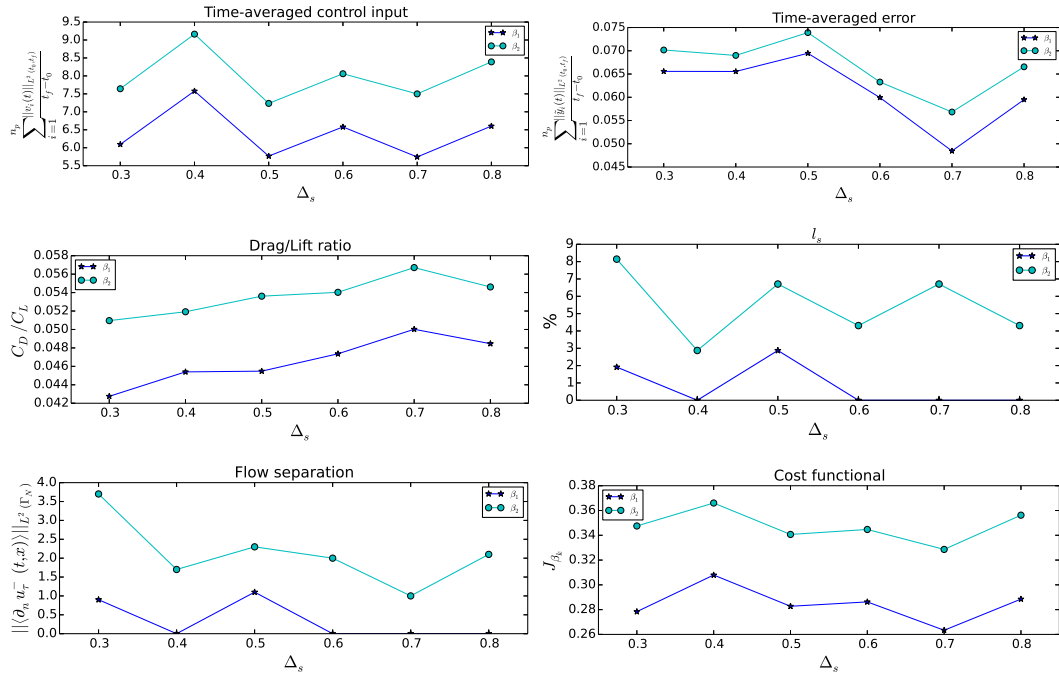
Figure 5.8: Comparison of the SISO simulation results for $\mathcal{C}_j$, $j = 1, ..., 6$ in the two scenarios $\beta(t) = \beta_k(t)$, $k = 1, 2$.

cidence: this highlights the great potential of robust feedback laws. Figure 5.8 shows a comparison between the different SISO configurations, in the two different scenarios $\beta(t) = \beta_1(t)$, $\beta(t) = \beta_2(t)$: although the time-averaged drag-to-lift ratio increases, both the separation bubble and the time-averaged regulation error decrease, as the sensor is moved downstream, while, given a reference set Ω_ε, the time-averaged control input increases with the distance Δ_s. The performance of each configuration is globally evaluated by the chosen cost functional (5.28), which seeks a trade-off between power input, output tracking error and drag-to-lift ratio reduction, thus identifying $\mathcal{C}_5$ as the best configuration for the SISO case. As in the previous chapter, the inverse of the aerodynamic efficiency is considered here in order to perform a minimisation of the former along with the control variable, while avoiding eventual infinite terms due to zero denominators. Here, a theoretical model of the actuator is considered, whose parameters have to be characterised according to the considered power converter. Therefore, an accurate realistic estimation of the power input cannot be given because it depends on the efficiency of the specific power converter in use. An example of a PSI-MCPG2503C power amplifier device is given in Appendix A: the peak-to-peak voltage range is $V^{(j)}(t) =$1-2.5kV, where $V^{(j)}(t)$ is the amplitude variation of the operational volt-

age, while $v_j(t) = V^{(j)}(t)/V_m$ is the corresponding non-dimensionalised voltage input, scaled by V_m [kV]. The power consumption is around 1W.

5.5.2 MIMO Case: $n_p = 2$

As discussed in the previous section, having only one actuator/sensor pair requires choosing a balance between robustness and dynamic performance, by varying the distance between the actuator and the sensor, along with the corresponding output reference. Thus, increasing the number of pairs might lead to a greater flexibility in the choice of the configuration. Furthermore, in practical applications, the maximum available voltage of the power converters used to generate the plasma is limited and might not be sufficient to suppress the flow separation in the most critical situations, *e.g.*, high Reynolds number and/or large angles of attack. Therefore, increasing the number of converters might be desirable, in order to avoid the saturation of the input.

In this section, sixteen different MIMO configurations are considered (see table 5.2) with $n_p = 2$ actuator/sensor pairs, whose simulation results are shown in figures 5.13 - 5.26.
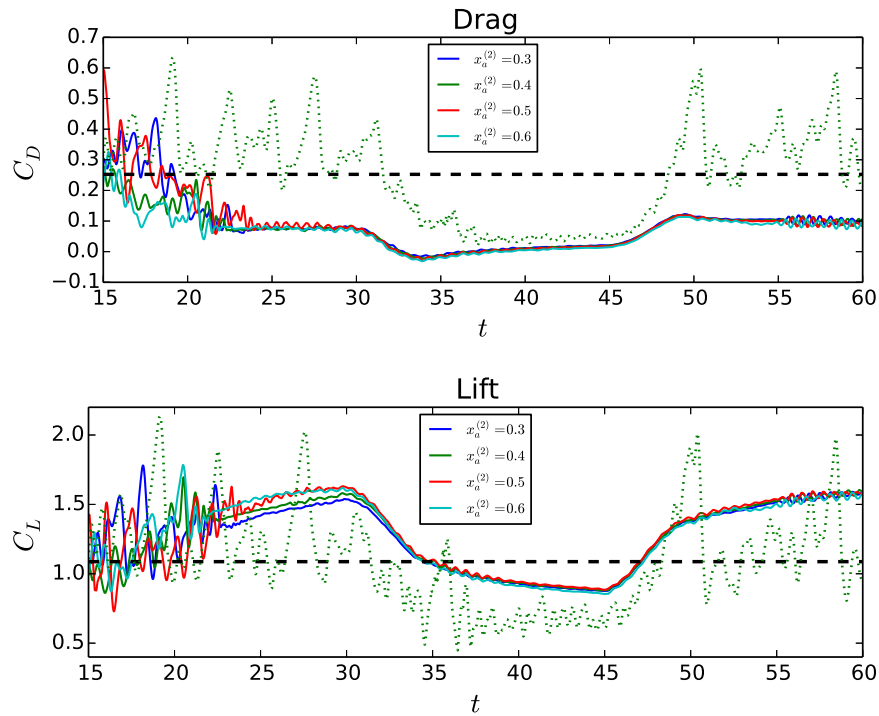

Figure 5.9: Drag and lift coefficients of the configurations $\mathcal{C}_j$, $j = 7, ..., 10$ in the scenario $\beta(t) = \beta_1(t)$ with (solid lines) and without actuation (dashed lines, green for time histories and black for time-averaged). The variation of β occurs between $t = 30$ and $t = 35$, from 15° to 5°, and between $t = 45$ and $t = 50$, from 5° to 15°.

| Configuration	n_p	$\bar{x}_a^{(1)}$	$\bar{x}_a^{(2)}$	$\Delta_s^{(1)}$	$\Delta_s^{(2)}$	Ω_{ε_1}	Ω_{ε_2}
$\mathcal{C}_7$	2	0.02	0.3	0.2	0.5	[0.05,0.1]	[0.05,0.1]
$\mathcal{C}_8$	2	0.02	0.4	0.2	0.4	[0.05,0.1]	[0.05,0.1]
$\mathcal{C}_9$	2	0.02	0.5	0.2	0.3	[0.05,0.1]	[0.05,0.1]
$\mathcal{C}_{10}$	2	0.02	0.6	0.2	0.2	[0.05,0.1]	[0.05,0.1]
$\mathcal{C}_{11}$	2	0.02	0.3	0.2	0.2	[0.05,0.1]	[0.05,0.1]
$\mathcal{C}_{12}$	2	0.02	0.4	0.2	0.2	[0.05,0.1]	[0.05,0.1]
$\mathcal{C}_{13}$	2	0.02	0.5	0.2	0.2	[0.05,0.1]	[0.05,0.1]
$\mathcal{C}_{14}$	2	0.02	0.6	0.2	0.2	[0.05,0.1]	[0.05,0.1]
$\mathcal{C}_{15}$	2	0.02	0.3	0.2	0.2	[0.1,0.15]	[0.05,0.1]
$\mathcal{C}_{16}$	2	0.02	0.4	0.2	0.2	[0.1,0.15]	[0.05,0.1]
$\mathcal{C}_{17}$	2	0.02	0.5	0.2	0.2	[0.1,0.15]	[0.05,0.1]
$\mathcal{C}_{18}$	2	0.02	0.6	0.2	0.2	[0.1,0.15]	[0.05,0.1]
$\mathcal{C}_{19}$	2	0.02	0.3	0.2	0.2	[0.05,0.1]	[0.1,0.15]
$\mathcal{C}_{20}$	2	0.02	0.4	0.2	0.2	[0.05,0.1]	[0.1,0.15]
$\mathcal{C}_{21}$	2	0.02	0.5	0.2	0.2	[0.05,0.1]	[0.1,0.15]
$\mathcal{C}_{22}$	2	0.02	0.6	0.2	0.2	[0.05,0.1]	[0.1,0.15]

Table 5.2: MIMO configurations for $n_p = 2$.
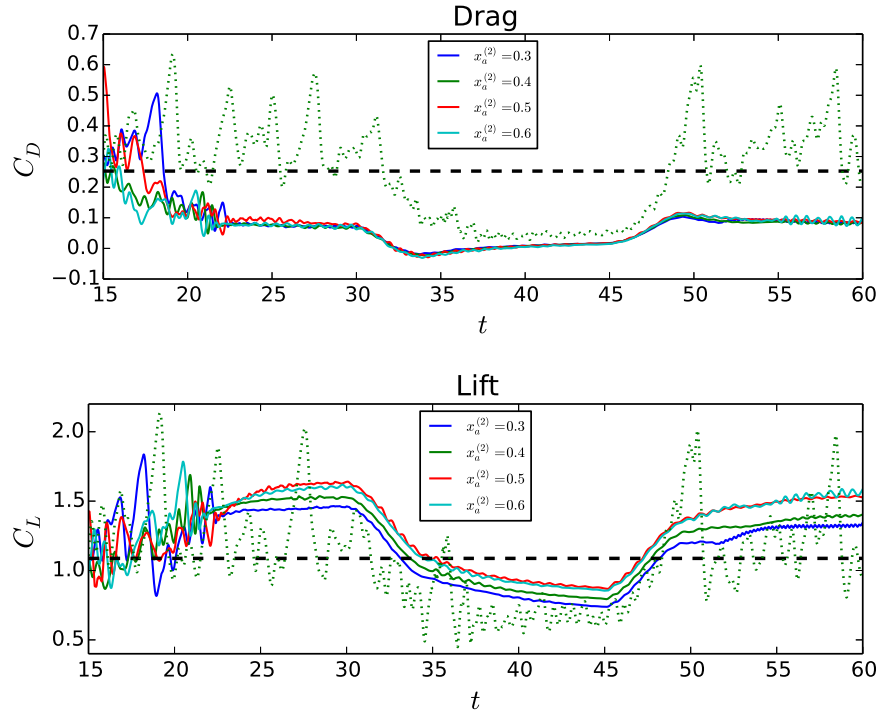
Figure 5.10: Drag and lift coefficients of the configurations $\mathcal{C}_j$, $j = 11, ..., 14$ in the scenario $\beta(t) = \beta_1(t)$ with (solid lines) and without actuation (dashed lines, green for time histories and black for time-averaged). The variation of β occurs between $t = 30$ and $t = 35$, from $15°$ to $5°$, and between $t = 45$ and $t = 50$, from $5°$ to $15°$.
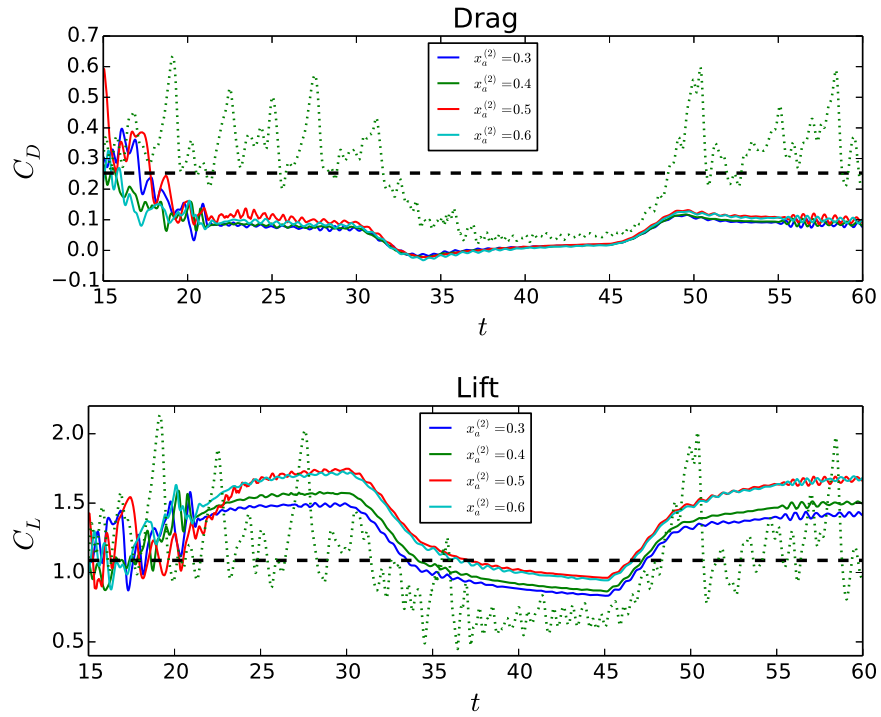
Figure 5.11: Drag and lift coefficients of the configurations $\mathcal{C}_j$, $j = 15, ..., 18$ in the scenario $\beta(t) = \beta_1(t)$ with (solid lines) and without actuation (dashed lines, green for time histories and black for time-averaged). The variation of β occurs between $t = 30$ and $t = 35$, from $15°$ to $5°$, and between $t = 45$ and $t = 50$, from $5°$ to $15°$.
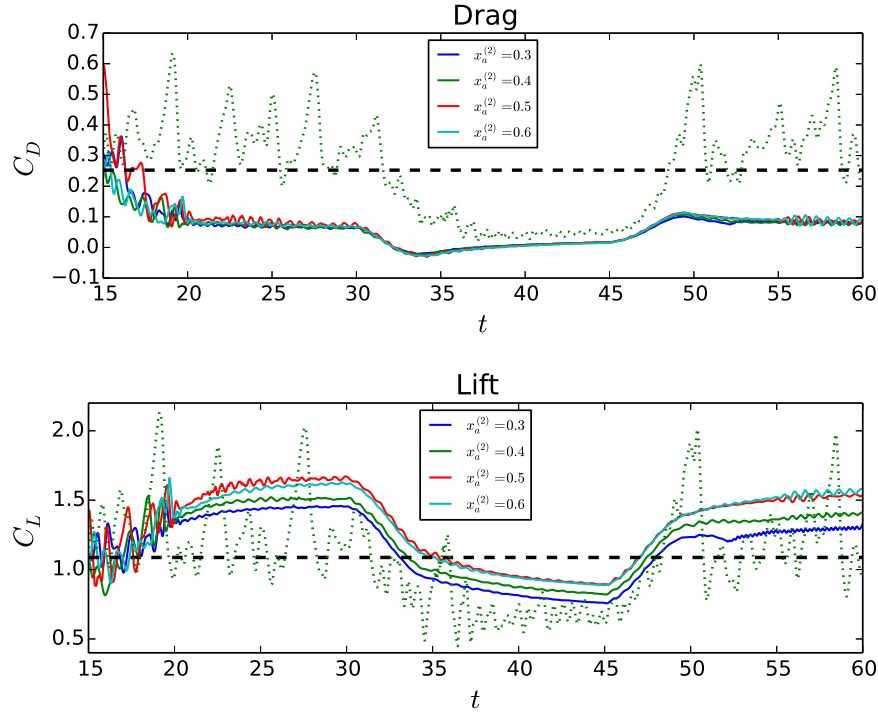
Figure 5.12: Drag and lift coefficients of the configurations $\mathcal{C}_j$, $j = 19, ..., 22$ in the scenario $\beta(t) = \beta_1(t)$ with (solid lines) and without actuation (dashed lines, green for time histories and black for time-averaged). The variation of β occurs between $t = 30$ and $t = 35$,from 15° to 5°, and between $t = 45$ and $t = 50$, from 5° to 15°.

The chosen control gains are $k_1 = 20$, $k_2 = 5$. The first pair is fixed at $(\bar{x}_a^{(1)} = 0.02, \bar{x}_s^{(1)} = 0.22)$, while the influence of both the variation of the position of the second actuator $\bar{x}_a^{(2)}$, given a fixed sensor position $\bar{x}_s^{(2)}$, and the variation of the position of the second pair $(\bar{x}_a^{(2)}, \bar{x}_s^{(2)})$, given a fixed distance $\Delta_s^{(2)}$ between the second sensor and actuator, is analysed, for difference reference sets. In the four configurations $\mathcal{C}_7$, $\mathcal{C}_8$, $\mathcal{C}_9$, $\mathcal{C}_{10}$, both the second sensor position $\bar{x}_s^{(2)} = 0.8$ and the reference sets $\Omega_{\varepsilon_1} = \Omega_{\varepsilon_2} = [0.05, 0.1]$ are fixed, while the position of the second actuator is varied between $\bar{x}_a^{(2)} = 0.3$ and $\bar{x}_a^{(2)} = 0.6$. In the remaining twelve configurations the distance $\Delta_s^{(2)} = 0.2$, between the second actuator and the second sensor, is fixed and the reference sets Ω_{ε_1} and Ω_{ε_2} are varied: four configurations $\mathcal{C}_{11}$, $\mathcal{C}_{12}$, $\mathcal{C}_{13}$, $\mathcal{C}_{14}$ have the same reference sets Ω_{ε_1} and Ω_{ε_2} of the previous case; $\mathcal{C}_{15}$, $\mathcal{C}_{16}$, $\mathcal{C}_{17}$, $\mathcal{C}_{18}$ have an increased upstream reference set, i.e., $\Omega_{\varepsilon_1} = [0.1, 0.15]$; $\mathcal{C}_{19}$, $\mathcal{C}_{20}$, $\mathcal{C}_{21}$, $\mathcal{C}_{22}$ have an increased downstream reference set, i.e., $\Omega_{\varepsilon_2} = [0.1, 0.15]$.
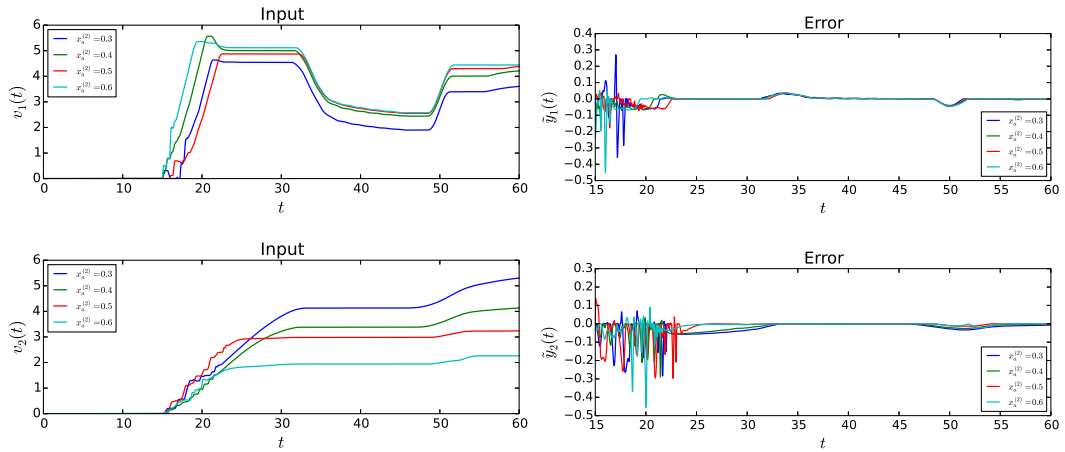
Figure 5.13: MIMO simulation results for $\mathcal{C}_j$, $j = 7, ..., 10$ in the scenario $\beta(t) = \beta_1(t)$: controlled inputs (left) and output errors (right). The variation of β occurs between $t = 30$ and $t = 35$, from $15°$ to $5°$, and between $t = 45$ and $t = 50$, from $5°$ to $15°$.
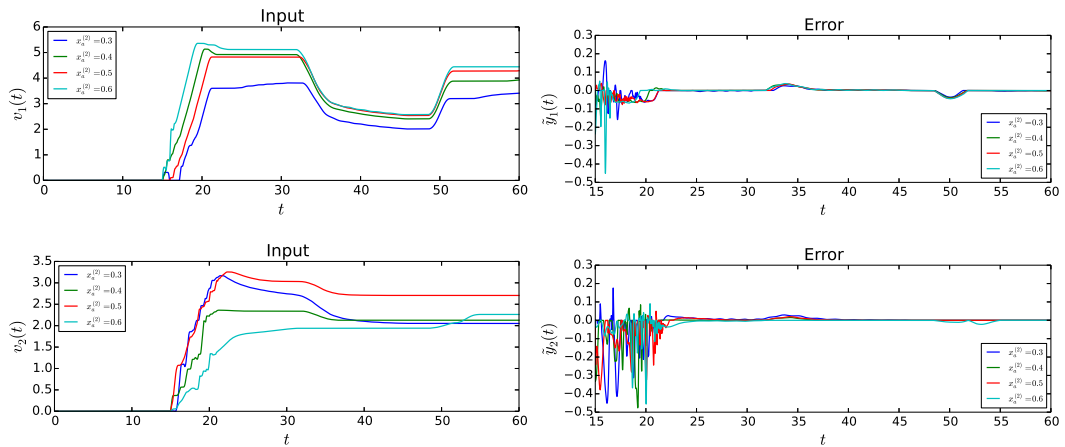

Figure 5.14: MIMO simulation results for $\mathcal{C}_j$, $j = 11, ..., 14$ in the scenario $\beta(t) = \beta_1(t)$: controlled inputs (left) and output errors (right). The variation of β occurs between $t = 30$ and $t = 35$, from $15°$ to $5°$, and between $t = 45$ and $t = 50$, from $5°$ to $15°$.

The corresponding simulation results are depicted in figures 5.9 - 5.16, for $\beta = \beta_1$, and 5.18 - 5.25, for $\beta = \beta_2$. The time histories (solid lines) of the drag and lift coefficients ($C_D = 2F_x/(\rho U_\infty^2 c)$ and $C_L = 2F_y/(\rho U_\infty^2 c)$, respectively, where F_x, F_y denote the total forces per span length) are compared with the corresponding time histories (dashed green) and time averaged coefficients (dashed black) for the simulations without actuators (see figures 5.9-5.12, 5.18-5.21). Note that the
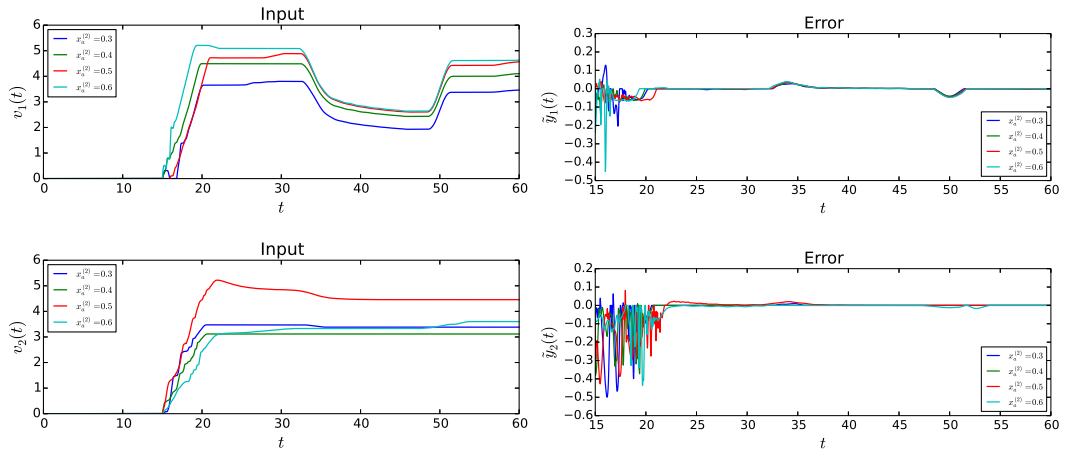
Figure 5.15: MIMO simulation results for $\mathcal{C}_j$, $j = 15, ..., 18$ in the scenario $\beta(t) = \beta_1(t)$: controlled inputs (left) and output errors (right). The variation of β occurs between $t = 30$ and $t = 35$,from $15°$ to $5°$, and between $t = 45$ and $t = 50$, from $5°$ to $15°$.
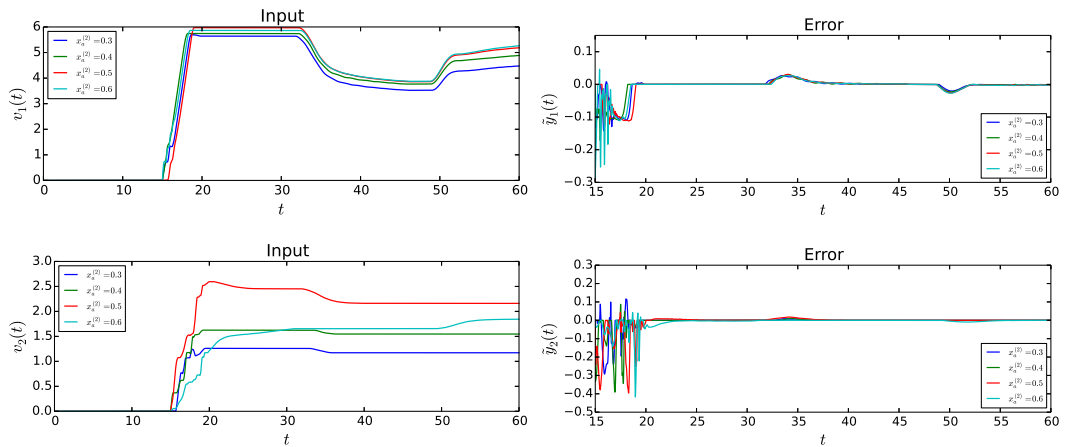

Figure 5.16: MIMO simulation results for $\mathcal{C}_j$, $j = 19, ..., 22$ in the scenario $\beta(t) = \beta_1(t)$: controlled inputs (left) and output errors (right). The variation of β occurs between $t = 30$ and $t = 35$,from $15°$ to $5°$, and between $t = 45$ and $t = 50$, from $5°$ to $15°$.

drag and lift coefficients are computed from the total force, which includes the input of energy from the actuator. Thus, as explained before, when the angle of attack is decreased, the streamwise coefficient C_D becomes negative during the closed-loop transients because it includes the active contribution of the actuators, which produces a force in the opposite direction of the drag force.

Figures 5.17 and 5.26, show a comparison between the different MIMO configura-
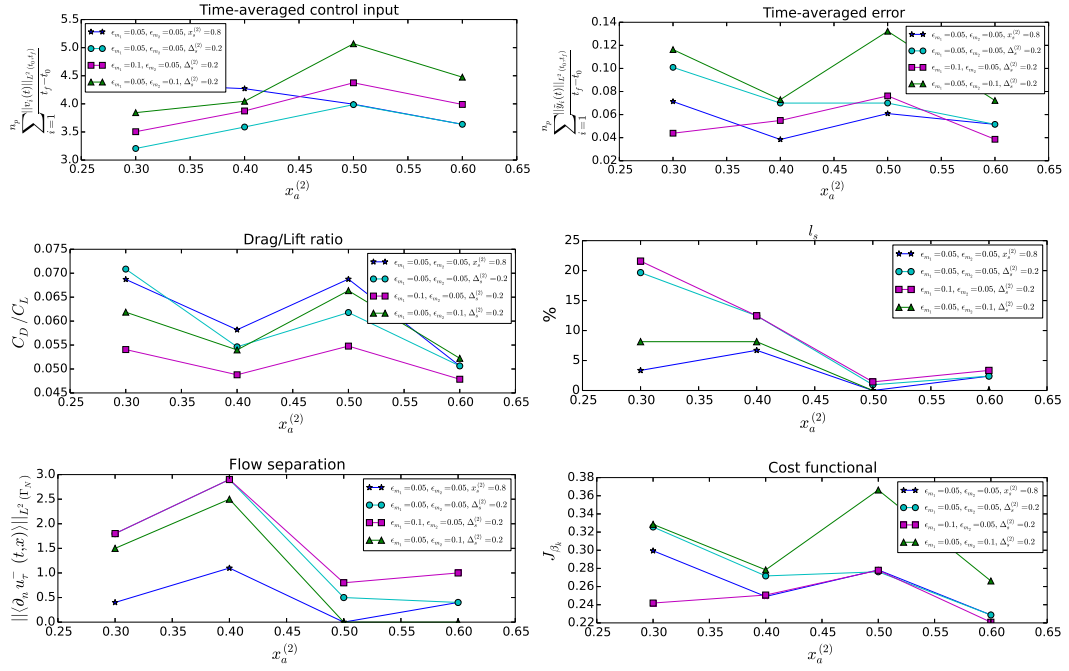
Figure 5.17: Comparison of the MIMO simulation results for $\mathcal{C}_j$, $j = 7, ..., 22$ in the scenario $\beta(t) = \beta_1(t)$.

tions, for $\beta(t) = \beta_1(t)$ and $\beta(t) = \beta_2(t)$, respectively. Note that configuration $\mathcal{C}_{14}$ is equivalent to $\mathcal{C}_{10}$.

The best overall performance is achieved by the four configurations $\mathcal{C}_{15}$, $\mathcal{C}_{16}$, $\mathcal{C}_{17}$, $\mathcal{C}_{18}$ with a higher output reference for the upstream sensor in both scenarios, while the maximum values of the chosen cost functional (5.28) occur at $\mathcal{C}_{19}$, $\mathcal{C}_{20}$, $\mathcal{C}_{21}$, $\mathcal{C}_{22}$, with a higher output reference for the downstream sensor. In particular, $\mathcal{C}_{18}$ is identified as the optimal configuration minimising (5.28), among the sixteen considered MIMO configurations with two actuator/sensor pairs: it shows both the lowest drag-to-lift ratio and the lowest time-averaged regulation error, along with a significant reduction of the separation bubble.
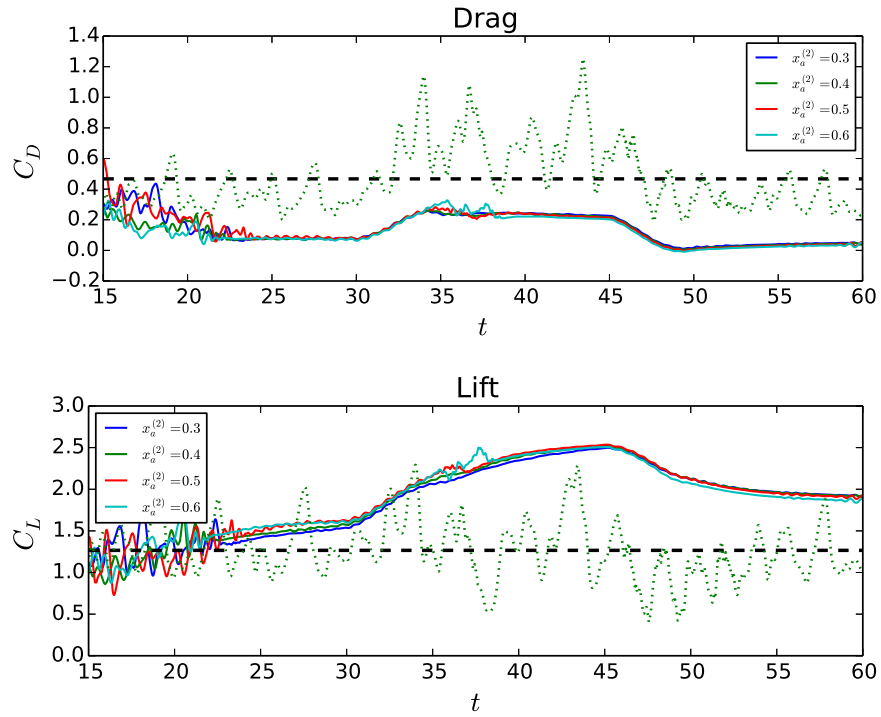
Figure 5.18: Drag and lift coefficients of the configurations $\mathcal{C}_j$, $j = 7, ..., 10$ in the scenario $\beta(t) = \beta_2(t)$ with (solid lines) and without actuation (dashed lines, green for time histories and black for time-averaged). The variation of β occurs between $t = 30$ and $t = 35$, from $15°$ to $25°$, and between $t = 45$ and $t = 50$, from $25°$ to $15°$.

Figure 5.19: Drag and lift coefficients of the configurations $\mathcal{C}_j$, $j = 11, ..., 14$ in the scenario $\beta(t) = \beta_2(t)$ with (solid lines) and without actuation (dashed lines, green for time histories and black for time-averaged). The variation of β occurs between $t = 30$ and $t = 35$,from $15°$ to $25°$, and between $t = 45$ and $t = 50$, from $25°$ to $15°$.
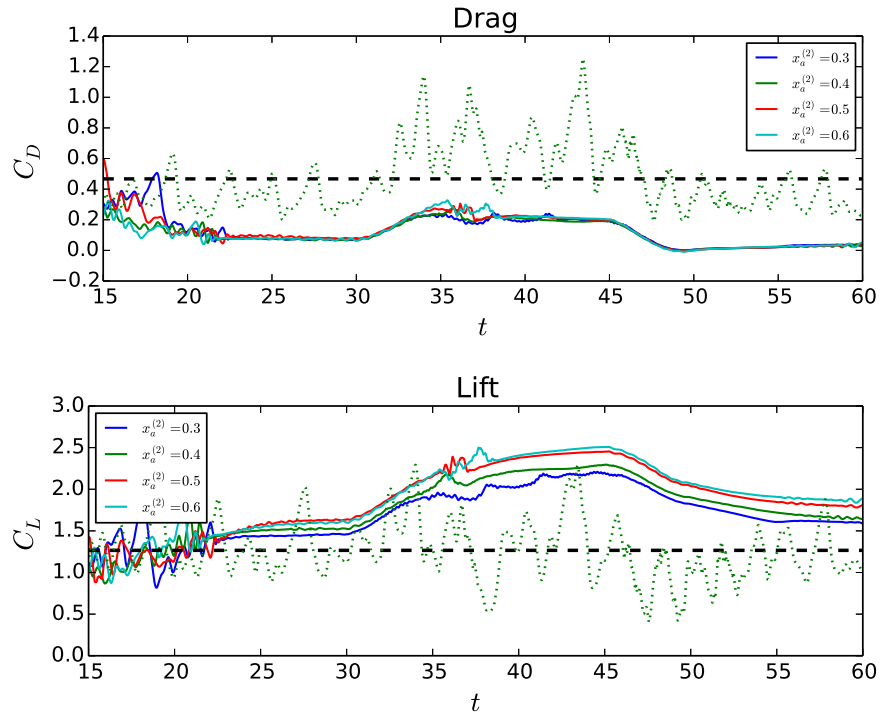
Figure 5.20: Drag and lift coefficients of the configurations $\mathcal{C}_j$, $j = 15, ..., 18$ in the scenario $\beta(t) = \beta_2(t)$ with (solid lines) and without actuation (dashed lines, green for time histories and black for time-averaged). The variation of β occurs between $t = 30$ and $t = 35$,from $15°$ to $25°$, and between $t = 45$ and $t = 50$, from $25°$ to $15°$.
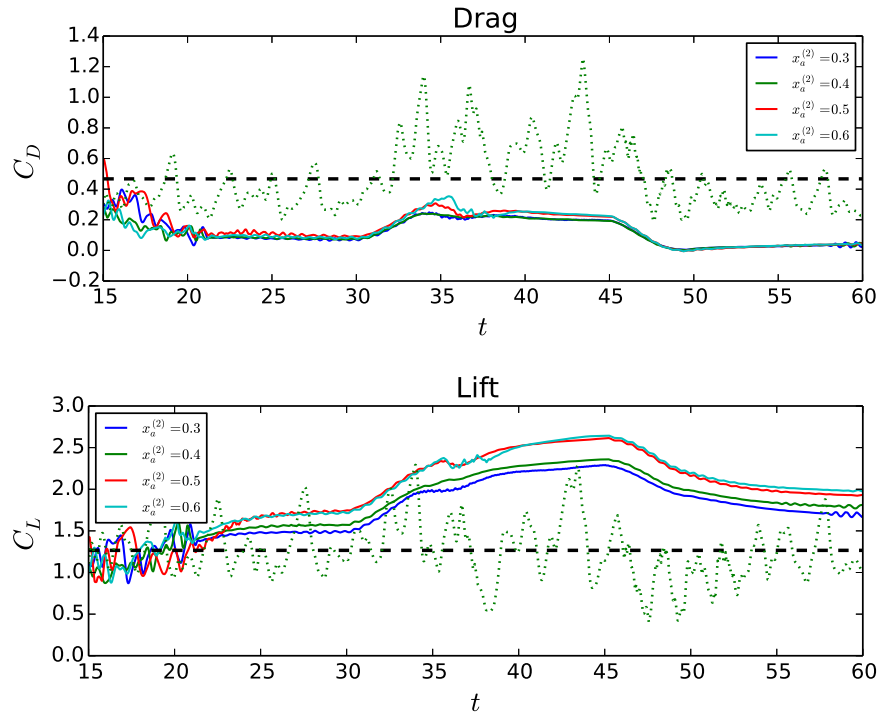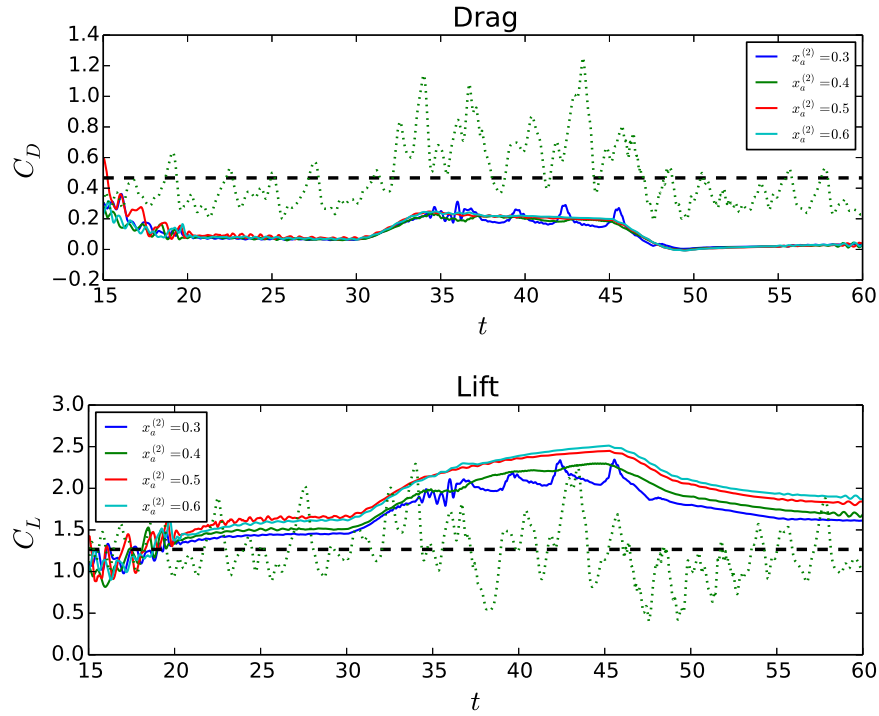
Figure 5.21: Drag and lift coefficients of the configurations $\mathcal{C}_j$, $j = 19, ..., 22$ in the scenario $\beta(t) = \beta_2(t)$ with (solid lines) and without actuation (dashed lines, green for time histories and black for time-averaged). The variation of β occurs between $t = 30$ and $t = 35$, from $15°$ to $25°$, and between $t = 45$ and $t = 50$, from $25°$ to $15°$.

Figure 5.22: MIMO simulation results for $\mathcal{C}_j$, $j = 7, ..., 10$ in the scenario $\beta(t) = \beta_2(t)$: controlled inputs (left) and output errors (right). The variation of β occurs between $t = 30$ and $t = 35$, from $15°$ to $25°$, and between $t = 45$ and $t = 50$, from $25°$ to $15°$.

Figure 5.23: MIMO simulation results for $\mathcal{C}_j$, $j = 11, ..., 14$ in the scenario $\beta(t) = \beta_2(t)$: controlled inputs (left) and output errors (right). The variation of β occurs between $t = 30$ and $t = 35$, from $15°$ to $25°$, and between $t = 45$ and $t = 50$, from $25°$ to $15°$.
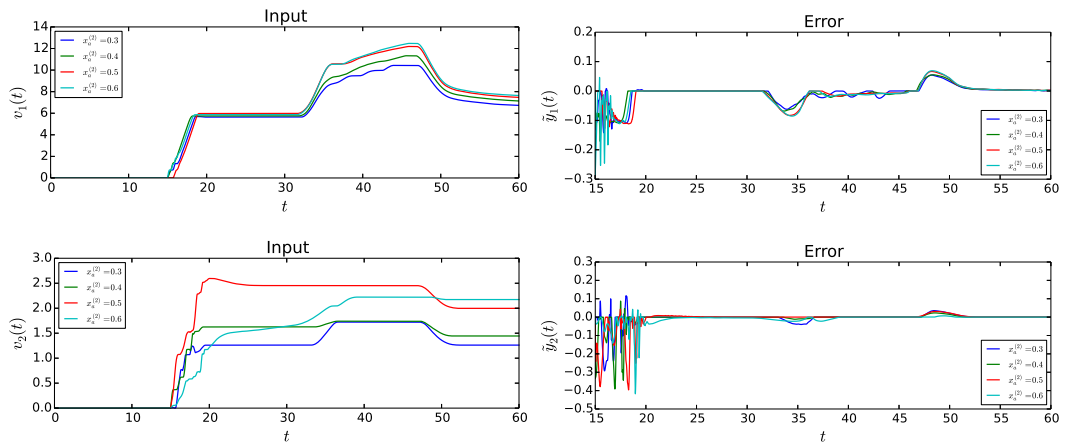
Figure 5.24: MIMO simulation results for $\mathcal{C}_j$, $j = 15, ..., 18$ in the scenario $\beta(t) = \beta_2(t)$: controlled inputs (left) and output errors (right). The variation of β occurs between $t = 30$ and $t = 35$, from $15°$ to $25°$, and between $t = 45$ and $t = 50$, from $25°$ to $15°$.
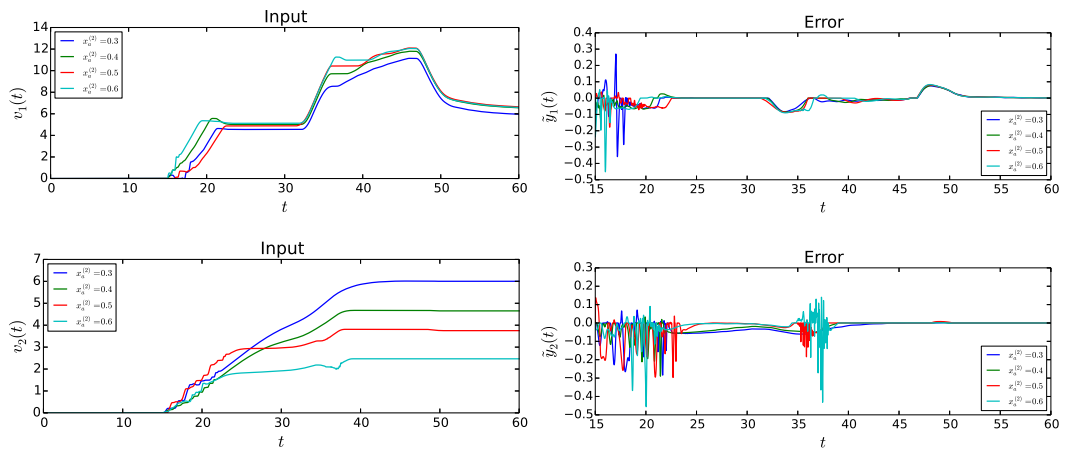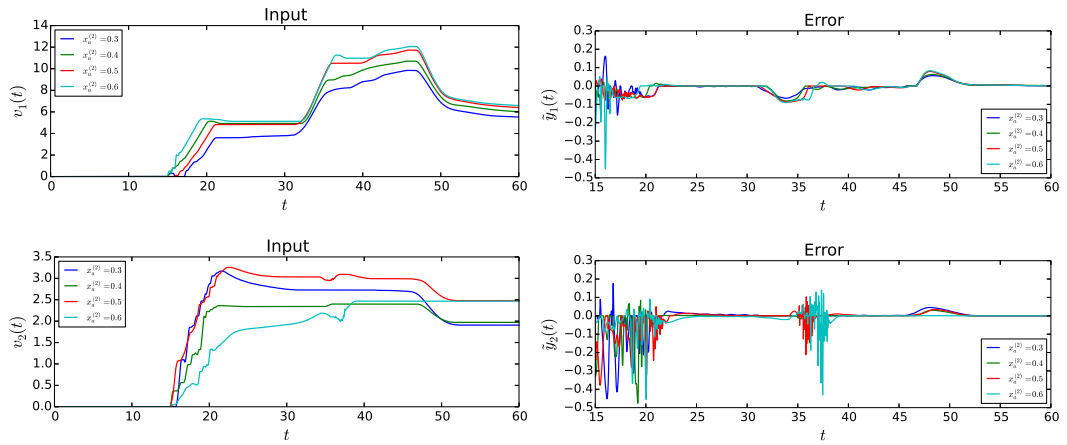
Figure 5.25: MIMO simulation results for $\mathcal{C}_j$, $j = 19, ..., 22$ in the scenario $\beta(t) = \beta_2(t)$: controlled inputs (left) and output errors (right). The variation of β occurs between $t = 30$ and $t = 35$, from $15°$ to $25°$, and between $t = 45$ and $t = 50$, from $25°$ to $15°$.
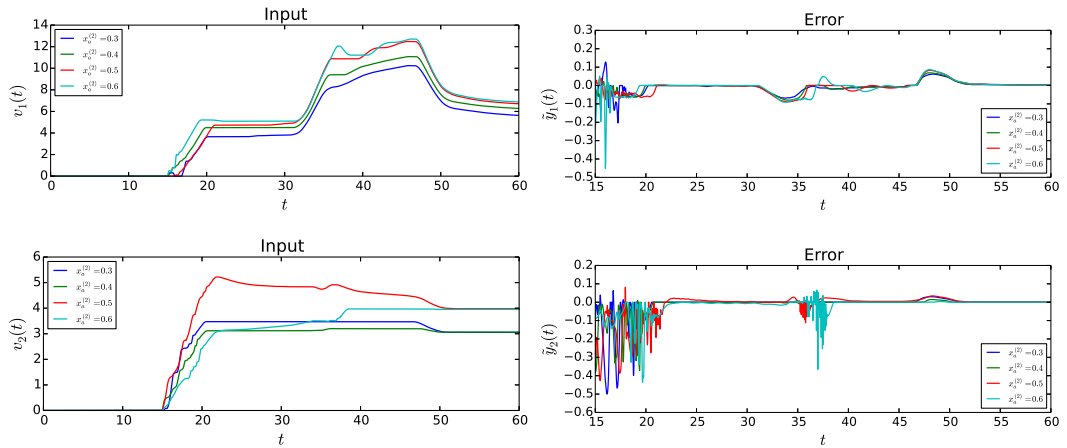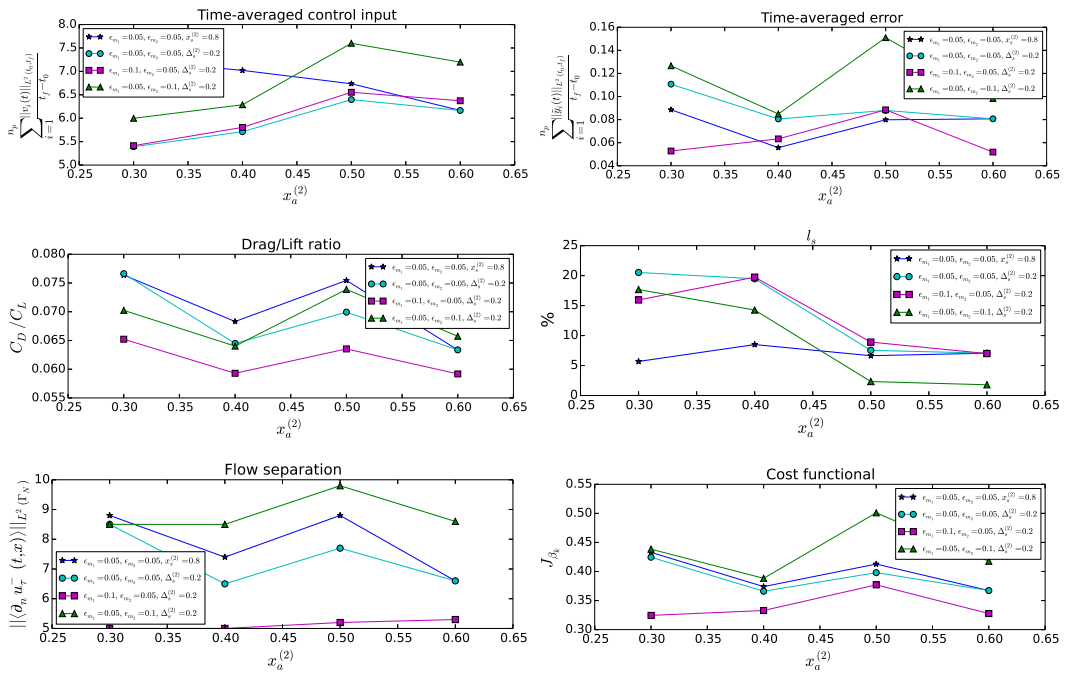

Figure 5.26: Comparison of the MIMO simulation results for $\mathcal{C}_j$, $j = 7, ..., 22$ in the scenario $\beta(t) = \beta_2(t)$.

5.5.3 MIMO Case: $n_p = 3$

Figures 5.27- 5.30, show the simulation results for three different MIMO configurations with $n_p = 3$ actuator/sensor pairs (see table 5.3). The aim of this section is to analyse the influence of the reference sets, given a fixed position of actuator/sensor pairs. The chosen control gains are $k_1 = 20$, $k_2 = 5$, $k_3 = 5$. In the considered configurations $\mathcal{C}_{23}$, $\mathcal{C}_{24}$, $\mathcal{C}_{25}$ the positions of the three pairs are fixed at $(\bar{x}_a^{(1)} = 0.02, \bar{x}_s^{(1)} = 0.22)$, $(\bar{x}_a^{(1)} = 0.3, \bar{x}_s^{(1)} = 0.5)$, $(\bar{x}_a^{(1)} = 0.6, \bar{x}_s^{(1)} = 0.8)$, with the same distance $\Delta_s^{(i)} = 0.2$ between sensors and actuators, while the

Configuration	n_p	$\bar{x}_a^{(1)}$	$\bar{x}_a^{(2)}$	$\bar{x}_a^{(3)}$	$\Delta_s^{(1)}$	$\Delta_s^{(2)}$	$\Delta_s^{(3)}$	Ω_{ε_1}	Ω_{ε_2}	Ω_{ε_3}
$\mathcal{C}_{23}$	3	0.02	0.3	0.6	0.2	0.2	0.2	[0.025,0.075]	[0.025,0.075]	[0.05,0.1]
$\mathcal{C}_{24}$	3	0.02	0.3	0.6	0.2	0.2	0.2	[0.05,0.1]	[0.025,0.075]	[0.025,0.075]
$\mathcal{C}_{25}$	3	0.02	0.3	0.6	0.2	0.2	0.2	[0.05,0.1]	[0.05,0.1]	[0.05,0.1]

Table 5.3: MIMO configurations for $n_p = 3$.

reference sets Ω_{ε_i} are varied. In particular: $\mathcal{C}_{23}$ has lower reference sets $\Omega_{\varepsilon_1} = \Omega_{\varepsilon_2} = [0.025, 0.075]$ for the first two outputs, corresponding to the sensors that are located further upstream, and a higher reference set $\Omega_{\varepsilon_3} = [0.05, 0.1]$ for the last output, which corresponds to the sensor that is located further downstream; $\mathcal{C}_{24}$ has a higher reference set $\Omega_{\varepsilon_1} = [0.05, 0.1]$ for the first output, and lower reference sets $\Omega_{\varepsilon_2} = \Omega_{\varepsilon_3} = [0.025, 0.075]$ for the last two outputs; $\mathcal{C}_{25}$ has the same reference sets for the three outputs $\Omega_{\varepsilon_1} = \Omega_{\varepsilon_2} = \Omega_{\varepsilon_3} = [0.05, 0.1]$.

The time histories (solid lines) of the drag and lift coefficients are compared with the corresponding time histories (dashed green) and time averaged coefficients (dashed black) for the simulations without actuators (see figures 5.27,5.28). As explained above, when the angle of attack is decreased, C_D becomes negative during the transients because it includes the actuators' contribution.

It is worth to notice that the time history of the control input $v_1(t)$ exhibits a very similar behaviour in all the configurations having the same parameters relative to the first pair, *i. e.*, $\bar{x}_a^{(1)}$, $\Delta_s^{(1)}$ and Ω_{ε_1}, despite the different parameters relative to the other pairs. This can be noted, for instance, in figure 5.30, thus justifying Assumption 4. Configuration $\mathcal{C}_{23}$ shows poor dynamic performance with a high overshoot for the second input (see figures 5.29, 5.30). This behaviour could be improved using a non-zero anti-windup term, *i. e.*, $\mu_2 \neq 0$, but the corresponding simulations are not reported here, since it is out of the scope of this work.

Figure 5.27: Drag and lift coefficients of the configurations $\mathcal{C}_j$, $j = 23, 24, 25$ in the scenario $\beta(t) = \beta_1(t)$ with (solid lines) and without actuation (dashed lines, green for time histories and black for time-averaged). The variation of β occurs between $t = 30$ and $t = 35$, from $15°$ to $5°$, and between $t = 45$ and $t = 50$, from $5°$ to $15°$.

Figure 5.31 shows a comparison between the different configurations with $n_p = 3$ actuator/sensor pairs. As in the case with two actuator/sensor pairs, the configuration $\mathcal{C}_{24}$ with an increased output reference for the upstream sensor achieves the best overall performance.
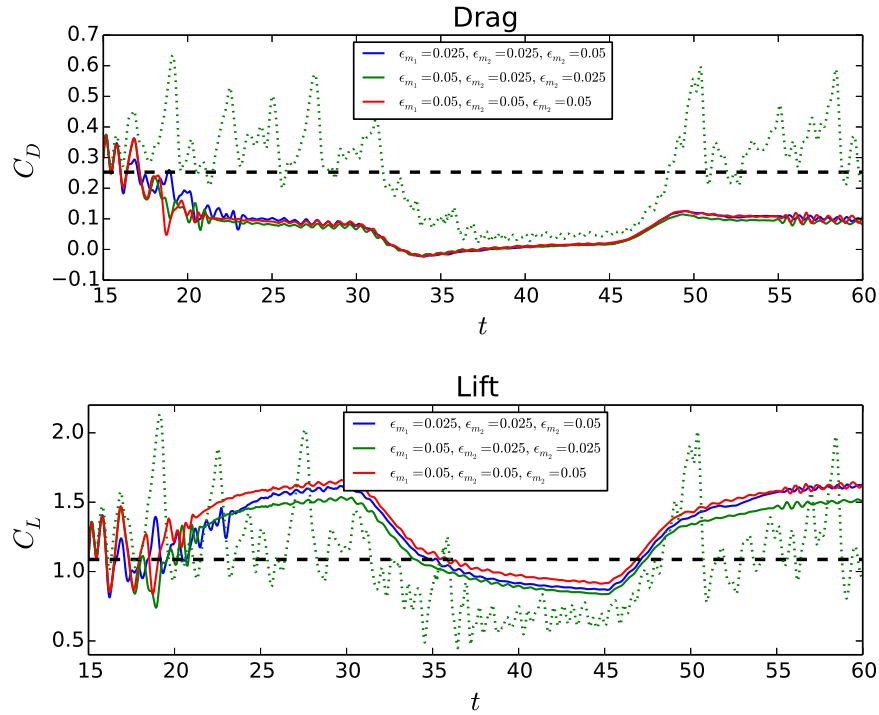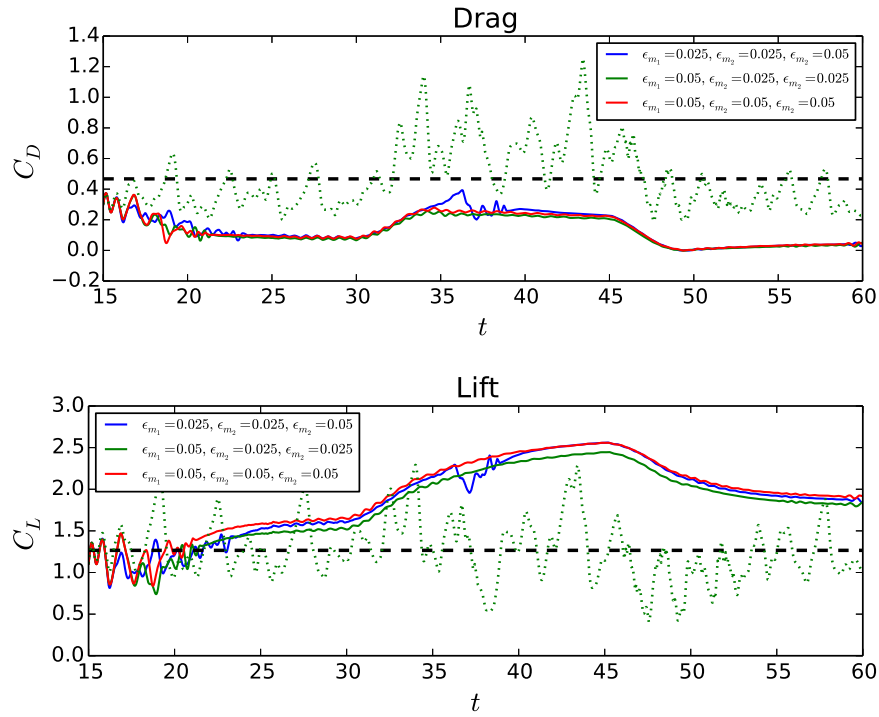
Figure 5.28: Drag and lift coefficients of the configurations $\mathcal{C}_j$, $j = 23, 24, 25$ in the scenario $\beta(t) = \beta_2(t)$ with (solid lines) and without actuation (dashed lines, green for time histories and black for time-averaged). The variation of β occurs between $t = 30$ and $t = 35$,from $15°$ to $25°$, and between $t = 45$ and $t = 50$, from $25°$ to $15°$.

Figure 5.29: MIMO simulation results for $\mathcal{C}_j$, $j = 23, 24, 25$ in the scenario $\beta(t) = \beta_1(t)$: controlled inputs (left) and output errors (right). The variation of β occurs between $t = 30$ and $t = 35$,from $15°$ to $5°$, and between $t = 45$ and $t = 50$, from $5°$ to $15°$.

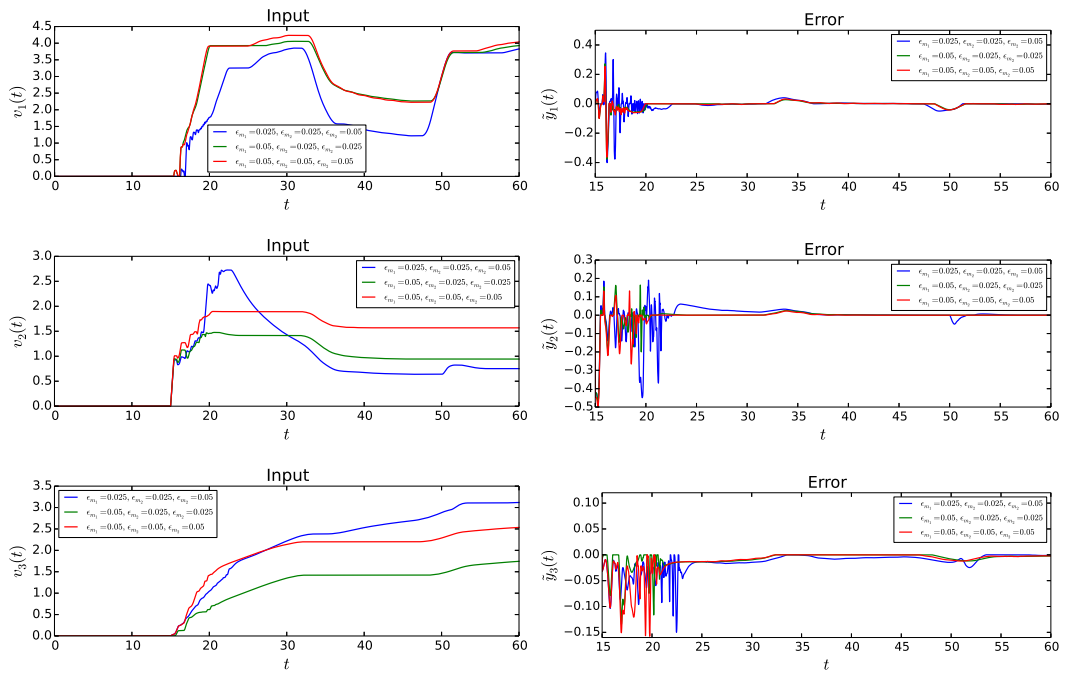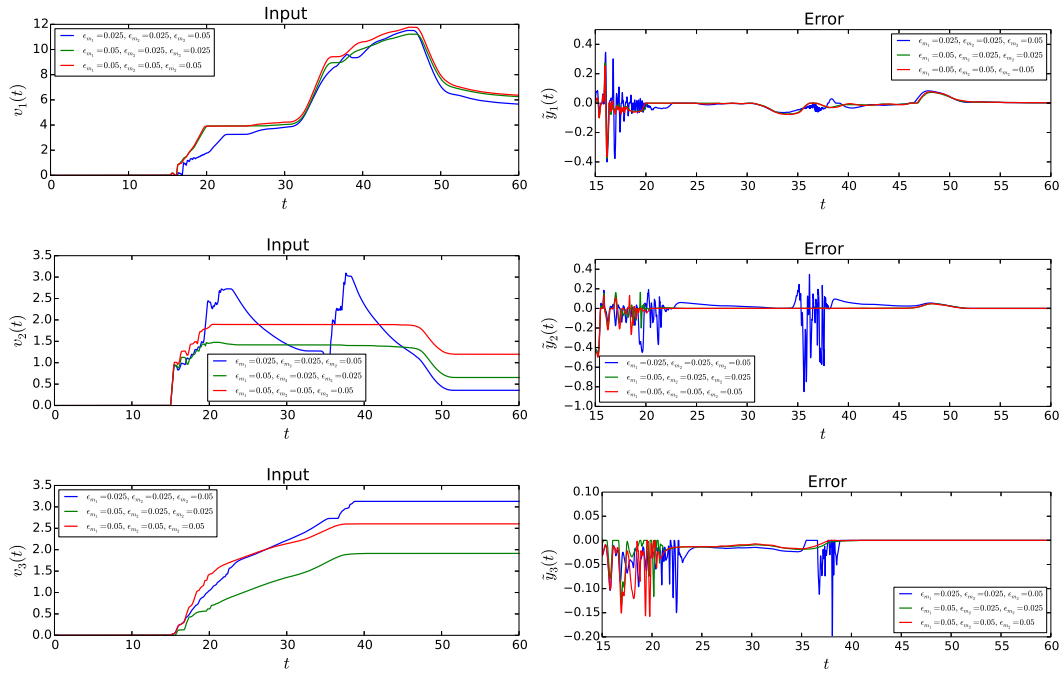Figure 5.30: MIMO simulation results for $\mathcal{C}_j$, $j = 23, 24, 25$ in the scenario $\beta(t) = \beta_2(t)$: controlled inputs (left) and output errors (right). The variation of β occurs between $t = 30$ and $t = 35$, from $15°$ to $25°$, and between $t = 45$ and $t = 50$, from $25°$ to $15°$.
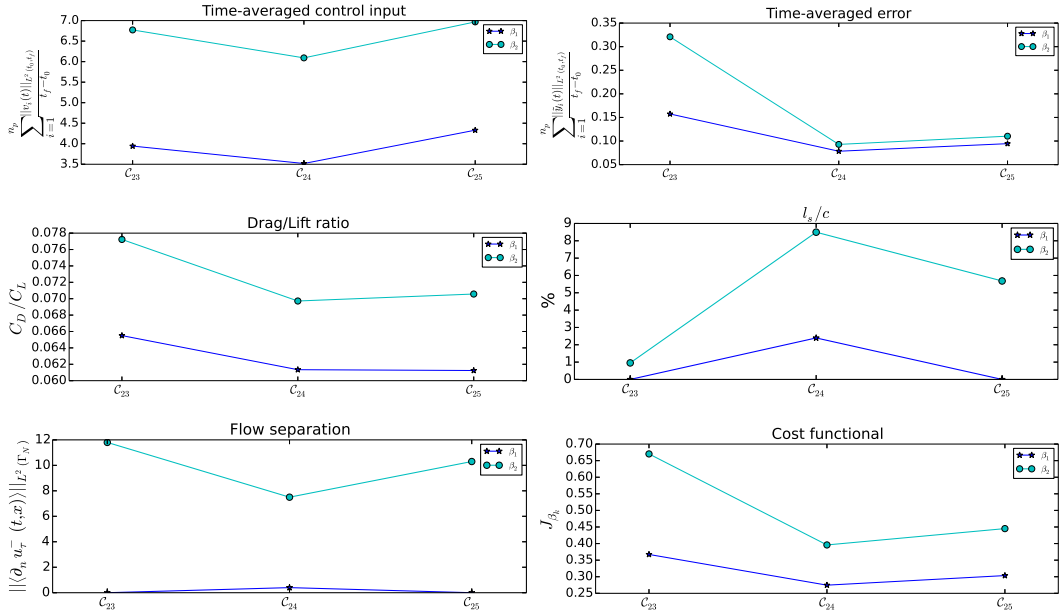

Figure 5.31: Comparison of the MIMO simulation results for $\mathcal{C}_j$, $j = 23, 24, 25$.

5.5.4 Optimal Configuration

The results in sections 5.5.1, 5.5.2 and 5.5.3 show the variation of the performance of the closed-loop system with respect to the chosen configuration. In particular: *i)* the steady-state gains $P_{ii}(0) > 0$ decrease with both the distance $\Delta_s^{(i)}$ between the sensors and the actuators and the location $(\bar{x}_a^{(i)}, \bar{x}_s^{(i)})$ of the pairs, with respect to the chord length; *ii)* the further upstream a pair is placed, the better dynamic performance is obtained, *i.e.*, the faster the regulation error converges to zero; *iii)* the robustness of the control system with respect to the variation of the angle of attack increases with the references ε_{m_i}, for fixed sensors' positions $\bar{x}_s^{(i)}$, and *vice versa*; *iv)* the ratio C_D/C_L between the drag and the lift coefficient increases with the number of pairs n_p. In particular, $\mathcal{C}_5$, $\mathcal{C}_{18}$, $\mathcal{C}_{24}$, minimise $J(\mathcal{C}_j)$ for $n_p = 1$, $n_p = 2$, $n_p = 3$, respectively. An optimal configuration $\mathcal{C}^* = \mathcal{C}_{18}$ can be thus identified, whose performance are shown in figures 5.33, 5.34, 5.35.

The total cost functional (5.36) is shown in figure 5.32 and allows for a formal comparison of the performance for the 25 tested configurations. The time histories (blue) and time average (dashed cyan) of the drag and lift coefficients are compared (top figures) with the corresponding time histories (green) and time average (dashed red) coefficients for the simulations with no actuation in figures 5.33, 5.34 for the scenarios $\beta_1(t)$ and $\beta_2(t)$, respectively: a significant reduction of the drag coefficient, along with a significant increase of the lift coefficient, is robustly achieved in the presence of the time-varying angle of attack, during both the transient and the steady-state regimes. In particular, a 75% average drag reduction, for both $\beta_1(t)$ and $\beta_2(t)$, along with a 20%, for $\beta_1(t)$ and 50%, for $\beta_2(t)$, average lift increase is obtained. The inputs show smooth, fast transient performances (solid cyan lines in figures 5.15, 5.24) and the output measurements are robustly regulated to their corresponding reference region, which is shown with a dashed cyan line in figures 5.33, 5.34. The regulation of the outputs $\mathrm{y}_i(t)$ to Ω_{ε_i} implies the solution of the flow separation problem along the whole aerofoil, as it is shown in figure 5.35, which depicts the time-averaged tangential velocity at the first cell centre above the aerofoil.

The vorticity contours in the stationary regimes, with angle of attack 5°, 15° and 25°, are shown in figure 5.36; 101 non-dimensional vorticity levels over the range $[-15, 15]$, results both with and without the actuation are reported for comparison purposes. Some discontinuities might be visible in the vorticity field, which are due to graphical issues in visualising the gradients at the intersection between
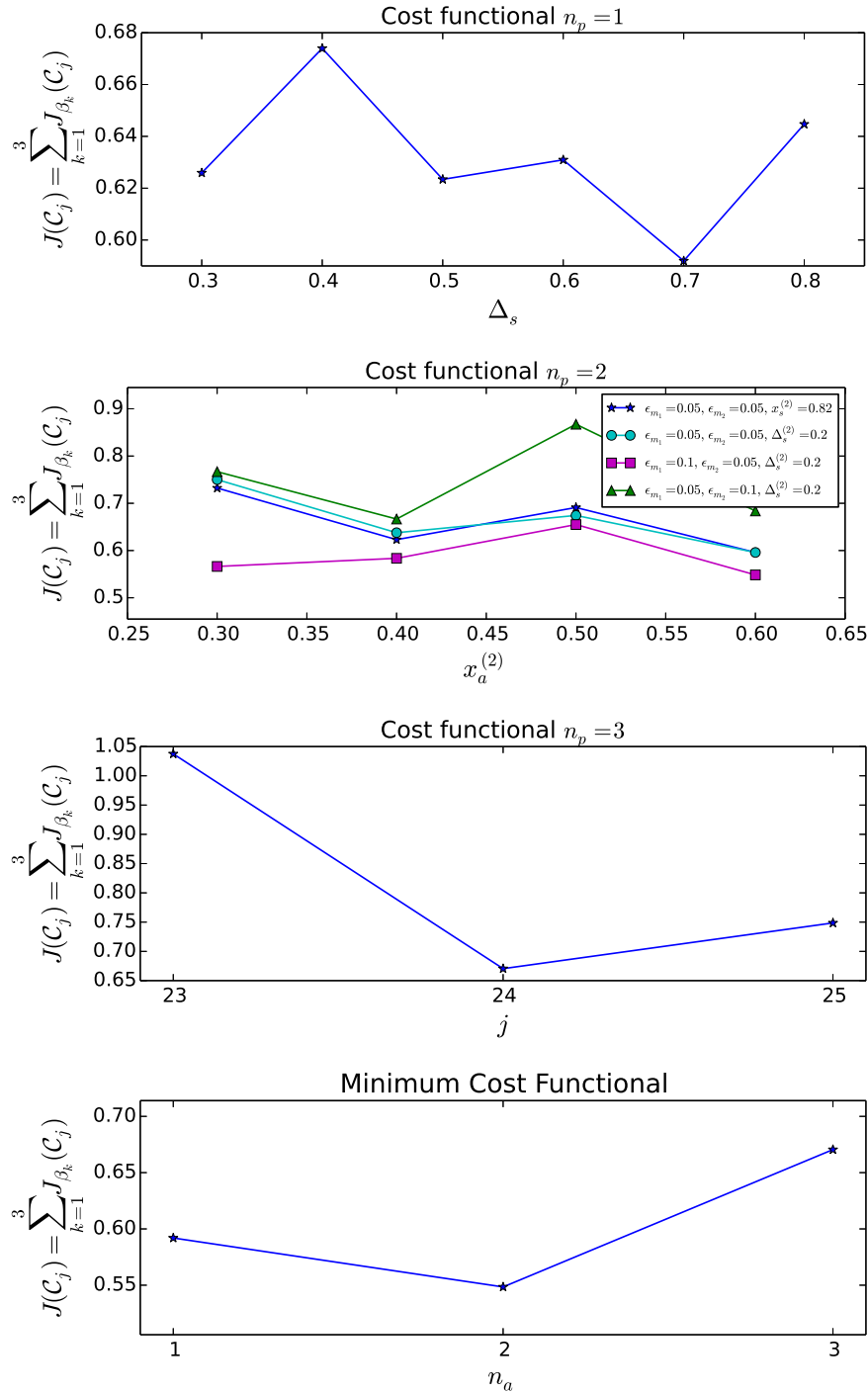
Figure 5.32: Comparison of the all simulation results: from top to bottom, total cost functional $J(\mathcal{C}_j)$ for $j = 1, ..., 6$, $j = 7, ..., 22$, $j = 23, ..., 25$ and $j = 6, 22, 24$ in the two scenario $\beta(t) = \beta_k(t)$, $k = 1, 2$.

two grid sets. Without the actuation, strong vortex structures are generated as a consequence of both the strong adverse pressure gradients and the boundary
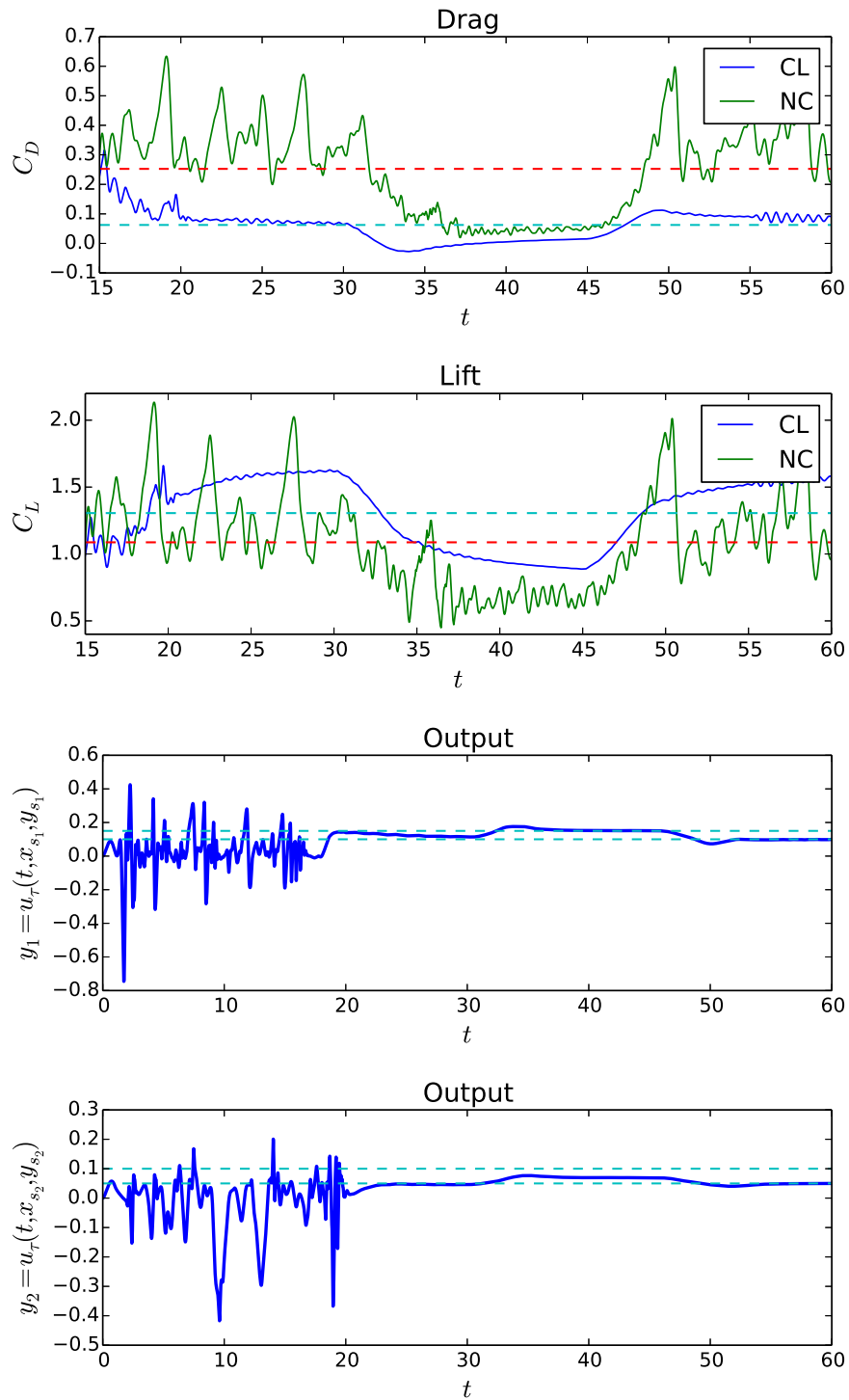
Figure 5.33: Simulation results for $\mathcal{C}^* = \mathcal{C}_{18}$ in the scenario $\beta(t) = \beta_1(t)$: time histories (solid lines, blue for closed-loop and green for not controlled scenarios) and time-average (dashed lines, cyan for closed-loop and red for not controlled scenarios) of drag and lift coefficients (top); controlled outputs (bottom).

Figure 5.34: Simulation results for $\mathcal{C}^* = \mathcal{C}_{18}$ in the scenario $\beta(t) = \beta_2(t)$: time histories (solid lines, blue for closed-loop and green for not controlled scenarios) and time-average (dashed lines, cyan for closed-loop and red for not controlled scenarios) of drag and lift coefficients (top); controlled outputs (bottom).
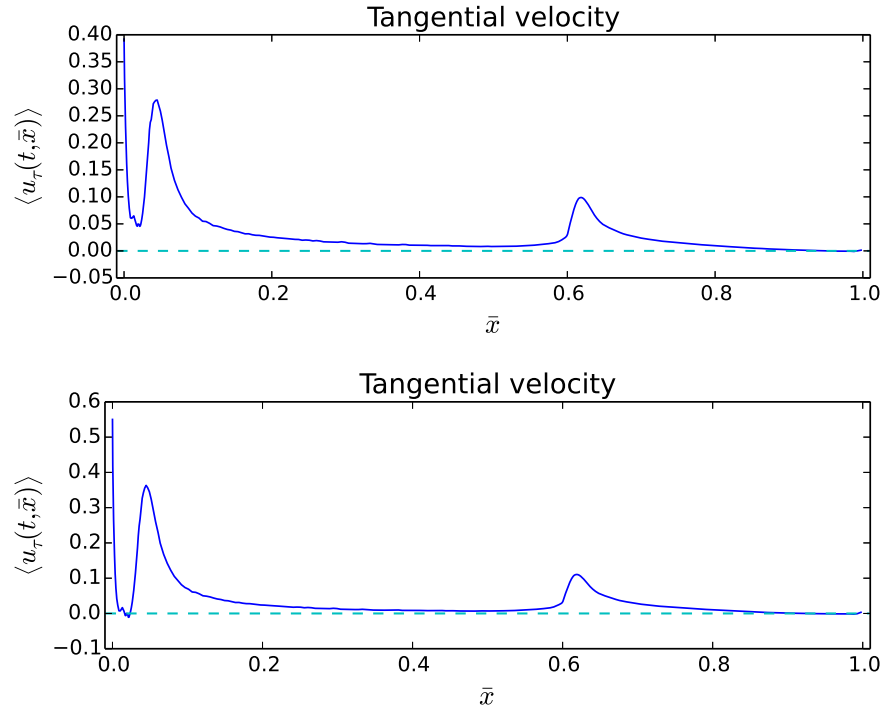
Figure 5.35: Time-averaged tangential velocity for $\mathcal{C}^* = \mathcal{C}_{18}$ in the scenario $\beta(t) = \beta_1(t)$ (top) and $\beta(t) = \beta_2(t)$ (bottom).
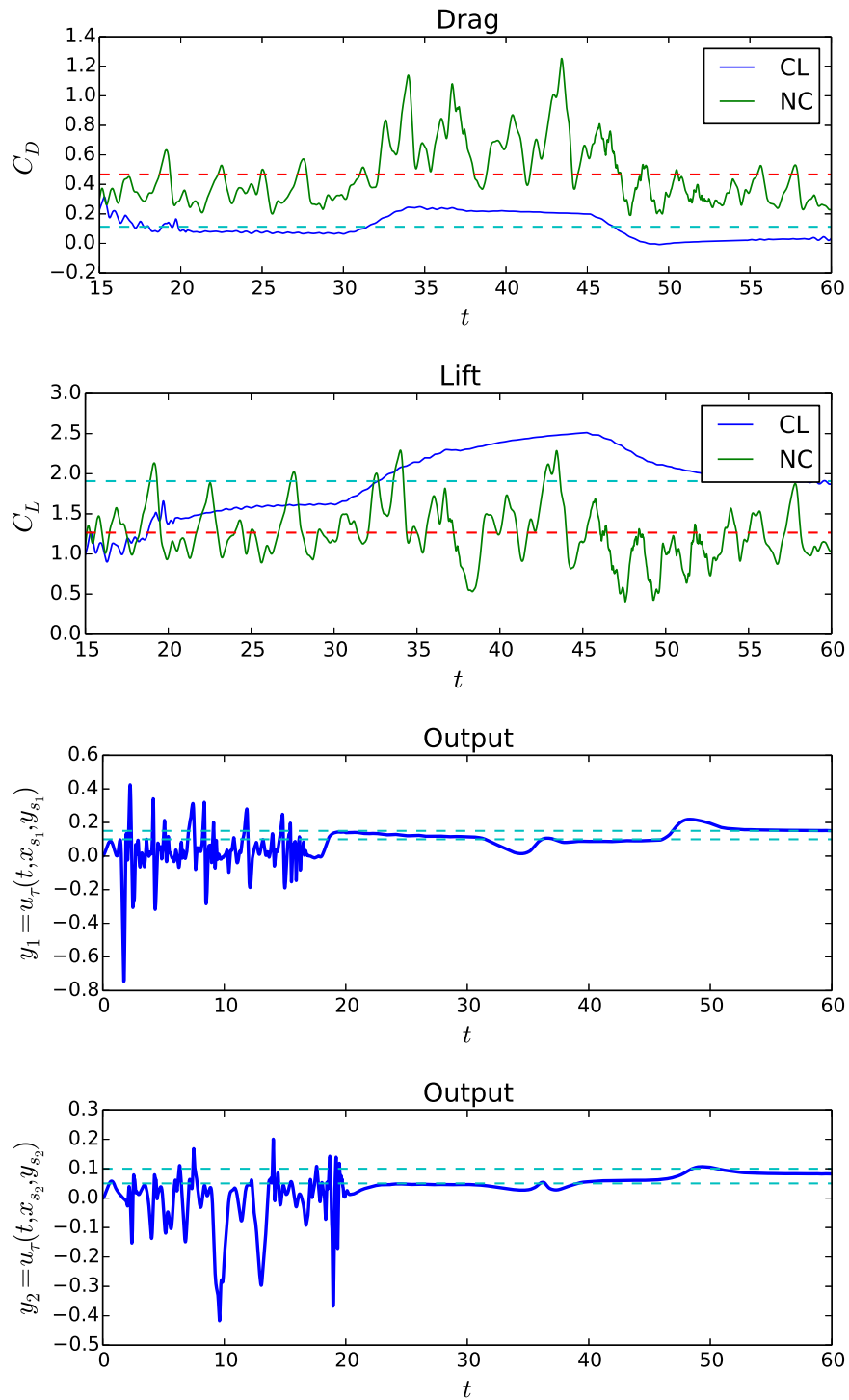
layer separation, which occurs on the upper side of the profile; as expected, larger vortices are shed at larger angle of attack. The activation of the control on the NACA profile suppresses the boundary layer separation and avoids the generation of any vortical structure. An inception of wake instability can be observed in the far wake. A detailed view of the instantaneous streamlines in the region close to the NACA profile is shown in figure 5.37, both cases with and without actuation are reported for comparison. Clearly, the control effectively suppressed the separation bubble, as well as the shedding vortices.

The most critical transients, from 5° to 15° and from 15° to 25°, are shown in figure 5.38 for the scenarios $\beta_1(t)$ and $\beta_2(t)$, respectively. The time instants, at which these snapshots are taken, are highlighted by the blue dots in figure 5.2. The pictures clearly show how the proposed control is able to efficiently suppress any occurrence of boundary layer separation even during transient regimes, denoting both robustness and good dynamic performance.

Figure 5.36: Instantaneous vorticity contours for $\mathcal{C}^* = \mathcal{C}_{18}$ using 101 levels over the range $[-15, 15]$ without (left) and with (right) closed-loop control for: $\beta = 5°$ (top); $\beta = 15°$ (middle); $\beta = 25°$ (bottom).

5.6 Simulation Results: χnavis, 3D case

In this section, the proposed multivariable control algorithm (5.13), (5.14) is tested in 3D configurations, in order to show its ability to control 3D separated turbulent flows. The simulations are performed using the in-house solver χnavis, described in Chapter 3. For the three dimensional test case, a fixed angle of attack $\beta = 5°$ is considered. The wing is modelled with infinite span by using periodic boundary conditions. The two-dimensional actuator grids and the fine C-type inner grid around the profile have been extended in the spanwise direction using 64 uniformly distributed grid volumes, for the coarse grid, and 128 uniformly distributed grid volumes, for the fine grid; the 2D outer grids have been extended in the spanwise direction using half the grid volumes of the inner grid, *i.e.* 32 uniformly distributed grid volumes, for the coarse grid, and 64 uniformly distributed grid volumes, for the fine grid; the spanwise length is 0.2. Both the spanwise dimension and discretisation are similar to those found in the literature (see, for example, Jones et al., 2008; Riherd and Roy, 2013; Sato et al., 2015b).
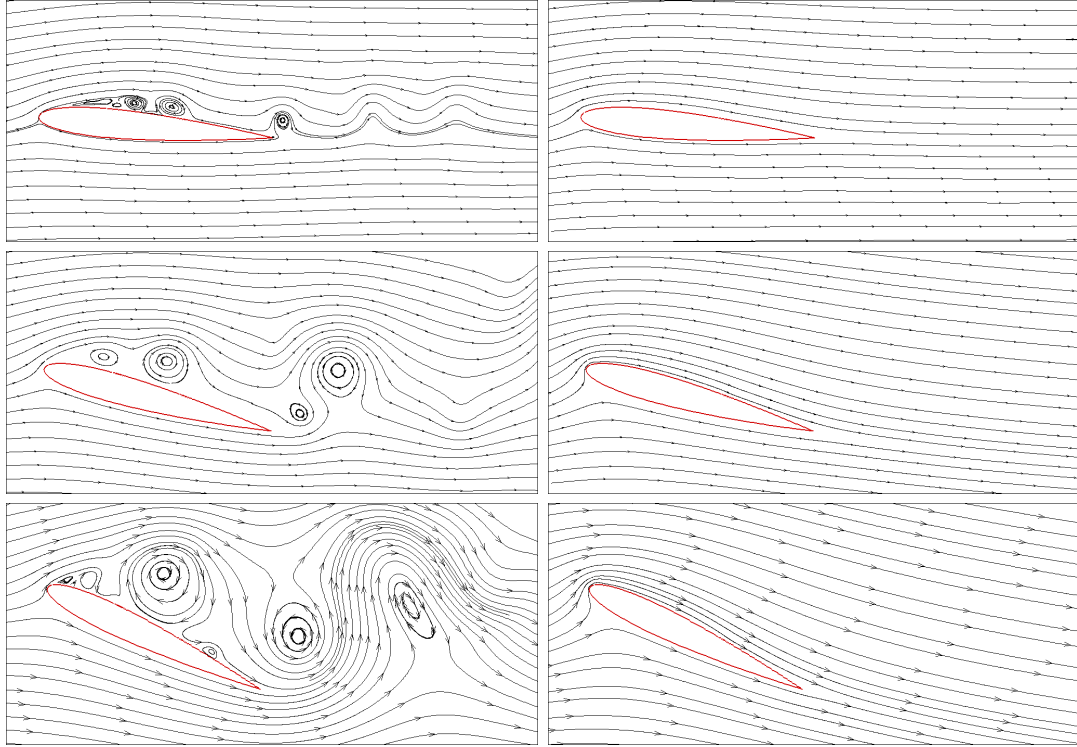
Figure 5.37: Instantaneous streamlines for $\mathcal{C}^* = \mathcal{C}_{18}$ without (left) and with (right) closed-loop control for: $\beta = 5°$ (top); $\beta = 15°$ (middle); $\beta = 25°$ (bottom).

Accurate Large Eddy Simulations (LES) at $Re = 20,000$ are performed using the well-established Sub-Grid Scale (SGS) Smagorinsky turbulence model (Akin et al., 2003; Smagorinsky, 1963; Toda et al., 2015), which has been chosen because of its simplicity. This model is based on the decomposition of the stress tensor in three terms, accounting for the large scale contribution of the filtered field, the mixed stress (pairing between filtered and unfiltered scales) and the Reynolds stress. This latter tensor is modelled as directly proportional to the strain rate tensor of the filtered field. In particular, the Navier-Stokes equations are filtered through a convolution with a filter function $f : \mathbb{R} \times \mathbb{R}^3 \to \mathbb{R}$ with the following properties:

1. is of C^∞ class;

2. decays exponentially at infinity;
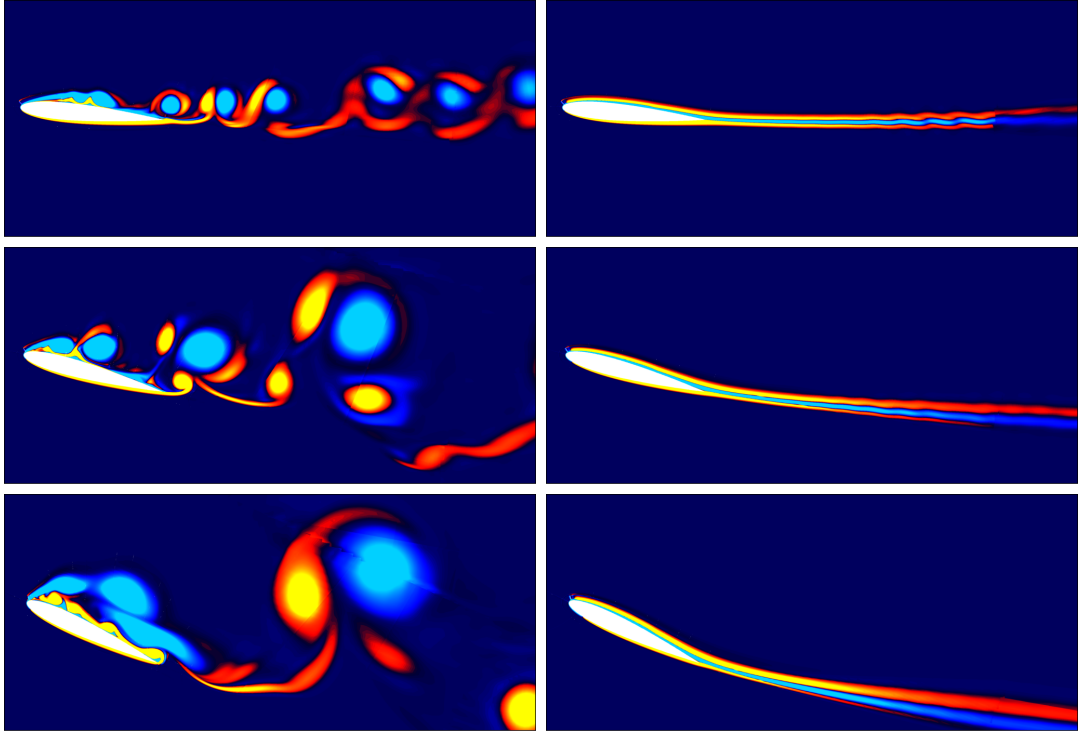
3. has unitary integral on $\mathbb{R} \times \mathbb{R}^3$.
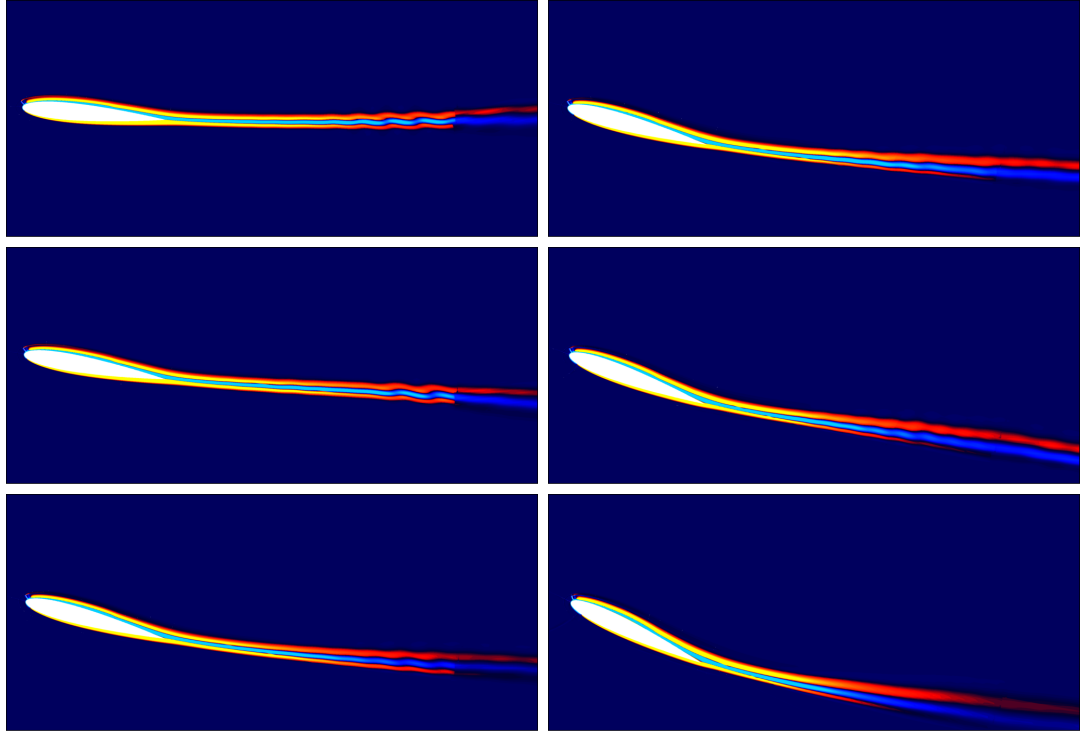
Figure 5.38: Instantaneous vorticity contours for $\mathcal{C}^* = \mathcal{C}_{18}$ using 101 levels over the range $[-15, 15]$. $\beta(t) = \beta_1(t)$ (left column): $t = 45$ (top), $t = 47.5$ (middle) and $t = 50$ (bottom). $\beta(t) = \beta_2(t)$ (right column): $t = 30$ (top), $t = 32.5$ (middle) and $t = 35$ (bottom).

Let δ_s and δ_t be the spatial and temporal amplitudes, respectively. The filter is defined as:

$$\mathcal{H}_f[g](\boldsymbol{x}, t) = \frac{1}{\delta_s^3 \delta_t} \int_{\mathbb{R}^3} d\boldsymbol{y} \int_{-\infty}^{+\infty} d\tau \ f(\frac{t - \tau}{\delta_t}, \frac{\boldsymbol{x} - \boldsymbol{y}}{\delta_s}) \ g(\tau, \boldsymbol{y}) \qquad (5.45)$$

By indicating with an overline the filtered fields, the unfiltered small scale quantities $\boldsymbol{u}' = \boldsymbol{u} - \overline{\boldsymbol{u}}$ can be defined, where $\boldsymbol{u}$ is the unfiltered velocity field vector. For an incompressible fluid, the filtered velocity remains solenoidal, $i.\ e.$:

$$\boldsymbol{\nabla} \cdot \overline{\boldsymbol{u}} = 0 \qquad (5.46)$$

implying that the non filtered velocity field $\boldsymbol{u}'$ is solenoidal too. The problem in the filtering operation is the treatment of the diadic product $\boldsymbol{u}\boldsymbol{u}$, coming from the convective term. The filtering returns:

$$\overline{u_i u_j} = \overline{u}_i \overline{u}_j + \tau'' \qquad (5.47)$$

for $i, j = 1, 2, 3$. The filtered components $\overline{u}_i$ are directly known by the motion equation integration, while the tensor τ'' reads:

$$\tau''_{ij} = (\overline{\overline{u}_i \overline{u}_j} - \overline{u}_i \overline{u}_j) + (\overline{u'_i \overline{u}_j} + \overline{\overline{u}_i u'_j}) + \overline{u'_i u'_j} \tag{5.48}$$

At the right-hand side, the first term represents the large (filtered) scales contribution, the second is the mixed stress, which represents the pairing between the large and small (unfiltered) scales, and the last one is the SGS term, called Reynolds stress. The Smagorinsky model assumes that the entire tensor $\boldsymbol{\tau}''$ without its trace is proportional to the strain rate tensor $\overline{\boldsymbol{S}}$ as:

$$\boldsymbol{\tau}'' - \mathrm{tr}(\boldsymbol{\tau}'')\boldsymbol{I}/3 = \nu'' \, \overline{\boldsymbol{S}} \tag{5.49}$$

where $\overline{S}_{ij} = (\partial_j \overline{u}_i + \partial_i \overline{u}_j)/2$ depends only on the filtered velocity field and

$$\nu'' = (C_s \Delta)^2 |\boldsymbol{S}|$$

where Δ is a characteristic length depending on the grid resolution, while C_s is the Smagorinsky constant which needs an ad-hoc calibration (in the present study $C_s = 0.1$). The global effect of the Smagorinsky model is to increase the real viscosity ν of the fluid with an apparent eddy viscosity ν'' depending on the flow field. The interested Reader is referred to Smagorinsky (1963) for more details on the method.

As in the 2D case, the considered geometry is a NACA 0012 aerofoil (extruded in the spanwise direction), denoted by Γ_N, and the domain boundaries are $\partial\Omega = \Gamma_{\mathrm{in}} \cup \Gamma_0 \cup \Gamma_{\mathrm{out}} \cup \Gamma_{\mathrm{span}}$. Here, the wall boundary is $\Gamma_0 = \Gamma_N$ and Γ_{span} denotes the boundaries where the periodic conditions are applied. The inflow boundary condition on Γ_{in} is a constant velocity profile

$$\boldsymbol{g}(t, \boldsymbol{x}) \equiv \boldsymbol{U}_\infty, \tag{5.50}$$

where $\boldsymbol{U}_\infty = (1, 0, 0)$ is the non-dimensionalised inflow velocity. The three-dimensional computational grid is obtained by extending the two-dimensional one, which has been described in the previous section, in the spanwise direction. First, some preliminary tests are performed on a coarser grid, with $N = 1,212,508$ total volumes. Then, the optimal configuration $\mathcal{C}^* = \mathcal{C}_{18}$ is tested on the fine grid, with $N = 8,992,992$ total volumes.

As in the previous section, it is assumed, based on both the obtained simple linear ROM and Assumption 2, a positive sign of the steady-state gains of the transfer

function between any pair, *i.e.*, $P_{ii}(0) > 0$, $i = 1, ..., n_p$, if the sensor is close enough to the actuator, *i.e.*, the distance $\Delta_s^{(i)}$ is sufficiently small. The output measurements $y_i(t) = u_{\boldsymbol{\tau}}(t, \boldsymbol{x}_{s_i})$ are taken at $y_n = 0.0005$ above the aerofoil, which is approximately half the thickness of the boundary layer ($\approx 10^{-4}$). For the sake of simplicity, it is set $\mu_i = 0$ in all the simulations, while the control gains k_i are chosen so that Assumption 5 is satisfied.

These three-dimensional tests are performed in order to show that the extension of the proposed approach to 3D configurations is straightforward. The aim of this section is to prove the effectiveness of the designed control algorithm at controlling turbulent flows, *i.e.*, in conditions that are significantly different from those of the design stage, where a stable, linear dynamical model was assumed. The control objective is to suppress the laminar separation bubble, while avoiding the transition to turbulence.

The promotion of turbulent transition is often considered to be responsible for airflow reattachment by using non-thermal plasma discharges (see, for example, Asada and Fujii, 2010; Jukes and Choi, 2009). Jukes and Choi (2009) suggested that the promotion of laminar-to-turbulent transition in the boundary layer causes the flow separation delay. However, recent experimental studies showed how the turbulent transition is not responsible for airflow reattachment (Benard and Moreau, 2011, 2013) and a loss in the lift occurs, due to shortening of the laminar separation bubble through the promotion of turbulent transition (Mabe et al., 2009). Wind tunnel tests of flows past a NACA 0012 profile at $Re = 20,700$ showed a large decrease in lift when the turbulence level was increased (Laitone, 1997). In Bénard et al. (2009) the flow remained fully detached when a laminar-to-turbulent transition was obtained by a tripper placed at the leading edge and the control effectiveness was not affected by the presence of the turbulent boundary layer. The authors concluded that the mechanism behind the flow separation control is not related to a laminar-to-turbulent transition. On the other hand, a total separation suppression was achieved in Sato et al. (2015a) through direct momentum addition: the lift coefficient was improved not by the reattachment through turbulent transition but by the large-scale vortex shedding induced by the actuation. Benard and Moreau (2011) investigated and identified the mechanism responsible for the flow reattachment: the momentum transfer that lead to the separation suppression was shown to come from the outer flow and not from the actuator itself. The authors showed how the DBD actuator acts as a catalyser

and the control process is based on a reinforcement of the vortex shedding rather than on early turbulent transition. The above findings appear contradictory and indicate that the control mechanism remains unclear (Sato et al., 2015b).

However, a clear definition of the flow separation problem (5.1) is given in this thesis, where the control objective is to totally suppress (and not just delay) the real-time (and not the time-averaged) flow separation. This can be achieved through direct momentum addition by the plasma actuators, which directly provide positive momentum, uniformly distributed in the spanwise direction, into the boundary layer. The proposed control algorithm is, therefore, able to achieve real-time flow separation suppression. Furthermore, the ability of the controller to achieve relaminarisation of the turbulent boundary layer will be discussed in section 5.6.2. Both noise reduction and increased performance are obtained by the designed feedback approach and can be desirable, for example, for wind turbines applications. Furthermore, the proposed method can be applied to plasma actuation in burst mode in order to improve the efficiency of the separation control mechanism (Sato et al., 2015a,b).

5.6.1 Coarse Grid

Three configurations are tested: In the SISO configurations $\mathcal{C}_1^{3D}$ and $\mathcal{C}_2^{3D}$ the

Configuration	n_p	$\bar{x}_a^{(1)}$	$\bar{x}_a^{(2)}$	$\Delta_s^{(1)}$	$\Delta_s^{(2)}$	Ω_{ε_1}	Ω_{ε_2}
$\mathcal{C}_1^{3D}$	1	0.02	-	0.2	-	[0.02,0.025]	-
$\mathcal{C}_2^{3D}$	1	0.02	-	0.2	-	[0.1 ,0.15]	-
$\mathcal{C}_3^{3D}$	2	0.02	0.6	0.2	0.2	[0.1 ,0.15]	[0.05,0.1]

Table 5.4: Three-dimensional configurations.

actuator is placed at $\bar{x}_a^{(1)} = 0.02$ and the distance between the sensor and the actuator is fixed at $\Delta_s^{(1)} = 0.2$, while the reference set is varied: $\mathcal{C}_2^{3D}$ is the 3D version of the optimal solution 3 (obtained in section 4.7) depicted in figures 4.19, 4.20, which had quite a low value of $\langle v \rangle$ in the 2D case; $\mathcal{C}_1^{3D}$ has a decreased lower reference $\varepsilon_m^{(1)} = 0.02$. Configuration $\mathcal{C}_3^{3D}$ is the 3D version of the optimal MIMO configuration $\mathcal{C}^* = \mathcal{C}_{18}$, obtained in the previous section: the first actuator/sensor pair is placed as in $\mathcal{C}_1^{3D}$ and $\mathcal{C}_2^{3D}$, while a second pair is added at $\bar{x}_a^{(2)} = 0.6$ and $\Delta_s^{(2)} = 0.2$.

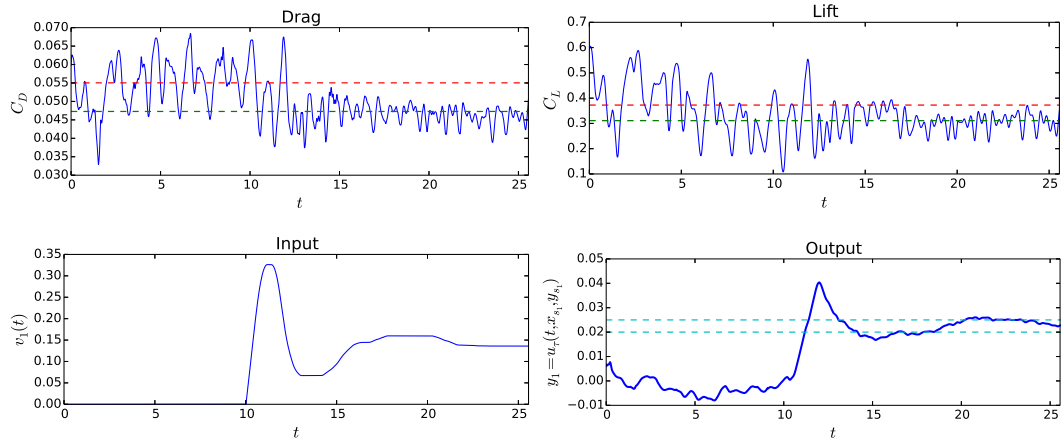The controller is activated at $t_0 = 10$. The simulation results for the three

Figure 5.39: Simulation results for $\mathcal{C}_1^{3D}$ and $\beta = 5°$, $Re = 20,000$: time history (blue solid line for closed-loop scenario) and time-average (dashed lines, green for closed-loop and red for not controlled scenarios) of drag and lift coefficients (top); control input and measured output (bottom).
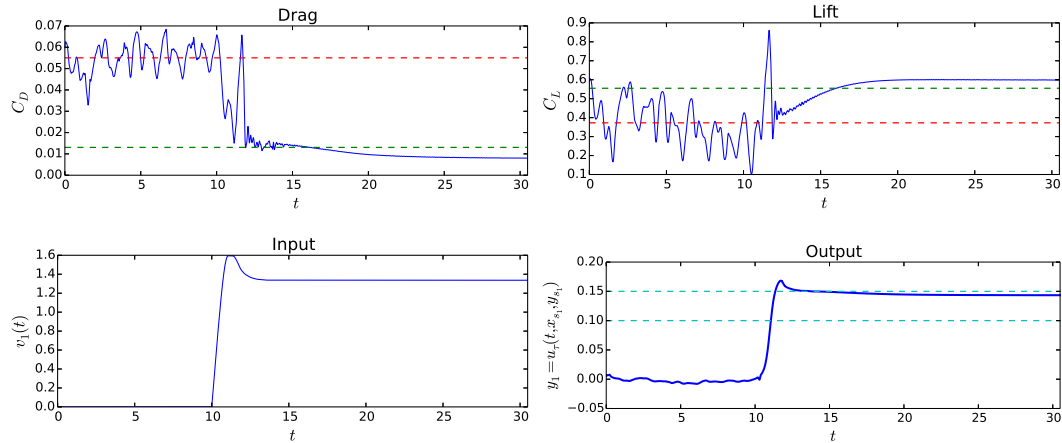
Figure 5.40: Simulation results for $\mathcal{C}_2^{3D}$ and $\beta = 5°$, $Re = 20,000$: time history (blue solid line for closed-loop scenario) and time-average (dashed lines, green for closed-loop and red for not controlled scenarios) of drag and lift coefficients (top); control input and measured output (bottom).

different configurations $\mathcal{C}_1^{3D}$, $\mathcal{C}_2^{3D}$, $\mathcal{C}_3^{3D}$ are shown in figures 5.39-5.41. The time-averaged tangential velocities, computed at half the span length, with and without control are compared in figure 5.42. In figure 5.43, the instantaneous velocity magnitude, along with the coherent structures using the λ_2 criterion (coloured by the velocity magnitude), are shown (see Jeong and Hussain, 1995, for more details
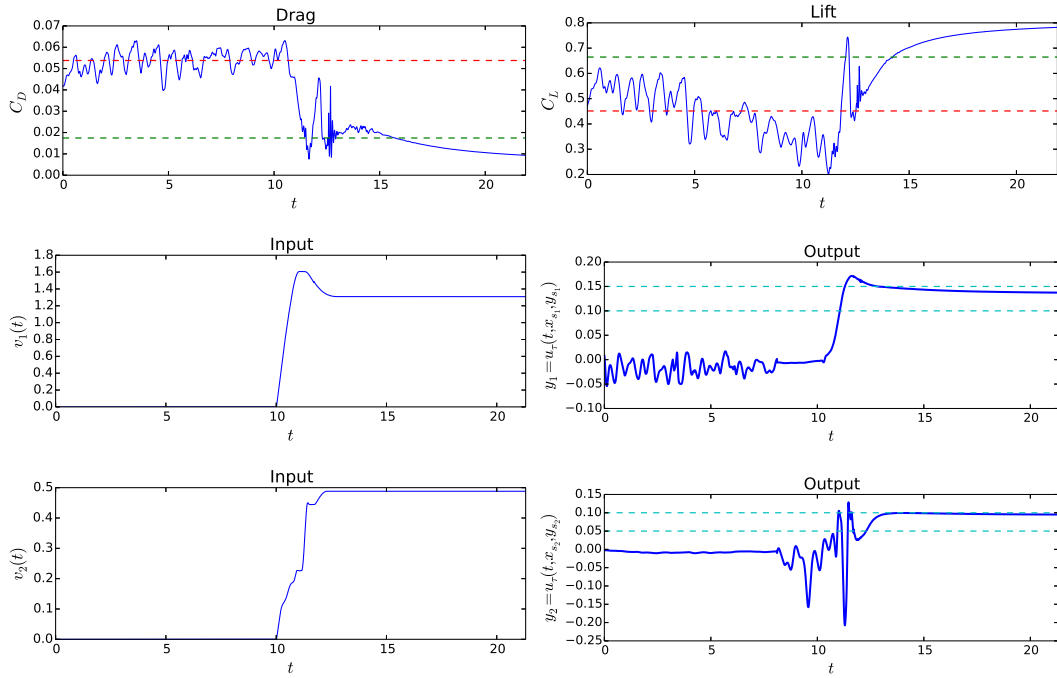
Figure 5.41: Simulation results for $\mathcal{C}_3^{3D}$ and $\beta = 5°$, $Re = 20,000$: time history (blue solid line for closed-loop scenario) and time-average (dashed lines, green for closed-loop and red for not controlled scenarios) of drag and lift coefficients (top); control input and measured output (bottom).
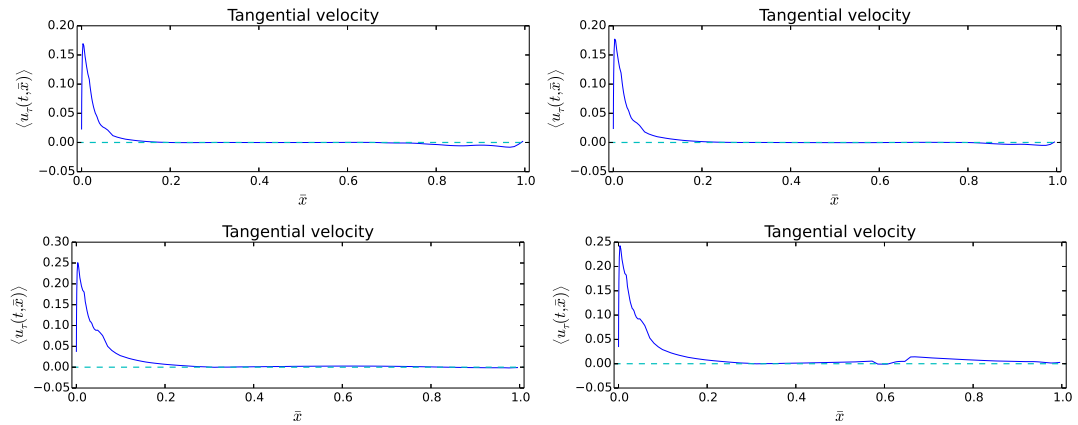

Figure 5.42: Time-averaged tangential velocity for $\beta = 5°$, $Re = 20,000$ at half the span length: without control (top left) and for $\mathcal{C}_1^{3D}$ (top right), $\mathcal{C}_2^{3D}$ (bottom left), $\mathcal{C}_3^{3D}$ (bottom right).

on the method). Figure 5.44 depicts the instantaneous spanwise vorticity field, with and without control, using 101 levels over the range $[-25, 25]$. Figure 5.45 shows the instantaneous velocity magnitude contours, with and without control,

Figure 5.43: Simulation results without control (top left) and for $\mathcal{C}_1^{3D}$ (top right), $\mathcal{C}_2^{3D}$ (bottom left), $\mathcal{C}_3^{3D}$ (bottom right): instantaneous velocity magnitude and iso-contours for $\lambda_2 = -10$, $\beta = 5°$, $Re = 20,000$.
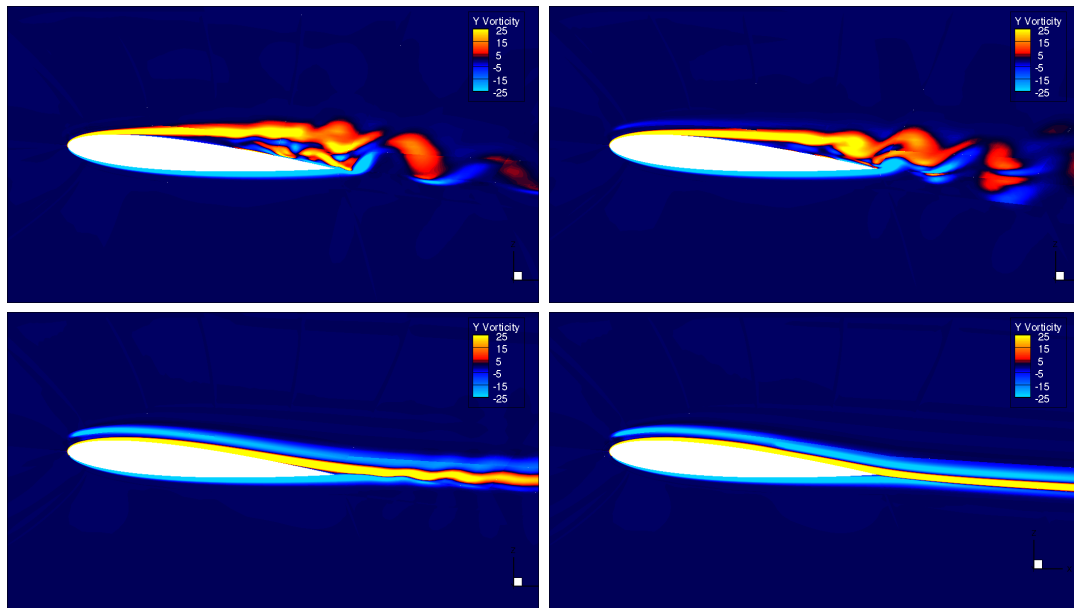
Figure 5.44: Simulation results without control (top left) and for $\mathcal{C}_1^{3D}$ (top right), $\mathcal{C}_2^{3D}$ (bottom left), $\mathcal{C}_3^{3D}$ (bottom right): instantaneous spanwise vorticity contours for $\beta = 5°$, $Re = 20,000$ using 101 levels over the range $[-25, 25]$.

using 101 levels over the range $[0, 1.3]$. The snapshots of the tangential velocity distribution along the aerofoil are depicted in figures 5.46-5.49.

The simulations correctly predict the presence of a laminar boundary layer both
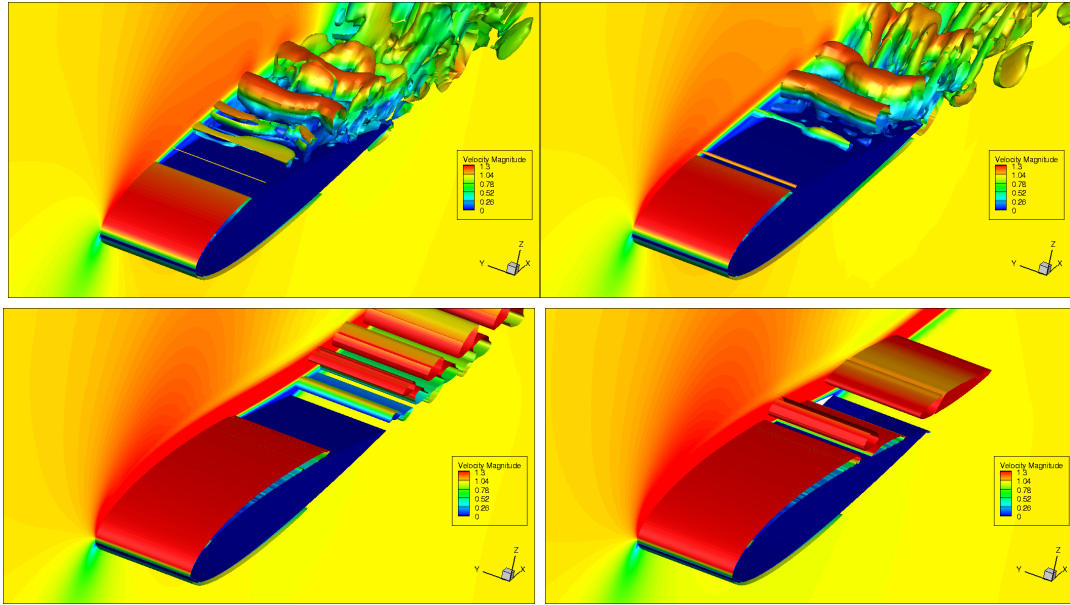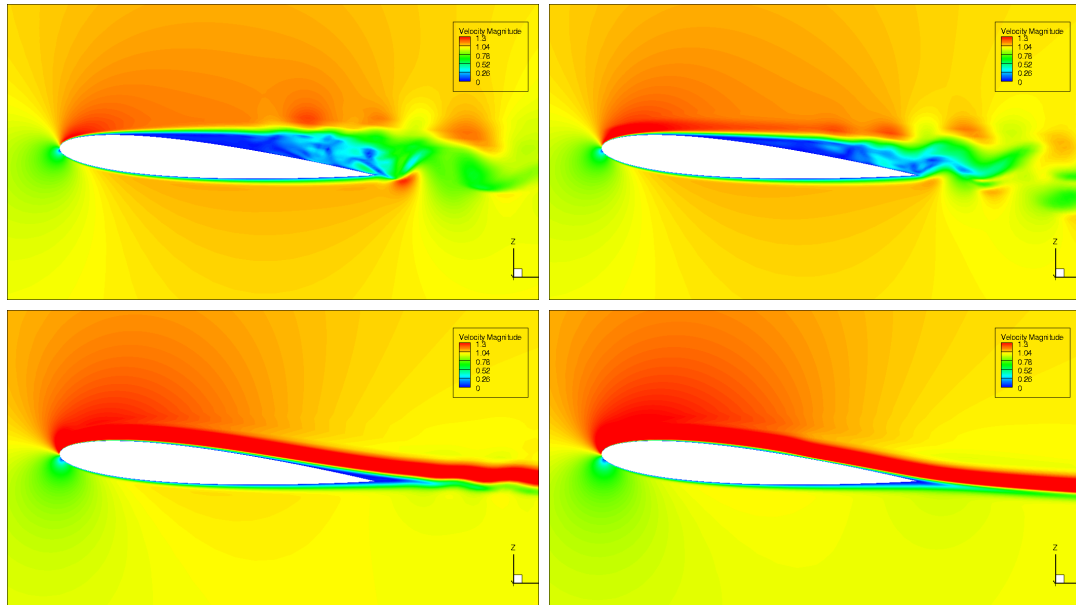
Figure 5.45: Simulation results without control (top left) and for $\mathcal{C}_1^{3D}$ (top right), $\mathcal{C}_2^{3D}$ (bottom left), $\mathcal{C}_3^{3D}$ (bottom right): instantaneous velocity magnitude contours for $\beta = 5°$, $Re = 20,000$ using 101 levels over the range $[0, 1.3]$.
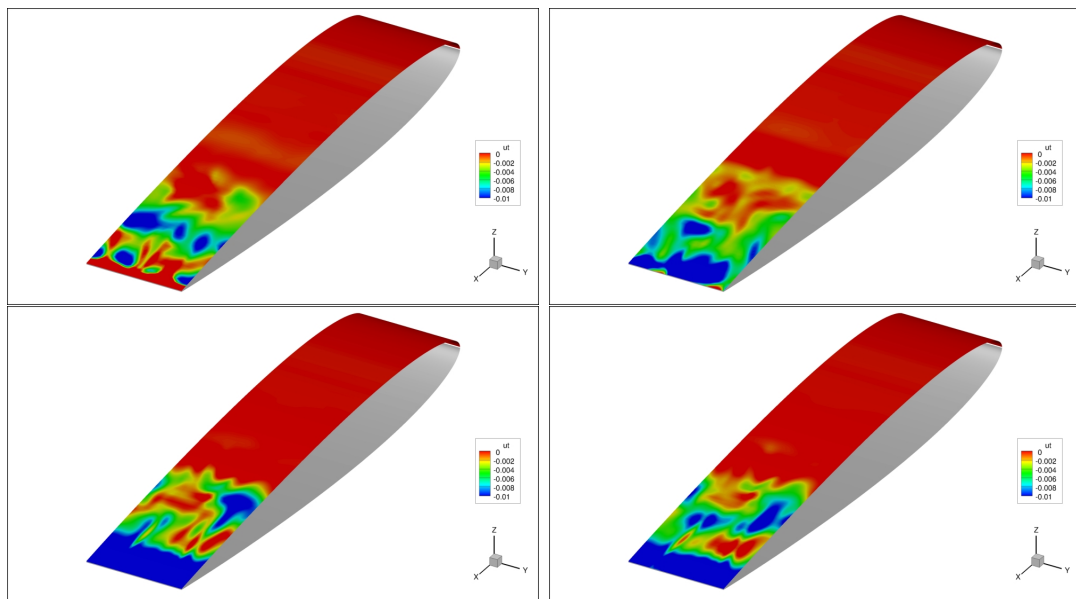
Figure 5.46: Instantaneous contours of the tangential velocity on the aerofoil for $\beta = 5°$, $Re = 20,000$ without control.

on the pressure side of the NACA profile and on the first part of the suction side. Due to the adverse pressure gradients, a laminar separation occurs on the suction side. The transition to turbulence follows, with a turbulent reattachment close to the profile trailing edge (see figure 5.46). Due to the momentum injection by the
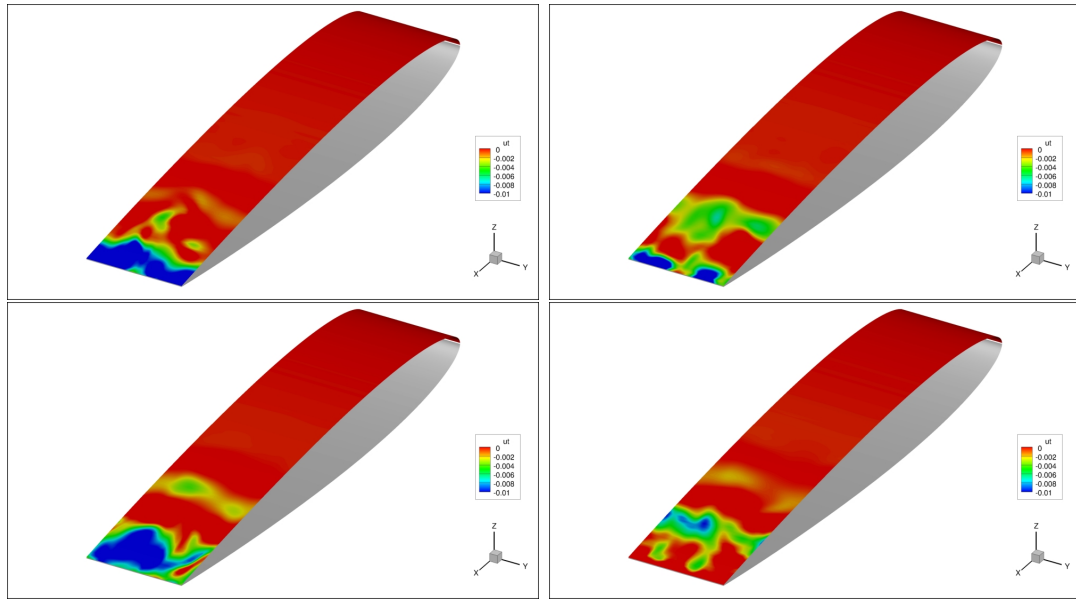
Figure 5.47: Instantaneous contours of the tangential velocity on the aerofoil for $\mathbb{C}_1^{3D}$ and $\beta = 5°$, $Re = 20,000$ during the transients (just after the controller is activated).
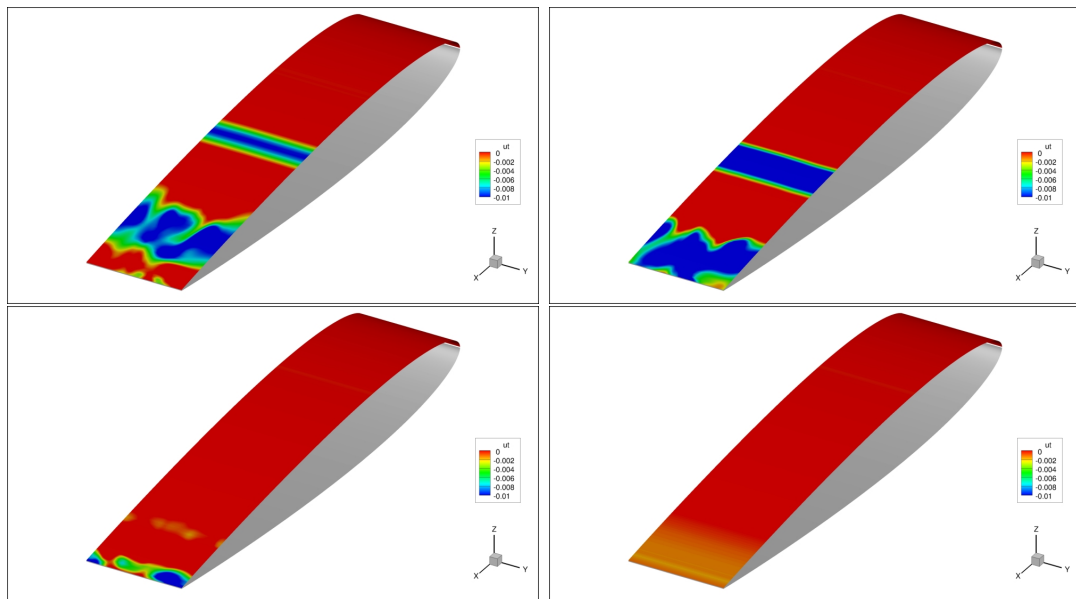
Figure 5.48: Instantaneous contours of the tangential velocity on the aerofoil for $\mathbb{C}_2^{3D}$ and $\beta = 5°$, $Re = 20,000$ during the transients (just after the controller is activated).

plasma actuators, the boundary layer transition is delayed or even suppressed by the designed controller in all the considered scenarios $\mathbb{C}_1^{3D}$, $\mathbb{C}_2^{3D}$, $\mathbb{C}_3^{3D}$.

Configuration $\mathbb{C}_1^{3D}$, which is characterised by a low reference set, is tested in or-
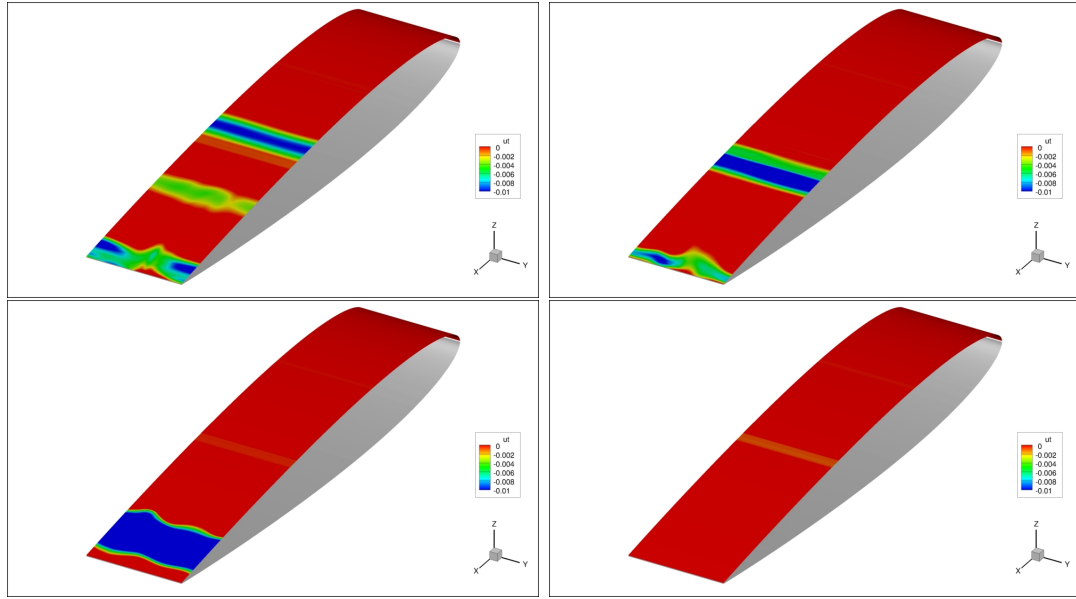
Figure 5.49: Instantaneous contours of the tangential velocity on the aerofoil for $\mathcal{C}_3^{3D}$ and $\beta = 5°$, $Re = 20,000$ during the transients (just after the controller is activated).

der to show the effectiveness of the proposed control algorithm in the presence of three-dimensional turbulent dynamics: although the required steady-state control input is very low, the drag-to-lift ratio decreases, the drag and lift coefficients are stabilised and the controlled output quickly converges to its reference region (see figure 5.39). The flow separation along the aerofoil is suppressed in the upstream region only, while the separation bubble is moved downstream (see figures 5.42, 5.47).

The time-averaged drag and lift coefficients of the uncontrolled 3D simulations at $\beta = 5°$ are very close to the 2D values (see figures 5.39, 5.40, 5.41, 5.4). As in the 2D case, configuration $\mathcal{C}_2^{3D}$ significantly reduces the boundary layer separation and avoids the generation of large vortical structures (see figures 5.43, 5.44, 5.45). A very small separation bubble is seen close to the trailing edge (see figure 5.42) and the steady-state tangential velocity distribution on the suction side of the wing is negative on less than 10% of the total surface (bottom right in figure 5.48), causing a weak wake instability (see figure 5.45). On the other hand, the required steady-state input is much lower compared to the 2D results (see figures 4.16, 5.40). This is due both to the lower angle of attack (5° in the 3D case and 15° in the 2D case) and to the greater control effort needed to suppress the laminar separation bubble, which has an increased dimension in the 2D case as shown in

Jones et al. (2008), where DNS of flows past a NACA 0012 profile at $Re = 50,000$ and $\beta = 5°$ were performed: the mean C_L in the 2D case was ≈ 0.499 while the mean lift coefficient increased to ≈ 0.62 in the 3D simulations. The controlled output quickly converges to a constant value in its reference region (see figure 5.40). Furthermore, the transition to turbulence is avoided and the flow is kept laminar by the feedback controller (see figure 5.43).

The optimal MIMO configuration $\mathcal{C}_3^{3D}$ achieves the best performance in terms of flow separation suppression: the flow is completely laminar and reattached along the wing (see figures 5.42, 5.43, 5.44, 5.45). The steady-state tangential velocity distribution on the suction side of the wing (bottom right in figure 5.49) is positive on the whole surface, except for a small region where a discontinuity is present, due to graphical issues in visualising the field at the actuator's grid boundaries. A 81% drag reduction, along with almost an 80% lift increase is obtained (see figure 5.41) in the steady-state regime, compared with the time averaged values without actuation.

These percentages are higher than the ones of the 2D case because of the lower resolution of the coarse grid, which is used in this section for the preliminary tests only. Both the controlled outputs quickly converge (in about two non-dimensional temporal units) to constant values in their corresponding reference regions (see figure 5.41). The first actuator/sensor pair shows the same dynamic behaviour of configuration $\mathcal{C}_2^{3D}$ (bottom frames in figure 5.40), thus highlighting the independence of the dynamics of the upstream pairs on those of the downstream ones, coherently with assumption 4. As for the SISO configuration $\mathcal{C}_2^{3D}$, the required steady-state input for $\mathcal{C}_3^{3D}$ is much lower compared to the results for the corresponding 2D configuration $\mathcal{C}_{18}$ (see figures 5.15, 5.41).

5.6.2 Fine Grid

The two-dimensional numerical grid has been extended in the spanwise direction using 128 uniformly distributed grid volumes; the spanwise length is 0.2. As discussed above, the 2D grid, along with both the spanwise dimension and discretisation (see Jones et al., 2008), are similar to those found in the literature (see, for example, Riherd and Roy, 2013; Sato et al., 2015b). The 3D simulations on the fine grid have been performed on the CINECA servers, thanks to an ISCRA Grant (code HP10CXD3Z9) of 200,000 computational hours.

The chosen optimal configuration $\mathcal{C}_3^{3D}$ is tested in this section. Flow control mech-

anisms resulting from a steady open-loop actuation by a single plasma actuator are presented in Benard and Moreau (2011), where the authors suggested that the addition of a second actuator located at about mid-chord should be further investigated. The results showed that the flow remains attached at the leading edge without intermittent separated regimes. Flow reattachment for up to 70% of the chord length was obtained. Downstream of this position, a moving separation point appeared, initiating a partial flow detachment at the end of the airfoil profile. It is shown in this section how the latter is avoided by the optimal closed-loop configuration $\mathcal{C}_3^{3D}$ with two actuator/sensor pairs, thus highlighting the advantage of the proposed MIMO feedback approach: the separation point is moved farther downstream by the first actuator while the second actuator, which is placed before the former, reattaches the flow up to the trailing edge. The controller is
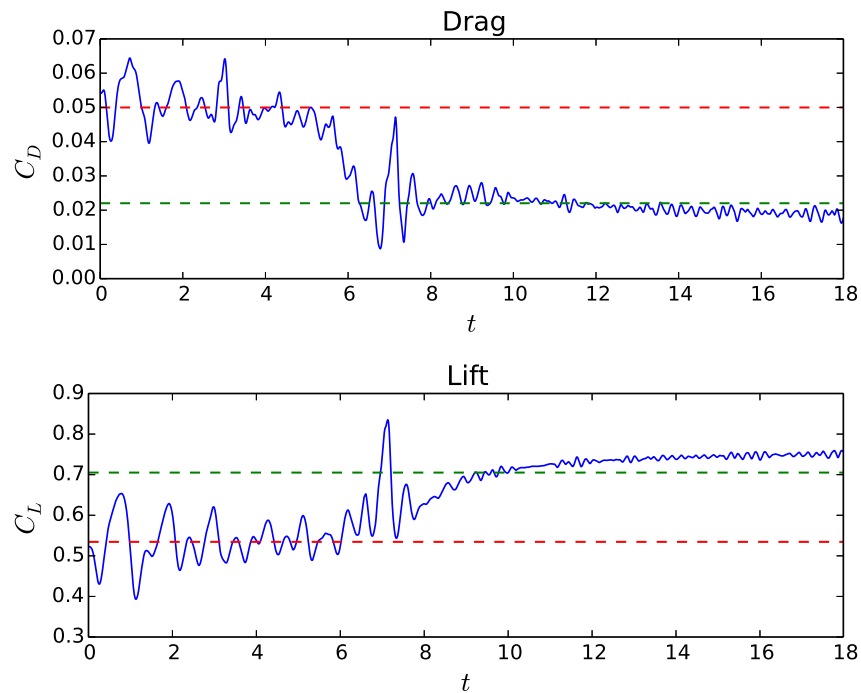
Figure 5.50: Simulation results for $\mathcal{C}_3^{3D}$, $\beta = 5°$, $Re = 20,000$: time history (blue solid line for closed-loop scenario) and time-average (dashed lines, green for closed-loop and red for not controlled scenarios) of drag and lift coefficients.

activated at $t_0 = 5.9$. The simulation results are shown in figures 5.50-5.62. The time histories (blue) of the drag and lift coefficients are shown in figure 5.50, along with the corresponding time averaged coefficients without (dashed red) and with (dashed green) control: both a significant drag reduction and lift enhancement are achieved. In particular, a 60% drag reduction, along with almost a 40% lift
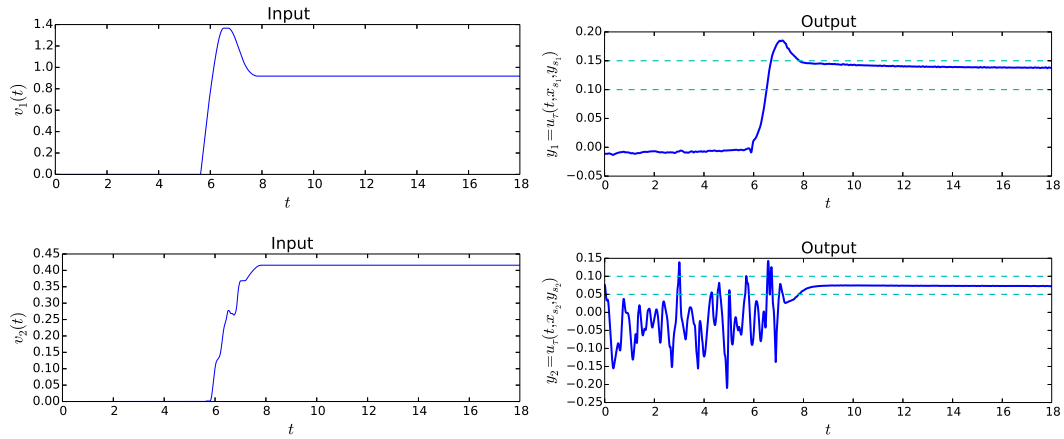
Figure 5.51: Simulation results for $\mathcal{C}_3^{3D}$ and $\beta = 5°$, $Re = 20,000$: control input (left) and measured output (right).
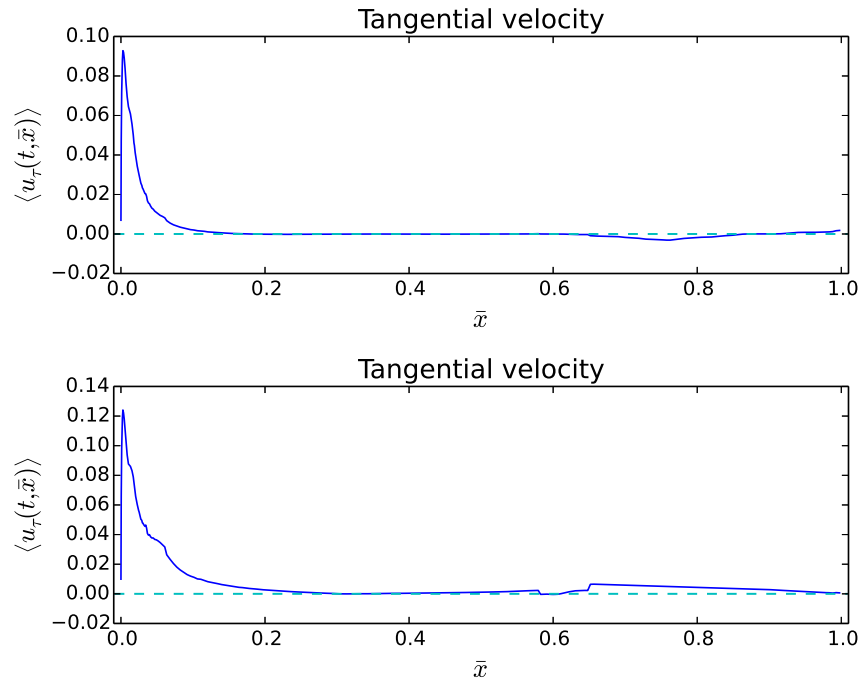
Figure 5.52: Time-averaged tangential velocity at half the span length for $\beta = 5°$, $Re = 20,000$: without control (top) and for $\mathcal{C}_3^{3D}$ (bottom).

increase is obtained (see figure 5.50) in the steady-state regime, compared with the time averaged values without actuation.

The time-averaged drag and lift coefficients without actuation are close to those obtained experimentally in Feng et al. (2015) for a NACA 0012 at $Re = 20,000$ and $\beta = 5°$. In particular, the same mean C_D around 0.05 is obtained while the mean C_L (≈ 0.5) is higher compared to the experimental results (≈ 0.4) in Feng
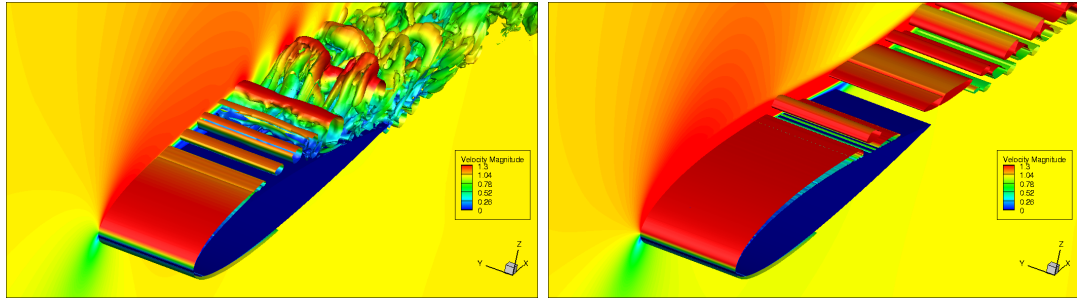
Figure 5.53: Simulation results without control (left) and for $\mathcal{C}_3^{3D}$ (right): instantaneous velocity magnitude and iso-contours for $\lambda_2 = -10$, $\beta = 5°$, $Re = 20,000$.
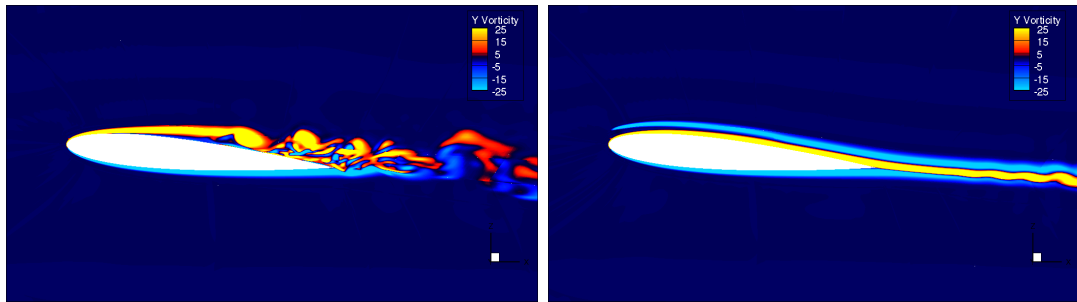
Figure 5.54: Simulation results without control (left) and for $\mathcal{C}_3^{3D}$ (right): instantaneous spanwise vorticity contours for $\beta = 5°$, $Re = 20,000$ using 101 levels over the range $[-25, 25]$.
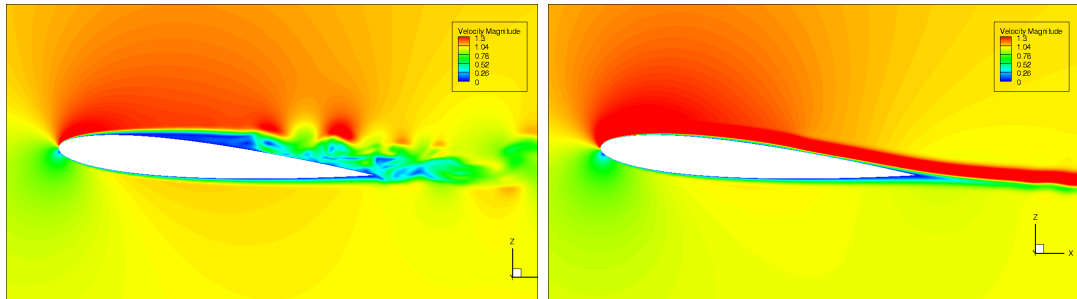
Figure 5.55: Simulation results without control (left) and for $\mathcal{C}_3^{3D}$ (right): instantaneous velocity magnitude contours for $\beta = 5°$, $Re = 20,000$ using 101 levels over the range $[0, 1.3]$.

et al. (2015) for a NACA 0012 at $Re = 20,000$ and $\beta = 5°$. One of the reasons for this difference is the presence of a 0.5% turbulence level in the wind tunnel test section in Feng et al. (2015) which is absent in the present study. Laitone (1997) showed that an increase in the turbulence level yields a consistent loss of the lift for the NACA 0012 at Reynolds number below $50,000$. In particular, at $Re = 20,700$ the NACA 0012 profile showed a large decrease in the lift coefficient (from around
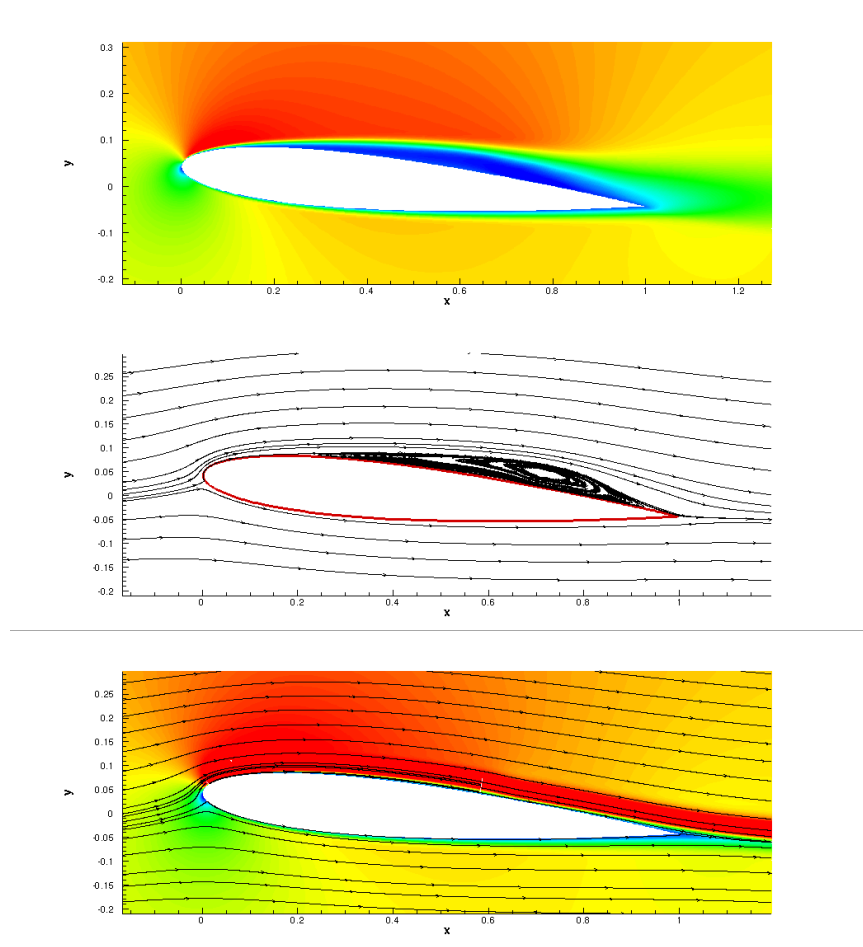
Figure 5.56: Time-averaged streamwise velocity contours using 101 levels over the range $[-0.1, 1.3]$ and time-averaged streamlines for $\beta = 5°$, $Re = 20,000$ without control (top and middle) and for $\mathcal{C}_3^{3D}$ (bottom).

0.45 to 0.2) when the turbulence level was greatly increased to correspond to that of the wind tunnel tests in Schmitz (1967), while the lift-drag ratio decreased 49% from 7.4 to 3.8. Therefore, the higher lift values of the present simulations might be caused by the lack of turbulence level due to the wind tunnel.

Furthermore, the boundary effects of the finite-span wing used in Feng et al. (2015) are neglectable in this numerical study, as suitable periodic conditions have been applied at the boundaries in order to model a wing of infinite span as in other numerical studies of boundary layer control by plasma devices (*e.g.*, Riherd and Roy, 2013; Sato et al., 2015b). The spanwise length of the wing is $0.2c$ in the present numerical study and $2.5c$ in Feng et al. (2015). The reason behind the choice of the length is the need of having a high resolution in the spanwise direction while avoiding prohibitive computational costs (as in Jones et al., 2008;
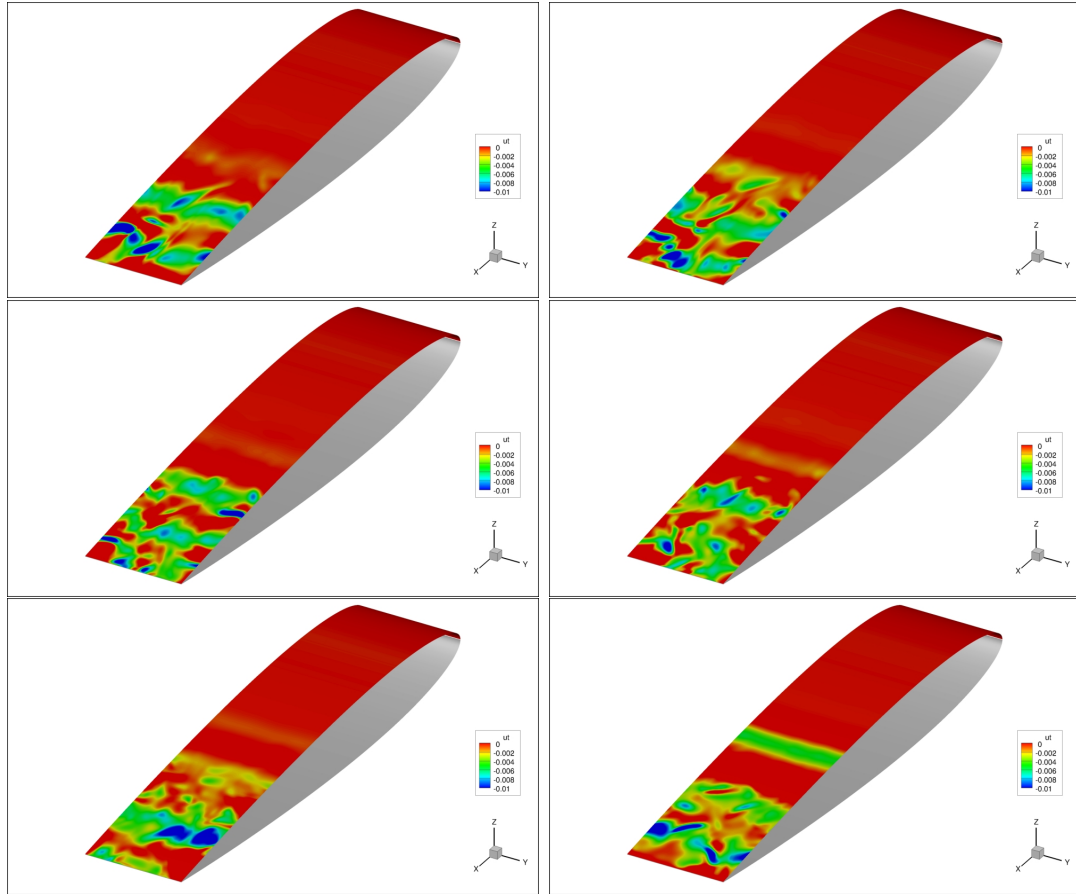
Figure 5.57: Instantaneous contours of the tangential velocity on the aerofoil at different times for $\beta = 5°$, $Re = 20,000$ and $t \in [0, 5.9]$ without control. From top to bottom and left to right: $t = 0.0$, $t = 1.0$, $t = 2.0$, $t = 3.0$, $t = 4.0$, $t = 5.5$ and $t = 5.9$.

Riherd and Roy, 2013).

The proposed control algorithm yields a significant increase of the lift coefficient because it has been designed with the aim of completely suppressing the separation bubble. This is particularly desirable either during take-off or in order to avoid stall conditions during sudden manoeuvres (*e.g.*, for UAVs applications). However, lower references $\varepsilon_m, \varepsilon_M$ can be selected, depending on the specific application, in order to reduce the control effort.

Both the controlled outputs quickly converge to constant values in their corresponding reference regions (see figure 5.51). The two actuator/sensor pairs show a similar dynamic behaviour compared to the results of the same configuration on the coarser grid (bottom frames in figure 5.41). However, the steady-state input values are slightly lower in this case, due to the different grid resolution
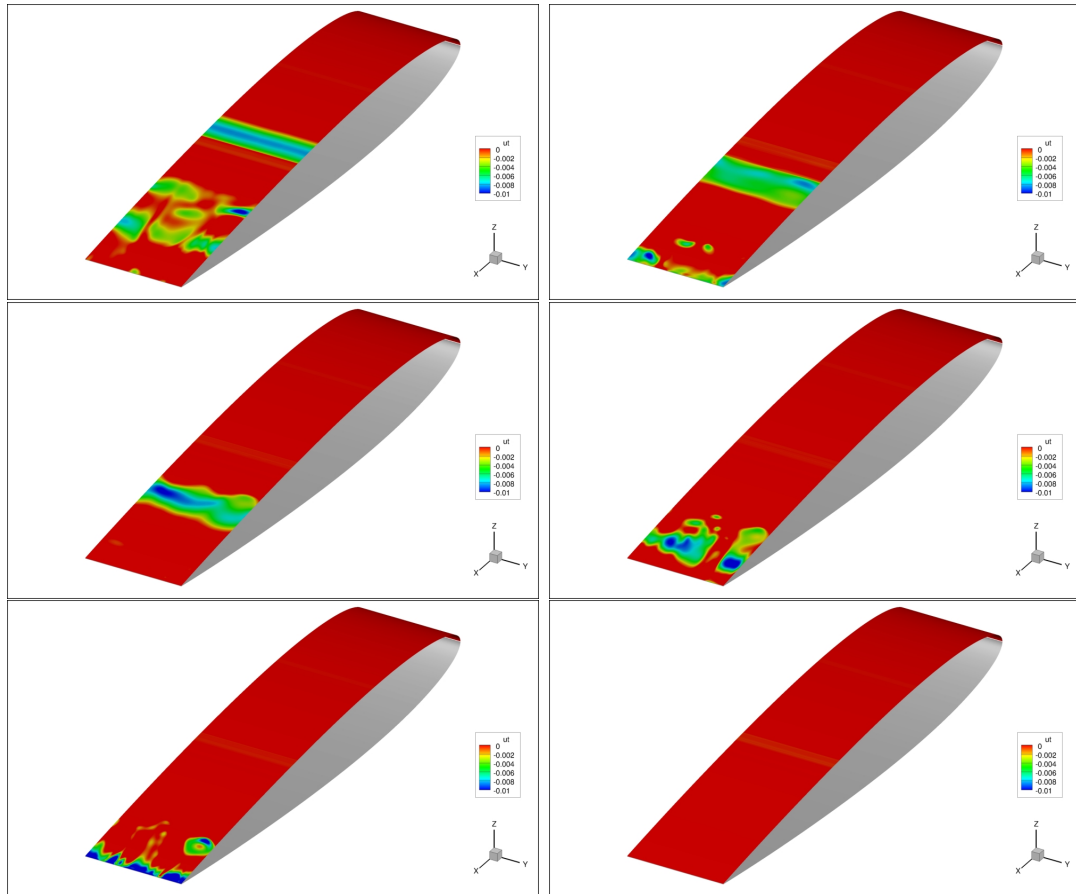
Figure 5.58: Instantaneous contours of the tangential velocity on the aerofoil at different times for $\mathcal{C}_3^{3D}$, $\beta = 5°$, $Re = 20,000$ and $t \in [6,9]$. From top to bottom and left to right: $t = 6.0$, $t = 6.5$, $t = 7.0$, $t = 7.5$, $t = 8.0$, $t = 8.5$ and $t = 9.0$.
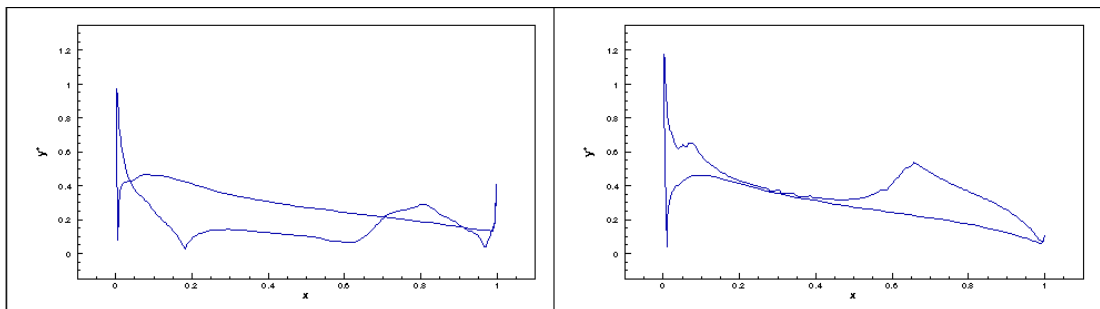
Figure 5.59: Wall coordinate y^+ without (left) and with (right) actuation.

in the boundary layer, which affects the number of cells between the sensor and the wing boundary. This difference in the control inputs, along with the different turbulent dynamics that show smaller scale structures in the case of the finer grid (see figures 5.43, 5.53), produces different values of the drag and lift coefficients, thereby making the improvement less evident compared to the results of the same
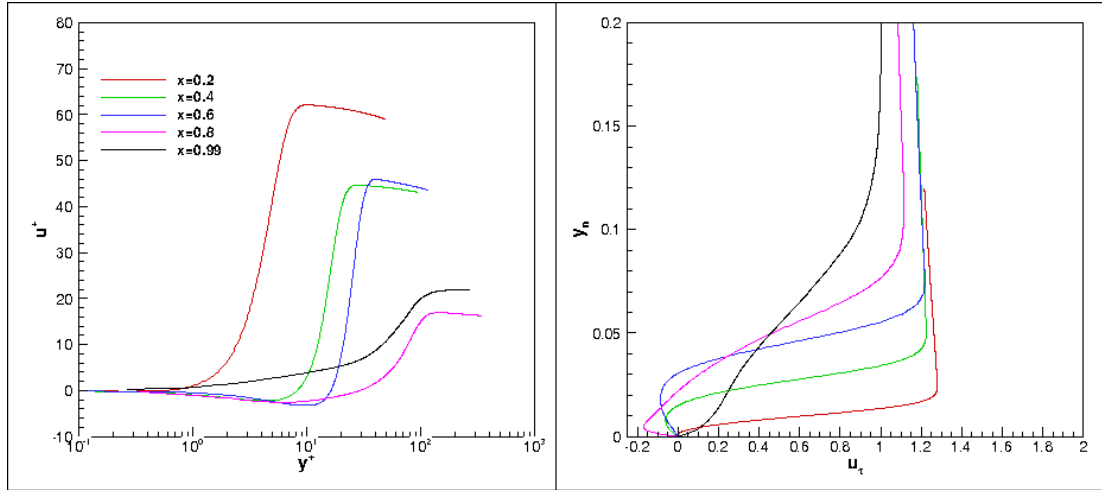
Figure 5.60: Simulation results without actuation: non-dimensional velocity u^+ as a function of the natural logarithm of the wall coordinate y^+ (left) and u_τ as a function of the distance y_n from the aerofoil (right).
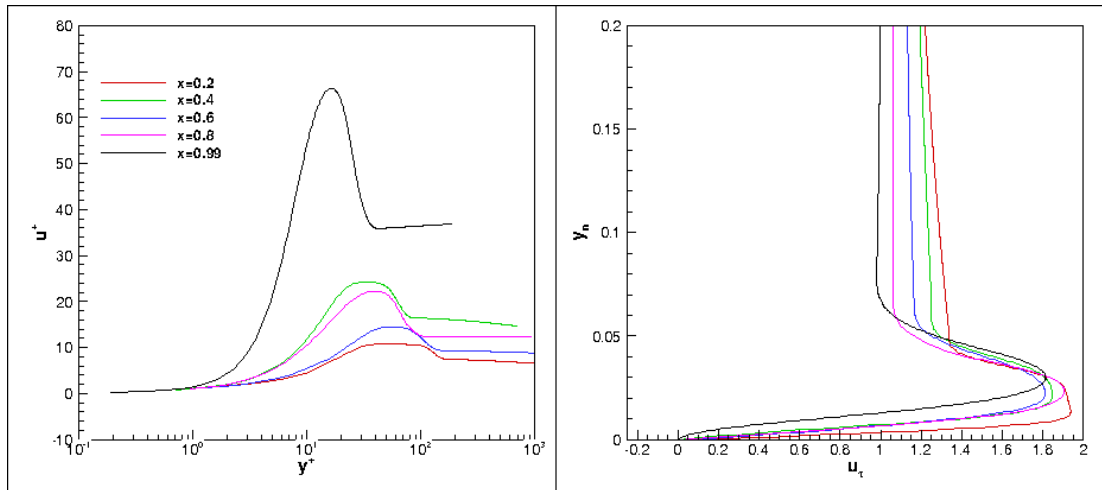
Figure 5.61: Simulation results with feedback control: non-dimensional velocity u^+ as a function of the natural logarithm of the wall coordinate y^+ (left) and u_τ as a function of the distance y_n from the aerofoil (right).

configuration on the coarse grid. Compared to the results of the corresponding 2D configuration $\mathcal{C}^* = \mathcal{C}_{18}$ (cyan line in the left frames of figure 5.15) in the scenario $\beta(t) = \beta_1(t)$ (the angle of attack is 5° between $t = 35$ and $t = 45$ in figure 5.15), the computed steady-state inputs are much lower in the 3D case. The 2D simulations yield a larger separation bubble with a large-scale vortex shedding due to strong adverse pressure gradients while in the 3D case, turbulence occurs and the energy is dissipated at the smaller scales, thus yielding smaller vortex structures.
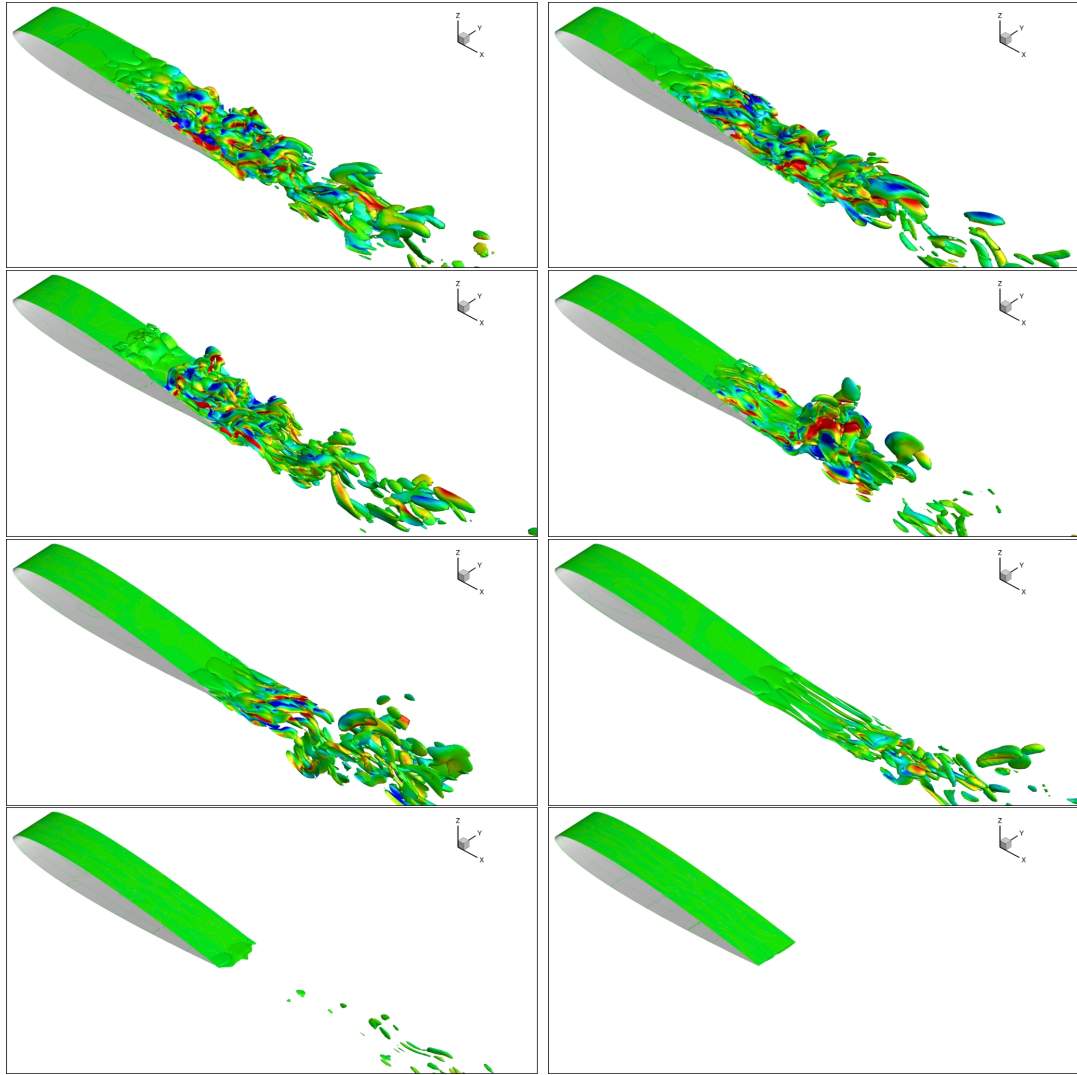
Figure 5.62: Instantaneous iso-contours of the swirl for $\boldsymbol{u} \cdot (\nabla \times \boldsymbol{u})/\|\boldsymbol{u}\|^2 = 10$ coloured by the spanwise velocity using 21 levels in the range [-0.2,0.2] in the scenario $\mathcal{C}_3^{3D}$ and $\beta = 5°$, $Re = 20,000$ during the transients (from just after the controller is activated until it reaches the steady-state). From top to bottom and left to right: $t = 6.0$, $t = 6.5$, $t = 7.0$, $t = 7.5$, $t = 8.0$, $t = 8.5$ and $t = 9.0$.

This, in turn, requires a greater control effort in the 2D case in order to reattach the flow.

The time-averaged tangential velocities, computed at half the span length, with and without control are compared in figure 5.52. In figure 5.53, the instantaneous velocity magnitude, along with the coherent structures using the λ_2-criterion (coloured by the velocity magnitude), are shown (see Jeong and Hussain, 1995, for more details on the method). Figure 5.54 depicts the instantaneous span-

wise vorticity field, with and without control, using 101 levels over the range $[-25, 25]$. Figure 5.55 shows the instantaneous velocity magnitude contours, with and without control, using 101 levels over the range $[0, 1.3]$. In figure 5.56 the time-averaged streamwise velocity contours using 101 levels over the range $[-0.1, 1.3]$ and the time-averaged streamlines for $\beta = 5°$ without control (top and middle) are compared to those of the optimal feedback configuration $\mathcal{C}_3^{3D}$ (bottom): the designed control algorithm successfully suppressed the laminar separation bubble. The latter, in the scenario with no actuation, is located closer to the leading edge compared to the one obtained experimentally in Feng et al. (2015). This might depend on the higher resolution of the numerical grid in the boundary layer (the first cell centre is $\approx 10^{-4}$ above the aerofoil and the separation bubble is extremely "thin" close to the leading edge) compared to the time-resolved Particle Image Velocimetry (PIV) used in Feng et al. (2015), as well as on both the inflow turbulence levels (see Laitone, 1997, for detailed explanation of turbulence levels on a NACA 0012 at low Reynolds numbers) and the boundary effects of the finite-span wing, which are present in Feng et al. (2015) and neglectable in this numerical study. The snapshots of the tangential velocity distribution along the aerofoil are depicted in figures 5.57-5.58.

Figure 5.59 shows the height of the first cell above the wall

$$y^+ = \frac{y_n u^*}{Re}, \tag{5.51}$$

where

$$u^* = \sqrt{\frac{\tau_w}{\rho}} \tag{5.52}$$

is the non-dimensional friction velocity (or shear velocity), as a function of the distance $\bar{x}$ from the leading edge, with respect to the chord length, in both the uncontrolled (left) and closed-loop (right) scenarios. All the variables are both span-averaged and time-averaged.

The absolute value of y^+ is everywhere smaller than 1, except from the first cell centre when the actuator is on, thus indicating that an appropriate grid resolution has been obtained. The flow separates at around $\bar{x} = 0.2$ (where $y^+ = 0$) in the uncontrolled scenario, with a laminar separation up to $\bar{x} = 0.6$, after which a significant increase of y^+ (*i.e.* τ_w) occurs due to the laminar-to-turbulent transition. A turbulent reattachment is observed at around $\bar{x} = 0.95$. In the closed-loop scenario, the designed feedback control achieves full reattachment and no separation

occurs. Both

$$u^+ = \frac{u_\tau}{u^*}, \tag{5.53}$$

as a function of the natural logarithm of the wall coordinate y^+ (left), and the tangential velocity u_τ, as a function of the distance y_n from the aerofoil (right), are averaged in both time and spanwise direction and plotted in figures 5.60, 5.61, in order to compare the simulation results without and with feedback control, respectively, at different positions with respect to the chord length.

In the uncontrolled scenario (figure 5.60), a laminar velocity profile, with a wall shear stress close to zero, is observed between the leading edge at $\bar{x} = 0$ and $\bar{x} = 0.2$. The velocity profiles at $\bar{x} = 0.4$ and $\bar{x} = 0.6$ indicate that the flow is separated but still laminar, at $\bar{x} = 0.8$ the flow is still separated but the shape of the profile (with a small linear region in the semi-log plot) indicates a turbulent profile, while at $\bar{x} = 0.99$ a turbulent attached velocity profile is seen.

The closed-loop simulation results (figure 5.61) prove the effectiveness of the designed feedback control algorithm at both relaminarising and fully reattaching the flow over the wing: all the velocity profiles are laminar and no separation occurs. The peaks observed in the tangential velocitiy profiles are due to the flow acceleration induced by the actuator.

Figure 5.62 shows the instantaneous iso-contours of the swirl for $\boldsymbol{u} \cdot (\nabla \times \boldsymbol{u})/\|\boldsymbol{u}\|^2 = 10$ coloured by the spanwise velocity using 21 levels in the range [-0.2,0.2] in the scenario $\mathcal{C}_3^{3D}$ and $\beta = 5°$ during the transients (from just after the controller is activated until it reaches the steady-state). In particular, from left to right and top to bottom, the snapshots are shown for $t = 6.0$, $t = 6.5$, $t = 7.0$, $t = 7.5$, $t = 8.0$, $t = 8.5$ and $t = 9.0$.

The simulations correctly predict the presence of a laminar boundary layer both on the pressure side of the NACA profile and on the first part of the suction side. Without feedback control, due to the adverse pressure gradients, a laminar separation occurs on the suction side. The transition to turbulence follows, with a turbulent reattachment close to the profile trailing edge (see figures 5.52, 5.56 and 5.57, 5.59, 5.60, 5.61).

The feedback controller efficiently laminarises the turbulent flow field (see figures 5.53, 5.59, 5.61 and 5.62), thereby yielding a completely two-dimensional attached flow (see figures 5.56, 5.58, 5.59, 5.61), in less than three non-dimensional temporal units (see figures 5.58 and 5.62). The boundary layer transition is thus effectively avoided by the designed control algorithm (see figures 5.53, 5.54, 5.55, 5.56, 5.59,

5.61, and 5.62). The steady-state tangential velocity distribution on the suction side of the wing (bottom right in figure 5.58) is positive on the whole surface, except for a small region where a discontinuity is present, due to graphical issues in visualising the field at the actuator's grid boundaries.

The chosen MIMO configuration $\mathcal{C}_3^{3D}$ achieves very good performance in terms of flow separation suppression: the flow is completely laminar and reattached along the wing (see figures 5.52, 5.53, 5.54, 5.55, 5.56, 5.58, 5.62).

5.7 Summary

This chapter addressed the practical problem of robustly controlling the unsteady flow separation over an aerofoil, using the plasma actuators' voltage as the control inputs and realistically available real-time velocity measurements as the control outputs.

In particular, the flow separation problem has been formulated as a simple output regulation problem, which was solved by designing a simple multivariable robust output feedback control, thus allowing for testing different configurations, with multiple actuator/sensor pairs. The proposed controller guarantees the exponential regulation of the output measurements to some suitable reference sets, when the steady-state gains of each actuator/sensor pair are non-zero and of known sign.

The underlying assumption is that there exist suitable configurations of actuator/sensor pairs, along with suitable references for the outputs, which guarantee that, given a certain range for both Re and β, the solution of the output regulation problem implies the solution of the flow separation problem. A suitable cost functional has been defined in order to provide a criterion for selecting optimal configurations, whose reference sets are such that the former assumption holds.

Accurate two-dimensional numerical simulations of flows past a pitching NACA 0012 at Reynolds $Re = 20,000$ are performed in order to test the control effectiveness and validate the modelling assumptions. The objective of the 2D analysis was, also, to perform a parametric study aimed at finding an optimal configuration $\mathcal{C}^*$, to be implemented in realistic flow control applications. Both the transient and steady-state performance have been investigated in different scenarios, for time-varying angles of attack between 5° and 25°. Although the proposed controller is simple, as it is based on an integral action, it is able to effectively suppress the separation bubble, as well as the shedding vortices, while achieving robust dynamic performances, with respect to the variation of the uncertain angle of incidence. An optimal configuration with two actuator/sensor pairs, which minimises the chosen cost functional, has been identified: a fast flow reattachment is achieved, in the presence of time-varying angles of attack.

Furthermore, 3D LES simulations have been performed to show the ability of the designed control algorithm to both delay the transition to turbulence and suppress the flow separation on a more realistic three-dimensional wing. It has been shown that a MIMO feedback control based on an integral action only (no proportional

or derivative terms are present in the designed algorithm) is sufficient to reattach turbulent flows over 3D wings. A major advantage of the proposed approach is that the chosen outputs can be easily measured in realistic applications; moreover, the resulting control scheme is simple and computationally cheap.

Chapter 6

Conclusions and Further Work

The problem of modelling and controlling the unsteady flow separation over an aerofoil in the presence of DBD plasma actuators has been addressed. The main contributions of the thesis can be summarised as follows:

- Analytical and numerical modelling of the closed-loop incompressible Navier-Stokes equations, in the presence of body force fields generated by plasma actuators.

- Implementation of a novel control-oriented model reduction method (balanced DMD) for controlled nonlinear systems evolving on attractors.

- Design, development and testing of a novel multivariable robust feedback control algorithm for flow separation suppression around a NACA 0012 aerofoil, using the plasma actuators' voltage as the control inputs and real-time velocity measurements as the control outputs.

- Optimisation of the closed-loop system in order to identify suitable numbers and positions of the actuator/sensor pairs along the aerofoil.

- Development of the hardware interface for both data acquisition (real-time velocity measurements from hot wire and piezoelectric cantilever sensors) and control of the high voltage power converter, which generates the plasma over the aerofoil (see Appendix A).

Despite the complexity of the dynamics of interest, it is shown how the flow separation problem can be formulated and solved as a simple output regulation problem, so that a simple control strategy may be used. A robust multivariable feedback

control algorithm is designed, on the basis of a novel low-order, linear, dynamical model approximating the incompressible Navier-Stokes equations, using the plasma actuators' voltage as the control inputs and realistically available real-time velocity measurements as the control outputs.

Under some simplifying assumptions, the flow separation problem is solved by designing a simple MIMO robust feedback control, consisting of n_p SISO regulators. The proposed controller is computationally cheap and only requires non-zero steady-state gains of known sign, for each actuator/sensor pair. Furthermore, the chosen output can be experimentally measured in realistic applications.

Accurate numerical simulations have been performed at different Reynolds numbers ($Re \in [10^3, 2 \cdot 10^4]$) and angles of attack ($\beta \in [5°, 25°]$) in order to test the control effectiveness in the presence of complex dynamics, which are neglected in the control design. Several configurations have been investigated, with the aim of identifying optimal numbers and positions of the actuator/sensor pairs along the aerofoil, together with the corresponding references for the available real-time velocity measurements.

In particular, a 2D RANS parametric study has been performed, for both SISO and MIMO systems, aimed at identifying optimal configurations, which guarantee that, given a certain range for both the Reynolds number Re and the angle of attack β, the solution of the output regulation problem implies the solution of the flow separation problem. The chosen optimal configuration with $n_p = 2$ actuator/sensor pairs has been tested in realistic 3D LES simulations in order to show the effectiveness of the designed robust regulator at controlling turbulent flows. The 3D LES simulations have been performed on the CINECA servers, thanks to an ISCRA Grant (code HP10CXD3Z9) of 200,000 computational hours.

Although the proposed controller is simple, as it is based on an integral action, it effectively delays the transition to turbulence and it robustly suppresses the separation bubble along the wing, in both transient and steady-state regimes, in all the considered scenarios. Fast flow reattachment is achieved, along with both stabilisation and increase/reduction of the lift/drag, respectively.

The results highlighted the following conclusions: *i)* the steady-state gains between any actuator/sensor pair decrease with the distance between sensors and actuators, as well as with the location of the pairs; *ii)* the further upstream a pair is placed, the better dynamic performance is obtained, *i.e.*, the faster the regulation error converges to zero; *iii)* the robustness of the control system with

respect to the variation of the angle of attack increases with the output references, for fixed sensors' positions, and *vice versa*; *iv)* both the drag-to-lift ratio and the total input power increase with the number of pairs n_p; *v)* on the other hand, an increase in the number of pairs n_p yields increased robustness of the closed-loop system, as well as a reduced maximum steady-state input voltage for the single actuators.

A hardware interface (see Appendix A) has been built in order to show the practical feasibility of the proposed approach. The real-time velocity measurements are acquired from both hot wire and piezoelectric cantilever sensors. The designed feedback control scheme has been implemented in a XMC4500 Relax Kit microcontroller in order to automatically regulate the high voltage of the PSI-MCPG2503C power converter, which generates the surface plasma on the wing. The hardware-in-the-loop functionality test showed the effectiveness of the developed layout: an accurate data acquisition is achieved, along with a fast regulation of the converter's output voltage magnitude.

The results of this thesis move in the direction of filling the gap between theory and practice through the use of rigorous analytical arguments to prove the effectiveness of relatively simple and widely-applicable control schemes. A major advantage of the proposed approach is that the chosen outputs can be easily measured in realistic applications. Furthermore, its range of applicability is extremely wide: the proposed control algorithm was shown to be effective in very different scenarios, ranging from two-dimensional low Reynolds number flows to three-dimensional turbulent aerodynamics, in the presence of time-varying angles of attack, thus emphasising the great potential of the designed robust feedback controller.

The natural next step would be to test the developed hardware interface in a wind tunnel experiment. Furthermore, different reference signals could be further investigated. A set-point tracking scheme has been considered in this thesis in order to avoid the transition to turbulence and to suppress the separation bubble. This leads to both reduced skin-friction drag and enhanced lift, thus yielding reduced fuel consumption, noise and vibration in aerodynamic applications (*e.g.*, UAVs or wind turbines).

On the other hand, there are applications in which accelerating the laminar to turbulent transition might be desirable in order to enhance flow mixing (*e.g.*, gas turbine engines). For example, the proposed feedback control algorithm can

be directly applied to plasma actuation in burst mode in order to improve the efficiency of the separation control mechanism: this approach yields increased turbulence and a partial reattachment but a much lower power consumption (Sato et al., 2015a,b). Furthermore, following Marino and Tomei (2015), the designed robust control algorithm can be easily extended to biased multi-sinusoidal references with known frequencies, which can be computed, for instance, in order to initiate Tollmien-Schlichting waves. Therefore, it might be worth to further investigate different applications of the proposed approach, in which the objective would be to trigger known instabilities in laminar boundary layers, thus forcing the transition to turbulence.

Appendices

Appendix A

Experimental Setup

This last chapter shows the final assembly of the electronic interface for both data acquisition (real-time measurements from hot wire and piezoelectric cantilever sensors) and control of the high voltage power converter, which generates the plasma over the aerofoil. The resulting layout is shown in figure A.1. The con-
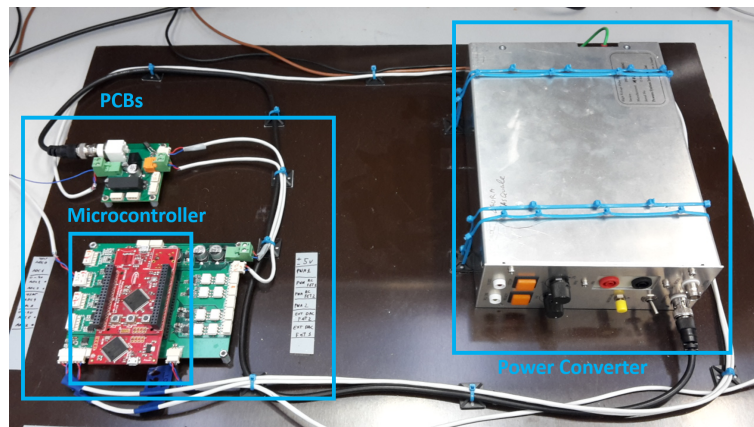
Figure A.1: Circuit layout.

verter is a PSI-MCPG2503C power amplifier device (top left in figure A.2) that operates from DC36V electrical supplies to convert the power into high-voltage and high-frequency for generating surface plasma. Both the output voltage and the output frequency can be changed by turning the control dial in the range of 1-2.5kV and 15-25kHz, respectively. The voltage output can be monitored down to 1/1000 using a voltage dividing monitor. The converter has been modified in order to be able to automatically adjust the output voltage, based on the designed feedback control algorithm (5.13), (5.14).

In particular, the action of the knob (see figure A.3), which regulates the magni-

tude of the applied voltage, has been replaced by an AD5293 digital potentiometer with a 1024-position resolution. The control algorithm (5.13), (5.14) has been implemented in a XMC4500 Relax Kit microcontroller (bottom left in figure A.2) that reads the voltage signals coming from the MEMS-based cantilever sensors (see Segawa et al., 2010), which provide the measurements of both sign and magnitude of the tangential velocity on the aerofoil (top right in figure A.2), *i.e.*, the chosen controlled outputs (5.5). The schematics of the closed-loop are summarised

Figure A.2: Power converter (top left), MEMS-based cantilever sensor (top right), XMC4500 Relax Kit (bottom left) and AFG3000 (bottom right).

in figure A.3. An open-loop functionality test has been performed to evaluate the
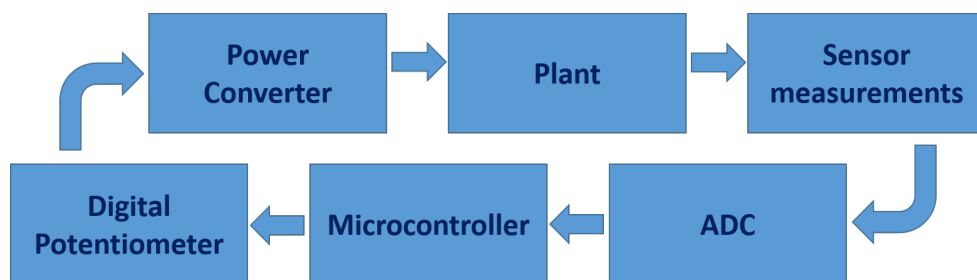
Figure A.3: Schematic of the closed-loop.

performance of the circuit. An AFG3000 arbitrary function generator (bottom right in figure A.2) translated the simulation data of the optimal configuration $\mathcal{C}^* = \mathcal{C}_{18}$ for $\beta(t) = \beta_2(t)$ (see figure 5.34) into voltage signals, thus simulating the output measurements coming from the sensors (see figure A.4). An oscilloscope
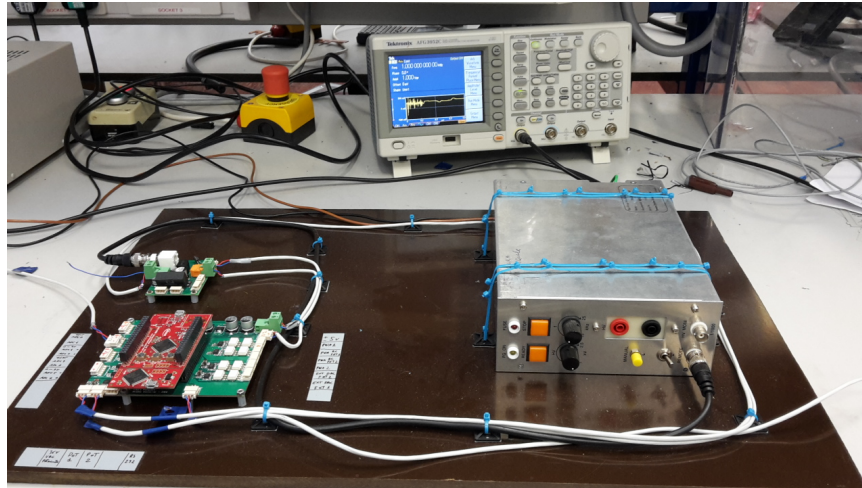
Figure A.4: Layout of the circuit, connected to the AFG3000.

was used to visualise the simulated signals read by the ADC (see figure A.5). The
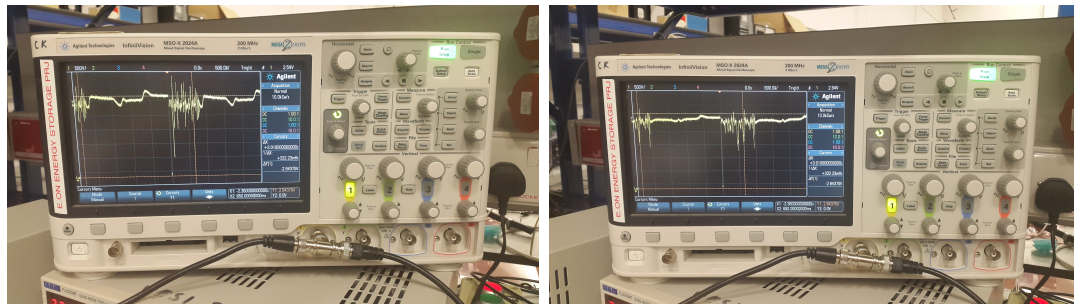
Figure A.5: Output signals read by the oscilloscope.

control inputs are computed by the XMC4500 Relax Kit as in (5.13), (5.14), with the same references and control gains of configurations $\mathcal{C}^* = \mathcal{C}_{18}$. The corresponding results are shown in figure A.6. The control algorithm correctly computed the input voltages, yielding the same results of the simulations. Measurements of the converter's output voltage, whose magnitude changes accordingly to (5.13), (5.14), have been performed in order to prove the effectiveness of the developed layout: an accurate data acquisition is achieved, along with a fast regulation of the converter's output voltage magnitude.
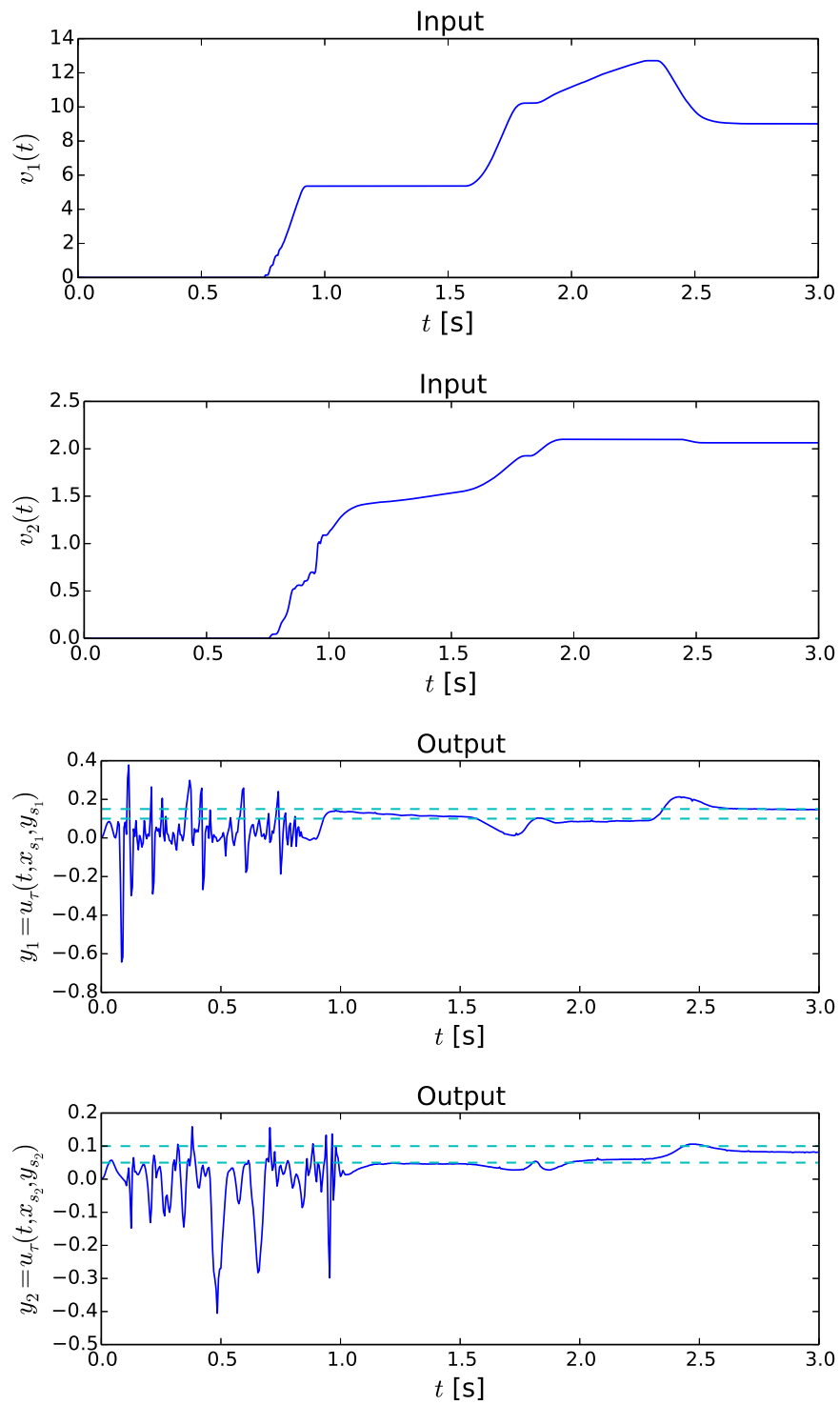
Figure A.6: Open-loop functionality test: control inputs (top); measured outputs (bottom).

Bibliography

Ahlborn, B. K. (2006). *Zoological physics: Quantitative models of body design, actions, and physical limitations of animals.* Springer Science & Business Media.

Ahuja, S. and Rowley, C. W. (2008). Low-dimensional models for feedback stabilization of unstable steady states. *AIAA Paper*, 553:2008.

Ahuja, S. and Rowley, C. W. (2010). Feedback control of unstable steady states of flow past a flat plate using reduced-order estimators. *Journal of Fluid Mechanics*, 645:447–478.

Ahuja, S., Rowley, C. W., Kevrekidis, I. G., Wei, M., Colonius, T., and Tadmor, G. (2007). Low-dimensional models for control of leading-edge vortices: equilibria and linearized models. *AIAA Paper*, 709.

Akin, J. E., Tezduyar, T., Ungor, M., and Mittal, S. (2003). Stabilization parameters and smagorinsky turbulence model. *Journal of Applied Mechanics*, 70(1):2–9.

Annoni, J. and Seiler, P. (2015). A method to construct reduced-order parameter varying models. *International Journal of Robust and Nonlinear Control*, 00:1–30.

Asada, K. and Fujii, K. (2010). Computational analysis of unsteady flow-field induced by plasma actuator in burst mode. *AIAA paper*, 5090:2010.

Astolfi, A. (2010a). Model reduction by moment matching for linear and nonlinear systems. *IEEE Transactions on Automatic Control*, 55(10):2321–2336.

Astolfi, A. (2010b). Model reduction by moment matching, steady-state response and projections. *49th IEEE Conference on Decision and Control*, pages 5344–5349.

Bagheri, S. (2013). Koopman-mode decomposition of the cylinder wake. *Journal of Fluid Mechanics*, 726:596–623.

Bai, Z. (2002). Krylov subspace techniques for reduced-order modeling of large-scale dynamical systems. *Applied Numerical Mathematics*, 43:9–44.

Baker, C. (2010). The flow around high speed trains. *Journal of Wind Engineering and Industrial Aerodynamics*, 98(6):277–298.

Baker, C., Jones, J., Lopez-Calleja, F., and Munday, J. (2004). Measurements of the cross wind forces on trains. *Journal of Wind Engineering and Industrial Aerodynamics*, 92(7):547–563.

Barbagallo, A., Sipp, D., and Schmid, P. J. (2009). Closed-loop control of an open cavity flow using reduced-order models. *Journal of Fluid Mechanics*, 641:1–50.

Beam, R. M. and Warming, R. F. (1978). An Implicit Factored Scheme for the Compressible Navier-Stokes Equations. *AIAA Journal*, 16:393–402.

Bechert, D., Bruse, M., Hage, W., Van der Hoeven, J. T., and Hoppe, G. (1997a). Experiments on drag-reducing surfaces and their optimization with an adjustable geometry. *Journal of fluid mechanics*, 338:59–87.

Bechert, D. W. and Bartenwerfer, M. (1989). The viscous flow on surfaces with longitudinal ribs. *Journal of Fluid Mechanics*, 206:105–129.

Bechert, D. W., Bruse, M., Hage, W., van der Hoeven, J. G. T., and Hoppe, G. (1997b). Experiments on drag-reducing surfaces and their optimization with an adjustable geometry. *Physics of Fluids*, 338:59–87.

Belson, B. A., Tu, J. H., and Rowley, C. W. (2014). Algorithm 945: `modred`-a parallelized model reduction library. *ACM Transactions on Mathematical Software*, 40(4):30.

Bénard, N., Jolibois, J., and Moreau, E. (2009). Lift and drag performances of an axisymmetric airfoil controlled by plasma actuator. *Journal of Electrostatics*, 67(2):133–139.

Benard, N. and Moreau, E. (2011). On the vortex dynamic of airflow reattachment forced by a single non-thermal plasma discharge actuator. *Flow, turbulence and combustion*, 87(1):1–31.

Benard, N. and Moreau, E. (2013). Response of a circular cylinder wake to a symmetric actuation by non-thermal plasma discharges. *Experiments in Fluids*, 54(2):1467.

Benard, N., Moreau, E., Griffin, J., and Cattafesta, L. N. (2009). Plasma flow controlautonomous lift improvement by slope-seeking. *Proceedings of the 39th AIAA fluid dynamics conference*, pages 22–25.

Benner, P. (2009). System-theoretic methods for model reduction of large-scale systems: Simulation, control, and inverse problems. *Proceedings of MATHMOD*, 2009:126–145.

Bergmann, M., Bruneau, C. H., and Iollo, A. (2009). Enablers for robust POD models. *Journal of Computational Physics*, 228(2):516–538.

Bergmann, M. and Cordier, L. (2008). Optimal control of the cylinder wake in the laminar regime by trust-region methods and POD reduced-order models. *Journal of Computational Physics*, 227:7813–7840.

Bewley, T. R. (2001). Flow control: new challenges for a new renaissance. *Progress in Aerospace Sciences*, 37:21–58.

Bistrian, D. A. and Navon, I. M. (2014). Comparison of optimized dynamic mode decomposition vs POD for the shallow water equations model reduction with large-time-step observations. *International Journal for Numerical Methods in Fluids*, 00:1–25.

Brandt, A. (1984). *Multi-grid Techniques: 1984 Guide with Application to Fluid Dynamics*. The Weizmann Institute of Science, Rehovot (Israel).

Broglia, R., Di Mascio, A., and Amati, G. (2007a). A Parallel Unsteady RANS Code for the Numerical Simulations of Free Surface Flows. In *Proceedings of 2nd International Conference on Marine Research and Trasportation*, Ischia, Naples, Italy.

Broglia, R., Di Mascio, A., and Muscari, R. (2007b). Numerical Study of Confined Water Effects on a Self–Propelled Submarine in Steady Manoeuvres. *Int. J. of Offshore and Polar Engineering*, 17:89–96.

Broglia, R., Zaghi, S., Muscari, R., and Salvadore, F. (2014). Enabling hydro-dynamics solver for efficient parallel simulations. In *Proceedings International Conference on High Performance Computing & Simulation (HPCS)*, pages 803–810, Bologna, Italy.

Brunton, S. L. and Noack, B. R. (2015). Closed-loop turbulence control: Progress and challenges. *Applied Mechanics Reviews*, 67(5):050801.

Buder, U., Petz, R., Kittel, M., Nitsche, W., and Obermeier, E. (2008). Aeromems polyimide based wall double hot-wire sensors for flow separation detection. *Sensors and Actuators*, A 142:130–137.

Bui-Thahn, T. (2008). Model-constrained optimization methods for reduction of parameterized large-scale systems. *SIAM Journal of Scientific Computation*, 30(6):3270–3288.

Burkardt, J., Gunzburger, M., and Lee, H. C. (2006). POD and CVT-based reduced-order modeling of navierstokes flows. *Computer Methods in Applied Mechanics and Engineering*, 196(1):337–355.

Caiazzo, A., Iliescu, T., John, V., and Schyschlowa, S. (2014). A numerical investigation of velocity-pressure reduced order models for incompressible flows. *Journal of Computational Physics*, 259:598–616.

Cammilleri, A., Gueniat, F., Carlier, J., Pastur, L., Memin, E., Lusseyran, F., and Artana, G. (2013). POD-spectral decomposition for fluid flow analysis and model reduction. *Theoretical Computational Fluid Dynamics*, 27:787–815.

Cattafesta, L. and Sheplak, M. (2011). Actuators for active flow control. *Annual Review of Fluid Mechanics*, 43:247–272.

Chen, K. K., Tu, J. H., and Rowley, C. W. (2012). Variants of dynamic mode decomposition: boundary condition, koopman, and fourier analyses. *Journal of nonlinear science*, 22(6):887–915.

Chen, X., Diez, M., Kandasamy, M., Zhang, Z., Campana, E., and Stern, F. (2015). High-fidelity global optimization of shape design by dimensionality reduction, metamodels and deterministic particle swarm. *Engineering Optimization*, 47(4):473–494.

Cho, Y. C. and Shyy, W. (2011). Adaptive flow control of low-reynolds number aerodynamics using dielectric barrier discharge actuator. *Progress in Aerospace Sciences*, 47:495–521.

Choi, K. S., Gadd, G. E., Pearcey, H. H., Savill, A. M., and Svensson, S. (1989). Tests of drag-reducing polymer coated on a riblet surface. *Journal of Applied Science Research*, 46:209–216.

Choi, K.-S., Jukes, T. N., and Whalley, R. D. (2011). Turbulent boundary-layer control with plasma actuators. *Philosophical Transactions of the Royal Society: A*, 369:1443–1458.

Chorin, A. J. (1968). Numerical solution of the navier-stokes equations. *Mathematics of Computation*, 22(104):745–762.

Clerc, M. (2006). Stagnation analysis in particle swarm optimization or what happens when nothing happens. *Online at http://clerc. maurice. free. fr/pso.*

Collis, S. S., Chang, Y., Kellogg, S., and Prahbu, R. D. (2000). Large eddy simulation and turbulence control. *AIAA paper*, 2564:2000.

Collis, S. S. and Joslin, R. D. (2004). Issues in active flow control: theory, control, simulation, and experiment. *Progress in Aerospace Sciences*, 40:237–289.

Corke, T. C., Enloe, C. L., and Wilkinson, S. P. (2007). SDBD plasma enhanced aerodynamics: concepts, optimization and applications. *Progress in Aerospace Sciences*, 43:193–217.

Corke, T. C., Post, M., and Orlov, D. (2010). Dielectric barrier discharge plasma actuators for flow control. *Annual Review of Fluid Mechanics*, 42:505–529.

Courant, R. (1937). *Differential and Integral Calculus*, volume I. Blackie and Son.

Dean, B. and Bhushan, B. (2010). Shark-skin surfaces for fluid-drag reduction in turbulent flow: a review. *Philosophical Transactions of the Royal Society of London A: Mathematical, Physical and Engineering Sciences*, 368(1929):4775–4806.

Di Mascio, A., Broglia, R., and Favini, B. (2001). *A Second Order Godunov–Type Scheme for Naval Hydrodynamics*, pages 253–261. Kluwer Academic/Plenum Publishers.

Di Mascio, A., Broglia, R., and Muscari, R. (2007a). On the Application of the One–Phase Level Set Method for Naval Hydrodynamic Flows. *Computers and Fluids*, 36(5):868–886.

Di Mascio, A., Broglia, R., and R., M. (2007b). Prediction of Hydrodynamic Coefficients of Ship Hulls by Godunov-Type Methods. In *MARINE 2007*, Barcelona, Spain.

Di Mascio, A., Muscari, R., and Broglia, R. (2006). An Overlapping Grids Approach for Moving Bodies Problems. In *Proceedings of 16th Int. Offshore and Polar Engineering Conference*, San Francisco, California (USA).

Dubbioso, G., Broglia, R., and Zaghi, S. (2017). Cfd analysis of maneuvering characteristics of a submarine model. *Ocean Engineering*, 129:459–479.

Dubbioso, G., Durante, D., Mascio, A. D., and Broglia, R. (2016). Turning ability analysis of a fully appended twin screw vessel by cfd. part ii: Single vs. twin rudder configuration. *Ocean Engineering*, 117:259–271.

el Hak, M. G. (2000). Flow control: passive, active, and reactive flow management. *Cambridge University Press*.

Enloe, C. L., McLaughlin, T. E., Dyken, R. D. V., Kachner, K. D., Jumper, E. J., and Corke, T. C. (2004). Mechanisms and responses of a single dielectric barrier plasma actuator: plasma morphology. *AIAA J.*, 42(3):589–594.

Fahl, M. (2000). *Trust-region methods for flow control based on reduced order modeling*. Ph.D. Thesis, Trier University, Germany.

Favini, B., Broglia, R., and Di Mascio, A. (1996). Multi–grid Acceleration of Second Order ENO Schemes from Low Subsonic to High Supersonic Flows. *International journal for numerical methods in fluids*, 23(6):589–606.

Feng, L.-H., Choi, K.-S., and Wang, J.-J. (2015). Flow control over an airfoil using virtual gurney flaps. *Journal of Fluid Mechanics*, 767:595–626.

Francis, B. A. and Wonham, W. M. (1976). The internal model principle of control theory. *Automatica*, 12:457–465.

Frings, B. (1988). Heterogeneous drag reduction in turbulent pipe flows using various injection techniques. *Rheologica Acta*, 27:92–110.

Fujimoto, K. and Hikaru, M. (2006). Weighted balanced truncation for unstable nonlinear systems using coprime factorizations. *45th IEEE Conference on Decision and Control.*

Fukagata, K., Kern, S., Chatelain, P., Koumoutsakos, P., and Kasagi, N. (2000). Evolutionary optimization of an anisotropic compliant surface for turbulent friction drag reduction. *Journal of Fluid Mechanics*, 9(35):1–17.

Gad-el Hak, M. (1989). Flow control. *Applied mechanics reviews*, 42(10):261–293.

Gad-el Hak, M. and Tsai, H. M. (2006). *Transition and turbulence control*, volume 8. World Scientific.

Gaitonde, D. V., Visbal, M. R., and Roy, S. (2005). Control of flow past a wing section with plasma-based body forces. *AIAA paper*, 5302:2005.

Gilliéron, P. and Kourta, A. (2010). Aerodynamic drag reduction by vertical splitter plates. *Experiments in Fluids*, 48(1):1–16.

Grandemange, M., Ricot, D., Vartanian, C., Ruiz, T., and Cadot, O. (2014). Characterisation of the flow past real road vehicles with blunt afterbodies. *International Journal of Aerodynamics*, 4(1-2):24–42.

Greenblatt, D. and Wygnanski, I. J. (2000). The control of flow separation by periodic excitation. *Progres in Aerospace Science*, 36(7):487–545.

Gupta, V. K., Zhang, Z., and Sun, Z. (2011). Modeling and control of a novel pressure regulation mechanism for common rail fuel injection systems. *Applied Mathematical Modelling*, 35(7):3473–3483.

Hanson, R. E., Bade, K. M., Belson, B. A., Lavoie, P., Naguib, A. M., and Rowley, C. W. (2014). Feedback control of slowly-varying transient growth by an array of plasma actuators. *Physics of Fluids*, 26:024102.

Hanson, R. E., Lavoie, P., Naguib, A. M., and Morrison, J. (2010). Transient growth instability cancellation by a plasma actuator array. *Experiments in Fluids*, 49:1339–1348.

Harten, A., Engquist, B., Osher, S., and Chakravar thy, S. R. (1987). Uniformly High Order Accurate Essentially Non–Oscillatory Schemes. *Journal of Computational Physics*, 71:231–303.

Hirsch, C. (2007). *Numerical computation of internal and external flows: The fundamentals of computational fluid dynamics.* Butterworth-Heinemann.

Hoyt, J. W. (1975). Hydrodynamic drag reduction due to fish slimes. *Swimming and Flying in Nature*, 2:653–672.

Huang, J., Corke, T. C., and Thomas, F. O. (2006). Plasma actuators for separation control of low-pressure turbine blades. *AIAA Journal*, 44(1):51–57.

Huang, S. C. and Kim, J. (2008). Control and system identification of a separated flow. *Physics of Fluids*, 20:101509.

Ilak, M., Brandt, L., Rowley, C. W., and Henningson, D. S. (2010). Model reduction of the nonlinear complex ginzburglandau equation. *SIAM Journal of Applied Dynamical Systems*, 9(4):1284–1302.

Ilak, M. and Rowley, C. W. (2006). Reduced-order modeling of channel flow using traveling POD and balanced POD. *3rd AIAA Flow Control Conference, San Francisco, California*, (3194).

Ilak, M. and Rowley, C. W. (2008). Modeling of transitional channel flow using balanced proper orthogonal decomposition. *Physics of Fluids*, 20(3):034103.

Ionescu, T. C. and Astolfi, A. (2011). Moment matching for linear systems-overview and new results. *Proceedings of the 18th IFAC World Congress*, pages 12739–12744.

Jaimoukha, I. M. and Kasenally, E. M. (1997). Implicitly restarted krylov subspace methods for stable partial realizations. *SIAM Journal on Matrix Analysis and Applications*, 18(3):633–652.

Jayaraman, B. and Shyy, W. (2008). Modeling of dielectric barrier discharge-induced fluid dynamics and heat transfer. *Progress in Aerospace Sciences*, 44:139–191.

Jeong, J. and Hussain, F. (1995). On the identification of a vortex. *Journal of Fluid Mechanics*, 285:69–94.

Jones, L., Sandberg, R., and Sandham, N. (2008). Direct numerical simulations of forced and unforced separation bubbles on an airfoil at incidence. *Journal of Fluid Mechanics*, 602:175–207.

Joshi, S. S., Speyer, J. L., and Kim, J. (2007). A systems theory approach to the feedback stabilization of infinitesimal and finite-amplitude disturbances in plane poiseuille flow. *Journal of Fluid Mechanics*, 39:383–417.

Juang, J. N. and Pappa, R. S. (1985). An eigensystem realization algorithm for modal parameter identification and model reduction. *Journal of Guidance Control and Dynamics*, 8(5):620–627.

Jukes, T. N. and Choi, K.-S. (2009). Control of unsteady flow separation over a circular cylinder using dielectric-barrier-discharge surface plasma. *Physics of Fluids*, 21(9):094106.

Karabelas, S., Koumroglou, B., Argyropoulos, C., and Markatos, N. (2012). High reynolds number turbulent flow past a rotating cylinder. *Applied Mathematical Modelling*, 36(1):379–398.

Kennedy, J. and Eberhart, R. (1995). Particle swarm optimization. In *Proceedings of the IEEE International Conference on Neural Networks*, volume 4, pages 1942–1948.

Kim, J. (2011). Physics and control of wall turbulence for drag reduction. *Philosophical Transactions of the Royal Society of London A: Mathematical, Physical and Engineering Sciences*, 369(1940):1396–1411.

Kim, J. and Bewley, T. R. (2007). A linear systems approach to flow control. *Annual Review of Fluid Dynamics*, 39:383–417.

Koopman, B. O. (1931). Hamiltonian systems and transformation in hilbert space. *Proceedings of the National Academy of Sciences*, 17(5):315–318.

Kotsonis, M., Ghaemi, S., Veldhuis, L., and Scarano, F. (2011). Measurement of the body force field of plasma actuators. *Journal of Physics D: Applied Physics*, 44:045204.

Kunhardt, E. E. (1980). Electrical breakdown of gases: the pre-breakdown stage. *IEEE Transactions on Plasma Science*, 8:130–138.

Kutay, A. T., Culp, J. R., Muse, J. A., Brzozowski, D. P., Glezer, A., and Calise, A. J. (2007). A closed-loop flight control experiment using active flow control actuators. *45th AIAA Aerospace sciences meeting and exhibit*, Reno, Nevada:2007–114.

Laitone, E. V. (1997). Wind tunnel tests of wings at reynolds numbers below 70 000. *Experiments in Fluids*, 23(5):405–409.

Lall, S., Marsden, J. E., and Glavaski, S. (1999). Empirical model reduction of nonlinear controlled systems. *Proceedings of the IFAC World Congress*, pages 473–478.

Lall, S., Marsden, J. E., and Glavaski, S. (2002). A subspace approach to balanced truncation for model reduction of nonlinear systems. *International Journal of Robust and Nonlinear Control*, 12:519–535.

Lee, C., Cortellezzi, L., Kim, J., and Speyer, J. (2001). Application of reduced-order controller to turbulent flows for drag reduction. *Physics of Fluids*, 13(5):1321–1330.

Lee, C., Kim, J., Babcock, D., and Goodman, R. (1997). Application of neural networks to turbulence control for drag reduction. *Physics of Fluids*, 9(6):1740–1747.

Liebeck, R. H. (1978). Design of subsonic airfoils for high lift. *Journal of Aircraft*, 15:547–561.

Litrico, X. and Georges, D. (1999). Robust continuous-time and discrete-time flow control of a dam–river system.(ii) controller design. *Applied Mathematical Modelling*, 23(11):829–846.

Logg, A., Mardal, K.-A., and Wells, G. N. (2012). Automated Solution of Differential Equations by the Finite Element Method. In *Lecture Notes in Computational Science and Engineering*, volume 84. Springer Science & Business Media.

Lumley, J. L. (1967). The structure of inhomogeneous turbulence. *Atmospheric Turbulence and Wave Propagation*, 12:166–178.

Ma, Z., Ahuja, S., and Rowley, C. W. (2011). Reduced-order models for control of fluids using the eigensystem realization algorithm. *Theoretical Computational Fluid Dynamics*, 25:233–247.

Mabe, J. H., Calkins, F. T., Wesley, B., Woszidlo, R., Taubert, L., and Wygnanski, I. (2009). Single dielectric barrier discharge plasma actuators for improved airfoil performance. *Journal of Aircraft*, 46(3):847.

Maki, K., Sbragio, R., and Vlahopoulos, N. (2012). System design of a wind turbine using a multi-level optimization approach. *Renewable Energy*, 43:101–110.

Marino, R., Pasquale, L., Scalzi, S., and Verrelli, C. M. (2015). Automatic rotor speed reference generator for electric vehicles under slip constraints. *IEEE Trans. on Intelligent Transportation Systems*, 16(6):3473–3478.

Marino, R. and Tomei, P. (2015). Output regulation for unknown stable linear systems. *IEEE Transactions on Automatic Control*, 60(8):2213–2218.

Marino, R., Tomei, P., and Verrelli, C. M. (2008). An adaptive tracking control from current measurements for induction motors with uncertain load torque and rotor resistance. *Automatica*, 44(10):2593–2599.

Merkle, C. L. and Athavale, M. (1987). Time–Accurate Unsteady Incompressible Flow Algorithm Based on Artificially Compressibility. *AIAA paper, 8th Computational Fluid Dynamics Conference Honolulu, U.S.A.*, 87–1137.

Mezić, I. (2005). Spectral properties of dynamical systems, model reduction and decompositions. *Journal of Nonlinear Dynamics*, 41:309–325.

Mezić, I. (2013). Analysis of fluid flows via spectral properties of the koopman operator. *Annual Review of Fluid Mechanics*, 45:357–378.

Mezić, I. and Banaszuk, A. (2004). Comparison of systems with complex behaviour. *Physica*, 197:101–133.

Moin, T. R. B. P. and Temam, R. (2001). Dns-based predictive control turbulence:an optimal benchmark for feedback algorithms. *Journal of Fluid Mechanics*, 447:179–225.

Moore, B. C. (1981). Principal component analysis in linear systems: controllability, observability, and model reduction. *IEEE Trans. on Automatic Control*, AC(1).

Moreau, E. (2007). Airflow control by non-thermal plasma actuators. *J of Physics D: Applied Physics*, 40:605–636.

Muscari, R. and Di Mascio, A. (2005). Simulation of the flow around complex hull geometries by an overlapping grid approach. In *Proceedings 5th Osaka Colloquium*, Osaka, Japan.

Muscari, R., Di Mascio, A., and Verzicco, R. (2013). Modeling of vortex dynamics in the wake of a marine propeller. *Computers and Fluids*, pages 65–79.

Noack, B. R., Papas, P., and Monkewitz, P. A. (2005). The need for a pressure-term representation in empirical galerkin models of incompressible shear flows. *Journal of Fluid Mechanics*, 523:339–365.

Orlov, D., Corke, T., and Patel, M. (2006). Electric circuit model for aerodynamic plasma actuator. *AIAA paper*, 1206:2006.

Ozaki, Y., Ohyama, T., Yasuda, T., and Shimoyama, I. (2000). An air flow sensor modeled on wind receptor hairs of insects. *IEEE 13th Annual Int. Conference on Micro Electro Mechanical System*, pages 531–536.

Pellegrini, R., Campana, E. F., Diez, M., Serani, A., Rinaldi, F., Fasano, G., Iemma, U., Liuzzi, G., Lucidi, S., and Stern, F. (2014). Application of derivative-free multi-objective algorithms to reliability-based robust design optimization of a high-speed catamaran in real ocean environment. In *Engineering Optimization IV - Rodrigues et al. (Eds.)*, page 15. CRC Press.

Pfeiffer, J. and King, R. (2012). Multivariable closed-loop flow control of drag and yaw moment for a 3d bluff body. *AIAA Paper, 6th AIAA Flow Control Conference, New Orleans, U.S.A.*, pages 2012–2802.

Pinto, A., Peri, D., and Campana, E. F. (2007). Multiobjective optimization of a containership using deterministic particle swarm optimization. *Journal of Ship Research*, 51(3):217–228.

Prahbu, R. D., Collis, S. S., and Chang, Y. (2000). The influence of control on proper orthogonal decomposition of wall-bounded turbulent flows. *Physics of Fluids*, 13(2):520–537.

Ravindran, S. S. (2000). A reduced-order approach for optimal control of fluids using proper orthogonal decomposition. *Internal Journal of Numerical Methods in Fluids*, 34:425–448.

Ravindran, S. S. (2002). Control of flow separation over a forward-facing step by model reduction. *Computational Methods in Applied Mechanics and Engineering*, 191:4599–4617.

Ravindran, S. S. (2006). Reduced-order controllers for control of flow past an airfoil. *International Journal for Numerical Methods in Fluids*, 50:531–554.

Riherd, M. and Roy, S. (2013). Serpentine geometry plasma actuators for flow control. *Journal of Applied Physics*, 114:083303.

Rowley, C. W. (2005). Model reduction for fluids, using balanced proper orthogonal decomposition. *International Journal of Bifurcation and Chaos*, 15(3):997–1013.

Rowley, C. W., Mezi/'c, I., Bagheri, S., Schlatter, P., and Henningson, D. S. (2009). Spectral analysis of nonlinear flows. *Journal of Fluid Mechanics*, 641:115–127.

Rowley, C. W., Mezi/'c, I., Bagheri, S., Schlatter, P., and Henningson, D. S. (2010). Reduced-order models for flow control: balanced models and koopman modes. *Seventh IUTAM Symposium on Laminar-Turbulent Transition*, pages 43–50.

Saad, Y. and Schultz, M. H. (1980). Variations on arnoldis method for computing eigenelements of large unsymmetric matrices. *Linear Algebra Applications*, 34:269–295.

Samimy, M., Kim, J.-H., Kastner, J., Adamovich, I., and Utki, Y. (2007). Active control of a mach 0.9 jet for noise mitigation using plasma actuators. *AIAA journal*, 45(4):890.

Santillo, M. A., Hoagg, J. B., Bernstein, D. S., and Powell, K. (2007). Adaptive disturbance rejection for flow in a duct with time-varying upstream velocity. *Proceedings of the 2007 American Control Conference, New York City.*

Sato, M., Aono, H., Yakeno, A., Nonomura, T., Fujii, K., Okada, K., and Asada, K. (2015a). Multifactorial effects of operating conditions of dielectric-barrier-discharge plasma actuator on laminar-separated-flow control. *AIAA journal.*

Sato, M., Nonomura, T., Okada, K., Asada, K., Aono, H., Yakeno, A., Abe, Y., and Fujii, K. (2015b). Mechanisms for laminar separated-flow control using dielectric-barrier discharge plasma actuator at low reynolds number. *Journal of Applied Physics*, 27:117101.

Scherpen, J. M. A. (1993). Balancing for nonlinear systems. *Systems and Control Letters*, 21:143–153.

Scherpen, J. M. A. (1996). H-infinity balancing for nonlinear systems. *International Journal of Robust and Nonlinear Control*, 7:475–505.

Scherpen, J. M. A. and van der Schaft, A. J. (1994). Normalized coprime factorizations and balancing for unstable nonlinear systems. *International Journal of Control*, 60(6):1193–1222.

Schmid, P. J. (2010). Dynamic mode decomposition of numerical and experimental data. *International Journal of Control*, 656:5–28.

Schmitz, F. W. (1967). *Aerodynamics of the Model Airplane: Airfoil measurements.* Translation Branch, Redstone Scientific Information Center, Research and Development Directorate, US Army Missile Command.

Seatzu, C. (2000). Decentralized controllers design for open-channel hydraulic systems via eigenstructure assignment. *Applied Mathematical Modelling*, 24(12):915–930.

Segawa, T., Pang, J., Ikehara, T., Maeda, R., and Yoshida, H. (2010). Mems-based cantilever sensor for fluid dynamics measurements. *Research Signpost ISBN: 978-81-308-0220-6*, pages 217–243.

Seifert, A., Darabi, A., and Wygnanski, I. (1996). Delay of airfoil stall by periodic excitation. *Journal of Aircraft*, 33:691–698.

Serani, A., Leotardi, C., Iemma, U., Campana, E., Fasano, G., and Diez, M. (2016). Parameter selection in synchronous and asynchronous deterministic particle swarm optimization for ship hydrodynamics problems. *Applied Soft Computing*, 49:313 – 334.

Shewchuk, J. R. (2002). Delaunay refinement algorithms for triangular mesh generation. *Computational Geometry*, 47(7):741–778.

Shyy, W., Jayaraman, B., and Andersson, A. (2002). Modeling of glow discharge-induced fluid dynamics. *Journal of Applied Physics*, 92(11):6434.

Singh, S. and Mittal, S. (2005). Flow past a cylinder: shear layer instability and drag crisis. *International Journal for Numerical Methods in Fluids*, 47(1):75–98.

Skarolek, V. and Karabelas, S. J. (2016). Energy efficient active control of the flow past an aircraft wing: RANS and LES evaluation. *Applied Mathematical Modelling*, 40(2):700–725.

Slotine, J.-J. E. and Li, W. (1991). *Applied nonlinear control*, volume 199. Prentice Hall Englewood Cliffs.

Smagorinsky, J. (1963). General circulation experiments with the primitive equations: I. the basic experiment. *Monthly Weather Review*, 91(3):99–164.

Spazzini, P. G., Iuso, G., Onorato, M., and Zurlo, N. (1999). Design, test and validation of a probe for time-resolved measurement of skin friction. *Measurement Science and Technology*, 10(7):631.

Spazzini, P. G., Iuso, G., Onorato, M., Zurlo, N., and Di Cicca, G. M. (2001). Unsteady behavior of back-facing step flow. *Experiments in Fluids*, 30(5):551–561.

Stratford, B. S. (1959). An experimental flow with zero skin friction throughout its region of pressure rise. *Journal of Fluid Mechanics*, 5:17–35.

Taira, K. and Colonius, T. (2009). Effect of tip vortices in low-reynolds-number post stall flow control. *AIAA Journal*, 47(3:749–756.

Thomas, F. O., Kozlov, A., and Corke, T. C. (2008). Plasma actuators for cylinder flow control and noise reduction. *AIAA journal*, 46(8):1921.

Tian, Y., Song, O., and Cattafesta, L. (2006). Adaptive feedback control of flow separation. *AIAA paper, Third AIAA Flow Control Conference, San Francisco, California*, 3016(2006).

Toda, H. B., Truffin, K., Bruneaux, G., Cabrit, O., and Nicoud, F. (2015). Assessment of subgrid-scale models for large-eddy simulation of complex flows. *Book of Abstracts-Extract*, page 11.

Unfer, T. and Boeuf, J. P. (2009). Modelling of a nanosecond surface discharge actuator. *Journal of Physics D: Applied Physics*, 42:194017–194029.

Van Leer, B. (1979). Towards the ultimate conservative difference scheme V. A second-order sequel to Godunov's method. *Journal of Computational Physics*, 32:101–136.

Wang, J. J., Choi, K.-S., Feng, L. H., Jukes, T. N., and Whalley, R. D. (2013). Recent developments in DBD plasma flow control. *Progress in Aerospace Sciences*, 62:52–78.

Whittlesey, R. W., Liska, S., and Dabiri, J. O. (2010). Fish schooling as a basis for vertical axis wind turbine farm designthe technology described in this paper is protected under both us and international pending patents filed by the california institute of technology. *Bioinspiration & Biomimetics*, 5(3):035005.

Willcox, K. and Peraire, J. (2002). Balanced model reduction via the proper orthogonal decomposition. *AIAA Journal*, 40(11):2323–2330.

Willcox, T. B.-T. K., Ghattas, O., and van Bloemen Waanders, B. (2007). Goal-oriented, model-constrained optimization for reduction of large-scale systems. *Journal of Computational Physics*, 224(2):337–355.

Xu, S., Rempfer, D., and Lumley, J. (2003). Turbulence over a compliant surface: numerical simulation and analysis. *Journal of Fluid Mechanics*, 478):11–34.

Yang, Q. and Chung, Y. M. (2015). Numerical study of reducing turbulent skin-friction drag using DBD plasma actuators. *EDRFCM 2015, Cambridge*.

Zaghi, S., Broglia, R., and Di Mascio, A. (2011). Analysis of the interference effects for high-speed catamarans by model tests and numerical simulations. *Ocean Engineering*, 38(17):2110–22.

Zaghi, S., Di Mascio, A., Broglia, R., and Muscari, R. (2015). Application of dynamic overlapping grids to the simulation of the flow around a fully-appended submarine. *Mathematics and Computers in Simulation*, 116:75–88.

Zhou, K., Salomon, G., and Wu, E. (1999). Balanced realization and model reduction for unstable systems. *Internatioal Journal of Robust and Nonlinear Control*, 3:183–198.